Investigation of the Precipitation Behavior in Aluminum Based Alloys

Dissertation by:

Muna Saeed Khushaim

In Partial Fulfillment of the Requirements for the Degree of Doctor of Philosophy

Materials Science and Engineering

King Abdullah University of Science and Technology

Thuwal, Kingdom of Saudi Arabia

November 2015

The dissertation of Muna Khushaim is approved by the examination committee:

Committee Chair: Alexander Rothenberger

Committee member: Udo Schwingenschlögl

Committee member: Boon S. Ooi

Committee member: Hala Aljawhari

Abstract

Investigation of the Precipitation Behavior in Aluminum Based Alloys

Muna Saeed Khushaim

The transportation industries are constantly striving to achieve minimum weight to cut fuel consumption and improve overall performance. Different innovative design strategies have been placed and directed toward weight saving combined with good mechanical behavior. Among different materials, aluminum-based alloys play a key role in modern engineering and are widely used in construction components because of their light weight and superior mechanical properties. Introduction of different nano-structure features can improve the service and the physical properties of such alloys. For intelligent microstructure design in the complex Al-based alloy, it is important to gain a deep physical understanding of the correlation between the microstructure and macroscopic properties, and thus atom probe tomography with its exceptional capabilities of spatially resolution and quantitative chemical analyses is presented as a sophisticated analytical tool to elucidate the underlying process of precipitation phenomena in aluminum alloys.

A complete study examining the influence of common industrial heat treatment on the precipitation kinetics and phase transformations of complex aluminum alloy is performed. The qualitative evaluation results of the precipitation kinetics and phase transformation as functions of the heat treatment conditions are translated to engineer a complex aluminum alloy. The study demonstrates the ability to construct a robust microstructure with an excellent hardness behavior by applying a low-energy-consumption, cost-effective method. The proposed strategy to engineer complex aluminum alloys is based on both mechanical strategy and intelligent microstructural design.

An intelligent microstructural design requires an investigation of the different strengthen phases, such as $T_1(Al_2CuLi)$, $\theta'(Al_2Cu)$, $\beta'(Al_3Zr)$ and $\delta'(Al_3Li)$. Therefore, the early stage of phase decomposition is examined in different binary Al-Li and Al-Cu alloys together with different ternary Al-Li-Cu alloys. Atom probe tomography and statistical testing are combined to investigate the fine scale segregation effects of dilute solutes in aluminum alloys.

The optimum application of atom probe tomography in a wide range of materials is enabled by the integration of a laser pulse mode in the atom probe analysis. However, the nature of the laser mechanism used during atom probe tomography analyses is still debated. Systematic investigation of the microstructural change of $\delta'(Al_3Li)$ precipitates influenced by different pulsed laser energies are used to describe the important phenome associated with the laser pulse mode. In this study, atom probe tomography presented a series of snapshots during *in-situ* reversion of $\delta'(Al_3Li)$ precipitates, initiated by laser irradiation, using different laser energies for the first time. An estimation method to investigate real sample temperatures during laser-APT analyses using an interface reaction itself as a probe has been proposed.

Finally, the considerable potential of aluminum liquid is demonstrated as a powerful synthesis solvent of important intermetallic phases such as: Mg_2Si, Al_2Mg and *CaMgSi* .The atom probe tomography technique is utilized to characterize the intermediate reaction steps of the flux-grown intermetallic phases. The study proposed a direct approach to investigate the involved reactions during the formation of the synthesized intermetallic phase.

Acknowledgment

Firstly, I would like to express my deepest gratitude to Prof. Talaat Al-Kassab, my ex-supervisor in nano-tomography group. Neither this work nor to the PhD would have been possible without his endless supply of enthusiasm and knowledge.

My appreciation and sincere thanks to my advisor, Prof. Alexander Rothenberger, for his continuous help, for the provided opportunity to carry on this research project and for his continuous support during my whole stay in his group.

Enormous thanks to Dr. Ryota Gemma, research scientist in nano-fabrication core lab, who was my daily supervisor and mentor. His great experience with the tool together with his pragmatic knowledge of the atom probe helped me during my work.

Gratitude thanks to Dr. Torben Boll and Dr. Catharina Wille, who were my earlier teachers on atom probe. Many thanks for them for giving me an opportunity of learning from their expertise, patience, persistence and knowledge.

Thank you to all members of Rothenberger group. I enjoyed the friendly atmosphere, and in particular, special thanks to Dr. Bambar Davaasuren. His advices and always wise words helped me to overcome the difficulties found during this work.

I shall not forget about Prof. Ferdinand Haider and his group in Augsburg University, who welcomed me during my several business visits. I had a great opportunity to learn and gain knowledge directly from experts.

Finally, My heartfelt gratitude is extended to my husband, kids, parents, family and friends for the encouragement to pursue my dreams, for helping me surpass the difficulties and foremost for their love and comprehension.

Table of contents

Page

Abstract 3
Acknowledgment 5
List of Abbreviation 10
List of Figures 12
List of Tables 21
Chapter 1: Introduction 22
1.1 Objective and structure of dissertation 22
1.2 Al-based alloy; an age-hardenable alloy 24
1.2.1 The $T_1(Al_2CuLi)$ phase 26
1.2.2 The $\theta'(Al_2Cu)$ phase 29
1.2.3 The $\delta'(Al_3Li)$ phas 29
1.2.4 The $\beta'(Al_3Zr)$ phase 32
1.2.5 Other important phase 32
1.3 Theory of precipitation hardening 34
Chapter 2: Experimental Methods and Techniques 39
2.1 Field ion microscopy (FIM) and atom probe tomography (APT) 39
2.1.1 Sample preparation by means of electro-polishing 39
2.1.2 Sample preparation by means of focused ion beam (FIB) 41
2.1.3 Field ion microscopy (FIM) 43
2.1.4 Atom probe tomography (APT) 46
2.1.5 Reconstruction methods and algorithms 53
2.1.5.1 Proximity histogram (proxigram) 53

2.1.5.2 Concentration depth profile…….54

2.1.5.3 Cluster identification algorithm...……55

2.1.5.4 The χ^2 test……..…….56

2.2 Transmission electron microscopy (TEM)…….……...……57

2.3 Hardness test (HT)……,……..59

2.4 Differential scanning calorimetry (DSC)……..…….……61

2.5 Inductively coupled plasma optical emission spectrometry (ICP-OES)……62

2.6 Scanning electron microscopy and X-ray spectrometry (SEM/ EDX)…..….63

2.7 X-Ray diffraction…….……64

Chapter 3: Results and Discussion……..……..……66

3.1 Influence of industrial heat treatment on precipitation kinetics in a complex aluminum alloy……..66

3.1.1 Materials and methods…….……...……70

3.1.2 Hardness properties……...……72

3.1.3 TEM evolution of the microstructure……....…….73

3.1.4 Thermal characterization……..……...……76

3.1.5 FIM evolution of the microstructure……..……79

3.1.6 APT analysis……..…….……80

3.1.6.1 Naturally aged samples at T4 temper…….……..…81

3.1.6.2 Cold working and artificial aging of the sample at T8 temper……...……84

3.1.6.3 Artificial aging of the sample at T6 sample……89

3.1.7 Conclusion……..…….…….92

3.2 Characterization and engineering of an Al alloy AA 2195…….……93

3.2.1 Characterization of an Al alloy AA2195…….……..93

3.2.1.1 Materials and methods……96

3.2.1.2 STEM evolution of the microstructure…….…..……97

3.2.1.3 APT analyses……..98

3.2.1.4 Conclusion…….…….……..…….111

3.2.2 Engineering of an Al alloy AA2195……...…….…….112

3.2.2.1 Materials and methods……...……113

3.2.2.2 Hardness curves…….…….…...……115

3.2.2.3 APT analysis……..…….……..117

3.2.2.4 Conclusion…….…….……..120

3.3 Early stage of precipitation on binary Al – Li, Al – Cu alloys and ternary Al – Li – Cu alloys……...120

3.3.1 Materials and methods…….……122

3.3.2 APT analyses…….…..123

3.3.3 Conclusion……...……140

3.4 Laser-induced reversion of δ' precipitate in Al – Li alloys: study of temperature rise in the pulsed-laser atom probe……..142

3.4.1 Materials and methods……..……144

3.4.2 Experimental results and theoretical model……..145

3.4.3 Conclusion……..……..162

3.5 APT study of the growth of a single crystal phase synthesized using a molten Al flux…….……..163

3.5.1 Materials and methods……...……..164

3.5.2 Basic characterization……...……...166

3.5.3 APT analyses……..…….170

3.5.4 Conclusion…….…….…….177

Chapter 4: Summary and Future Work…….……..178

4. 1 Summary……..……178

4. 2 Future work…….……180

Appendixes……..……..……182

Appendix A: Influence of laser pulse mode on the microstructure of different Al-based alloy……...182

Appendix B: Synthesis of Al – Cu – Zn alloys…….……..…184

References.....192

Publications…….……...……..203

List of Abbreviations

Definition	Abbreviation
Atom probe tomography	APT
Back scattering electrons	BSEs
Differential scanning calorimetry	DSC
Electron energy loss spectroscopy	EELS
Field ion microscopy	FIM
First stage of heat treatment	1S
Focused ion beam	FIB
Guinier and Perston Zones	GP
High-angle annular bright field	HAABF
High-angle annular dark field	HAADF
Hardness test	HT
High resolution transmission electron microscopy	HRTEM
International alloy designations system	IADS
Inductively coupled plasma optical emission spectrometry	ICP-OES
Laser assisted wide angle tomographic atom probe	LAWATAP
Local electrode atom probe	LEAP
Micro channel plates	MCPs
Normal direction	NR
Optical rectification	OR
Precipitate free zone	PFZ
Region of interest	ROI
Roll direction	RD

Scanning electron microscopy	SEM
Scanning transmission electron microscopy	STEM
Secondary electrons	SEs
Second stage of heat treatment	2S
Selected area diffraction pattern	SADP
Small angle X-ray scattering	SAXS
Super-saturated solid solution	SSSS
Time of flight	TOF
Third stage of heat treatment	3S
Thermal pulse model	TPM
Transmission electron microscopy	TEM
Vickers hardness number	VHN
X- Ray diffractometer	XRD
X - ray spectroscopy	EDX

List of Figures

Page

Figure 1.1 Major steps of the heat treatment…….. 27

Figure 1.2 Diagram showing steps of common heat treatment temper…… 28

Figure 1.3 Al – Li – Cu phase diagram (Isothermal section at 350˚C)…….. 30

Figure 1.4 Crystal structure for the T_1 phase……... 30

Figure 1.5 Al-rich corner of the Al – Cu phase diagram…… 31

Figure 1.6 Crystal structure for the θ′ phase…… 31

Figure 1.7 Binary Al – Li phase diagram…… 32

Figure 1.8 Crystal structure for the β′ and δ′ phases……... 33

Figure 1.9 Al-rich side of Al – Zr phase diagram…… 34

Figure 1.10 Crystal structure of $MgCaSi$ and Mg_2Si phases……..…. 36

Figure 1.11 Relationship between strength and particle size for a typical age-hardening alloy…….…….. 37

Figure 2.1 Bulk samples in blanks (matchstick shaped) and in wire shape. Sample has to be fixed in Cu holder prior to electro-polishing procedure…… 40

Figure 2.2 Schematic diagram and photos of the experimental set-up for standard electro-polishing procedure…… 41

Figure 2.3 Optical micrograph of polished samples (a) An ideal shape. (b) Examples of bad shaped samples…… 42

Figure 2.4 Steps of preparation APT sample using lifted-out method (a) Selection the region of interest. (b) Deposition of Pt protection layer. (c) Cutting cross section lamella. (d) Lift out the sample by using Omniprobe. (e) An image of a commercial microtip array. (f) Lift-out lamella attached to the Si microtip by using Pt deposition…. 44

Figure 2.5 An annular milling of the tip. (a) Milling pattern. (b) The final ideal shape of APT tip…….. 45

Figure 2.6 Schematic drawing of a field ion microscope…… 45

Figure 2.7 Imaging mechanism in FIM (a) Schematic drawing of the field ionization process of imaging gas atoms over the hemi-spherical tip surface. (b) Field ion micrograph of Al – Cu alloy illustrating the position of different crystallographic poles in the tip……. 47

Figure 2.8 Representation of tip apex at atomic scale showing the preferential ionization sites……. 48
Figure 2.9 Schematic representation of needle-shaped sample used in APT…… 48
Figure 2.10 Schematic drawing of FIM and APT. For FIM operation the MCP/Screen stands in front of the sample tip, while for APT mode this screen is down. The used detector is the delay line detector……. 50
Figure 2.11 Schematic drawing of the delay-line detector……. 51
Figure 2.12 Obtained mass spectrum for complex Al alloy…….. 52
Figure 2.13 Atom map showing distribution of Al, Cu, Li, Mg and Ag atoms in a complex Al alloy……. 53
Figure 2.14 Pictures of used APTs…….. 55
Figure 2.15 Schematic view of the TEM……. 58
Figure 2.16 Schematic drawing of a diamond indenter in micro- and nano-indentation tests……. 60
Figure 2.17 Differential scanning calorimetry, sample and reference holder (Top view)……. 61
Figure 2.18 Schematic view of an ICP-OES…… 63
Figure 2.19 Illustration of the interaction zone of electrons and specimen atoms below a specimen surface…… 64
Figure 3.1 typical relationships between strength and toughness for complex Al alloy.. 68
Figure 3.2 Required tools for heat treatment procedure……. 72
Figure 3.3 SEM micrographs of the prepared APT tips. (a) An ideal tip. (b) An oxide tip……. 73
Figure 3.4 A deep insight on the microstructure of the APT tip of complex Al alloy prepared via the FIB method showing the presence of damaging……. 74
Figure 3.5 The top view of the reconstructed volume of the AA2195 alloy shows the position of crystallographic pole and the sub-volume showing the perpendicular atomic planes to this pole……. 75
Figure 3.6 Hardness evolution during the heat treatment of the alloy for different temper conditions; T4, T8 and T6……..… 76
Figure 3.7 Evolution of the microstructure as observed by TEM. (a) Typical bright field image of the specimen after conducting the T4 heat treatment shows the presence of β′ precipitates within the microstructure and the corresponding [101] selected area

diffraction pattern (SADP). (b) Bright field image of the microstructure conducting T8 heat treatment condition shows a complex microstructure with the T_1, θ' and β' precipitates and the corresponding [101] selected area diffraction pattern (SADP). (c) Microstructure of the specimen after the T6 heat treatment condition consists of T_1 precipitates as the primary strengthening phase and the corresponding [101] selected area diffraction pattern (SADP)…… 77

Figure 3.8 DSC traces of the specimens in three temper treatments; T4, T8 and T6… 78

Figure 3.9 Field ion micrographs for the alloy AA2195 after conducting the three industrial heat treatments, the (a) T4, (b) T8 and (c) T6 conditions (All of the precipitates are brightly imaged)…….. 81

Figure 3.10 The reconstructed volume of the sample in the T4 condition analyzed using LAWATAP. (a) Exploration of the distribution of the β' precipitates in an Al matrix. (b) A proxigram composition profile from the isoconcentration surface of 5 at.% Zr (c) The top view of the reconstructed volume displays separately the alloying elements: Zr, Li, Cu, Mg and Ag. The figure indicates the segregation behavior of solute atoms at the β'/ matrix interface……...…….. 83

Figure 3.11 The reconstructed volume and the FIM image for the specimen under T4 heat treatment condition showing the homogenous distribution of all alloying elements..... 84

Figure 3.12 LAWATAP analysis of the sample following T8 heat treatment (a) The reconstructed volume of the sample displayed with isoconcentration surfaces of 4 at.% Cu delineate θ'precipitates. (b) Corresponding combined proxigram composition profile based on these isoconcentration surfaces……. 86

Figure 3.13 LAWATAP analysis of the sample following T8 heat treatment. (a) The reconstructed volume shows the fine distribution of the T_1 platelets which intersect each other's. (b) The chemical composition as estimated from the concentration composition profile based on the isoconcentration surface containing more than 6 at.% Li……. 87

Figure 3.14 LAWATAP analysis of the sample at the later stage of the aging process shows the growth of the T_1 platelet via a ledge mechanism and absence of the θ'platelets in the microstructure……...…….. 89

Figure 3.15 LAWATAP analysis of the sample in T6 condition (a) The reconstructed volume of the microstructure shows a uniform distribution of the T_1 platelets. (b) A

combined proxigram profile corresponding to the T_1 platelets, which are delineate by 5 at.% Li isoconcentration surfaces. (c) An inhomogeneous distribution of Cu and Mg in the Al matrix indicates the growth of the T_1 platelet in the Mg enriched region, which contains localized Ag atoms. (d) Proxigram concentration profile quantifies the chemical composition of the enriched regions in (c)……..... 90

Figure 3.16 Coarsening behavior of the θ' platelets at T6 condition…….... 93

Figure 3.17 Schematic representation of the sub-structure of deformed Al alloy…… 95

Figure 3.18 High angle annular bright field scanning transmission electron microscopy image showing the heterogeneous formation of a bright imaging platelet precipitate at the grain boundary and the distribution of platelets and spherical precipitates within the matrix……. 98

Figure 3.19 TEM bright field image shows the nucleation of the T_1 platelet at the grain boundary and inside the grain…….. 99

Figure 3.20 LAWATAP analysis of the microstructure at 30 K and 20% of pulse fraction. (a) Reconstructed volume showing the distribution of the T_1 and θ' phases. (b) Corresponding proxigram composition profile for the T_1 platelet. (c) Corresponding combined proxigram composition profile for the θ' platelet…….…... 100

Figure 3.21 Rolling texture of FCC material…….. 102

Figure 3.22 Cutting APT sample in [112] direction and then rotating the sample to be in [111] direction…….. 103

Figure 3.23 LAWATAP analysis for the specimen with rolling texture with the same experimental parameters as in Figure 3.20. (a) Reconstructed volume showing three out of four orientations of the T_1 precipitate on the {111} matrix planes. (b) Magnified view of the T_1 platelet with resolved {111} planes reveals the distribution of Mg within the T_1 platelet. (c) Corresponding proxigram composition profile for the T_1 platelet on the {111} plane……. 104

Figure 3.24 Rotation of the reconstructed volume in Figure 3.23 by 60° around the z axis. (a) The presences of θ' platelet in the bottom part of the reconstructed volume (b) Proxigram composition profile for the θ' platelet…… 105

Figure 3.25 Estimation of the accurate thickness for the T_1 platelet……. 106

Figure 3.26 LAWATAP analysis with new experimental parameters 25 K and 22.5% of pulse fraction. (a) Reconstructed volume shows T_1 and θ' platelets. (b) Corresponding proxigram composition profile for θ' gives an optimistic chemical

composition (c) Corresponding combined proxigram composition profile for T_1 platelet……. 108

Figure 3.27 LEAP analysis at 22 K and 18% of pulse fraction. (a) Top view of the reconstructed volume of a sample shows the intersections of the T_1platelets with the (111) pole. (b) Corresponding combined proxigram composition profile for T_1 platelets…….. 111

Figure 3.28 The magnified view of the T_1 platelet showing the density of Cu, Li and Mg atoms at the matrix/ precipitates interface…… 112

Figure 3.29 Required geometry of tensile sample…….. 114

Figure 3.30 Required tool of ageing treatment of stretched Al alloy…… 116

Figure 3.31 Relationship between the ageing time and the hardness values for AA2195 alloys aged at 150 °C for (a) 0 %. (b) 1 %. (c) 2 %. (d) 3 %. (e) 4 %. (f) 5 % stretching levels…….. 117

Figure 3.32 LAWATAP analysis of sample at 1 % deformation level (Aged for 10 h at 150 °C) (a) The top view of the reconstructed volume showing the nice distribution of the nano-features. (b) Composition profile proxigram of the observed T_1 platelets…… 119

Figure 3.33 Summary of the preparation procedure of binary Al – Cu, Al – Li alloys and ternary Al – Cu – Li alloy…….. 125

Figure 3.34 Crystal structures of Cu rich phases in Al – Cu alloy. (a) For GPI-zone. (b) For GPII(θ'')-zone. (c) For θ' phase. (d) For θ phase……..… 126

Figure 3.35 Typical obtained mass spectrum of Al – 1.7 at.% Cu alloy showing the presence of hydrides peaks…… 127

Figure 3.36 Cu distribution within Al – 1.7 at.% Cu datasets corresponding to three stages of heat treatments: (a) 1S. (b) 2S. (c) 3S. (d) Binomial and experimental frequency distribution…… 129

Figure 3.37 Cu distribution within Al – 1.7 at.% Cu datasets corresponding to: (a) Heat treated with increasing aging time to 30 min at 200 °C (b) Binomial and experimental frequency distribution…… 130

Figure 3.38 Cu distributions within Al – 1.7 at.% Cu dataset corresponding to aging the alloy for 8 h at 160 °C. (a) The reconstructed volume showing the presence of platelet feature. (b) Binomial and experimental frequency distribution. (c) Composition profile of the θ' platelet from isoconcentration surface of 8 at.% Cu……..……. 131

Figure 3.39 Li distribution within Al-8.2 at.% Li datasets corresponds to two stages of the heat treatments(1S, 2S): (a) The reconstructed volume. (b) Binomial and experimental frequency distribution. (c) Distribution of Al-Li clusters with the chemical composition profile……. 134

Figure 3.40 Li distribution within Al-8.2 at.% Li dataset for the 3S aging condition. (a) The reconstructed volume. (b) Binomial and experimental frequency distribution. (c) Distribution of Al-Li clusters with the chemical composition profile and the inset corresponds to isoconcentration surface of 10 at.% Li…… 135

Figure 3.41 Cu and Li distribution within Al-4 at.% Li-1.7 at.% Cu datasets corresponding to the two stages of the heat treatments,1S and 2S. (a) The reconstructed volume. (b) Binomial and experimental frequency distribution for both Cu and Li atoms……. 137

Figure 3.42 Cu and Li distribution within Al – 4 at.% Li – 1.7 at.% Cu dataset corresponding the 3S aging condition. (a) The reconstructed volume showing inhomogeneity in Cu distribution. (b) Binomial and experimental frequency distribution for both Cu and Li atoms. (c) Proxigram through the 22 at.% Cu isosurface of the enriched Cu region visualizes the precipitation of the θ' platelet…….. 138

Figure 3.43 Cu and Li distribution within Al – 8.2 at.% Li – 1.7 at.% Cu dataset corresponding to the 3S aging condition. (a) The reconstructed volume. (b) Binomial and experimental frequency distribution for both Cu and Li atoms…….. 140

Figure 3.44 Cu and Li distribution within Al – 8.2 at.% Li – 1.7 at.% Cu dataset corresponding to aging the alloy for 30 min at 160 °C. (a) The reconstructed volume showing the presence of δ' particles (magnified view showing the distribution of δ' in the matrix based on 5 at.% Li isoconcentration surface). (b) Binomial and experimental frequency distribution for both Cu and Li atoms…… 141

Figure 3.45 Initial microstructure of the tip analyzed by the voltage mode. (a) The reconstructed volume showing the distribution of spherical δ' precipitates (b) Linear composition profile along the cylinder with the size of (x, y = 11 nm and z = 20 nm) perpendicular to the isoconcentration surfaces delineate region containing 14 at. % Li. The average concentration of Li in the precipitate is c_p = (22.6 ± 0.9) at.% and in the matrix is c_t = (5.4 ± 0.8) at.%..... 146

Figure 3.46 Field strength of evaporation E_F applied in reconstruction as a function of the laser energy E…….. 147

Figure 3.47 Comparison of the morphology of the δ' precipitates under illumination of the laser pulses at various values of energy *E* measured for different samples: (a) 10, (b) 30, (c) 40, (d) 50, (e) 60, (f) 80 and (g, h) 100 pJ…… 148

Figure 3.48 Scanning electron micrographs showing the geometry of the tip apex (a) before and (b) after APT analysis by the laser pulse mode at 100 pJ……. 150

Figure 3.49 Field ion micrographs of the aluminum lithium specimen (a) Taken for the specimen after analysis by the voltage pulse mode, shows the distribution of darkly imaged $\delta'(Al_3Li)$ precipitates as marked by circles. (b) Taken for the specimen after analysis by the laser pulse mode at the laser energy *E* = 100 pJ, shows a homogenous microstructure, with different concentric rings corresponding to different crystallographic poles…… 151

Figure 3.50 Measured matrix Li concentrations c_{Li} in the tip analyzed by the voltage pulse mode and by the laser pulse mode at different values of laser energy as a function of the laser energies *E* (in voltage mode, *E* = 0 pJ)……. 154

Figure 3.51 Arrhenius plot of effective diffusion coefficients *D* estimated by using Eqs. (3.5) and (3.6). Estimated values are compared with *D* values of the bulk Al-Li system [22] (broken line) calculated via Eq. (3.6)…….. 156

Figure 3.52 Laser-induced specimen temperature rise *dT* plotted against field strength of evaporation E_F. Inversely proportional relationship between E_F and *dT* is shown (At 100 pJ, *dT* is extrapolated from the linear relationship due to the lack of information on diffusion length *L)*……. 157

Figure 3.53 Comparison of the experimental Li concentrations and the estimated temperatures with an Al-Li phase diagram adapted from [22, 150]. The data obtained at *E* = 10 – 80 pJ agree with the miscibility gap, at well below the T_c. At 100 pJ, the tip temperature is estimated to be in the range of solvus temperature of δ' precipitates…… 160

Figure 3.54 Comparing of the morphology and composition of δ' precipitates before and after laser analysis: (a) The top view of the reconstructed volume of the tip analyzed by voltage pulse mode. (b) The top view of the reconstructed volume of the tip analyzed by laser pulse mode at 100 pJ. (c) The top view of the reconstructed volume of the tip analyzed by voltage mode after conducting laser analysis showing the permeant effect of the heating on the δ' precipitates(d) Composition profile along the cylinder with the size of (x, y = 15 nm and z = 80 nm) perpendicular to Li enriched

regions in (b). (e) Composition profile along the cylinder with the size of (x, y = 10 nm and z = 65 nm) perpendicular to Li enriched regions in (c)……. 161
Figure 3.55 Used Ta crucible for synthesize…… 165
Figure 3.56 Illustration Chart of the applied temperature program…….. 165
Figure 3.57 XRD diffraction pattern for the synthesized material…… 167

Figure 3.58 Optical micrograph of the microstructure of the synthesized material…… 168
Figure 3.59 SEM micrograph of the microstructure of the synthesized material……. 169
Figure 3.60 A magnified SEM image of the synthesized material showing the appearance of different phases: $CaMgSi$, Mg_2Si, Al_2Mg and $AlMg$……. 170
Figure3.61 SEM micrograph shows the selected areas of interest for the subsequent APT analysis…….. 171

Figure 3.62 APT analysis of the flux region. (a) SEM micrograph showing the measured radius at the apex of the prepared APT tip. (b) The reconstructed volume showing the distribution of different elements. (c) The desorption map. (d) The corresponding mass spectrum…….. 172
Figure 3.63 APT analysis of the Mg_2Si region. (a) SEM micrograph showing the position of the lamella for the prepared APT tip. (b) The reconstructed volume showing the distribution of different elements. (c) The desorption map. (d) The corresponding mass spectrum…… 173
Figure 3.64APT analysis of the interface region between the flux and single crustal phase. The top view of the reconstructed volumes illustrates the distribution of different phases……. 174
Figure 3.65 APT analysis at region of $CaMgSi$ phase…….……... 175
Figure 3.66 A series of the small cutting volumes together with their corresponding depth concentration profiles. (a) At Ca_2Si and Al_2Mg phases. (b) At $AlMg$ and $CaMgSi$ phases. (c) At Mg_2Si phase……. 176
Figure A.1 laser APT analysis of the Al-8.2 at. % Li alloy showing the presence of small clusters of Li atoms in the microstructure……. 182
Figure A.2 Top view of the reconstructed volume of laser APT analysis of the AA2195 showing the damaging effects of the laser on the microstructure……. 183
Figure B. 1 Image of glass carbon crucible……. 185
Figure B. 2 Illustration Chart of the as-cast condition…….. 185

Figure B. 3 Illustration Chart of the annealed condition…….. 186
Figure B. 4 synthesis alloys by using arc-melter method yielded good Al – Cu alloy and unsuccessful Al – Cu – Zn alloy…….. 186
Figure B. 5 Image of the indention impact on the alloy surface…….. 187
Figure B. 6 Hardness behavior for all synthesis alloys: Alloy 1 (Al – 30 at. % Cu – 20 at. % Zn), Alloy 2 (Al – 30 at. % Cu – 10 at. % Zn), Alloy 3 (Al – 30 at. % Cu – 4 at. % Zn) and Alloy 4 (Al – 33 at. % Cu). (AC) is referred to "as cast condition" and A is referred to "annealed condition"…….. 188

List of Tables

Page

Table 1.1 Aluminum alloy designations for wrought alloys……. 26

Table 1.2 Common industrial aluminum heat treatment tempers……. 28

Table 1.3 Phases of interest in commercially used Al-Li-Cu……. 29

Table 3.1 A summary of mechanical properties for AA2195 heat treated with T8, T6 and T4 tempers…….. 70

Table 3.2 Chemical composition of alloying elements in AA2195……. 71

Table 3.3 Names and description of the three applied aging conditions…… 123

Table 3.4 Comparing between nominal and measured chemical composition of analyzed Al – 1.7 at.% Cu alloy…… 126

Table 3.5 Summary of the data obtained for the diameter d, number density N_v, volume fraction f, Li composition c_{p} in the precipitates and Li composition c_{t} in the matrix for the sample analyzed both in the voltage mode and laser mode at various values of laser energy. f was calculated by Eq. (3.2)…….. 155

Table 3.6 The calculated diffusion lengths and effective diffusion coefficients for Li atoms from the precipitates and the estimated temperatures corresponding to each point of the laser energy…… 155

Table 3.7 A summary of the phases observed in the synthesized material and their chemical composition…… 172

Table B.1 A summary of the microstructure evaluation of synthesized alloys…….. 189

Chapter 1

Introduction

1.1 Objective and structure of dissertation:

A major challenge in modern metallurgy and materials physics is the improvement of the properties of the materials. When developing materials for industrial applications, it is important to achieve material properties that match the application. For instance, in an engineering application of structural materials, strength is, without a doubt, an important parameter. However, it is by no means the only important one, and, usually, a material must provide a combination of different important properties. To systematically create materials with desired properties, a deeper understanding of the underlying processes is required.

The safety and predictability of a material's behavior are key drivers in the selection of materials for aircraft parts, military applications and space applications. Additionally, weight reduction by employing lighter alloys or compositions and higher-strength materials with smaller cross sections are increasingly becoming keys to the success of an aircraft, automobiles and other means of transportation, where operating costs are paramount. Moreover, a need for less frequent maintenance by improving the corrosion resistance to stress corrosion and achieving better fatigue strength and greater tolerance to damage service are all important factors in the selection of materials for the above-mentioned applications [1].

Among different materials, aluminum-based alloys play a key role in modern engineering. They have been widely used in automotive, aerospace and construction engineering due to their good corrosion resistance, superior mechanical properties, good machinability, good weldability and relatively low cost [2, 3]. The progress in practical application has been determined by the intensive research and developmental works on such alloys.

For the past several decades, aluminum alloys have been the primary material choice for structural components of aircraft and automobiles. Well-known performance characteristics, known fabrication costs, design experience and established manufacturing methods are the reasons for the continued confidence in

aluminum alloys, ensuring their use in significant quantities for the rest of this century [4]. However, in the early years, aluminum alloys were developed by trial-and-error. For the time being, the improvement of Al – based alloy has been performed based on the understanding of the relationships among compositions, processing, microstructural characteristics and properties.

The main approach to develop the mechanical properties of aluminum alloys and, in particular, their strength is precipitation hardening, which was discovered by the German metallurgist Alfred Wilm [4], who was tried to improve the strength of Al-Cu alloy by applied the quenched procedure alone. This quenched procedure increased the strength of the steel samples, but did not show any effect in the case of Al-Cu alloy. Accidentally, some of quenched of Al-Cu alloys had been left for a period of time and then had been tested. Surpassingly, those samples showed increasing in their hardness. This improvement on the hardening behavior has been explained latter as a result of the formation of finely, dispersed particles with nano size known as precipitates. By this, the precipitation hardening phenomena was firstly recognized by Alfred William. Different nano-scale structure features, such as nano-precipitation, dislocation structure and segregation of solute atoms, further increase the alloy's strength. The nano-structure of the aluminum alloys can improve not only their mechanical strength but also their service, chemical and physical properties, making them attractive for structural and functional applications. However, the interactions between different nano-features, such as precipitates, which can be introduced into aluminum alloys during the thermo-mechanical process, are rather complex and have yet to be fully understood. Moreover, slight modification of the alloy composition alters all the properties of the alloy. Thus, tracing a local chemistry on an atomic scale is crucial.

Rapid development of the state-of-the art techniques for microstructural characterization at the nano and atomic scales has provided deeper insight into the microstructure-properties relationship. Owing to its exceptional capabilities of spatially resolution and quantitative chemical analyses, atom probe tomography (APT) has opened up a direct access to the local chemistry of materials since the late 1990s. Therefore, APT is presented as a sophisticated characterization tool to elucidate the underlying process of precipitation phenomena in aluminum alloys.

Within the frame of this work, a combination of structural characterizations by means of X-ray diffractometry (XRD), scanning electron microscopy (SEM), hardness testing (HT), inductively coupled plasma optical emission spectrometry (ICP-OES), differential scanning calorimetry (DSC), field ion microscopy (FIM) and transmission electron microscopy (TEM), in addition to quantitative chemical analysis by means of APT, have yielded the optimum analysis to systematically characterize the finest details of the precipitation sequence and kinetics. Moreover, an increasing demand for the improved control of the properties requires knowledge about diffusion processes, solute clustering, nucleation, growth and phase transformation. In this context, all of these phenomena in aluminum-based alloys have been investigated.

The theoretical background of the precipitation hardening phenomenon, thermodynamics and the phases of the investigated aluminum alloys will be discussed in within this chapter. Chapter 2 will introduce the experimental methods and techniques employed with consideration of algorithms and evolution procedures in combination with respective measurement conditions and preparation procedures. An overview of the results will be outlined in Chapter3, together with the discussion and literature. Finally, a summary and outlook are presented in Chapter 4.

1.2 Al-based alloy; an age-hardenable alloy:

The transportation industries are constantly striving to achieve minimum weight to cut fuel consumption and improve overall performance. Reducing the density of structural materials has been shown to be the most efficient solution to this problem [5]. Because aluminum alloys compose between 70 and 80% of the weight in current aircraft, recent alloy development programs have focused on reducing the density of these materials [6]. Lithium additions of aluminum provide the greatest reduction in density of any alloying element and offer the additional advantage of increasing the elastic model. When aluminum is alloyed with lithium, for every 1 wt.% addition of lithium, there is an approximately 3% reduction in alloy density and an increase in stiffness of approximately 6% [7]. On the downside, Al-Li alloys suffer from low toughness, poor ductility and poor weldability [8], which make these alloys an unattractive material for engineering applications.

Various modifications in alloy chemistry and fabricating techniques have been used in an attempt to improve ductility while maintaining high strength. Cu, Mg and

Zr solute additions have been shown to have beneficial effects [8]. Mg and Cu improve the strength of Al-Li alloys through solid solution and precipitate strengthening and can minimize the formation of precipitation-free zones (PFZ) near grain boundaries [9]. In the context of customizing the material properties to very specific applications, a series of high-strength Al-Li-Cu alloys containing minor additions of Mg, Ag and Zr, called Weldalite, have been developed. This series of alloys shows good characteristics of density and modulus with damage tolerance and corrosion properties to equivalent formerly used materials [10]. Moreover, the Weldalite family exhibits significant strength-toughness combinations upon application of heat treatment [11].

The generation of the Weldalite family contains different classes of alloys such as 2000, 7000 and 8000. The classification of the alloy is normally designated by a four-digit numerical system developed by the Aluminum Association [12]. The accepted nomenclature is called the international alloy designation system (IADS) [4]. According to this system, the first digit indicates the alloy group or micro-alloying addition (Table 1.1), the second digit indicates modifications of the original alloy or impurity limits, and the last two digits identify the specific aluminum alloy. For example, the name of complex Al alloy that has been investigated within this study is AA2195. From the abbreviation of the name of this alloy, we can know that it is aluminum alloy (AA), the major micro element is Cu as indicated by the first digit, 2. The modification on alloy's composition has been done by additions of Li, Mg, Ag and Cu as indicated by second digit, 1. The last two digits, i.e. 9 and 5, is a specific identification for the alloy. The development of the mechanical properties of the alloys from the Weldalite family has been performed through heat treatment processes. The heat treatment is of major importance because it is commonly used to alter the mechanical properties of Al alloys. The improvement in mechanical properties depends upon the change in the solubility of the alloying constituents with temperature.

Figure 1.1 shows Schematic view of the major steps of the heat treatment normally used to improve the mechanical properties of the system. The processing starts with solution treatment of the specimen at an elevated temperature within the single-phase region for sufficient time to dissolve the alloying elements. The next step is the rapid cooling or quenching, usually to room temperature, to obtain a super-saturated solid

solution (SSSS) of solute atoms. The final step is to control the decomposition of the SSSS to form a finely dispersed precipitate, usually by aging for convenient times at an intermediate temperature [13]. The heat treatment or temper nomenclature system developed by the Aluminum Association and has become a part of the IADS [4]. According to this system, the solution heat treatment and aged condition is designated by the letter T. Digits following T designate the type of aging treatment. Examples of the aging treatment types are: Natural aging alone, Artificial aging alone, combination of natural aging and artificial aging and applying plastic deformation prior to artificial aging. Table 1.2 details some examples of commonly applied heat treatments [14]. A diagram illustrating the steps of common heat treatment tempers is shown in Figure 1.2.

Table 1.1 Aluminum alloy designations for wrought alloys [4].

Four – digit series	Al content or main alloying element
1000	99% Al
2000	Copper
3000	Manganese
4000	Silicon
5000	Magnesium
6000	Magnesium and Silicon
7000	Zinc

The presence of different micro-alloying elements and an adequate heat treatment causes the precipitation of different phases in Al alloys. Details of different phases expected to be within Al-Li-Cu alloy that have contributed to its strength are summarized in Table 1.3 and explained in the following subsections.

1.2.1 The $T_1 (Al_2CuLi)$ phase:

The aging of the ternary Al-Cu-Li system can generate a number of phases (Figure 1.3), the most important of which is the T_1 phase (nominally Al_2CuLi).

However, depending on the alloy composition and processing conditions, other minor phases such as T_2 and T_B can be precipitated, particularly at the grain boundaries [15].

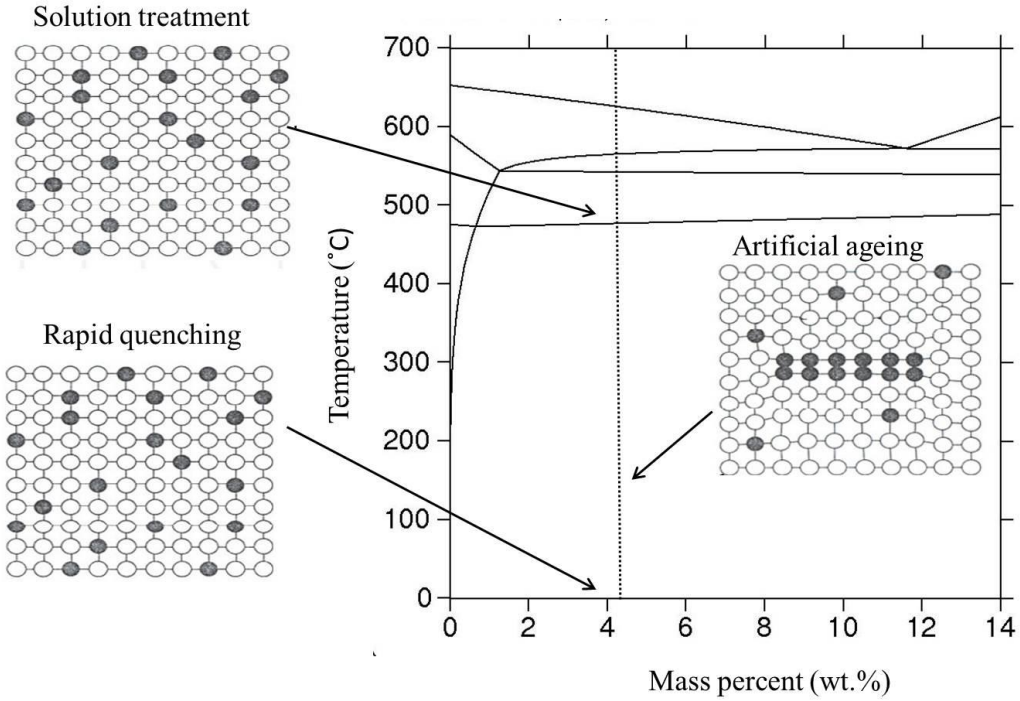

Figure 1.1 Major steps of the heat treatment [14].

The T_1 phase is thought to be responsible for the bulk of precipitation strengthening. The lattice structure for this phase was identified by Hardy and Silcock [16] as a hexagonal phase with lattice constants a = 0.496 nm, c = 0.935 nm, and the group symmetry is P6/mmm (Figure 1.4).

The T_1 phase has a plate-shaped morphology on the {111} planes of the Al matrix. When embedded in the Al matrix, it is usually extremely thin with a thickness of ~ 1.3 nm, which is equivalent to the stacking of only five {111} Al planes. Conversely, theses platelets can have a large extension, up to ~ 100 nm, without losing their coherency with the matrix. The orientation relationship with the Al matrix is $(0001)_p$ /// $(111)_{Al}$.

Table 1.2 Common industrial aluminum heat treatment tempers.

Name of treatment temper	Solution Treated	Quench	Stretch	Aging
T4	Yes	Yes	No	Naturally aging at room temperature (25˚C)
T8	Yes	Yes	Yes	Artificially aging at elevated temperature (100 – 156 ˚C)
T6	Yes	Yes	No	Artificially aging at elevated temperature (> 170 ˚C)

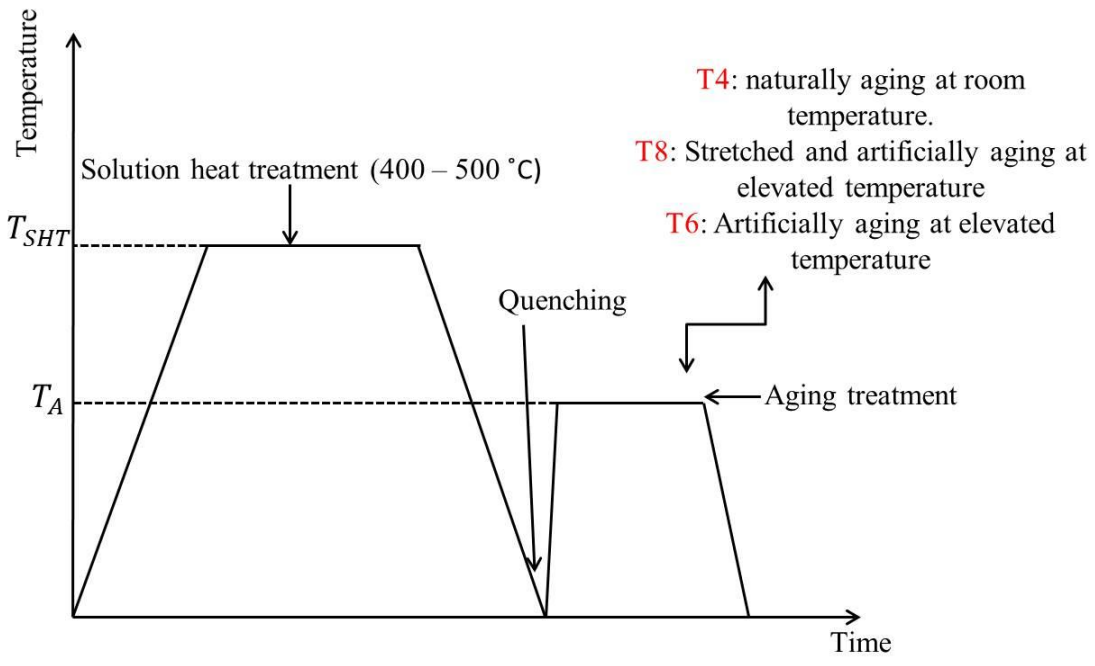

Figure 1.2 Diagram showing steps of common heat treatment tempers.

1.2.2 The $\theta'(Al_2Cu)$ phase:

The metastable $\theta'(Al_2Cu)$ phase is one of the main strengthening phases in complex Al-based alloy as well as binary Al-Cu alloy. Figure 1.5 shows the Al-rich corner of the equilibrium phase diagram, which includes the metastable solvus boundaries for different exciting zones and phases [18].

The structure of the θ' phase originally was proposed by Silcock [19]. According to Silcock, θ' has a tetragonal structure (Figure 1.6) with lattice constants a = 0.404 nm, c = 0.58 nm, and the group symmetry is $1\bar{4}$m2 [20]. θ' phase has a high-aspect ratio plate-like morphology with coherent $(001)_{\theta'}$// $(001)_{Al}$ interfaces parallel to their broad faces and semi-coherent interfaces at their peripheries [21].

Table 1.3 Phases of interest in commercially used Al-Li-Cu.

Phase	Crystal structure	Remarks
$\mathbf{T_1(Al_2CuLi)}$	Hexagonal a=0.496nm c=0.935nm	Thin shaped plates with {111} habit plane. Partially coherent. Orientation relationship: $(0001)_p$ /// $(111)_{Al}$
$\boldsymbol{\theta'(Al_2Cu)}$	Tetragonal a=0.404nm c=0.580nm	Semi-coherent plates nucleated at dislocation. Form on $\{100\}_{Al}$.
$\boldsymbol{\beta'(Al_3Zr)}$	Cubic ($L1_2$) a=0.400nm	Spherical, coherent and ordered dispersoid particles. Orientation relationship: cube-cube.
$\boldsymbol{\delta'(Al_3Li)}$	Cubic ($L1_2$) a=0.401nm	Metastable, coherent and ordered; spherical shape. Orientation relationship: cube-cube

1.2.3 The $\delta'(Al_3Li)$ phase:

The $\delta'(Al_3Li)$ is the metastable phase formed in a binary Al-Li system (Figure 1.7) [22]. δ' is the dominant strengthening phase in some of Al-based alloys. The actual degree of strengthening contributed by δ' is a function of the volume fraction and the size distribution of the δ' particles [23].

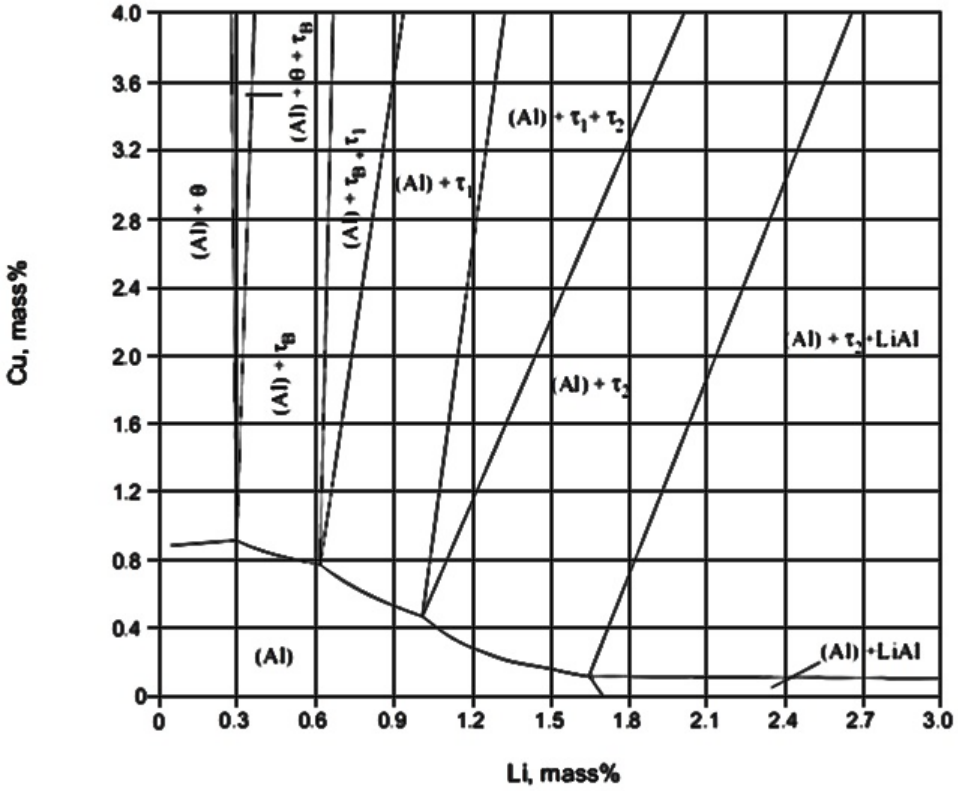

Figure 1.3 Al – Li – Cu phase diagram (Isothermal section at 350˚C) [17].

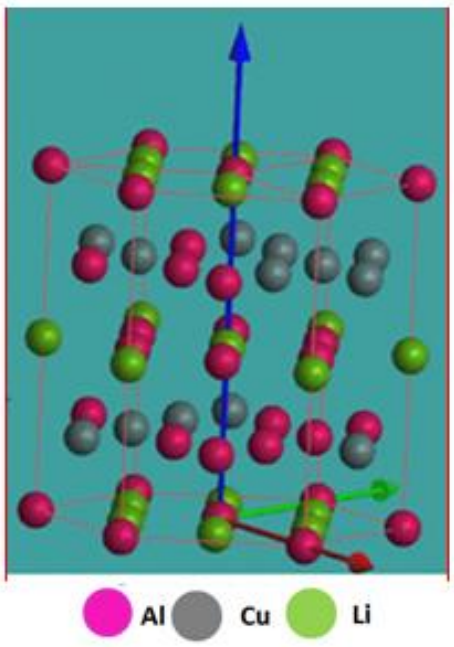

Figure 1.4 Crystal structure for the T_1 phase.

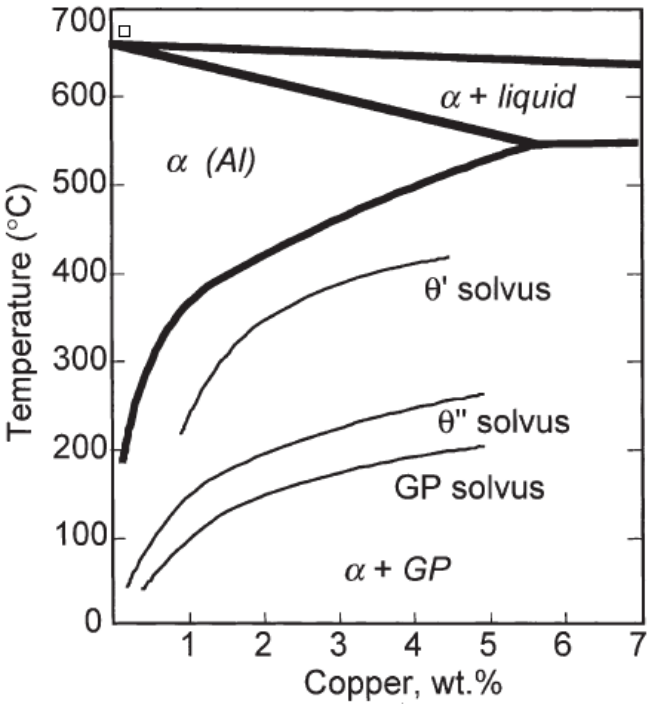

Figure 1.5 Al-rich corner of the Al – Cu phase diagram [18].

The δ' has an $L1_2$ structure (Figure 1.8) and is fully coherent with the face-centered cubic (FCC) Al matrix. It has a lattice parameter of a = 0.401 nm and a spherical morphology [24]. The strengthening associated with δ' phase is largely attributed to the order hardening [25].

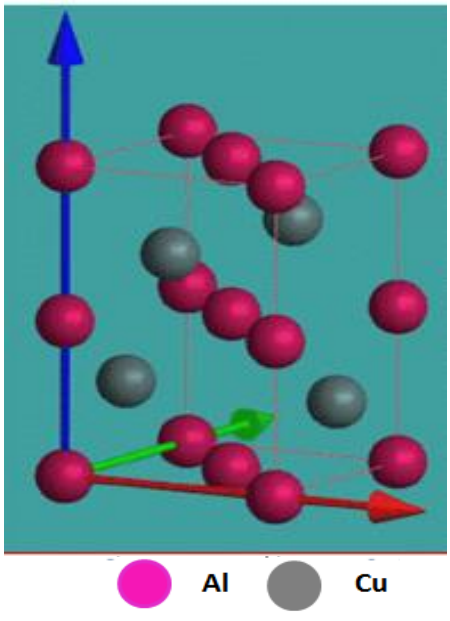

Figure 1.6 Crystal structure for the θ′ phase.

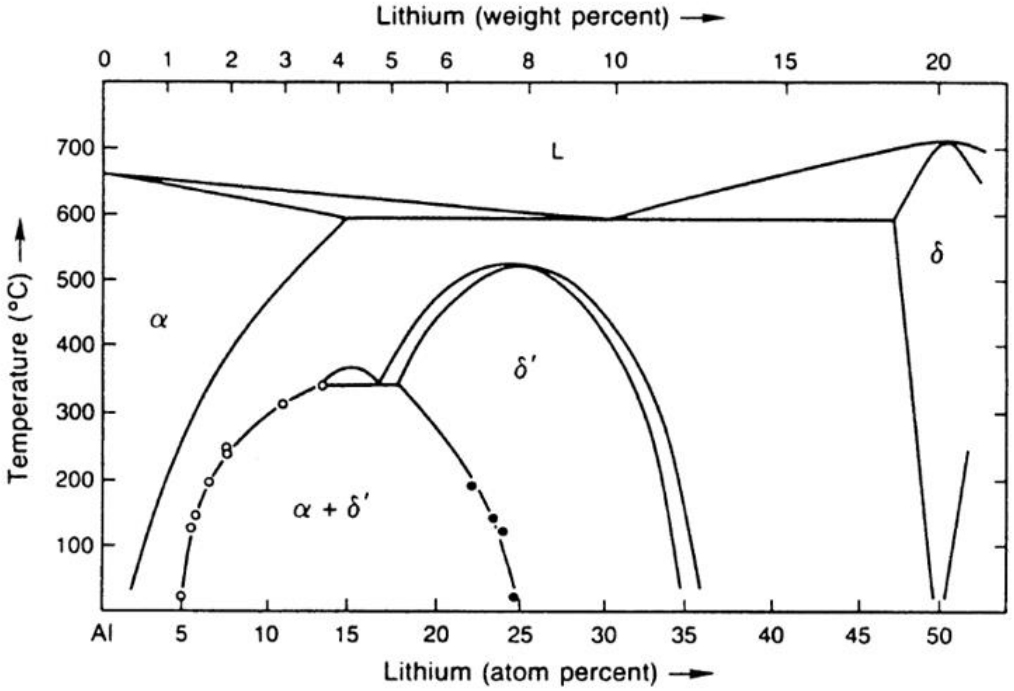

Figure 1.7 Binary Al – Li phase diagram [22].

1.2.4 The $\beta'(Al_3Zr)$ phase:

The β' phase will be present in Al-based alloy that contain Zr within small spherical Al_3Zr dispersiods [26]. The dispersiods are formed by a solid-solid reaction during homogenization of the sample. The main role of such dispersoids is to control the grain size and the resistance to recrystallization [4].

The crystal structure of the β' phase is the $L1_2$ structure, like the δ' phase (Figure 1.8). The β' phase usually appears to be fully coherent with the Al matrix because its lattice parameter a = 0.400 nm is close to that of Al matrix (a = 0.405 nm) [4]. Details of this phase can be found in a binary Al-Zr phase diagram in Figure 1.9 [27].

1.2.5 Other important phases:

In general, different lightweight elements such as Si, Ca and Mg are commonly added to improve the strength and ductility of Al alloys [28]. This has led to growing research interest in single-crystal phases such as Mg_2Si and $MgCaSi$.

Single-crystal $MgCaSi$ is an intermetallic phase that has recently been synthesized by Al-Mg flux mixture [29]. This phase has different application in the transportation industry and has also been used in hydrogen storage [29]. The $MgCaSi$ phase crystallizes in the orthorhombic $TiNiSi$ structure type. Details of atom positions and unit cell parameters can be found in reference [29].

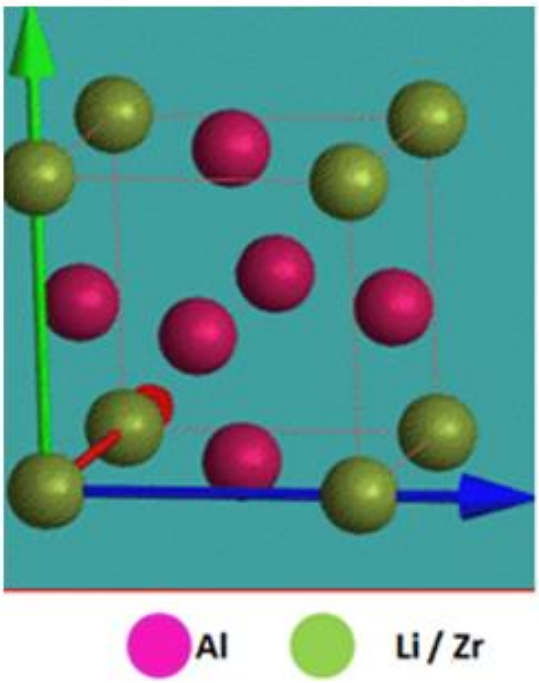

Figure 1.8 Crystal structure for the β′ and δ′ phases.

It is also reported that composite based on $Al - Mg_2Si$ alloy has shown considerable potential because of their low specific weight [30]. Hard Mg_2Si particles are usually embedded in Al matrix to improve its mechanical properties [31]. Moreover, Mg_2Si is an intermetallic compound that exhibits a high melting temperature (1085˚C), low density (1.99 gm / Cm^3), high compression strength (1640 MPa) and good elastic modulus (120 Gpa). All of these properties make metal matrix, such as Al, composites with Mg_2Si reinforcements as attractive candidate materials for aerospace, automotive and other applications [32]. Finally, a Mg_2Si phase displays a FCC lattice arrangement with lattice constant a = 0.633 nm [33]. Crystal structures of $MgCaSi$ and Mg_2Si phases are shown in Figure 1.10.

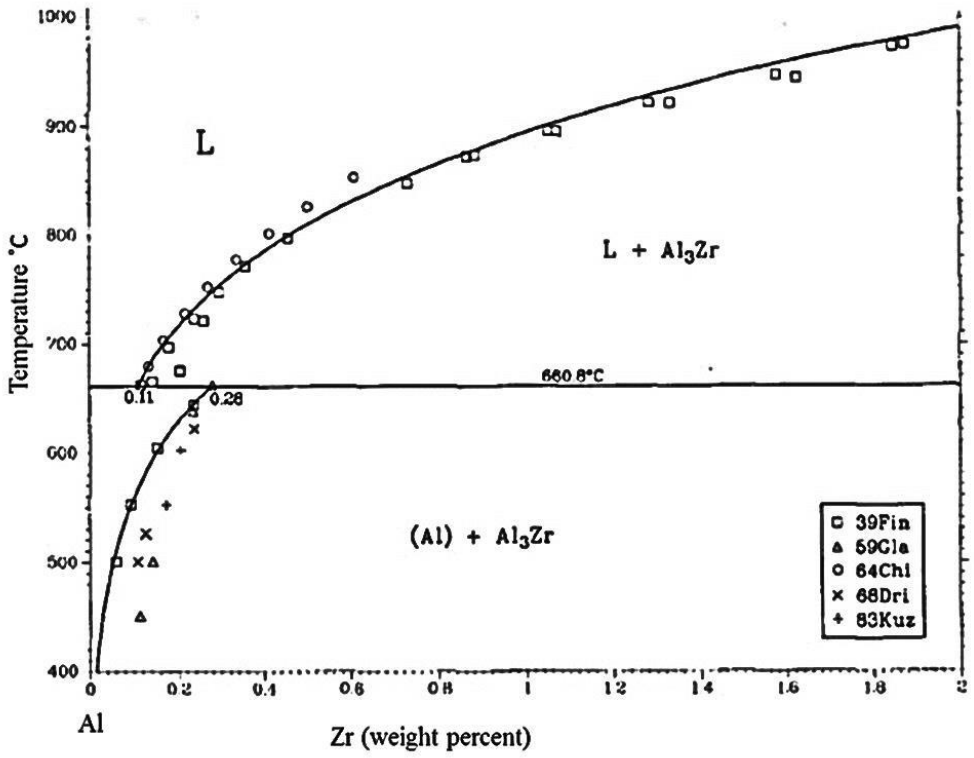

Figure 1.9 Al-rich side of Al – Zr phase diagram [27].

1.3 Theory of precipitation hardening:

The basic requirement for an alloy to be amenable to age-hardening is decreasing solid solubility of one or more of the alloying elements with decreasing temperature. Although there were early attempts to explain the hardening mechanisms in age-hardenable alloys, the understanding of this phenomena remains limited because of the lack of experimental data. Two conditions were postulated as important conditions to promote precipitation hardening. One was that hardening, the increased resistance of an alloy to deformation, is the result of interference to slip by particles precipitating on crystallographic planes. The other was that the maximum hardening was associated with a critical particle size. Modern theories of precipitation hardening are essentially based on these two conditions in relation to dislocation theory. This can be explained by the strength of an age-hardenable alloy being controlled by interaction of moving dislocation with precipitates. If the sizes of precipitate particles are small, the dislocations, which are exciting in the material, can cut and pass through the particles; hence, the strength will be comparatively small. On the other hand, if the precipitate

particles are large and widely spaced, the particles can be readily bypassed by the moving dislocations, which bow out between them and rejoin by a mechanism known as the Orowan process. In this case, the yield strength of the alloy will be low [4]. The most interesting and optimal situation arises when the precipitate particles are not small enough to be shared by dislocations and yet are too closely spaced to allow bypassing by dislocations. In such a case, the motion of dislocation lines would be possible if only one section of dislocation could pass over or under individual particles by a process called cross-slip. In this case, a high level of strengthening would be expected. The relationship between strength and particle size for an age-hardening alloy is shown in Figure 1.11. In this figure, curve "A" represents the precipitates that are shared by dislocations, whereas curve "B" represents precipitates that are not shared—i.e., bypassed—by dislocations. The intersection of the two curves represents the optimal condition that corresponds to the high strength. Different strategies can be followed in stimulating the formation of dispersions for precipitates that resist cutting dislocation. Examples of these strategies are co-precipitation of two or more intermetallic phases that form on different crystallographic planes so that the dislocation mobility is reduced and the nucleation of uniform dispersions of intermediate precipitates by the addition of specific elements [13].

The two processes that govern the formation of new phases are the formation of solid nuclei and the growth of this nuclei by consuming the melt [34]. In other words, the formation of the new phase such as the formation of as solid from a liquid or the precipitation of the rich solid phase from a super saturated solid solution requires the nucleation of the new phase in highly localized regions of the system following by the growth of this phase. The nucleation process can be homogeneous or heterogeneous depending on the available system. Homogeneous nucleation occurs in uniform regions of a system in the absence of special sites such as crystals defects or impurity particles, which may aid the nucleation processes. On the other hand, heterogonous nucleation occurs at such special sites [35]. The growth of phases has been achieved by long-range mass diffusion at the interface binding the growing phase with the matrix. However, this occurs whenever there is a change of composition at the interface [35]. The structure of the interface is important during this process.

Precipitation will generally involve the formation of critical nuclei possessing morphology (shape and crystal orientation) of minimum energy, and the system will follow the fastest path available. The energy is the sum of the bulk free-energy change due to the formation of new phases and the interfacial and strain energy (positive quantities that act as nucleation barriers). The interfacial energy is usually the more important barrier and depends upon the nuclei shape and the energies per unit area of the interface. The strain energy depends on the shape as well as the degree of coherence between the nucleus and matrix and the elastic module of the nucleus and matrix. If the energy of the precipitate/ matrix interface is isotropic and no elastic strain energy is present, the energy change due to the formation of precipitate is [35]:

$$\Delta G_N = \Delta G_N^{Bulk} + \Delta G_N^{Interfacial} = N(\mu^{\beta} - \mu^{\alpha}) + \eta N^{\frac{2}{3}}\gamma \qquad (1.1)$$

Where N is the number of atoms in cluster, μ^{β} and μ^{α} are the chemical potentials of the bulk α and β phase, η is a shape factor and γ is the interfacial energy per unit interfacial area.

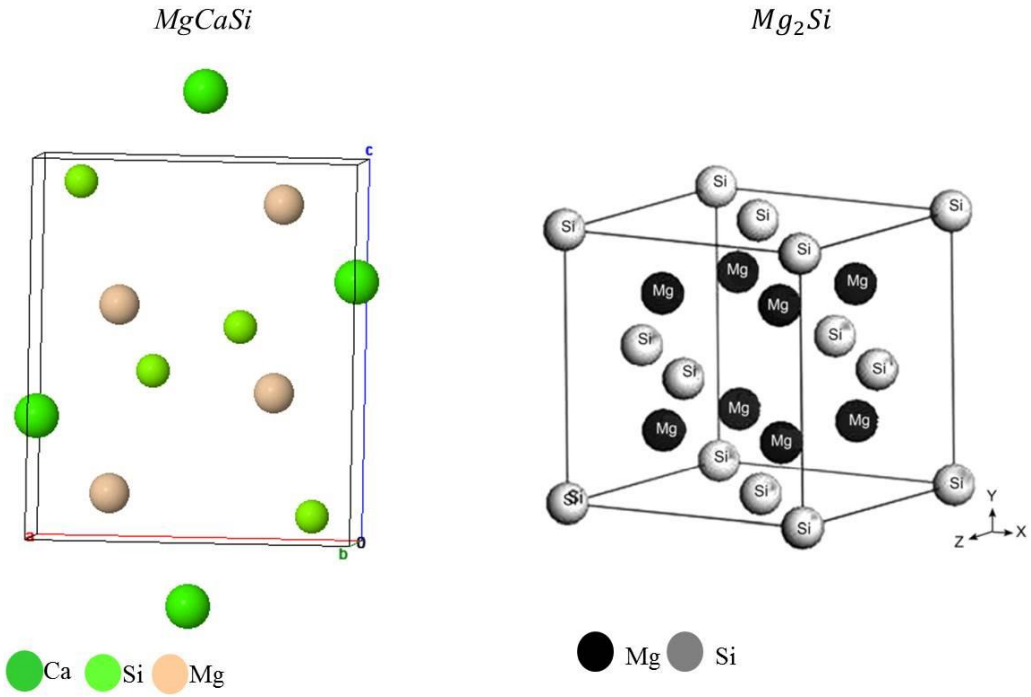

Figure 1.10 Crystal structure of $MgCaSi$ and Mg_2Si phases [29, 33].

Prior to the precipitation of new phases, random clustering of solute atoms usually occurs. The effects of this phenomenon on subsequent aging processes have been little understood [13]. There is some evidence of the potential role of clustering events on the promotion formation of exciting precipitate in alloys. Moreover, it has been shown that clusters play an important role in simulating the nucleation of new precipitates [36] and contribute to the actual age-hardening of certain alloys. The latter role is known as "cluster hardening", in which small, disordered cluster of atoms form immediately after quenching at ambient temperature before the artificial aging. The mechanism by which these clusters can cause hardening remains uncertain [13].

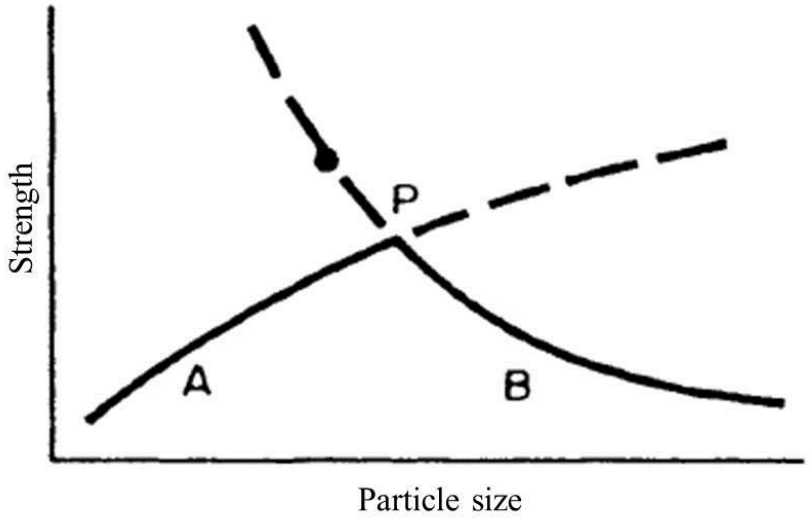

Figure 1.11 Relationship between strength and particle size for a typical age-hardening alloy [13].

It is recently recognized that the vacant lattice sites retained in the system after the quenching operation play an important role in the precipitation processes. These vacant lattice sites promote solute diffusion. Discs of vacancies may also condense and collapse to form dislocation loops, which provide sites that act as heterogeneous sites for the nucleation of precipitates [37].

In conclusion, precipitation occurs when a new phase forms discontinuously within a homogenous metastable phase to form two phase mixtures of lower energy. The process occurs by the nucleation and growth of the particles (precipitates) of the new phase embedded in the original phase. The form of precipitation may vary widely

depending upon several factors, including the degree of coherency between the precipitation and the matrix, the degree of super saturation and the availability of the heterogeneous nucleation sites.

Because metallurgy physics relates the properties of metals and alloys to their microstructure, it is very important to employ appropriate experimental methods to understand the relationship between alloy's properties and its microstructure. The most important properties from technical point of view are the mechanical properties. To understand different microstructure sensitive properties, it is important to decrease the scale of investigation to the sub nano-meter to allow the investigation of microstructure in term of crystallographic natures and the chemical natures. Utilizing an APT technique allows different alloying elements to be mapped out in three dimensional with atomic resolution. Because nearly every atom were identified and positioned in a volume, APT provides one of the most powerful tomography tool. Moreover, the correlation use of APT with other experimental techniques such as: TEM, STEM, SEM and DSC is likely lead to great integration of different experimental techniques to investigate the respective Al alloys.

Chapter 2

Experimental Methods and Techniques

Within this chapter, the experimental methods and techniques used for specimen preparation as well as the characterization analyses will be illustrated. Moreover, the evaluation methods and algorithms used within the frame of this work will be presented.

2.1 Field ion microscopy (FIM) and atom probe tomography (APT):

Because the scientific interest behind this study is to reveal the link between the physical properties of complex aluminum-based alloy and the arrangements of its constitutional different species at the atomic scale, APT has been selected to provide a deeper understanding of this relationship.

2.1.1 Sample preparation by means of electro-polishing:

APT is an analysis technique based on the emission of ionization species from a needle-shaped sample with apex radius < 100 nm. The emission of ionization species has been performed under the influence of a very strong electric field (~ 10–50 V/nm). The specimen is the primary optic of the probe microscopy. As such, specimen preparation is a critical step in successful APT analysis. It is essential in APT analysis to control the tip size and shape. The specimen must be sharp enough to allow field evaporation of ionization species to take place. It must also be robust enough to withstand the influence of the applied electric field to allow significant evaporation events to occur.

The most conventional method for preparing a needle-shaped specimen for APT is the electro-polishing method. This requires, primarily prior to the electro-polishing procedure, that the bulk samples be wire shaped (0.2 mm in diameter) or blanks (matchstick- shaped) (Figure 2.1). As illustrated in Figure 2.1, the blanks are match stick shaped, and should ideally be 10 mm long and approximately 0.3 mm by 0.3 mm wide. The blanks and wires are normally prepared by cutting specimens using a rotating diamond or rotating wire saw or by electro-discharge machined (spark-

machined). It is important that the cross section be square or circular in nature because asymmetric cross sections will lead to blade-shaped specimens.

The electro-polishing procedure requires positioning the top of the blank in the air, and the bottom is placed inside an appropriate electrolyte. A list of suitable electrolytes and conditions for a variety of materials can be found in reference [38]. However, the precise conditions vary among laboratories and with alloy composition. The other requirement for the electro-polishing procedure is to use a counter electrode, which is usually made of a noble material such as platinum. The counter electrode is positioned a short distance from the specimen (Figure 2.2).

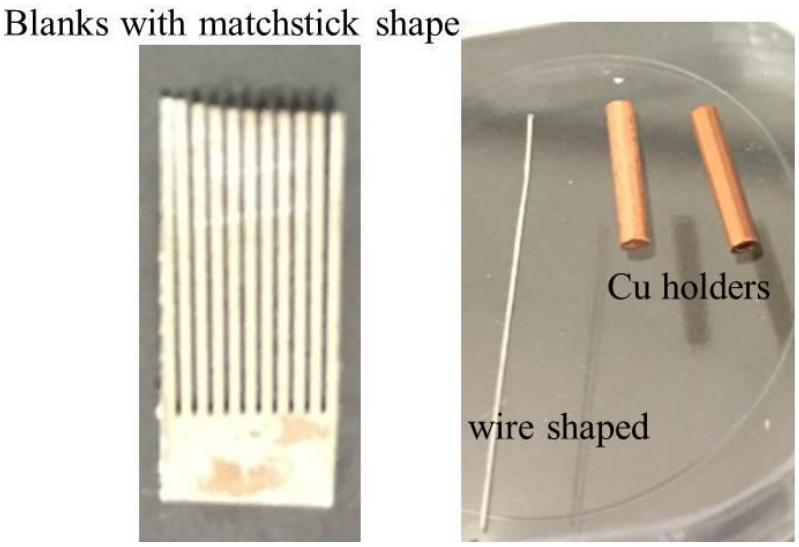

Figure 2.1 Bulk samples in blanks (matchstick shaped) and in wire shape. Sample has to be fixed in Cu holder prior to electro-polishing procedure.

The blank is connected to a positive DC voltage (sometimes AC is also employed), and a metal electrode is connected to the negative polarity. When voltage is applied between the specimen and the counter electrode, only the central section of specimen in the electrolyte is polished, and a neck region is gradually formed. Eventually, the weight of the lower portion of the wire will be too heavy to be supported by the necked region, and the lower half will be separated. This procedure requires a dynamic application of voltage between the electrolyte and the specimen based on the observed progress of the tip shape [39]. The shape of the tip will then be examined by using an optical microscope as shown in Figure 2.3. Figure 2.3 (a) illustrated the ideal

shape of the tip with a good surface finish and a small radius of the apex (~ 10 to 100 nm). Bad examples of the tip shapes can be seen in Figure 2.3 (b).

2.1.2 Sample preparation by means of focused ion beam (FIB):

The other important method with the ability to prepare a shape needle specimen is focused ion beam (FIB). FIB-based specimen preparation is usually selected when the material cannot be electro-polished or the specimen has unsuitable geometry or features of interest that must be presented near the apex region to ensure that such features are included in the collected data.

The FIB instrument generally operates in a similar way to scanning electron microscopy. The major difference is that the ions, usually Ga^{+}, are used to interact with the surface rather than electrons to produce a secondary electron (or ion) signal for imaging. The ion beam, which has a much larger mass than the electron beam, has the capability of spurting away atoms interacting with the beam, allowing the FIB to be used as a milling tool [40]. The combination of the capability to image specimens by using ions as a probe and secondary or backscattering electrons as the detected signal with the capability to remove substantial amounts of material using ions provides a tool that has been previously unavailable. This combination provides the ability to observe the feature of interest in a specimen at high magnification while being sharpened.

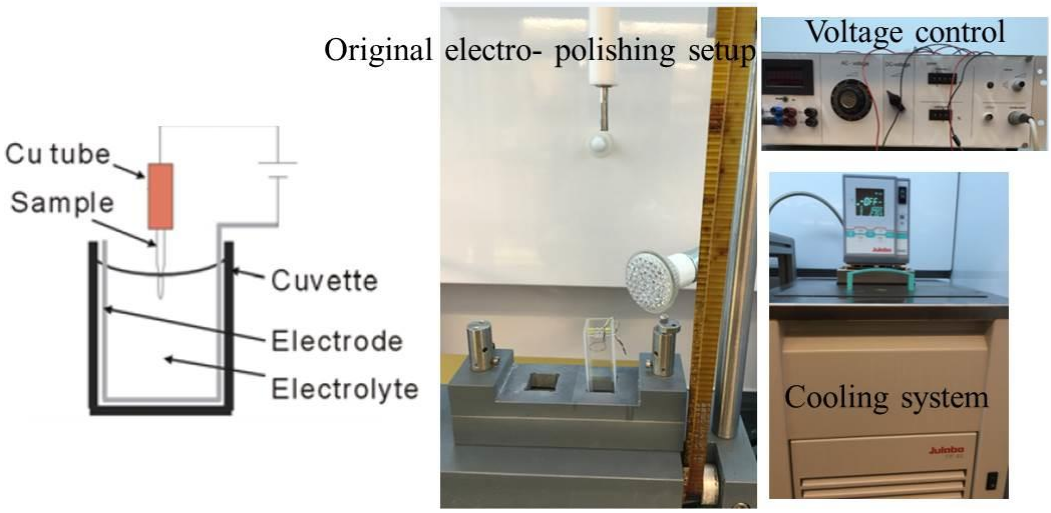

Figure 2.2 Schematic diagram and photos of the experimental set-up for standard electro-polishing procedure.

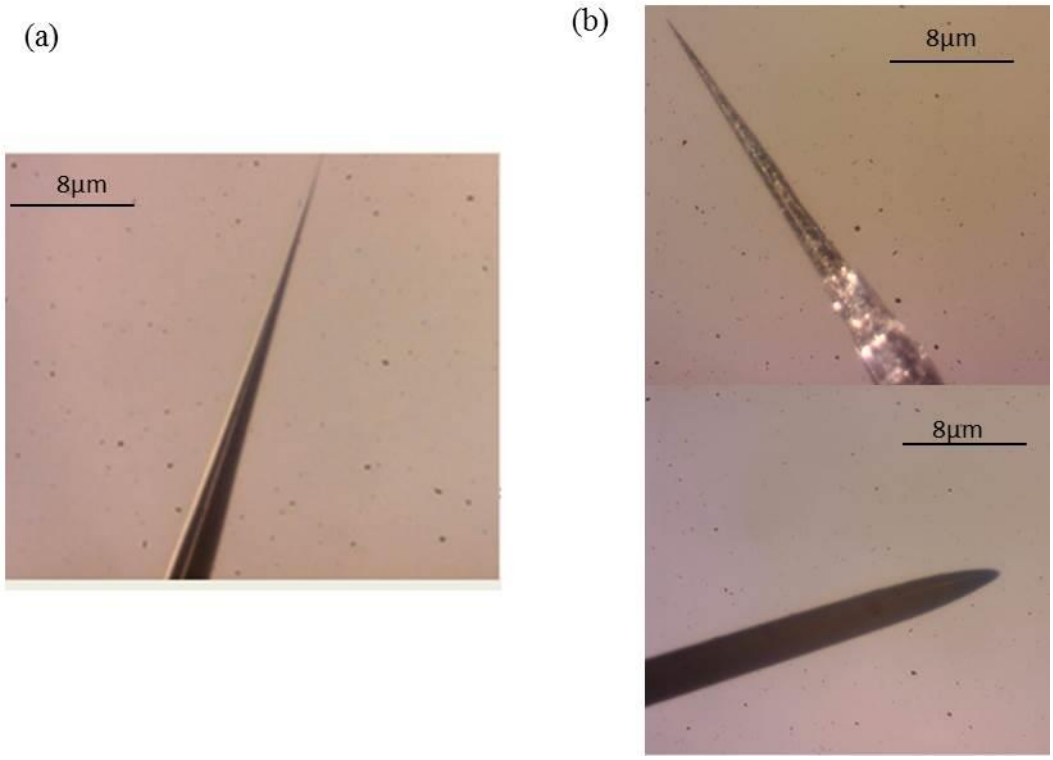

Figure 2.3 Optical micrograph of polished samples (a) An ideal shape. (b) Examples of bad shaped samples.

The dual beam FIB contains an electron column as well as the ion column, which images at an angle (typically 52°) to the ion beam. The FIB technique also interfaces with different other components, such as a micromanipulator, which is used to transfer small segments of a sample from its bulk to a mount on atom probe Si tips.

A number of FIB-based preparation techniques have been developed to create APT tips that contain the features of interest. The methods are described elsewhere [40-42]. Standard lift-out and sharpening methods have been used within the frame of this work.

Figure 2.4 illustrates the followed steps to prepare APT tips with the aid of the standard lift-out method. After imaging the surface of the sample using the backscattering signal, the region of interest has been selected (Figure 2.4 (a)). A FIB deposited platinum strip was added to protect the surface and mark the region to be extracted (Figure 2.4 (b)). The platinum layer is typically 2–3 µm wide and 2.5 µm thick with a length depending on the geometry of the region of interest (3µm in our

case). After depositing the Pt layer, staircase-shaped cross sections are cut on both sides beyond the Pt layer, resulting in a lamella of approximately 16 µm × 12 µm × 15 µm in size (Figure 2.4 (c)). A micrometer-sized needle, called an Omniprobe, is then introduced and attached to the lamella via Pt welding (Figure 2.4 (d)). After the lamella can be cut free, it will be manipulated and positioned on commercial arrays of post (micro-tip Tm arrays) in flat-topped form (Figure 2.4 (e)). The last step is to convert a left-out lamella in Figure 2.4(f) into a sub-100-nm diameter sharp needle. This is accomplished through a series of annular milling steps with progressively smaller beam currents and inner diameters (Figure 2.5(a)), until the desired radius has been achieved. The ideal shape of the tip prepared via this technique is shown in Figure 2.5(b).

Within the frame of this work FIB preparation of APT tip has been done using Helios FEI with Ga^+ ion accelerating voltage of 5 KV.

2.1.3 Field ion microscopy (FIM):

Field ion microscopy (FIM) provides a clear view of the location of individual atoms on a metal surface. It enables the investigation of the surface of a conductive sample with a magnification ~ 10^7 with the assistance of an imaging gas and its field ionization.

In this technique, a tip-shaped specimen with a radius of curvature of 10–100 nm at the apex is introduced into an ultrahigh-vacuum chamber with a residual pressure of ~ 10^{-7} Pa. The tip, represented in Figure 2.6, corresponds to a truncated cone caved with a hemispherical cap. This tip faces the imaging system, which consists of microchannel plates (MCPs) and a phosphor screen.

The image is produced by applying a positive direct voltage V_{DC} to the specimen after cooling it down to a cryogenic temperature of 20 – 60 K to suppress the lattice vibrations. The V_{DC} is applied between the specimen and the imaging system in the presence of a material-dependent imaging gas such as Ne or He at a pressure around 10^{-3} Pa.

As the V_{DC} is applied to the specimen, the imaging gas atoms in the vicinity of the apex of the needle-shaped specimen become polarized and attracted to the specimen because of the strong electric field (Figure 2.7(a)). After successive inelastic

collisions with the tip, the polarized atoms lose their kinetic energy at the surface and cool down to the tip surface, resulting in their entrapment in the ionization zone. The depth of the ionization zone is approximately 0.5 nm above the tip surface. When the field becomes high enough, the imaging gas atoms on the surface of the specimen can become field ionized by an electron tunneling process. These are reflected toward the phosphor screen. The collision of the ions with the screen results in spots of light (Figure 2.7(b)) [43]. These spots are interpreted as atomic terraces, and one series of spots produces a concentering ring that represents each crystallographic pole. The geographical relationship between different crystallographic poles can be considered approximately by stereographic projection [38].

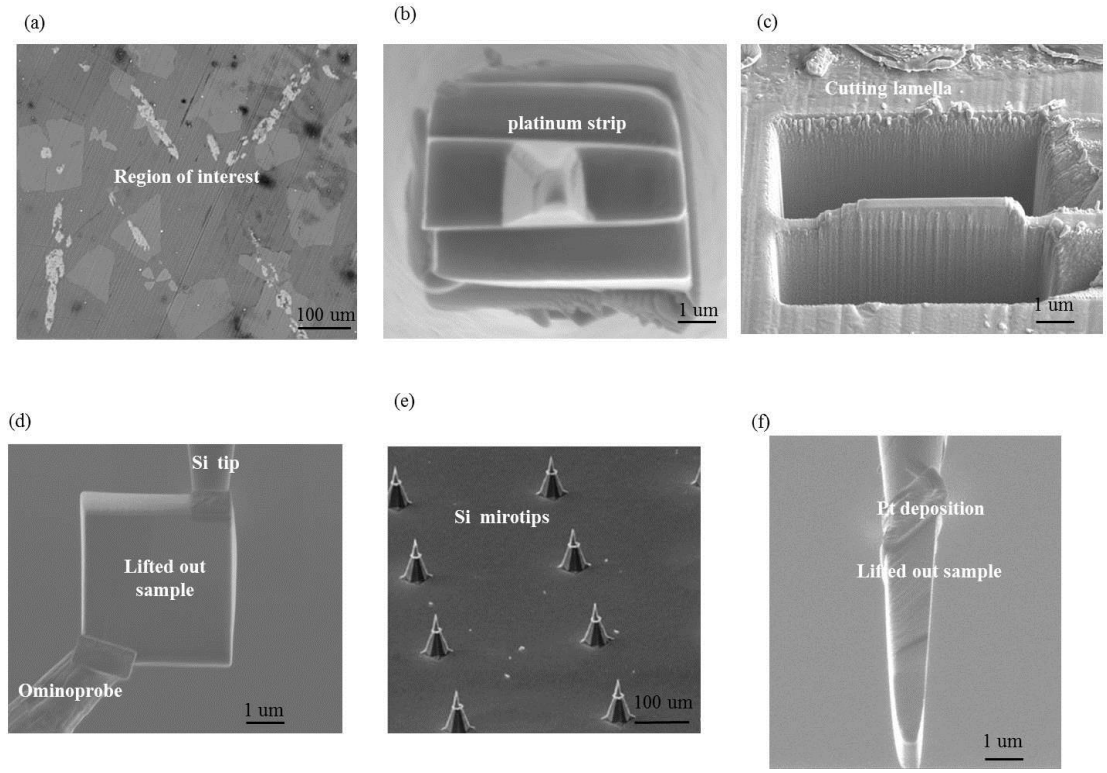

Figure 2.4 Steps of preparation APT sample using lifted-out method (a) Selection the region of interest. (b) Deposition of Pt protection layer. (c) Cutting cross section lamella. (d) Lift out the sample by using Omniprobe. (e) An image of a commercial microtip array. (f) Lift-out lamella attached to the Si microtip by using Pt deposition.

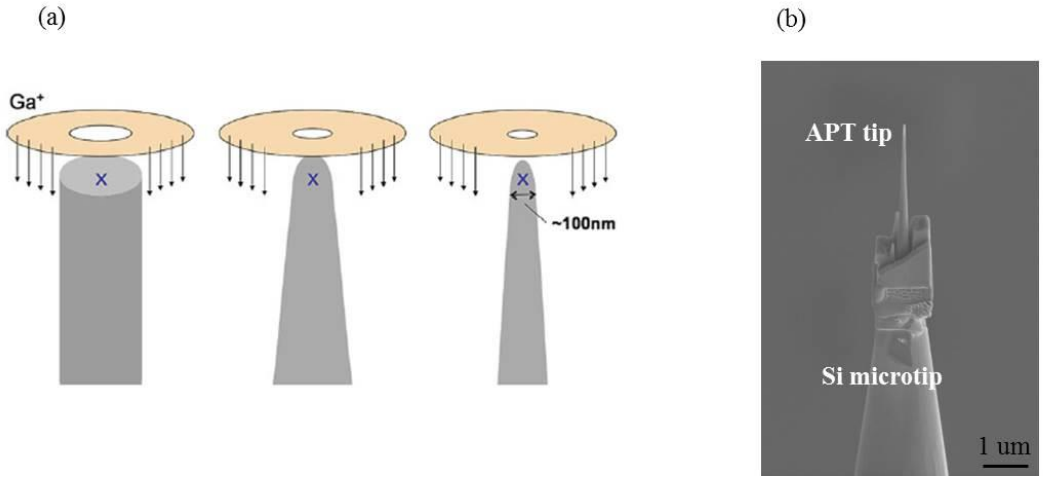

Figure 2.5 An annular milling of the tip. (a) Milling pattern [41]. (b) The final ideal shape of APT tip.

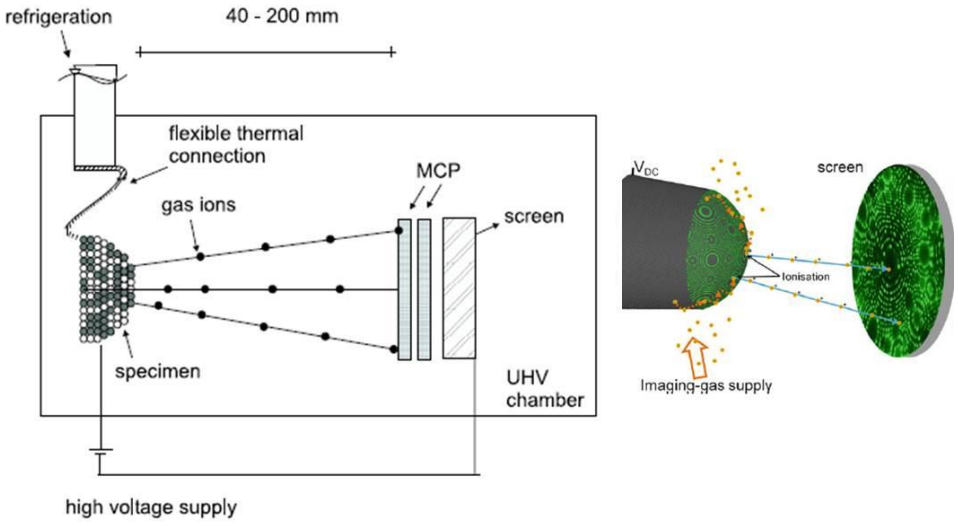

Figure 2.6 Schematic drawing of a field ion microscope [43].

To understand how atomic resolution arises, one should consider that the tip at the atomic scale as a set of hard spheres piled together (Figure 2.8). Each atom at surface constitutes a small protuberance that provides an additional local enhancement to the electric field in comparison to the others. By fine-tuning the bias voltage, the field ionization will occur at the local enhancement position right above each individual

atom on the surface of the tip apex. Each dot on the screen then corresponds to an individual atom on the tip surface.

Regarding the tip geometry, the three characteristic parameters are the tip length L, the apex radius R and the shank angle α (Figure 2. 9). Typically L ranges from 0.5 to 5 mm, R ranges from 10 to 100 nm, and α ranges from 2 to 15°. The magnitude of the electric field E_A at the apex, resulting from the externally applied voltage, can be estimated from this relation [38]:

$$E_A = V/\beta R \qquad (2.1)$$

Where V is the applied voltage, R is the apex radius, and β is a coefficient related to the geometry, known as the geometry factor. This geometry factor is considered because of the deviation for the hemispherical shape of the tip and ranges from 5 to 7 [38].

With the apex radius on the order of 10 nm, a strong electric field can be obtained with bias voltages of only few kilovolts. If the applied voltage is high enough to exceed field evaporation strength E_f (the electric field required to evaporate the ion species), the surface atoms will be ionized and evaporated layer by layer. With increasing voltage, the curvature radius of the tip increases. The processes can, therefore, be used to clean the surface of already prepared Al specimens before performing the APT analysis.

2.1.4 Atom probe tomography (APT):

Atom probe tomography (APT) involves one of the most spectacular microscopes in existence. It provides a three-dimensional (3D) image at the atomic scale with single-atom sensitivity in which each atom or isotope in the image is defined. The fundamental data format is the 3D position and identity of individual atoms in a volume that contains potentially millions of atoms; thus, different information about the analyzed material can be gleaned. Detailed information about APT can be found in Ref [38, 41].

APT analysis is based on the process of field evaporation. Once again, field evaporation occurs upon increasing the applied voltage, which causes the atoms of the

specimen to desorb. The specimen is eroded layer by layer; thus, the shaft angle of the tip becomes finite, and its radius increases with ongoing field evaporation.

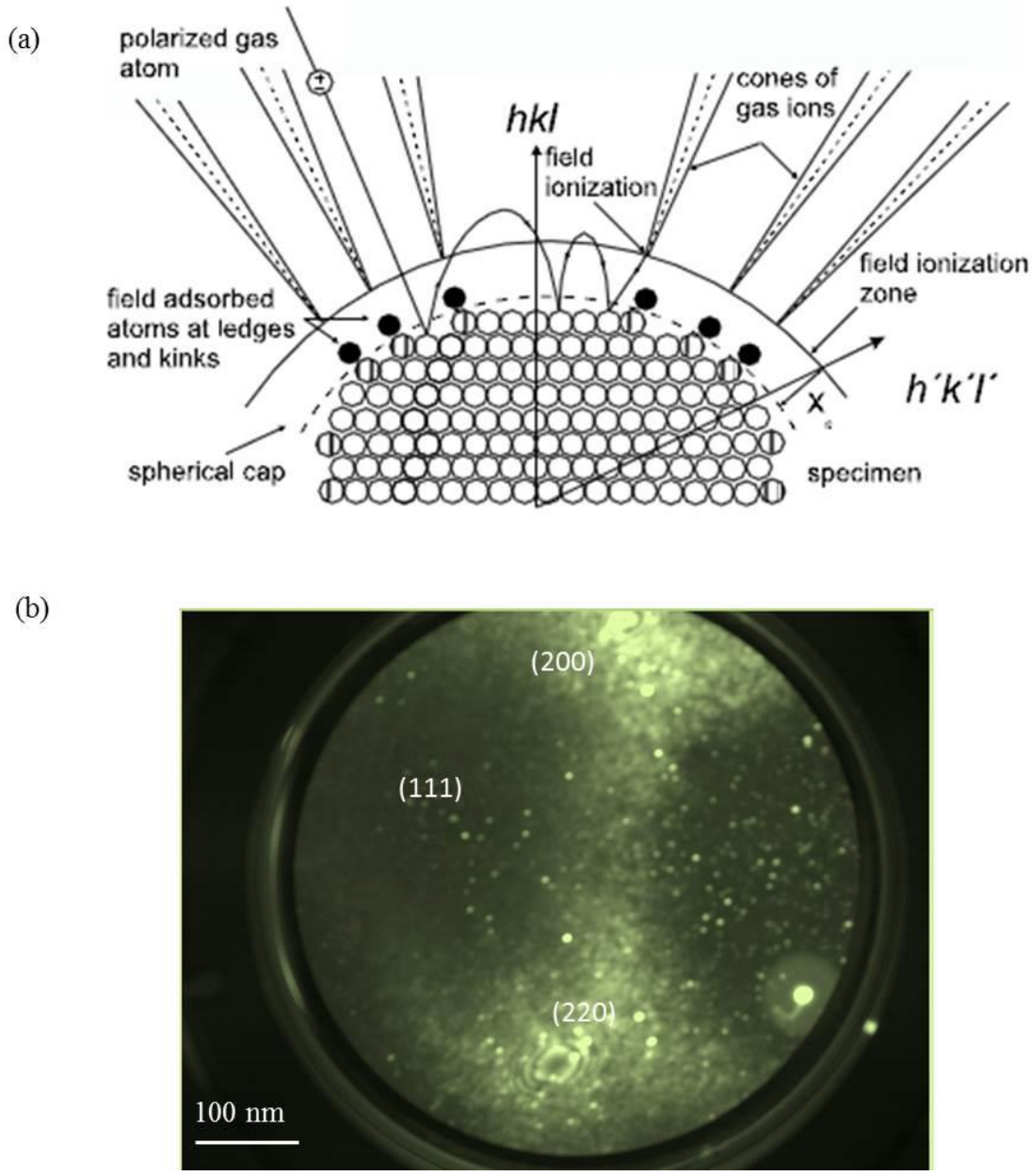

Figure 2.7 Imaging mechanism in FIM (a) Schematic drawing of the field ionization process of imaging gas atoms over the hemi-spherical tip surface [43]. (b) Field ion micrograph of Al – Cu alloy illustrating the position of different crystallographic poles in the tip.

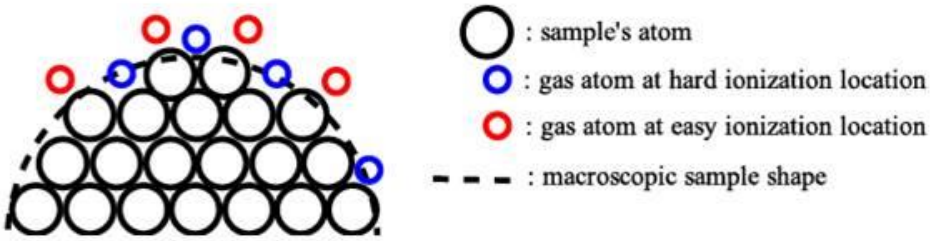

Figure 2.8 Representation of tip apex at atomic scale showing the preferential ionization sites.

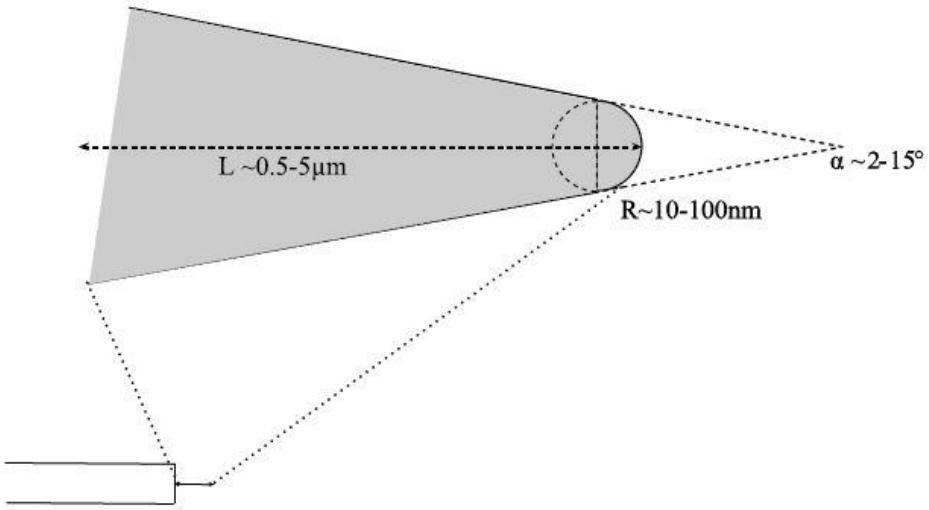

Figure 2.9 Schematic representation of needle-shaped sample used in APT.

In contrast to FIM, no image gas is present during APT. The direct voltage V_{DC} is superimposed by a pulsed voltage V_p. This superimposing increases the total voltage by 25%. The values of the pulse fraction (ratio between the pulse voltage V_p and the standing voltage V_{DC}) and analysis temperature must be carefully chosen to avoid any preferential evaporation when a multicomponent system is measured.

Figure 2.10 is a schematic picture of the FIM and APT. The imaging unit of MCPs and the phosphor screen is hinged down, providing a way for the ions to travel to the second set of MCPs. The second set connects to the delay line-based position sensitive detector [41, 42]. When a pulse voltage is applied—i.e., at the onset of the evaporation—the clock or timer for flight time measurement starts. The field evaporation ions reach their drift velocity and drift toward the detector. On the impinging of the ions at the delay line detector, the clock stops, and the time of flight is measured. The time of flight is included to calculate the mass-to-charge ratio ($\frac{m}{n}$) from the time of flight (t_f) and the applied voltage ($V_{DC} + V_p$).

The potential energy for the ions accelerated by the electrostatic field is:

$$E_p = neV \qquad (2.2)$$

Where *V* is the voltage and *ne* is charge of ion. The kinetic energy is:

$$E_k = \frac{1}{2}mv^2 \qquad (2.3)$$

Where *m* is the mass of the ion, and *v* is the field velocity given by $v = \frac{L_f}{t_f}$, where the time of flight (t_f) is indicated as (TOF), and L_f is length between the specimen and the detector.

Energy conservation yields the following equation:

$$\frac{m}{n} = 2e\left(V_{DC} + V_p\right)\left(\frac{t_f}{L_f}\right)^2 \qquad (2.4)$$

Where *m* is the mass, *n* is the ionization state, *e* is the elementary charge, *t* is the flight time, and L_f is the flight distance. $\frac{m}{n}$ can be directly determined based on experimental measurement, which enables the identification of the element nature.

The operation of the delay line detector, as illustrated in Figure 2.11, starts when filed evaporated ion hits the MCP .An electron cloud been produced by MCPs is then focused onto two polarized conductive lines. The passage of the electron cloud in the vicinity of the conductor wires induces two signals that are then propagated along the

conductors toward each end of these conductive lines. Detecting these signals enables the lateral impact coordinates X_D and Y_D to be deduced by using [41]:

$$X_D = L_x \frac{T_{x2} - T_{x1}}{2TP_x} \qquad (2.5)$$

$$Y_D = L_y \frac{T_{y2} - T_{y1}}{2TP_y}$$

Where L_x and L_y are the physical lengths of the lines. T_{x1}, T_{x2}, T_{y1} and T_{y2} are the times at the end of the lines, and TP_x, TP_y are the total propagation times along the two lines.

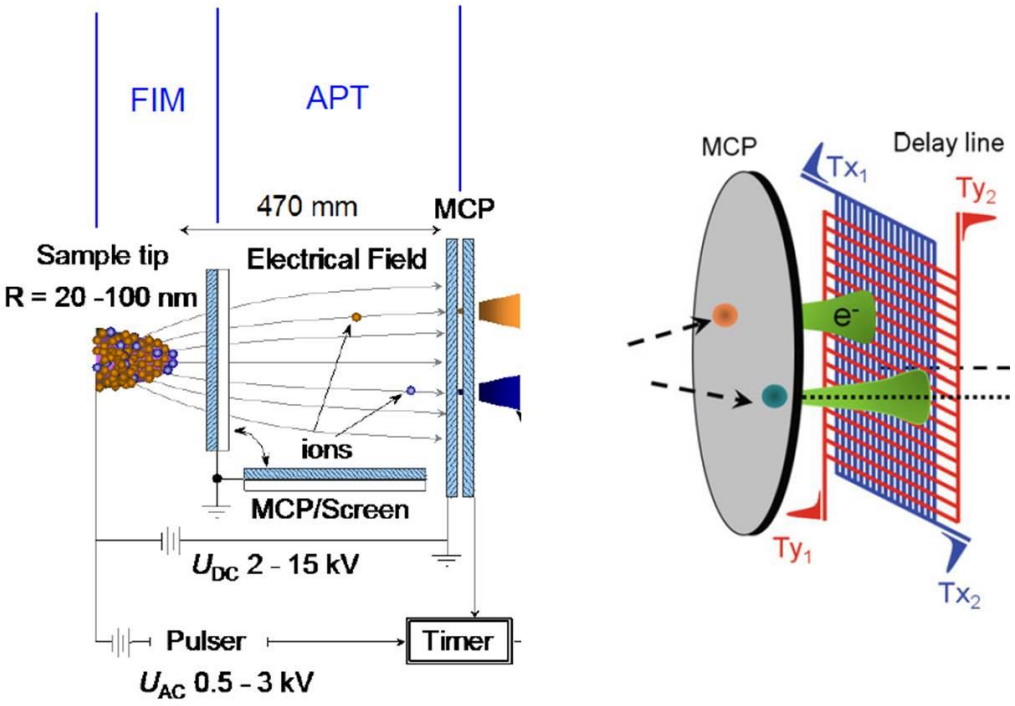

Figure 2.10 Schematic drawing of FIM and APT. For FIM operation the MCP/Screen stands in front of the sample tip, while for APT mode this screen is down. The used detector is the delay line detector [Part of the figure reproduced from dissertation of R. Gemma].

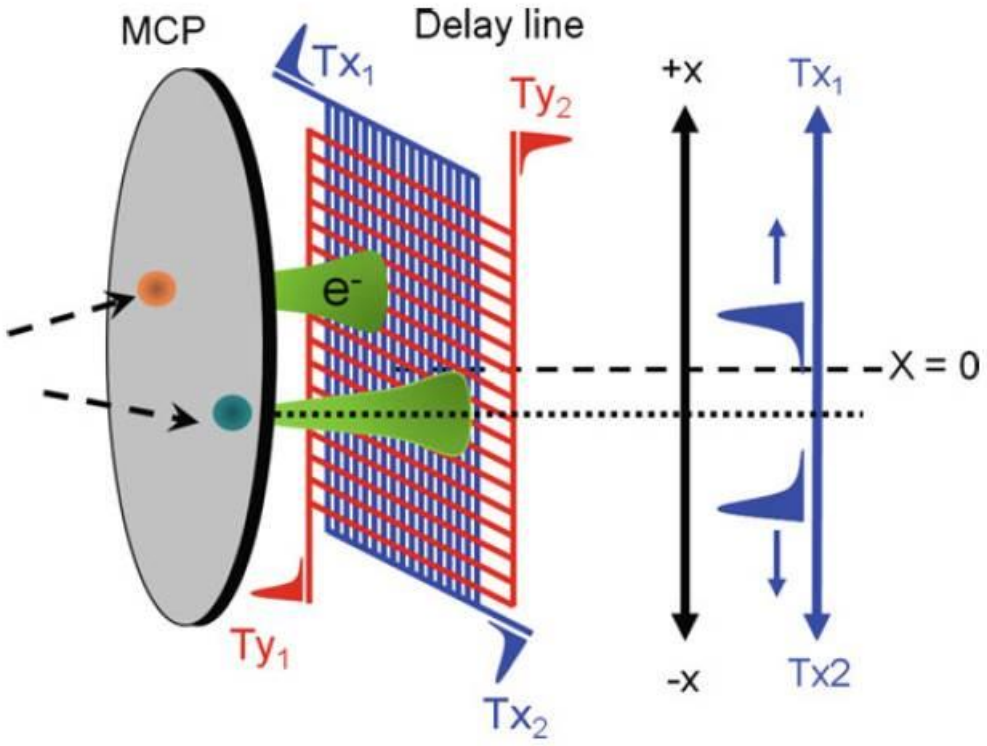

Figure 2.11 Schematic drawing of the delay-line detector [41].

In principle, the depth (z) coordinator can be calculated from the number of atoms removed from the surface by considering the atomic volume, detection efficiency of the detector and detector surface. According to equation (2.1), the change of curvature radius must be considered also.

The mass-to-charge ratios of the detected ions are generally represented in the form of a histogram called a mass spectrum. Figure 2.12 shows a section of the mass spectrum for a complex Al-based alloy plotted on logarithmic scales. As we handle multicomponent materials, a series of peaks corresponding to the each atomic species and their respective isotopes is found. The ability to distinguish the different isotopes, combined with the mass-to-charge ratio, enables unambiguous identification of the chemical nature of the ions associated with the mass peak [38].

After the raw data have been collected, the positions of the atoms inside the analyzed volume are reconstructed from the sequence of impact positions, corresponding flight time and tip voltages. The simple and most intuitive representation of the three-dimensional data is the atom or dot map [38]. In this type of representation, a dot or a small sphere is plotted at the x, y and z coordinates of the

atom. The volume of analysis is typically manipulated in the computer in real time, so the local arrangement of the atoms can be visualized. Examples of atom maps for complex Al alloys are shown in Figure 2.13. Different atom types may be visualized simultaneously with the use of color-coded dots or small spheres with different diameters.

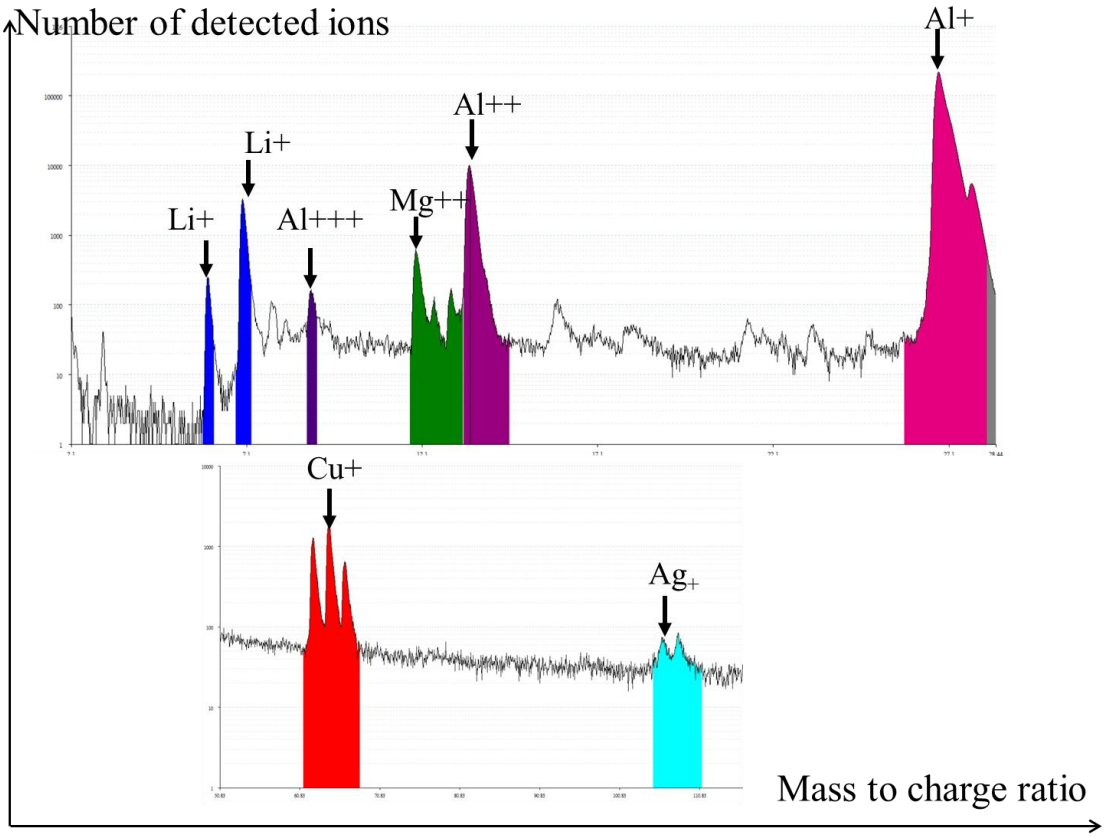

Figure 2.12 Obtained mass spectrum for complex Al alloy.

Within the frame of this work, two potential atom probes have been utilized. The first is a laser-assisted wide-angle tomographic atom probe (LAWATAP), and the second is a local electrode atom probe (LEAP) (Figure 2.14). Both tools were developed by French manufacturer Cameca. Analyses using two techniques require optimization of different parameters. The essential control parameters are the temperature, ratio between pulse and direct voltage (pulse fraction), pulse rate and flux of incoming atoms. A combination of low temperature (20–30 K), intermediate pulse fraction (18–25%), pulse rate of 1 – 100 kHz and low flux of 0.001–0.01 yielded the optimal result of the complex Al alloy samples. Although numerous

parameter combinations are superior, the failure of the specimen could not be systematically avoided.

The final step after the completion of the APT experiment is to apply different algorithms using high-performance workstation to visualize and analyze the data. In this study, different algorithms have been used to treat the dataset to deliver high-quality obtained results. Brief descriptions of these algorithms will be presented in the following sections.

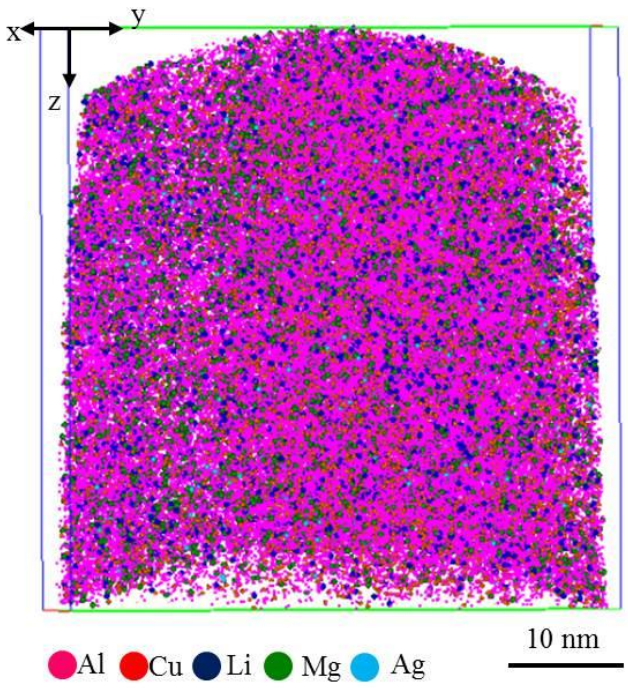

Figure 2.13 Atom map showing distribution of Al, Cu, Li, Mg and Ag atoms in a complex Al alloy.

2.1.5 Reconstruction methods and algorithms:

2.1.5.1 Proximity histogram (proxigram):

The development of a proximity histogram or proxigram algorithm has allowed measurement composition profiles in 3D. This algorithm is considered to be an efficient algorithm to extract useful information about the microstructural and interfacial characterization from the large dataset [44]. The first step of the algorithm

is to define an isoconcentration surface in the reconstructed volume. This isoconcentration surface helps identify a microstructural feature, precipitates in our case, and isolate it. An isoconcentration surface is a surface that envelopes a volume with concentrations higher than the selected concentration of one or more elements. This surface was obtained by sampling the atom probe tomography reconstruction with 0.8 × 0.8 × 0.8 nm^3 or 1 x 1 x 1 nm^3 voxels after applying a delocalization procedure by Hellman et al. [45] with smoothing parameters of 1.5 nm or 3 nm for the x and y coordinate and 0.75 nm or 1.5 nm for the z coordinate.

The algorithm generates a histogram measuring the population of atoms in a series of shells at increasing distances from the position of the isosurface. This can be explained as follows. Starting at the isoconcentration surface, which is the origin of the proxigram, and moving toward the center of the precipitate (positive distance), the composition of the precipitate is measured in discrete shells that take the shape of the isoconcentration surface and have fixed intervals. On the other hand, the matrix composition is obtained by starting at the isoconcentration surface and moving into the matrix (negative distance). A concentration distribution profile for the constituent elements is the final yield result of applying this algorithm.

2.1.5.2 Concentration depth profile:

The significance and correlation length of concentration variations can be determined via 1D-concentration depth profiles [38]. For this purpose, the area of interest is selected and marked by means of an analysis cylinder or cubic. Dividing the cylinder volume into blocks of either a constant volume or constant number of atoms, the respective concentration is computed. The composition of a small selected volume at a specific location in the analyzed volume is given by:

$$c_i = \frac{n_i}{n_t} \qquad (2.6)$$

Where n_i is the number of ions of solute *i*, and n_t is the total number of ions collected. The computed concentration is then plotted as a function of the depth.

2.1.5.3 Cluster identification algorithm:

The cluster identification algorithm is an accurate and efficient algorithm developed to characterize individual atomic clusters in terms of size, chemistry, morphology and distribution [46, 47]. The concept of “clustering” is considered to express the presence of two or more atoms that are somehow associated with one another.

Figure 2.14 Pictures of used APTs.

This approach is based on the assumption that the distance between two clustered solute atoms is smaller than the distance between two solute atoms found anywhere else in the microstructure. The algorithm groups atoms that are separated by less than a given distance (d_{max}). For example, if we have solute atoms $\boldsymbol{p}$ and $\boldsymbol{q}$, and these atoms are separated by a distance $d\ (p,q) \leq\ d_{max}$, the atoms p and q are defined to be clusters. Using d_{max} allowed the filtering of clustered from non-clustered atoms. This step is repeated in the algorithm for all solute atoms, and clusters are assembled by connecting atoms together via a network of common associations.

In conclusion, this algorithm is based on the selection of solute-rich regions. This is performed by connecting solute atoms that lie within a fixed distance ($d_{max} \sim 0.5\ nm$ in this study) and taking clusters above a certain number of solute atoms N_{min} ($N_{min} \sim 20$ in this study) [47].

2.1.5.4 The χ^2 Test:

The χ^2 test is a reliable method to assess whether a certain element is homogeneous or heterogeneously distributed within the analysis volume.

In the process, the measured concentration distribution of the component is compared to the binomial distribution with the same average component concentration. The χ^2 parameter for a measurement is

$$\chi_e^2 = \sum_{n=0}^{n=b} \frac{(e(n) - f_b(n))^2}{f_b(n)} \tag{2.7}$$

Where $e(n)$ is the measured number of voxels that contain n out of possible n_b atoms of the component, and $f(n)$ is the corresponding number estimated by the binomial distribution. The χ^2 statics, allow significant testing of the departure from randomness [41]. But in the case of the large dataset, i.e. APT's analysis volume, χ^2 cannot be used for direct comparison between different dataset with the different sizes. In this case the significance test will indicate to the existence of correlation between solute atoms which are actually random. Instead, the implementation of the Pearson coefficient (μ) was developed. This coefficient is used to normalize the dependence of χ^2 on the number of blocks sampled for the analysis volume (N) according to this equation:

$$\mu = \sqrt{\frac{\chi^2}{N+\chi^2}} \qquad (2.8)$$

The μ value lies between 0, in the case of random distribution and 1 in the case of a complete association between different solute atoms. Thus, the levels of clustering and segregation of solute atoms between different specimens can be obtained. On this basis, this algorithm has been used in this study to evaluate the early stage of the decomposition of the microstructural of different Al alloys.

2.2 Transmission electron microscopy (TEM):

Transmission electron microscopy (TEM) generates images of material microstructures with very high magnification and resolution. In this technique, the strong interaction of electrons with matter has been utilized. Electrons are either generated by a thermionic source (such as tungsten or lanthanum hexaboride LaB_6) or a field emitter (such as field emission guns). The electrons accelerate under a high electrical potential and condense by means of electromagnetic lenses to be projected on the specimen. The specimen should be thin enough to allow the transmission of electrons. The electrons that pass the specimen are collected and further viewed by an imaging system to produce a diffraction pattern or an image (Figure 2.15). A detailed description of the origin and operation principles of the TEM can be found in reference [48].

TEM analysis requires successfully prepared thin foils with a thickness of a few hundred nanometers or less from the bulk material [49]. The success of TEM analysis critically depends on the quality of the thin foils prepared. Basically, the preparation of the thin foils for TEM analysis comprises different steps: (1) obtaining a sample piece 1–2 mm thick (in this study, samples were sectioned from the bulk to smaller segments by using a model 650 low speed rotating diamond wheel saw with minimum supporting weight and wheel rotation speed of 85 RPM). (2) Cutting the sample on a 3-mm diameter disk before further reduction of thickness (in this study, this has been done by using a specially designed punch). (3) Grinding the disk to reduce its thickness to the range of ~ 100–200 μm (this has been done by mounting the disk samples in a goniometer holder and mechanically grinded by distilled water and SiC paper of 600, 1200 and 2400 grit size. This step is following by final polishing to

eliminate scratches by using colloidal silica on cloth). (4) Electro-polishing the sample to a thin foil, which enables sufficient electron beam penetration [50].

The method used for electrolytic thinning is twin-jet technique (Struers Tenupol-5). In this technique, a specimen is placed in an electrochemical cell to act as an anode. A suitable electrolyte (solution of 20 vol.% of nitric acid in methanol in this study) is used to electrochemically reduce the specimen thickness [51]. Electrolyte jet streams polish both sides of the specimen until transparency is detected by a light detector. The final product is the presence of a tiny hole in the middle of the specimen. The area around this hole contains thin sections of electron transparency.

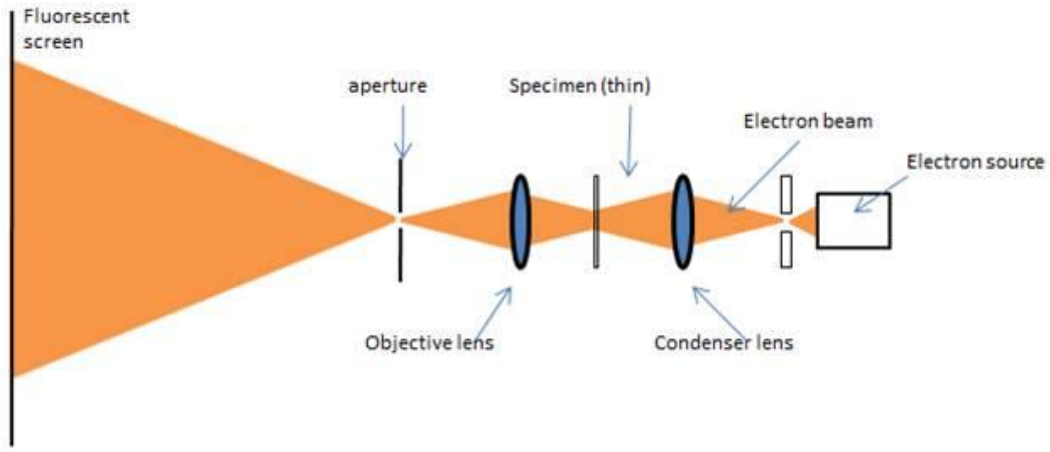

Figure 2.15 Schematic view of the TEM [48].

A TEM investigation within the frame of this work was carried out by the utilization of Jeol2100F operated at 200 kV and FEI titan Ct operated at 300 kV. The interaction of accelerated electrons within samples has been conducted under good vacuum conditions (10^{-5} Pa). The bright field images were used to characterize the microstructure. Selected area diffraction patterns (SADP) were obtained for structural analysis on corresponding alloy phase identification present within the samples.

Scanning transmission electron microscopy (STEM) was used to view high-angle annular bright field images (HAABF). In this mode, a very finely focused beam of electrons scans across the sample in a raster pattern. Interactions between the beam electrons and sample atoms generate a serial signal stream, which is correlated with beam position to build a virtual image [48]. Moreover, imaging the microstructure in

three dimensions has been performed by utilizing electron tomography. This mode depends on the acquisition of projected images from different perspectives because the sample is rotated incrementally about an axis perpendicular to the viewing direction. The images are then rendered into one 3D image. All obtained images were recorded digitally and further treated using Gatan digital micrograph software.

2.3 Hardness test (HT):

In this study, a hardness test (HT) was performed by using micro indentation tests. The aim is to estimate the mechanical properties of our system. The goal of the majority of indentation tests is to extract the elastic module and hardness of the specimen material from a load displacement measurement. Conventional indentation hardness tests involve the measurement of the size of a residual plastic impression in the specimen as a function of indenter load. This requires a measure of the area of contact for a given indenter load. In micro- and nano- indentation tests, the size of the residual impression is often a few microns or less, which makes it very difficult to obtain a direct measure of the size by using an optical microscope. Instead, the depth of penetration beneath the specimen surface is measured as the load is applied to the indenter taken in the consideration that the known geometry of the indenter allows the size of the contact area to be determined [52].

The indentation hardness tests are usually made with either spherical or pyramid indenters. The basic principle is to observe the ability of the material in question to resist plastic deformation from a standard source. An illustration of an example of the pyramid indenter shape is shown in Figure 2.16. As shown in this figure, the pyramid has a square base and an angle of 136° between opposite faces. The applied load usually varies between 0.1 and 10 kg. The full load is normally applied for 1 to 15 s. The hardness value is determined by the load over the surface area of the indentation—i.e., the ratio ***F/A***, where ***F*** is the applied force, and ***A*** is the surface area of the resulting indentation. From the geometry illustrated in Figure 2.16, ***A*** can be determined by the following [52]:

$$A = \frac{d^2}{2\sin(\frac{136^o}{2})} \tag{2.9}$$

Where *d* is the average length of the diagonal left by the indenter.

$$\text{Hardness value} = \frac{F}{A} \cong \frac{1.85\,F}{d^2} \qquad (2.10)$$

Based on the above equations, if the test material is soft, the projected area of the indenter and the depth of penetration become greater and hence the hardness value is small. On the other hand, if the material is hard enough to resist the deformation, the hardness value will be high and hence the depth of penetration becomes smaller.

Within this work, Vickers hardness test (Buehler II) and nano-indentation systems (Nano test Vantage) were used. The testing samples were prepared by using standard metallographic processes (grinding and polishing similar to the method of preparation for the TEM samples). The measurements were taken using a load of 0.2 kg applied to the samples for 10 s. The hardness value can be expressed in VHN (Vickers hardness number). This unit can also be converted to SI units (MPa or GPa).

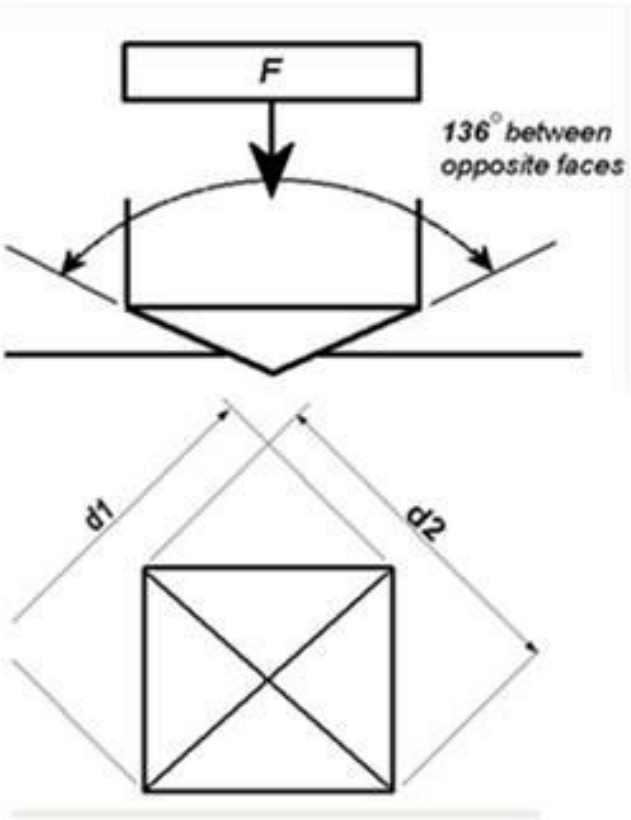

Figure 2.16 Schematic drawing of a diamond indenter in micro- and nano-indentation tests [52].

2.4 Differential scanning calorimetry (DSC):

Differential scanning calorimetry (DSC) uses as an instrument to measure the absorbed or emitted energy during heating or cooling of a specific amount of a sample. DSC monitors the heat effects associated with the phase transitions and chemical reactions as a function of temperature; thus, thermodynamic measurements can be determined.

In DSC, the difference in the heat flow to a sample and a reference at the same temperature is recorded while varying the temperature. The reference is an empty aluminum pan; the sample is weighed in and sealed into an identical aluminum pan (Figure 2.17). A flow of nitrogen gas is maintained over the samples to create a dry and inert atmosphere.

During the heating, the energy Q is needed to maintain a constant heating rate. When the sample undergoes a physical transition, more or less heat will need to flow to it than the reference to maintain the heating rate. The amount of heat flow to the sample depends on whether the sample undergoes exothermic processes (such as crystallization) or endothermic processes (such as transition from a solid phase to a liquid phase) [51].

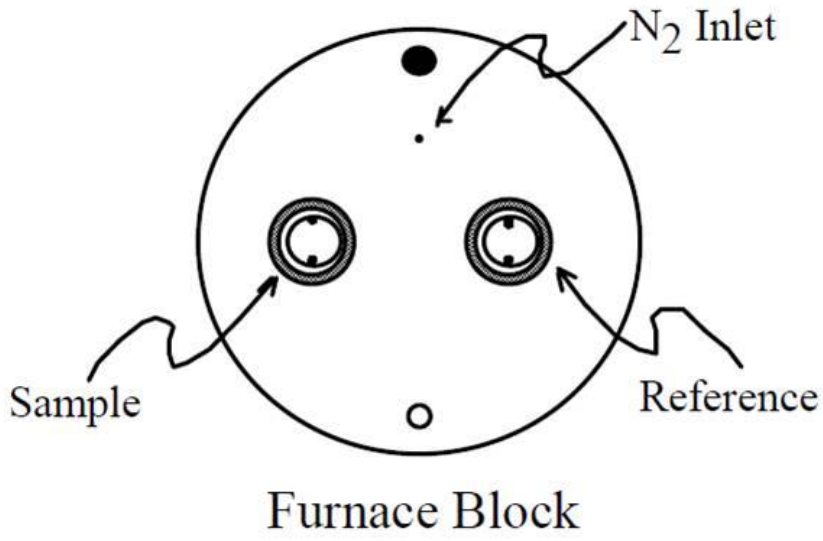

Figure 2.17 Differential scanning calorimetry, sample and reference holder (TOP view) [51].

DSC has been applied extensively to the analysis of light metals, especially Al-based alloys. It has been widely used for analysis of solid state reactions, such as precipitation, homogenization and crystallization. Moreover, it has been used in the analysis of solid-liquid reactions, such as incipient melting and solidification. Details of DSC studies on Al alloy can be found in reference [53].

Within this work, a Netzsh DSC 204 FI aperture was used at a heating rate of 10 K/min. The mass specimen between 12 and 16 mg was placed in an Al crucible in a dynamic nitrogen atmosphere (20 ml/min).

2.5 Inductively coupled plasma optical emission spectrometry (ICP-OES):

ICP-OES is an analytical technique used for the detection of trace metals. In this type of emission spectroscopy, inductively coupled plasma is used to produce excited atoms that emit electromagnetic radiation at wavelengths characteristic of a particular element. The intensity of this emission is indicative of the concentration of the element within the sample [54].

In this technique, a solid sample is normally first dissolved in a suitable chemical and mixed with water. The sample solution is transformed into an aerosol by a so-called nebulizer. The bigger droplets are separated from the smallest in a special spray chamber. The smallest droplets (1–10 μm) are transferred by an argon flow into the heart of the ICP-OES and are introduced directly inside the plasma flow. The bigger droplets are pumped to waste.

The sample immediately collides with the electrons and charged ions in the plasma and broken down into individual molecules that will subsequently fall apart into atoms and ions. The high energy is transferred to the atoms and ions, promoting the excitation of their electrons to higher energy levels. When these exited atoms and ions return to their ground state or to lower excitation states, they will emit electromagnetic radiation at the characteristic wavelength of the elements involved. The light is recorded by an optical spectrometer (Figure 2.18).

The intensity of each line is then compared to previously measured intensities of known concentrations of the elements, and then their concentrations are computed by interpolation along the calibration.

Within the frame of this work, ICP-OES 720-ES interment has been used to measure the chemical composition of complex Al alloys. The mass of the specimens were between 5 and 10 mg. The solid samples were dissolved in a mixture of 3 ml of hydrochloric acid and 1 ml of nitric acid.

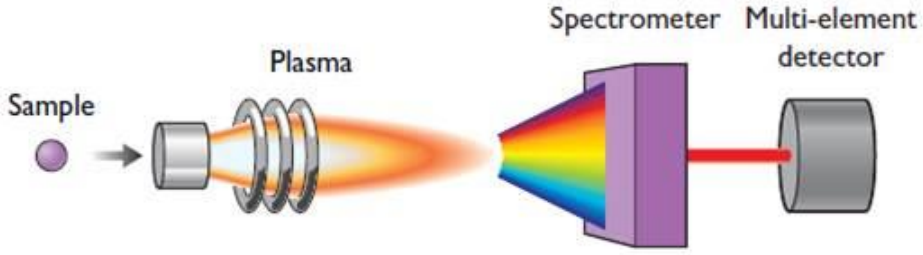

Figure 2.18 Schematic view of an ICP-OES [54].

2.6 Scanning electron microscopy and X-ray spectroscopy (SEM/ EDX):

Scanning electron microscopy (SEM) is the most widely used type of electron microscopy. It examines a microscopic structure by scanning the surface of materials. When high-energy electrons strike a specimen, they produce either elastic or inelastic scattering. Elastic scattering produces backscattering electrons (BSEs), which are incident electrons scattered by atoms in the specimen. Inelastic scattering produces secondary electrons (SEs), which are electrons ejected from atoms in the specimen [51]. SEs are the primary signals for achieving topographic contrast, whereas BSEs are useful for information regarding elemental composition contrast.

Within this work, a BSE detector [BSDE FEI] is used to detect the compositional contrast, which refers to the variation in the gray level of an SEM image. This variation corresponds to the variation in chemical composition in a specimen. The origin of composition contrast arises because the capability of BSEs to escape from the specimen depends on the atomic numbers of the specimen atoms. Thus, the different existing phases can be distinguished within the material.

X-ray photons can be generated during performing analysis by SEM. When an electron with high energy is incident on the specimen, it displaces an inner shell electron. Then, an electron in the outer shell decays to the inner shell to form

characteristic X-rays. X-ray generation is a function of the atomic number (z); thus, it allows chemical analysis and distribution analysis in the testing material by means of X - ray spectroscopy (EDX) [50]. An illustration of the interaction zone between electrons and specimen is shown in Figure 2.19 with different expected signals.

Within the frame of this work, elemental compositions of some specimens were assessed using a Quanta 200 SEM (with 30 kV accelerating voltage) equipped with EDAX FEI and Genesis software. Samples were grinded and mounted onto Al pucks with double-sided carbon tabs.

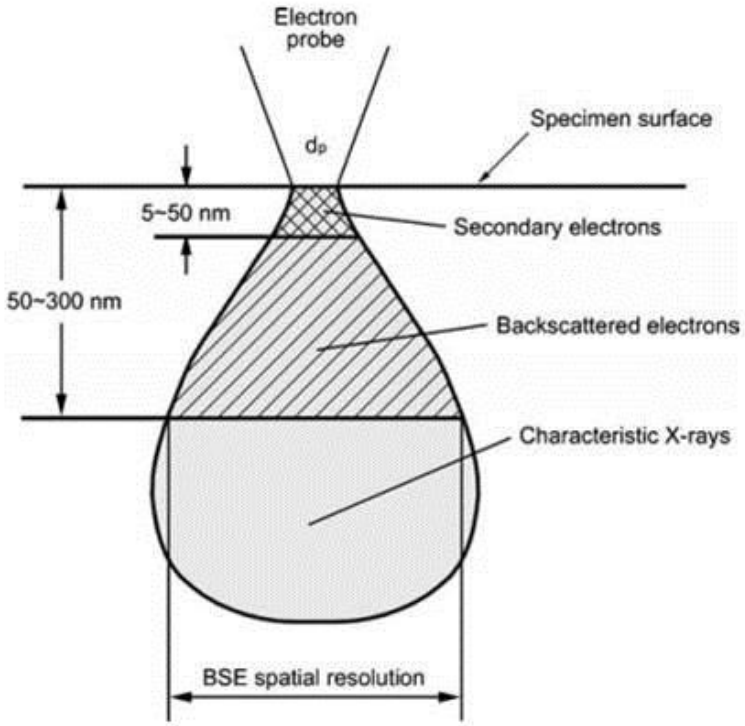

Figure 2.19 Illustration of the interaction zone of electrons and specimen atoms below a specimen surface [51].

2.7 X-ray diffraction:

X-ray diffraction is a widespread, versatile, nondestructive and cost-effective method. Thus, it is one of the most applied tools in material science to determine the structure of a material and the phases present therein. XRD patterns not only allow the qualitative and quantitative identification of the phases but also the determination between amorphous and crystalline materials and the parameters of the crystalline

structure. A detailed description of the origin of the X-ray and different methods can be found in reference [55].

Within the frame of this work, XRD experiments were run on STOE STADPIMP powder diffractometer equipped with Mythen 1k silicon detector cover 90˚ in 2θ and using $CuK\,\alpha_1$ radiation. The diffraction patterns were compared to the simulated phases deposited on ICSD Database. Powder X-ray diffraction samples were prepared by grinding the specimens in an agate mortar.

Chapter 3

Results and Discussion

3.1 Influence of industrial heat treatment on precipitation kinetics in a complex Al alloy:

In response to the demands of various industries for light structural materials, different aluminum lithium alloys have been developed [56]. These alloys are commonly selected because they exhibit an enhanced strength/weight ratio and therefore are typically applied as functional materials with high performance in the aerospace and automobiles industries. Economically, Al-Li alloys are only three times as expensive as conventional aluminum alloys, whereas competing hybrid materials such as new carbon fibre types (CNT) can be up to 10-30 times more expensive [57]. In the context of high fuel prices and fierce competition between composite, hybrid materials and aluminum alloys, different Al-Li-Cu alloys have been developed to overcome most of technical issues associated with the formerly available materials [4]. In the space industry, for instance, Al – Li – Cu based alloys are the candidate material for the construction of launch-vehicle liquid-propellant tanks because the ductility and toughness of the alloy are not affected at the lower temperatures. These alloys are known to be strengthened through precipitation hardening and are attracting strong interest in the framework of the development of new alloys, particularly for aerospace components [58]. The current study selects one of the widely used Al-Li-Cu alloys from the Weldalite family [56], namely, the commercial AA2195 (obtained from Construction & Real Estate, Minerals & Metallurgy). This alloy was developed to replace the AA2219 alloy, which was conventionally used in the US space shuttles [59]. AA2195 is considered to be the third generation of Al-Li alloy. It receives considerable attention from both industrial and scientific communities because of its attractive properties. It has low density, high stiffness, very high strength, good damage tolerance and good weldability. All of these characteristics make this alloy an appealing choice for direct and engineered substitution in all weight-critical applications. AA2195 has been used widely in high-performance military and commercial aircraft. Recently, this material has been successfully used by the National Aeronautics and Space Administration (NASA) in space shuttles for super

lightweight cryogenic tanks, which resulted in a significance increase in payload capacity [60]. This class of alloy is able to achieve superior mechanical properties in the stretched and artificially aged condition (termed as T8), artificially aged condition (termed as T6) and naturally aged condition (termed as T4) [61].

If AA2195 alloy is properly processed and heat treated, it will display higher fracture toughness at cryogenic temperatures than that at ambient temperatures to ensure proper quality. Well-defined behavior of the alloy can be achieved by the selection of good compositional control, thermomechanical processing and aging treatment [62]. For example, the alloy applied in highly stressed aerospace structures is usually supplied in T8 temper (Table 1.2), especially in welded structures. On the other hand, alloy treated with T6 condition (Table 1.2) is often infeasible after welding [63]. Based on this, it is clear that the aim of industrial engineering is to develop the alloy to reach an excellent fracture toughness/strength combination. A recent alloy design for high fracture toughness focused on composition and processing controls to minimize grain boundary precipitates and develop matrix precipitates that homogenize deformation, i.e. precipitates that are not shared by dislocations. As strength (a maximum stress withstand by the material) increases, ductility (The ability of material to be stretched) and fracture toughness (The resistance of the material to the fracture at small plastic deformation) usually decrease [4]. A typical relationship of decreasing toughness with increasing strength is illustrated in Figure 3.1. However, the balance between strength and toughness is greatly affected by different processing parameters such as quenching efficiency and selecting aging times and temperatures.

Previous studies revealed that the Al alloys in T4 temper leads to strengthening by a combination of the G.P zone and $\delta'(Al_3Li)$ precipitates [64]. The alloy in this temper displays a rapid and strong naturally aging response, even without prior cold working. For example, the tensile strength of Weldalite grade alloy in the T4 temper is 20% greater than that of the leading, weldable alloy AA2219 in the T87 temper [65].

The Al alloys with the T6 temper are reported to be strengthened primarily by the $T_1(Al_2LiCu)$ phase, with a minor presence of the $\theta'(Al_2Cu)$ phase [66]. The alloy in this temper exhibited resistance to corrosion during the retrogressed and raged process [67]. This corrosion resistance can be explained in the terms of the coarsening of the

grain boundary precipitates. In addition, the increase in the volume fractions of the second phase particles at the grain interiors was responsible for the increase in the strength of the alloy following this temper [68]. In addition, a two-step T6 aging treatment was demonstrated to result in strength and ductility comparable to those of samples in the T8 temper [67].

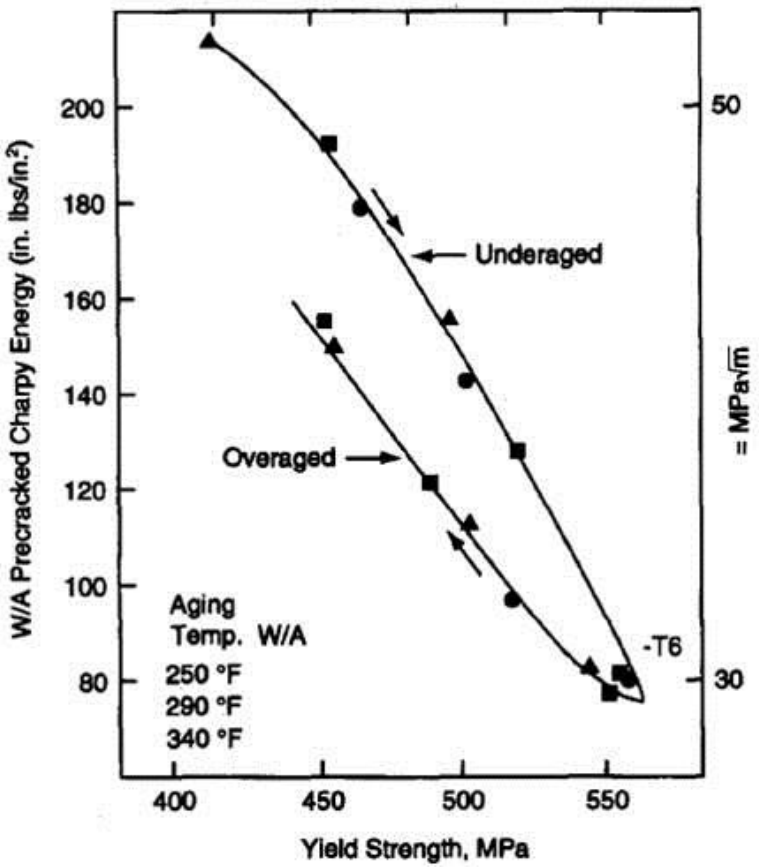

Figure 3.1 Typical relationship between strength and toughness for complex Al alloy [4].

For the Al alloy in the T8 condition, the microstructure, as revealed by transmission electron microscopy, mainly consisted of the $\delta'(Al_3Li)$ and $T_1(Al_2LiCu)$ precipitates as the primary strengthening phases [69]. The application of plastic deformation prior to artificial aging is used to promote a uniform distribution of heterogeneously nucleated T_1 precipitates. The distribution of the T_1 precipitates in the microstructure after conducting the T8 temper is considered to be responsible for the improvements in the strength and fracture toughness. The plastic deformation can

be effective for strengthening aluminum alloys processed at cryogenic and room temperatures.

In the quenched state and the early stage of aging, the microstructure shows a mixture of well-defined ordered $\delta'(Al_3Li)$ and complex $\delta'(Al_3Li)$ / $\beta'(Al_3Zr)$ ordered precipitates with spherical and polygonal shapes in the Zr containing alloy [70]. After solution aging treatment, most of the Zr are found within small spherical (Al_3Zr) dispersoids that are approximately 20 nm in diameter [26].

Generally, the aging of the Al-Li-Cu system can generate a number of phases, the most important being the $T_1(Al_2LiCu)$ phase. However, depending on the alloy composition and processing condition, other minor phases can be precipitated [15]. The addition of minor elements can result in a diversity of precipitates. For example, the addition of Mg to the Al-Cu-Li alloy promotes the formation of phases in the Al-Cu-Mg system [71]. As such, the combination of multi-species chemistry and the influence of the heat treatment on the phase transformations result in complex Al-Li alloys exhibiting a large of variety of precipitation kinetics, and the dependence of these kinetics on the aging treatment condition is still an area requiring a great deal of research. In fact, an understanding of phase transformations in metal alloys requires an understanding of the effect of both temperature and composition. A combination approach to such a problem is to have a rapid screening of the effects of heat treatment on the precipitation kinetics to investigate the competition of phase transformation during precipitation. In Al alloy, as a class important engineering material, subtle variations in chemistry can strongly influence the decomposition of the supersaturated solid solution and hence result in the development of different precipitate phases that can significantly modify the mechanical properties of the material.

The objective of this study is to investigate the dependence of the precipitation kinetics and the phase transformations in complex Al-Li alloys on the preformed heat treatment conditions. AA2195, a commonly used aluminum alloy, was selected as a model system. The heat treatments considered in this study were common industrial heat treatments: T8 temper (solution treated, cold working and artificially aging), T4 temper (solution treated and naturally aging) and T6 temper (solution treated and artificially aging). The selection of these heat treatment conditions are

based on the superior mechanical properties exhibited by the sample with these conditions (Table 3.1). The use of a combination of experimental methods – a laser-assisted wide angle tomographic atom probe (LAWATAP), field ion microscopy (FIM), transmission electron microscopy (TEM), differential scanning calorimetry (DSC) and Vickers micro hardness measurements – allowed for a qualitative evaluation of the precipitation kinetics and phase transformation as functions of the temper conditions.

3.1.1 Materials and methods:

Plates of 1-mm thick alloy AA2195 were subjected to the following treatment conditions: 1) T8 (solution treatment for 1 h at 510 °C, water quenching, plastic deformation of 3% and artificial aging for 30 h at 150°C), 2) T4 (solution treatment for 1 h at 530°C, water quenching and natural aging at room temperature for 4000 h), and 3) T6 (solution treatment for 2 h at 495 °C and for 4 h at 515 °C, water quenching and artificial aging for 20 h at 180 °C) (Figure 1.2). The solution treatment step was performed by using a molten salt bath (75 wt.% KNO_3, 20 wt. % $NaNO_3$, 5 wt. % $NaNO_2$) to prevent oxidization. The quenching step was performed by using water and ice. An electrical furnace was utilized to age the specimens placed in an oil bath or a quartzite ampule sealed under vacuum (Figure 3.2).

Table 3.1 A summary of mechanical properties for AA2195 heat treated with T8, T6 and T4 tempers [source: matweb.com].

	T8	**T6**	**T4**
Ultimate tensile strength	710 MPa	720 MPa	241 MPa
Yield strength	690 MPa	680 MPa	145 MPa
Shear strength	420 MPa	420 MPa	165 MPa
Elongation at break	5 %	4 %	22 %

The chemical compositions of the samples following treatment under the T8, T4 and T6 conditions are presented in Table 3.2. The measured compositions using inductively coupled plasma optical emission spectrometry using an ICP-OEC 720-ES instrument are in a good agreement with the nominal composition in all cases.

The influence of different heat treatment conditions on the mechanical properties was studied using the Vickers hardness test. The samples were grinded and polished as described in section 2.2 to remove oxide from the surface. The hardness was determined by averaging 10 measurements. The thermal properties of the AA 2195 at different tempers were examined by DSC as described in section 2.4. TEM analysis was also performed after each specific treatment.

Table 3.2 Chemical composition of alloying elements in AA2195.

Alloying element	Cu	Li	Mg	Ag	Zr	Al
Nominal (wt. %)	4	1	0.36	0.28	0.14	94.22
Nominal (at. %)	1.69	3.87	0.39	0.06	0.04	93.95
ICP – T8 (at. %)	1.74 ± 0.19	3.67 ± 0.05	0.36 ± 0.01	0.08 ± 0.02	0.04 ±0.004	94.11±0.27
ICP – T4 (at. %)	1.55 ± 0.1	4.23 ± 0.1	0.31 ± 0.04	0.08 ± 0.01	0.04 ±0.001	93.79±0.25
ICP – T6 (at. %)	1.58 ± 0.1	3.36 ± 0.1	0.3 ± 0.03	0.08 ± 0.01	0.04 ±0.001	94.64±0.24

Microstructural characterization at the atomic scale was performed using atom probe tomography (APT). Atom probe studies were performed using LAWATAP in the voltage mode at 30 K with a pulse fraction of 20 % and at a vacuum level of 10^{-8} Pa. Electro-polishing was performed using a solution of 30 vol % of nitric acid in methanol at – 20 °C in the range of 5 to 7 V. FIM images were obtained on LAWATP using Ne as the imaging gas at 25 K and 1.2×10^{-3} Pa. It is worth noting that the electro-polishing method was applied because the desired needle-shaped specimen with a clean surface can be produced by using this method. The quality of the tip is usually examined by SEM. Figure 3.3(a) shows an example of an ideal tip and a badly shaped tip is shown in Figure 3.3(b). It worth mentioning that using the FIB method to prepare tips from this respective material causes damage to the microstructure because of irradiation and ion implantation. An example of this damage can be seen in Figure 3.4, which represents the part of the reconstruction volume of a specimen prepared via FIB.

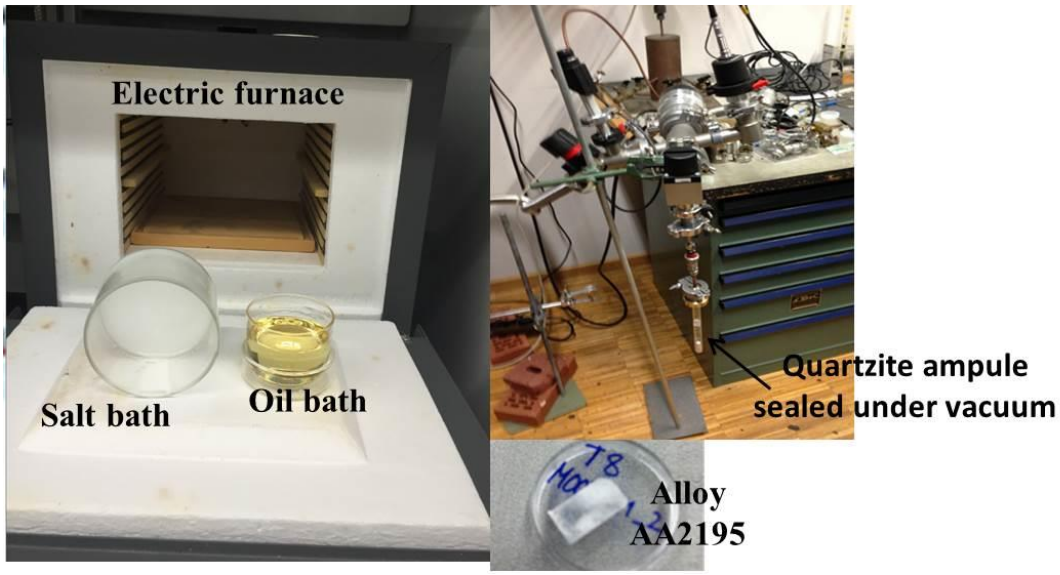

Figure 3.2 Required tools for heat treatment procedure.

The obtained APT data were visualized using the TAP3D and IVAS software programs provided by Cameca. Calibration of the main reconstruction parameters was performed by observing the atomic plane for the respective crystallographic pole. In APT data, different crystallographic information can be extracted. For every specific crystallographic direction, the atomic planes can be observed in the depth dimension of a 3D atoms map (Figure 3.5). Because the resolution is sufficient to resolve these atomic planes, the distance ***d*** between two atomic planes can be measured experimentally. By knowing the lattice parameter of our material (***a = 0.405*** **nm** for Al (FCC)), the miller incidences (***hkl)*** for the corresponding crystallographic pole can be determined. This crystallographic information has been used to achieve precise tomographic reconstruction. The composition of the different observed precipitates was measured quantitatively using the proximity histogram (prixogram) algorithm which was introduced in section 2.1.5.1.

3.1.2 Hardness properties:

Figure 3.6 shows the hardness evolution during the heat treatment of the alloy for different temper conditions: T4, T8 and T6. The first feature of interest is that the specimen in T8 temper has a higher hardness ((160.3 ± 7) HV/1.96) than those of the specimens in the T4 and T6 tempers. During T4 and T6 tempering, both specimens experience a significant and quite similar hardening response. The minimum

hardness value is reached in T6 tempering ((112 ± 5) HV/1.96). During the natural aging of the sample in the T4 temper, no significant change of hardness is observed ((125.2 ± 9) HV/1.96). This behavior can be attributed to the presence of different nano-scale structural features after the conducting of each heat treatment temper. The explanation of most of these features from the microstructure evaluation will be presented in the following section.

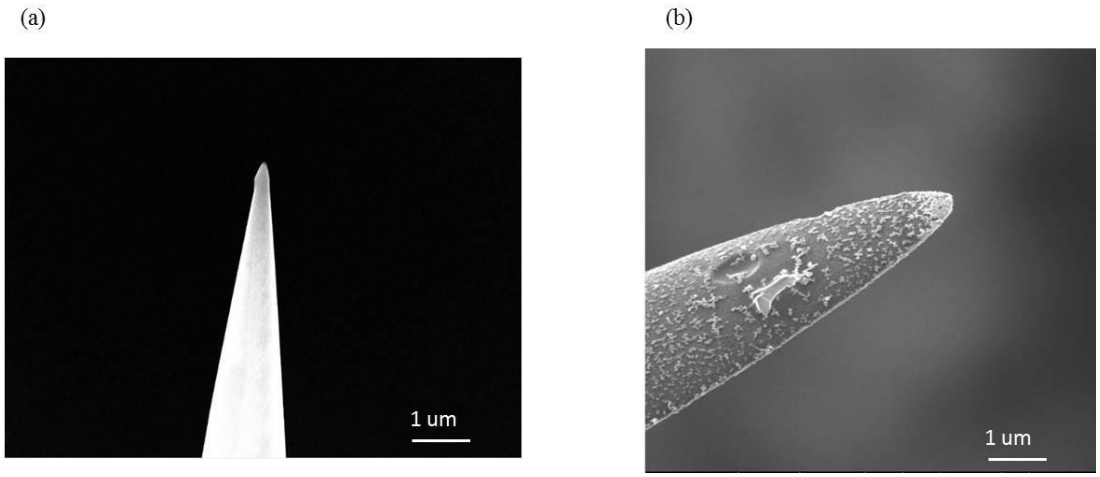

Figure 3.3 SEM micrographs of the prepared APT tips. (a) An ideal tip. (b) An oxide tip.

3.1.3 TEM evolution of the microstructure:

TEM analysis of the specimens conducting different temper conditions is shown in Figure 3.7. The microstructure of a naturally aged sample after conducting the T4 heat treatment is shown in Figure 3.7 (a). Precipitates were characterized using an exact [110] zone. The microstructure encompasses spherical precipitates with $L1_2$ structure. A schematic of the indexed selected area diffraction pattern (SADP) in the [101] direction is integrated with the bright field TEM image (Figure 3.7(a)). This observation indicates the presence of the supper lattice reflection, which originates from an $L1_2$ ordered structure representing $\beta'(Al_3Zr)$ precipitates. The $L1_2$ unit cell is based on the FCC structure of aluminum. However, the corner atoms are replaced by Zr atoms. This substitution means that all <100> directions are super structure directions. The spherical precipitates are assigned to be of the β'-type and not of the δ'-type because the Li composition in the investigated alloy is less than 5 at.% (Table 3.2). Hence, there is no expectation to observe $\delta'(Al_3Li)$ precipitates. However, the contrast of the spherical particles indicates that there are wings of low

intensity surrounding the β' particles. This observation could be due to the role of the β' phase on providing heterogeneous nucleation sites for the δ' phase or/and T_1 phase [11],[72].

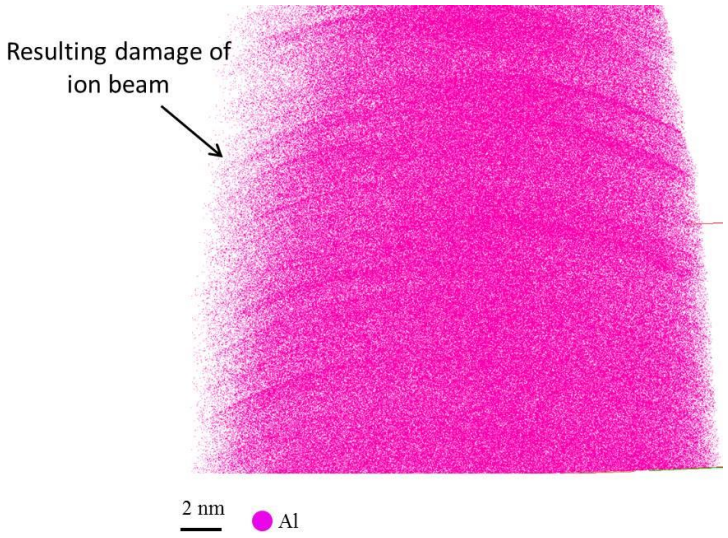

Figure 3.4 A deep insight on the microstructure of the APT tip of complex Al alloy prepared via the FIB method showing the presence of damaging.

Figure 3.7 (b) shows a TEM bright field image of the specimen conducting T8 heat treatment condition. The image revealed a complex microstructure, including different precipitates with platelets and spherical morphology. Once again, precipitates were characterized using an exact [110] zone. A schematic of the indexed selected area diffraction pattern in the [101] direction in Figure 3.7 (b) indicates the presence of two variants of the T_1 precipitates as streaks along the <111> directions in the pattern. The other two variants of this phase produce spots adjacent to the <200> positions. The streaks along the <200> directions reveal the presence of the θ'precipitates. Because this phase lies on three orthogonal cube axes, the diffraction patterns manifest themselves as vertical and horizontal streaks [24]. The super lattice reflection in the pattern is attributed to the β' precipitates. These observations provide evidence that the peak hardness microstructure consisted of the thin T_1 platelets associated with the smaller fraction of Cu-rich phase, i.e., θ' platelets and the β' phase.

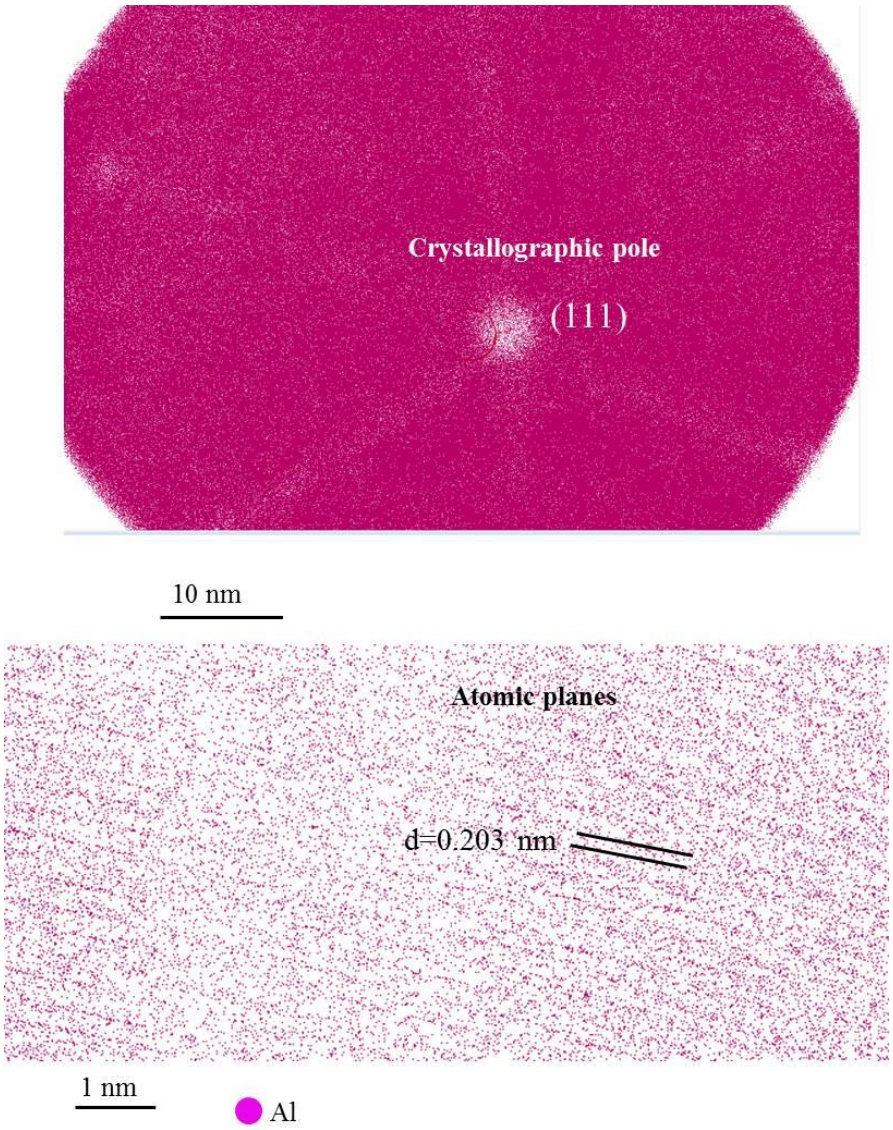

Figure 3.5 The top view of the reconstructed volume of the AA2195 alloy shows the position of crystallographic pole and the sub-volume showing the perpendicular atomic planes to this pole.

A TEM bright field image of the specimen after the T6 heat treatment is shown in Figure 3.7(c). In this case, the matrix contained the T_1 precipitates as the primary strengthening phase. It is difficult to observe any streaks along <200> directions, due to a negligible presence of the θ'precipitates in the microstructure for the specimen under the T6 condition. However, it is clear from Figure 3.7(c) that under T6 heat treatment the T_1 precipitates remain quite thin and in a good dispersion.

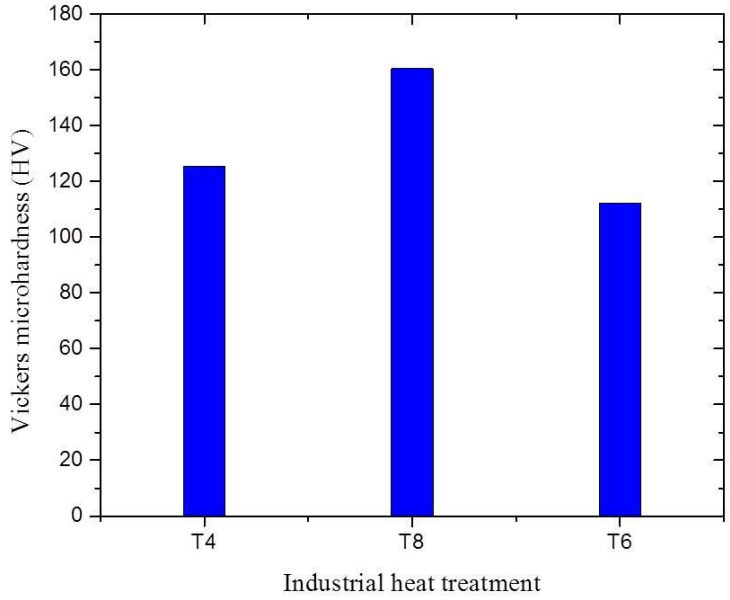

Figure 3.6 Hardness evolution during the heat treatment of the alloy for different temper conditions; T4, T8 and T6.

3.1.4 Thermal characterization:

Further confirmation of the precipitation kinetics during different temper treatments was obtained by performing DSC scans for the specimens under the T4, T8 and T6 conditions. The results of the thermal characterizations are shown in Figure 3.8, which presents the DSC traces of the specimens in all three temper treatments. The precipitate and dissolution reactions important for thermal stability and precipitation occur in the aluminum alloy in the range of temperature of 25- 350 °C [69].

The major thermal events for the specimens in the T8 condition are the endothermic dissolution peak spanning the range of ~ 180 – 220 °C and the exothermic precipitation peak spanning the range of ~ 220 – 280 °C. For the specimen in the T4 condition, the DSC signal shows the presence of two endothermic dissolution peaks: the first peak spanning the range of ~ 90 – 130 °C and the second spanning the range of ~ 190 – 230 °C. Moreover, the presence of an exothermic precipitation peak spanning the range of ~ 230 – 310 °C and an endothermic dissolution peak spanning the range of ~ 320 – 500 °C are observed. Finally, the signal for the specimen in the T6 condition shows an endothermic dissolution peak at elevated temperature spanning the range of ~ 320 – 500 °C.

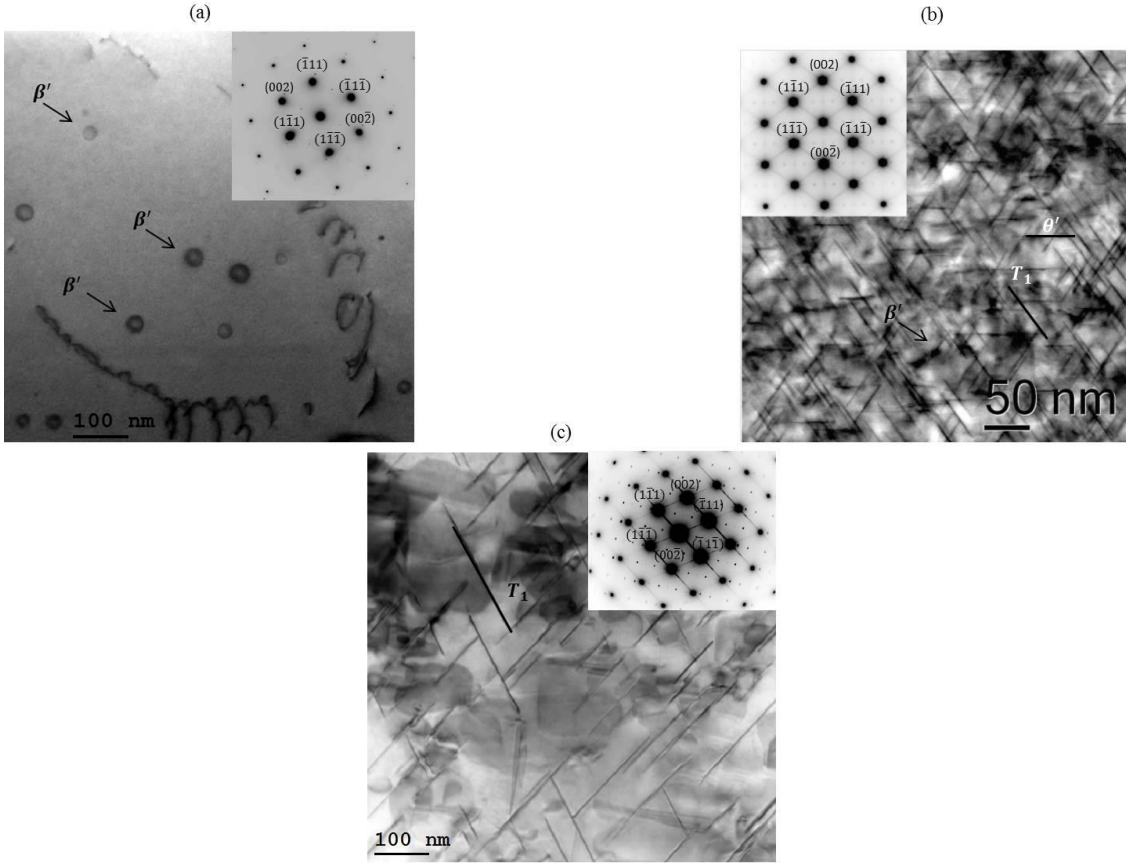

Figure 3.7 Evolution of the microstructure as observed by TEM. (a) Typical bright field image of the specimen after conducting the T4 heat treatment shows the presence of β′ precipitates within the microstructure and the corresponding [101] selected area diffraction pattern (SADP). (b) Bright field image of the microstructure conducting T8 heat treatment condition shows a complex microstructure with the T_1, θ' and β' precipitates and the corresponding [101] selected area diffraction pattern (SADP). (c) Microstructure of the specimen after the T6 heat treatment condition consists of T_1 precipitates as the primary strengthening phase and the corresponding [101] selected area diffraction pattern (SADP).

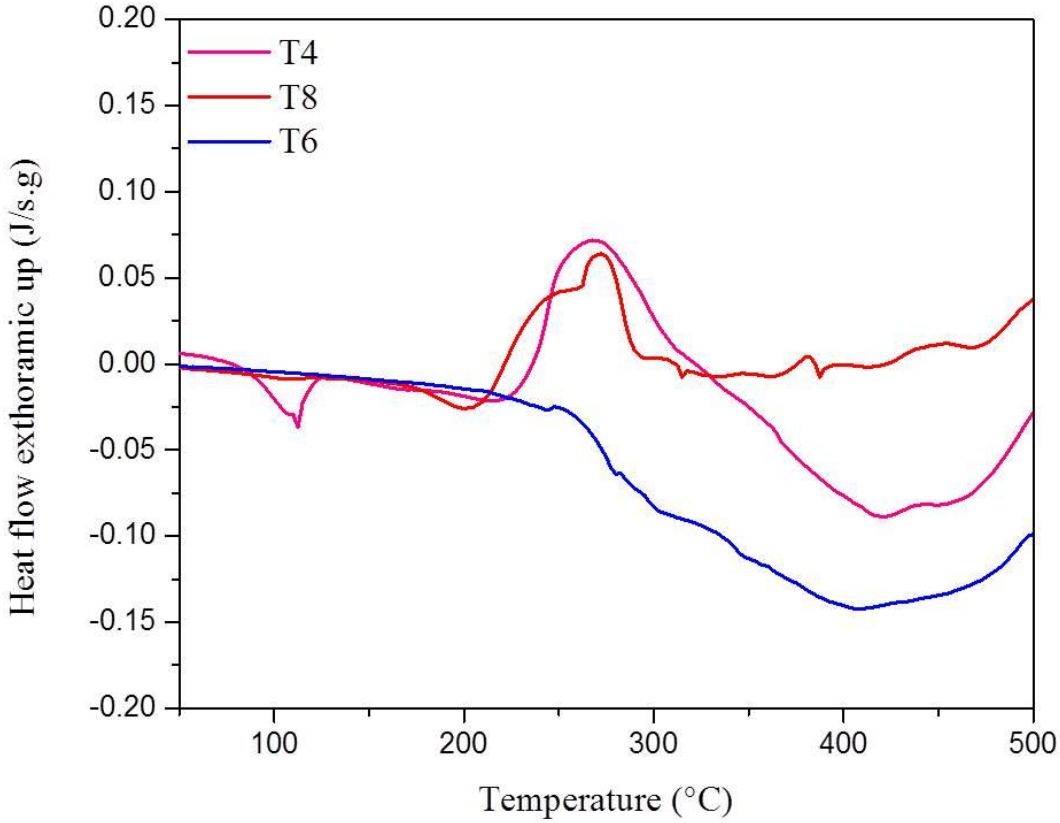

Figure 3.8 DSC traces of the specimens in three temper treatments; T4, T8 and T6.

Based on previous observations in the literature [69] and on the TEM analyses above, the peaks can be identified as the following. The endothermic dissolution peak spanning the range of ~ 90 – 130 °C in the T4 condition is the result of dissolution of the GP zone (precursor of the θ' phase). The second endothermic dissolution peak spanning the range of ~ 190 – 230 °C is due to the dissolution of the T_1 phase. The exothermic precipitation peak spanning the range of ~ 230 – 310 °C is due to the precipitation of the θ' phase. Finally, the last endothermic dissolution peak spanning the range of ~ 350 – 500 °C corresponds to the dissolution of the existing bulk phases [73].

For the T8 condition, the endothermic dissolution peak spanning the range of ~ 180 – 220 °C is assigned to the dissolution of the T_1 phase. However, the exothermic precipitation peak spanning the range of ~ 220 – 280 °C is assigned to the re-precipitation of the T_1 phase again. The re-precipitation phenomena under the

dynamic heating condition in DSC have been previously reported for under-aged Al-Li alloys [74]; the authors reported the retrogression of the δ' phase, which formed during the aging process, and the subsequent exothermic peak, which corresponds to the re-precipitation of the δ' phase, were explained in terms of the increase in the number of the solute atoms in super saturated solid solution, which causes the re-precipitation to occur. In our case, the strong re-precipitation of the T_1 phase observed for the specimen in T8 condition suggests that the T8 temper condition still exhibits an appreciable super saturation with respect to Cu and Li atoms. During the DSC scan with a heating rate of 10 K/min, this super saturation leads to the precipitation of an additional amount of the T_1 phase [73].

Finally, the endothermic dissolution peak spanning the range of ~ 320 – 500 °C in the T6 condition most probably originates from on going T_1 dissolution, which is considered to be the dominant phase in the microstructure, according to the TEM image (Figure 3.7(c)).

The variations and the similarities of the thermogram curves in Figure 3.8 reveal the changes of precipitation processes to some extent. It is worth to note that the identification of the precipitation kinetics and phase transformations has not been conclusively established by the DSC signals. Therefore, obtaining a clear picture of the precipitation kinetics and phase transformations from the naturally aged condition (T4) to the peak-aged state (T8) and then to the slightly over-aged state (T6) required a deeper insight into the microstructure-properties relationship at the nano-scale using a global characterization technique, such as APT.

3.1.5 FIM evolution of the microstructure:

Prior to performing the APT analysis, the FIM mode in the LAWATAP was used. FIM was mainly used to develop the needle shaped samples for the subsequent analysis by APT. Surface oxide and damage induced by using the standard electro-polishing method could thus be eliminated. In this method, Ne gas atoms are field ionized due to the presence of a high electric field at the tip surface. During the FIM imaging procedure, a heat-cooling cycle was applied. This cycle includes the increasing of the temperature without increasing the applied voltage. The next step is to reduce the temperature of the specimen and increase the applied voltage

concomitantly. Applying this procedure allows cracking of the oxide layer and achievement of an accurate image of the specimen surface.

Figure 3.9 shows the field ion micrographs for the alloy AA2195 after conducting the three industrial heat treatments, i.e., the T4, T8 and T6 conditions. Figure 3.9 (a) is the field ion micrograph for the sample undergoing the T4 heat treatment condition. This Figure revealed the presence of the spherical precipitates, which appear bright in the images. These spherical precipitates are most probably of the β'-type, as discussed above. Figure 3.9 (a), also clearly shows that the contrast within the matrix is very poor and that the Zr-rich precipitates appear very bright with respect to the dim Al matrix. This observation is due to the higher evaporation field of Zr (56 V/nm) compared to that of Al (19 V/nm) [38]. The difference on the microstructure after undergoing the T8 heat treatment condition is shown in Figure 3.9 (b). The presence of platelet shaped precipitates distributed within the matrix around the crystallographic pole that appear bright in the image is revealed. The microstructure of the sample under the T6 heat treatment condition is shown in Figure 3.9 (c). Once again, the sample consisted of platelet shaped precipitates. However, some of these platelets exhibit a slight coarsening behavior.

It is notable that all of the precipitates in this study are brightly imaged using the FIM mode. This observation can be explained by considering the field strengths of the existing precipitates, which contain Cu, Li and Zr, which are higher than that of the matrix, which is Al enriched. Accordingly, it is very likely in the FIM images that these precipitation regions protrude over the Al matrix and thus act as potential sites for imaging ions (Figure 2.8). This effect, in turn, causes the bright appearance of the precipitates in the micrographs [38].

3.1.6 APT analysis:

The ternary Al-Li-Cu system has a complex precipitation sequence, exhibiting aspects of both binary Al-Cu and Al-Li systems. This precipitation is further complicated by the addition of minor alloying elements, such as Mg, Ag and Zr. The aging of this complex alloy generates a number of different phases.

A detailed and robust investigation of the precipitation kinetics and complex phase transformations are discussed below.

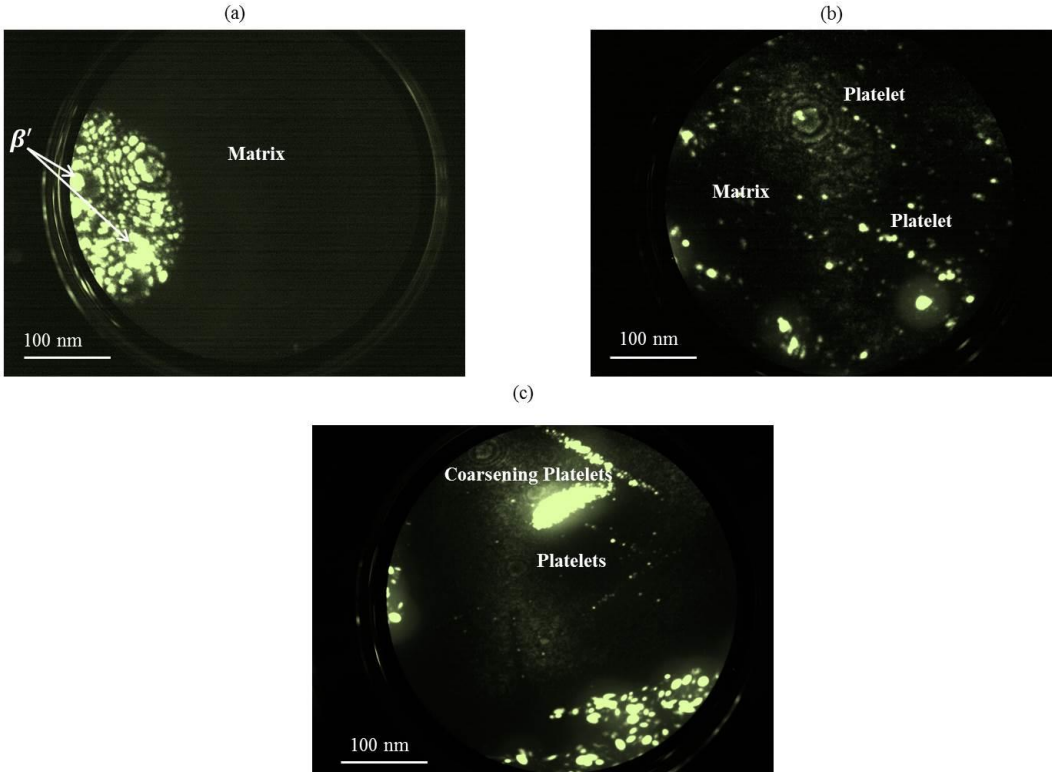

Figure 3.9 Field ion micrographs for the alloy AA2195 after conducting the three industrial heat treatments, the (a) T4, (b) T8 and (c) T6 conditions (All of the precipitates are brightly imaged).

3.1.6.1 Naturally aged samples at T4 temper:

Figure 3.10 shows the reconstructed volume of the sample in the T4 condition analyzed using LAWATAP. Based on the TEM and FIM observations above, the microstructure in this condition is expected to have only particles of $\beta'(Al_3Zr)$. Due to the fact of the large diameter (~ 20 nm) [26] and low number density of the β' phase in the microstructure, the APT analysis of such a phase is challenging. Different experimental analyses reveal the homogenous microstructure without any indication of the presence of any phases as shown in the reconstructed volume and FIM image in Figure 3.11. However, repeating the experimental analyses for the specimens in this condition permits the collection of two datasets, from which a statistically significant conclusion regarding this phase and its interface with the matrix are drawn.

Estimation of the β' precipitates was performed using a cluster identification algorithm which has been explained in section 2.1.5.3. Zr containing precipitates were identified by applying a maximum separation distance of 0.7 nm between the Zr atoms, with a minimum of 20 Zr atoms in each precipitates. Exploration of the distribution of the β' precipitates is shown in Figure 3.10 (a). The precipitates exhibit a somewhat spherical shape, with an average diameter of (10 ± 2) nm. The precipitates are then delineated by 5 at.% Zr isoconcentration surface. A proxigram composition profile from this isoconcentration surface gives the chemical composition of the β' phase as (23± 2) at.% Zr, (1.8 ± 0.5) at.% Li, (1.6 ± 0.4) at.% Cu (0.25 ± 0.1) at.% Mg and (0.4 ± 0.2) at.% Ag with an Al / Zr ratio close to 3:1 (Figure 3.10(b)). This result, also in a good agreement with the results reported by Sha and Cerezo [75], indicates precipitation of $\beta'(Al_3Zr)$.

The presence of β' particles in the microstructure of the naturally aged sample can be interpreted as a result of the formation of β' dispersoids from the super saturations. These β' dispersoids are very stable due to the low Zr solubility in the Al matrix, i.e., a small misfit and sluggish diffusion of Zr [15]. Zr is considered to be an important trace alloying element in a high strength Al alloy. Zr is often added to optimize the properties of the alloy and has different effects, such as refining the grain size, inhibiting the recrystallization and improving the corrosion cracking resistance [76] and quench sensitivity of the alloy [74]. To date, the ability of the main alloying elements, such as Li, Cu, Mg and Ag, to be dissolved into these particles remains unclear [75]. The alloying elements of Zr, Li, Cu, Mg and Ag are displayed separately in the top view of the reconstructed volume in Figure 3.10 (c). Clearly, inspection of this figure reveals the enrichment of the β'/ matrix interface with Li, Cu and Mg atoms, as indicated by the arrows. However, the enrichment of Li and Cu is more pronounced than that of other solute atoms. To quantify the enrichment of the β'/ matrix interface by solute atoms, the composition profile is drawn in the cylinder perpendicular to the interface. According to this profile, the compositions of Li and Cu atoms at the interface show an increase of approximately 2 at. % and 5 at.%, respectively. However, it seems that Mg atoms concomitantly segregated with Li and Cu atoms, whereas Ag did not. This observation, in combination with the TEM image (Figure 3.7(a)), indicates the strong segregation behavior of the Li and Cu atoms at the interface. This segregation suggests that β'

particles possibly favor preferred nucleation sites for the δ' phase or/and T_1 phase. As the Li content in the investigated alloy is less than 5 at.%, the presence of the δ' phase is not expected. On this basis, it can be concluded that β' dispersoids play a potential role as heterogeneous nucleation sites for the T_1 phase in the naturally aged sample.

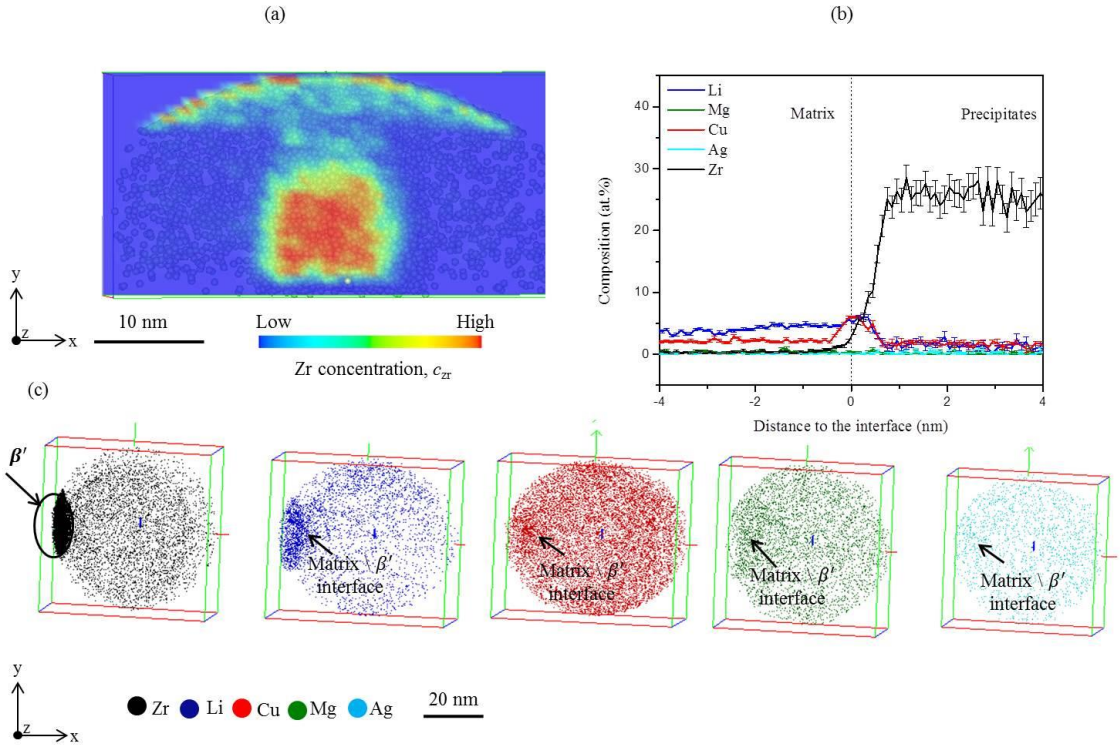

Figure 3.10 The reconstructed volume of the sample in the T4 condition analyzed using LAWATAP. (a) Exploration of the distribution of the β' precipitates in an Al matrix. (b) A proxigram composition profile from the isoconcentration surface of 5 at.% Zr (c) The top view of the reconstructed volume displays separately the alloying elements: Zr, Li, Cu, Mg and Ag. The figure indicates the segregation behavior of solute atoms at the β'/ matrix interface.

The enrichment of the β' \ matrix interface with solute atoms can be explained in the term of $L1_2$ order structure of this phase. It is expected that the solute atoms cannot be dissolved inside these precipitates; hence, they are rejected to the matrix. Understanding the nucleation mechanism of the T_1 phase requires the knowledge that the T_1 platelets usually nucleate on dislocation loops and/or on Zr-bearing

incoherent dispersoids when the alloy has undergone applied plastic deformation [72]. However, in the case of a naturally aging sample, it seems that in specimens that are naturally aged for long time (> 4000 h), the solution atoms—i.e., Li, Cu and Mg—are able to diffuse to the coherent interface between the β' precipitate and the matrix. This diffusivity induces the nucleation of the T_1 phase under this condition. The segregation behavior can be quantified using the APT method.

The good hardness response for this particular temper can be attributed to the presence of β' dispersoids, which is considered to be one of the hardening phases in a quenched sample [77].

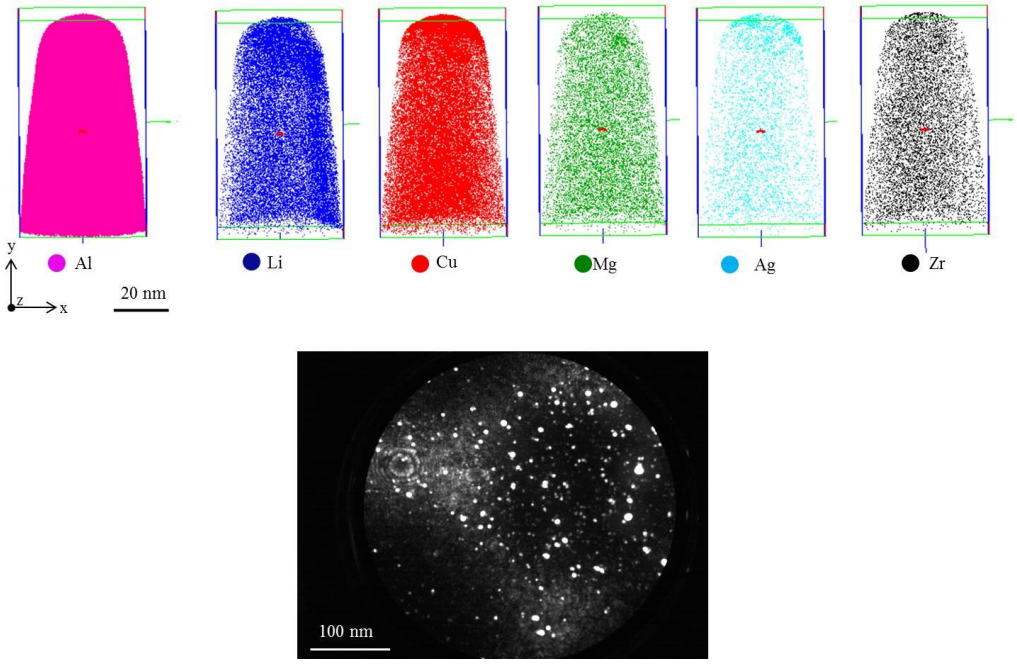

Figure 3.11 The reconstructed volume and the FIM image for the specimen under T4 heat treatment condition showing the homogenous distribution of all alloying elements.

3.1.6.2 Cold working and artificial aging of the sample at T8 temper:

To provide a qualitative assessment of the effect of the heat treatment condition on the precipitation kinetics and phase transformation through the transition from naturally aging condition to peak state aging, an APT analysis for the sample following T8 heat treatment was performed (Figure. 3.12).

Areas of higher Cu concentrations are visible in Figure 3.12 (a). Isoconcentration surfaces, which delineate regions containing more than 4 at.% Cu, are included to aid in the visualization of the θ'precipitates with platelet morphology, an average diameter of (1.8 ± 0.2) nm and an average length of (11 ± 1) nm.

Figure 3.12 (b) shows a combined proxigram concentration profile based on the isoconcentration surfaces of all of the highlighted θ'precipitates. Starting at the matrix/precipitate heterophase interface and moving into the precipitate, the chemical composition was determined to be (29.6 ± 1) at.% Cu, (3.2 ± 0.4) at.% Li and (1 ± 0.2) at.% Mg. Concomitantly, the Li concentration inside the precipitates was found to be the same as its value in the matrix. It is worth noting that the identification of the phase has been performed here based on its chemical compositions.

The recorded observation indicates the partitioning of the Li atoms within the θ'precipitates, as shown in Figure 3.12 (a). The partitioning of Li atoms to the θ' precipitates might indicate the possible occurrence of the phase transformation of the θ' precipitates at the later stages of the aging. It is worth noting the agreement of the experimental measured chemical composition of the θ' with the expected stoichiometric composition of (Al_2Cu).

In addition to the θ'precipitates, a variety of the T_1 platelet precipitates are found within the microstructure (Figure 3.13). This observation is consistent with the reported result by Decreus et al. [78], who proposed that the pre-deformation process mostly promotes the formation of the T_1 phase, which is associated with the precipitates from the Al-Cu binary system, i.e., the θ' phase. Note the fine distribution of the T_1 platelets with an average thickness of (1.4 ± 0.2) nm and an average length of (11.8 ± 2) nm within the microstructure (Figure 3.13 (a)). Moreover, the intersection of more than two platelets, as indicted by the lines in Figure 3.13(a), can be observed. These reported observations in this temper condition can be attributed to the applied plastic deformation prior to the artificial aging. The plastic deformation results in a high dislocation density, which results in a high density of nucleation sites for the $T_1$and θ' platelets and the presence of a high initial vacancy flux, which leads to the enhanced diffusion of the solute atoms.

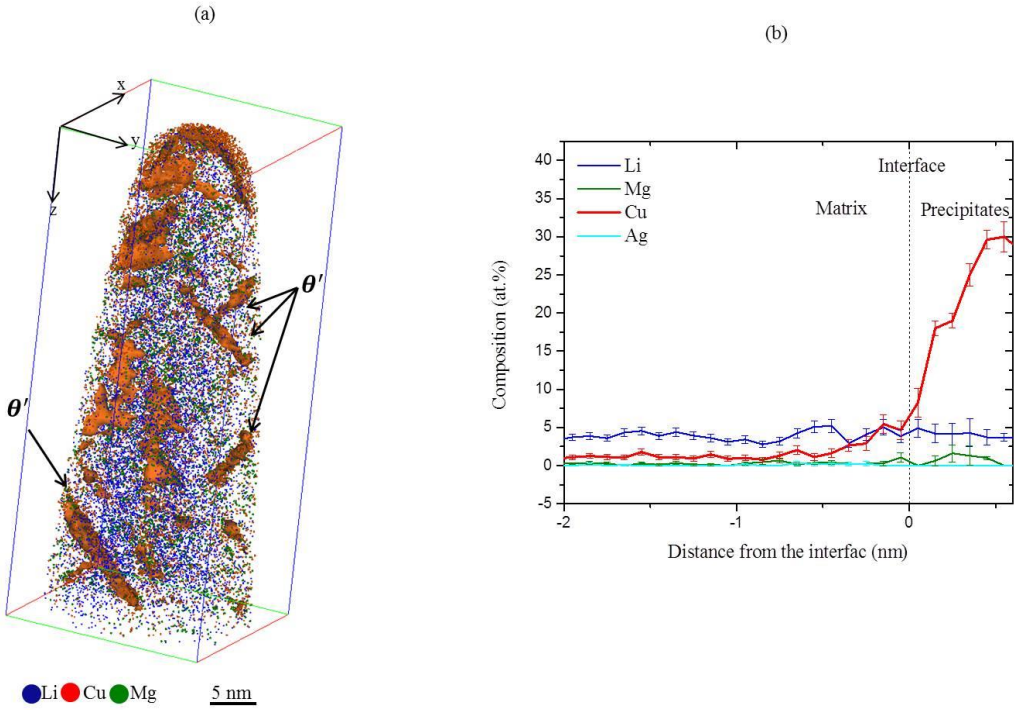

Figure 3.12 LAWATAP analysis of the sample following T8 heat treatment (a) The reconstructed volume of the sample displayed with isoconcentration surfaces of 4 at.% Cu delineate θ'precipitates. (b) Corresponding combined proxigram composition profile based on these isoconcentration surfaces.

The observed microstructure and good mechanical properties at this temper confirm that applying plastic deformation accelerates the precipitation kinetics by approximately one order of magnitude [79]. Quantitative evaluations of the T_1 platelets precipitates presented in Figure 3.13(b) show that the average chemical composition, as estimated from the concentration composition profile based on the isoconcentration surface that contains more than 6 at.% Li (calculated over 20 precipitates containing in different reconstructed volumes), is (13±1) at.% Li, (11±1) at.% Cu, (3±1) at.% Mg and (1.5±0.4) at.% Ag. This value shows a deviation from the (Al_2LiCu) stoichiometry of the bulk T_1 phase and the enrichment of this phase with Mg and Ag. The reason behind the deviation from the (Al_2LiCu) stoichiometry will be discussed later.

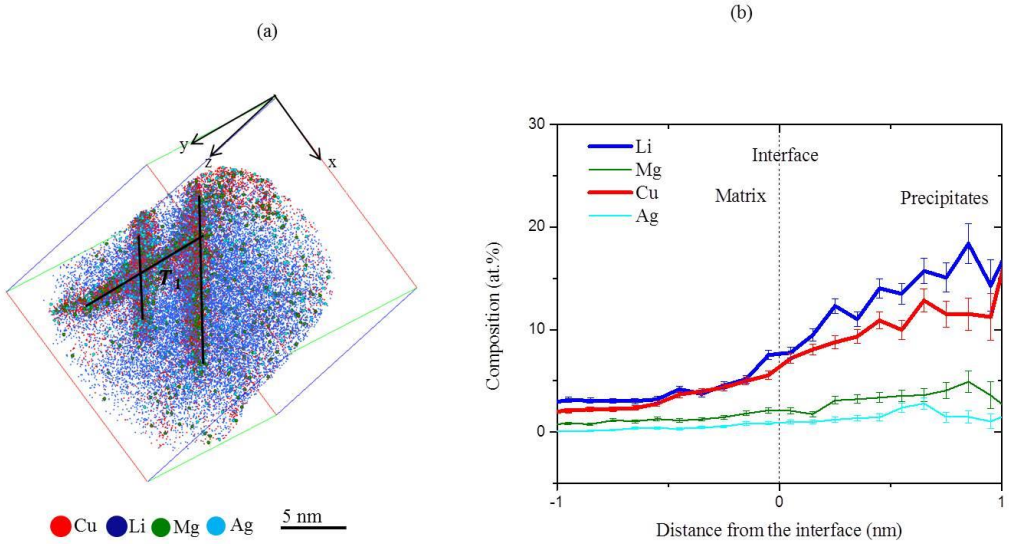

Figure 3.13 LAWATAP analysis of the sample following T8 heat treatment. (a) The reconstructed volume shows the fine distribution of the T_1 platelets which intersect each other's. (b) The chemical composition as estimated from the concentration composition profile based on the isoconcentration surface containing more than 6 at.% Li.

The enrichment of the T_1 platelets with Mg and Ag play an important role in the high harness value for the specimen in this condition. By considering the current model proposed by Cassada et al. [80] the precipitation of the T_1 phase on the {111} Al planes requires the presence of one or more partial dislocations bounded by a stacking fault. Because the stacking fault energy (SFE) of Al is very high (170 mJ m^{-2}), the dissociation of dislocations into partials, which is believed to be necessary for nucleating the T_1 phase, can occur. This process can be facilitated by elements known to decrease the SFE of Al; among these elements, Mg and Ag have been found to be highly effective [81]. This effect indicates the potential role of Mg and Ag on the nucleation mechanism of the T_1 phase. Regarding the effect of Mg and Ag enrichment inside the T_1 platelet on the mechanical properties of the alloy, the single addition of Ag in Al – Cu – Li – Zr alloys was found to have no effect on the age hardenable

curve, while Mg addition significantly raises the peak hardness and shortens the time to the peak [72]. The peak hardness further increases when Ag is added together with Mg. This effect is explained as follows. In the case of single addition of Ag, the T_1 platelet only nucleates on the dislocation loop around a Zr dispersoid. In contrast, Mg addition causes the formation of octahedral micro-voids and new GP zones on {111} Al planes; these structures act as nucleation sites for the T_1 phase, providing a fine dispersion and hence an increase in the hardness of the system. Moreover, the intersection of the T_1 platelets confirms that theses platelets favor a mechanism to hinder the movement of dislocations resulting in high hardness value (Figure 3.6). The suppression of dislocations glides by second-phase particles, i.e., T_1 precipitates in this case, will increase the stress required for the dislocation to move through the particles, which should also increase the yield strength [77].

To follow the precipitation kinetics and phase transformations at the later stage of the aging process, the samples in the T8 heat treatment condition were further aged for 12 h at 150 °C. The reconstructed volume of this sample after LAWATAP analysis is shown in Figure 3.14. In this Figure, only one T_1 platelet is observed, with a thickness of 1 nm and length of 62 nm in the [111] direction. This phase is also observed to be enriched with Mg and Ag, which indicates that both Mg and Ag are associated with coarsening resistance of the T_1 phase. The small thickness and large length of the observed T_1 platelet can be explained in terms of the high coherency of the edge of the T_1 precipitates with the {111} Al atomic planes. The final layer of the structure proposed for the T_1 platelet precipitates is found to have an extremely low lattice mismatch with the {111} Al atomic planes [82]. The observation in Figure 3.14 confirms that the T_1 platelet grows via a ledge mechanism [80], whereas both of the board faces of the T_1 platelet are coherent with the matrix. The value of the measured thickness of this platelet indicates that no thickening of the T_1 platelet is observed. It is surprising to observe the absence of the θ'platelets in the microstructure. This observation suggests the occurrence of the phase transformation in the form of the dissolution of the θ' phase upon further aging.

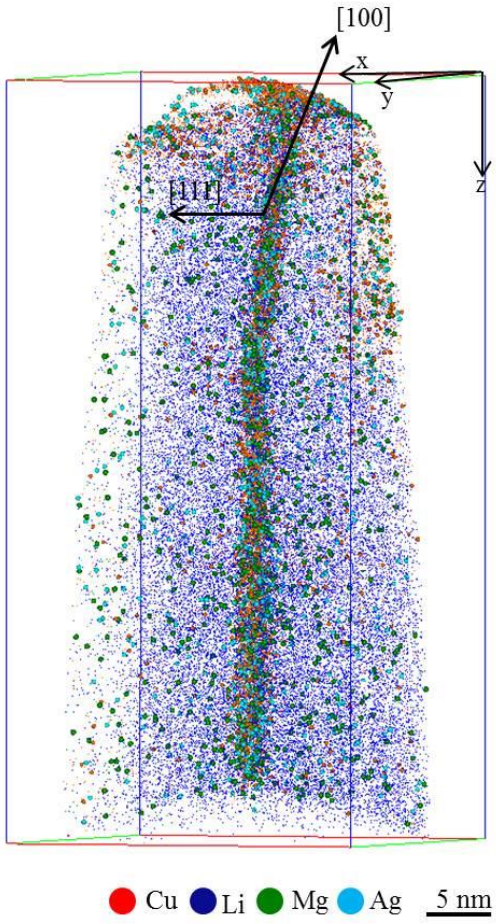

Figure 3.14 LAWATAP analysis of the sample at the later stage of the aging process shows the growth of the T_1 platelet via a ledge mechanism and absence of the θ'platelets in the microstructure.

3.1.6.3 Artificial aging of the sample at T6 sample:

Microstructure evaluation at the atomic scale was performed for the sample under the T6 heat treatment condition. In an effort to accelerate precipitation kinetics without applying plastic deformation, artificial aging is performed at a higher temperature, 180 °C in this case. After a long aging time of 20 h, the microstructure is found to be consists predominantly T_1 platelets (Figure 3.7 (c)). The reconstructed volume of the sample in T6 condition analyzed by LAWATAP is shown in Figure 3.15. In this case, the microstructure has a uniform distribution of the T_1 platelets, with an average thickness of (4.7± 1) nm and an average length of (40± 2) nm, without any indication of their intersection (Figure 3.15 (a)). A combined proxigram profile corresponding to theses T_1 platelets, which are delineate by 5 at.% Li isoconcentration surfaces, is shown in Figure 3.15(b). As illustrated in

this figure, the chemical composition of this phase in this temper condition was found to be (15.7±1) at.% Cu, (16.6±2) at.% Li, (2.4±1) at.% Mg and (1.4 ±0.4) at.% Ag. It is worth notable that the enrichment of the T_1 phase with Mg and Ag is similar to that of the specimen in the T8 condition.

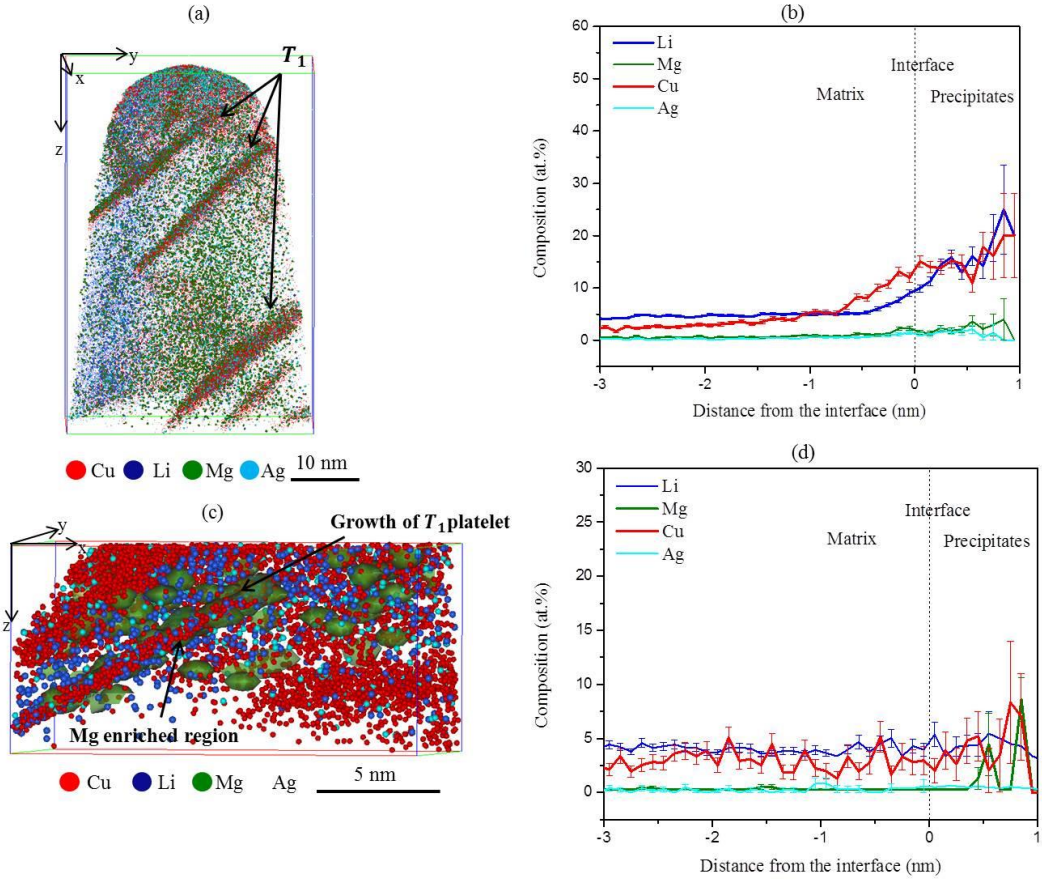

Figure 3.15 LAWATAP analysis of the sample in T6 condition (a) The reconstructed volume of the microstructure shows a uniform distribution of the T_1 platelets. (b) A combined proxigram profile corresponding to the T_1 platelets, which are delineated by 5 at.% Li isoconcentration surfaces. (c) An inhomogeneous distribution of Cu and Mg in the Al matrix indicates the growth of the T_1 platelet in the Mg enriched region, which contains localized Ag atoms. (d) Proxigram concentration profile quantifies the chemical composition of the enriched regions in (c).

The presence of the T_1 platelets and their enrichment with Mg and Ag are responsible to the age-hardenable behavior under his condition (Figure 3.6). Moreover, an inhomogeneous distribution of Cu and Mg was observed in the Al matrix (Figure 3.15(c)). The locations of Mg-enriched regions coincide with the Cu- and Li- enriched regions. Quantitative evolution of these enriched regions was performed through the proxigram composition profile from the isoconcentration surface of 0.5 at.% Mg (Figure 3.15 (d)). According to this proxigram, the chemical composition at these enriched regions was estimated as (7.1±3) at.% Cu, (3.8±1) at.% Li, (4.7±1) at.% Mg and (0.5 ±0.2) at.% Ag. From this dataset, the growth of the T_1 platelets in the Mg enriched region, which contains localized Ag atoms, is clearly observed. This observation suggests the potential role of Mg and Ag to catalyze the nucleation of the T_1 phase.

Mg and Ag are typically used to increase the number of dissociated dislocations and thus the nucleation sites of the T_1 phase [83]. Moreover, it has been reported that Mg atoms enhance the equilibrium vacancy concentration during solution treatment and help to retain these vacancies during the quenching operation. On this basis, the vacancies will provide a dual beneficial effect; enhanced nucleation and increase diffusivity [84]. This effect can be seen clearly in Figure 3.15(c). However, the distribution of these elements in the structure of the T_1 platelets as well as their portioning between precipitates and matrix is the subject of conflicting reports [85].

It is notable to mention that the T6 condition corresponds to a slightly over-aged condition and might represent a metastable equilibrium between different phases [84]. This fact has been confirmed in our study. In addition to the presence of the T_1 phase as the dominant strengthening phase, some platelets of the θ' phase have been observed in Figure 3.16. In this Figure, the reconstructed volume of the tip that has undergone the T6 condition is shown. It reveals the presence of a coarsening platelet. According to the measured chemical composition of this platelet, it is designated as θ' precipitate. This coarsening platelet also appears in the TEM image (Figure 3.16) and the FIM micrograph (Figure 3.9 (c)). Interestingly, this coarsening platelet is enriched by the Li. The distribution of Li atoms within the θ' platelet is also illustrated in the magnified view of this platelet. This indicates that the coarsening of θ' under an over-aged condition is associated with the enrichment of Li atoms, which supports the hypothesis of the probability of a phase transformation

event from the θ' phase to the T_1 phase. All solute atoms—Li, Cu, Mg and Ag—may incorporated together to form the T_1 phase.

3.1.7 Conclusion:

The influence of different industrial heat treatments, namely, the T4, T8 and T6 tempers, on the precipitation kinetics and phase transformation of an Al-Li alloy was investigated. Alloy AA2195 was selected as a model system in the present study. A detailed analysis of the correlation between the microstructure developments due to the respective treatment condition and the hardening process revealed the following:

1- The microstructure of the sample undergoing the T4 heat treatment reveals the enrichment of the β'/ matrix interface with Li, Cu and Mg atoms. This observation indicates the potential role of the β'phase as the nucleation site for the T_1 phase. The segregation of solute atoms to the β'/ matrix interface was quantified.

2- After conducting the T8 heat treatment, the fine distribution of the $\theta'$and T_1 phases within the microstructure was observed. The intersections of different platelets were used to suppress the movement of the dislocations, resulting in a high hardness value for the specimen. The growth of the T_1 platelet precipitate via a ledge mechanism was observed by increasing the aging time. The absence of θ'platelets from the microstructure after increasing the aging time suggests the occurrence of phase transformation in the form of the dissolution of the θ' phase with increasing aging time.

3- With the T6 heat treatment, the microstructure was dominated by the T_1 phase, which nucleated on Mg enriched regions that contain localized Ag atoms. The Mg atoms play an important role to enhance the nucleation of the T_1 phase at this heat treatment condition.

Presented data highlight the role of the industrial heat treatment on the developing of the microstructure, along with an in depth study of distribution of different alloying elements in the strengthening phases. A detailed analysis of the correlation between the microstructure developments owing to the respective treatment condition and the hardening process utilizing different experimental techniques allowed integrity

between different techniques. A very good agreement has been found on the obtained results from different methods.

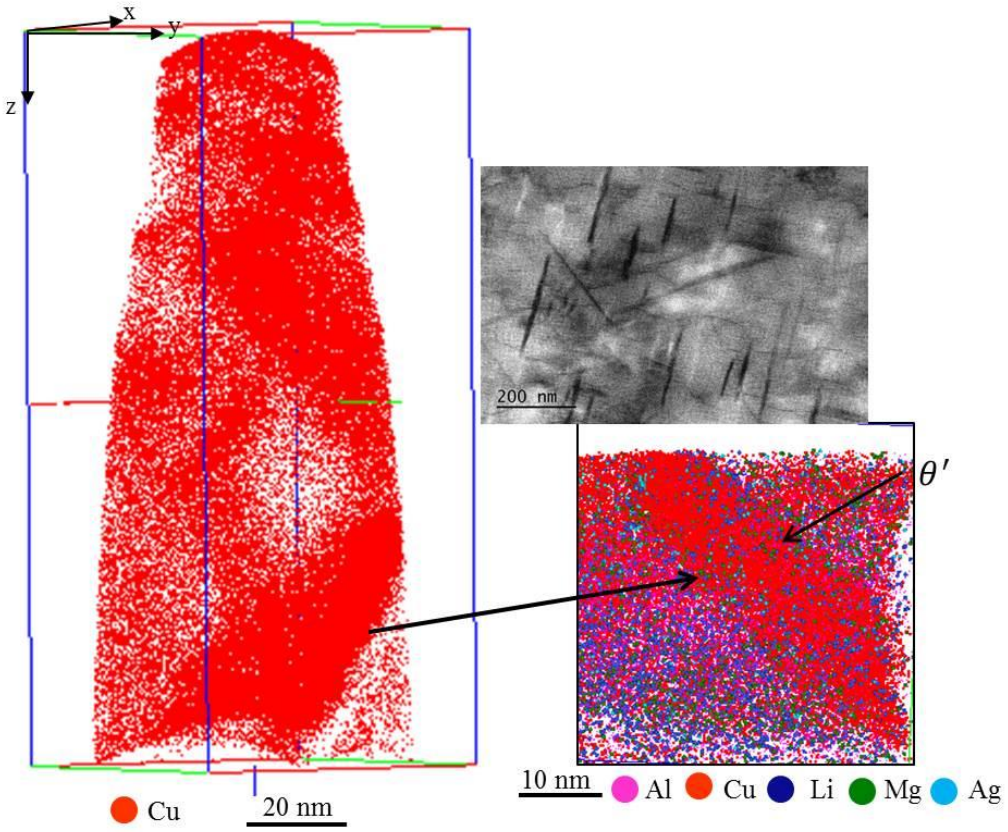

Figure 3.16 Coarsening behavior of the θ' platelets at T6 condition.

Based on the defined analysis above, it is clear that the optimal industrial heat treatment condition corresponds to T8. On this basis, the specimen under this temper condition has been selected to be subjected to more analyses.

3.2 Characterization and engineering of an Al alloy AA 2195:

3.2.1 Characterization of an Al alloy AA2195:

In this part of study, investigation on the commercial AA2195 alloy supplied with T8 temper will be presented. Once again, AA2195 is considered as a promising candidate for aerospace applications due to its high strength, high modulus, low density, good corrosion resistance, excellent fatigue properties and fracture toughness at cryogenic temperatures [86]. The alloy exhibits superior mechanical properties after processing a thermo-mechanical treatment termed ‘T8’. This treatment begins

with a solution treatment in a single phase region, followed by quenching to obtain a supersaturated solid solution. Plastic deformation (cold working) is then applied to the samples. The final stage is an artificial aging far below the temperature of the strengthening phase solvus line [87]. It has been shown that alloy conducting T8 tempering has a combination of excellent fracture toughness (~ 60 MPa$\sqrt{\mathrm{m}}$) and an improved strength (~ 550 MPa) [69]. The presence of various micro-alloying elements at a variable volume fraction and adequate subsequent treatment causes the precipitation of different possible phases within the Weldalite family such as $\mathrm{T}_1(\mathrm{Al}_2\mathrm{CuLi})$,$\theta'(\mathrm{Al}_2\mathrm{Cu})$, $\beta'(\mathrm{Al}_3\mathrm{Zr})$ and $\delta'(\mathrm{Al}_3\mathrm{Li})$.

The T_1 phase is thought to be responsible for the bulk precipitation strengthening. This phase is hexagonal (Figure 1.4) with symmetry P6/mmm, and forms as platelets on the {111} plane of the Al matrix. When embedded in the Al matrix, it is usually thin (~ 1.3 nm in thickness). The thickness is equal to the stacking of only five {111} atomic planes. On the other hand, the T_1 platelets can have a very large extension, between 50 and 100 nm, without losing their coherency with the matrix [78]. Despite the high coherency of the T_1 precipitates, it has been proved to be remarkably difficult to nucleate homogenously. To overcome this issue, plastic deformation must be applied before aging. As mention in section 3.1.6.2, this plastic deformation increases the precipitation kinetics in this system by one order of magnitude [79]. It has been concluded that the precipitation of this phase is also difficult without the presence of secondary alloying elements such as Mg and Ag, which can offer nucleation sites within the matrix for this phase [72]. The potential role of these micro-alloying elements is to simulate the nucleation of an exciting precipitate by reducing the interfacial energy between precipitate and matrix and by clustering together; hence, their clusters of atoms act as heterogonous nucleation sites for the new precipitates [13]. Once again, additional micro-alloying elements must associate with applied plastic deformation prior to artificially aging to increase the number of nucleation sites for the T_1 phase. An expected result of this thermomechanical treatment is a promotion of a uniform distribution of a heterogeneously nucleated T_1 phase. The T_1 platelets usually act as non-shearable obstacles to dislocation motion and promote slip homogenization [69].

The T_1 phase co-exists with the $\theta'(Al_2Cu)$ phase which lies as plates on the {100} matrix planes. This phase is dominant in the early stage of the heat treatment at elevated temperatures 588 – 644 K [88]. More details about the nucleation mechanism of this phase will be explained in the coming section.

In addition to the T_1 and θ' phases, Zr forms coherent spherical $\beta'(Al_3Zr)$ precipitates with $L1_2$-structure that can already form during the alloying process within the melt. As mentioned in section 3.1.6.1, the presence of β' particles is designed to control the grain structure and degree of crystallization after the solidification of the ingot [4]. An illustration of the fine distribution of β' dispersoids and how to serve the pin grain boundary during the thermomechanical processing of the complex alloy is shown in Figure 3.17 [13].

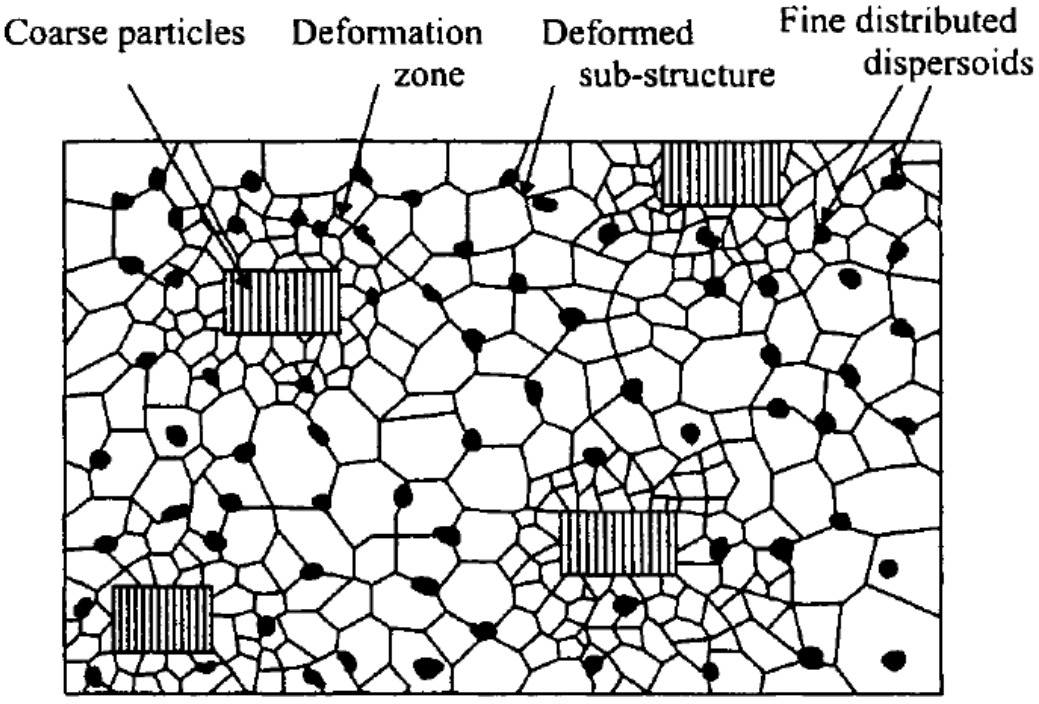

Figure 3.17 Schematic representation of the sub-structure of deformed Al alloy [13]

Finally, the $\delta'(Al_3Li)$ is usually reported to precipitate upon quenching from the melt for alloy compositions higher than 5 at.% Li in the matrix [89-91].

Atom probe studies have provided a range of information on the different types of precipitates present in Al-Li-Cu alloys. Murayama and Hono [36] reported on their

observation of Mg clusters at the early stage of aging and on the possibility of the segregation of Mg and Ag atoms to the broad interface of the T_1 plates. Moreover, Gault et al.[83] studied the early stages of clustering, precipitate interactions, solute segregation at the matrix/precipitate interfaces, and the chemical composition of the different phases.

The aim of this part of study is to characterize the different precipitates that dominate the microstructure of the AA2195 alloy. Since the composition evaluation of sub-nanometer scale platelet precipitates is extremely difficult, atom probe tomography has been employed to characterize the local chemical composition of the precipitates and to determine the location of the various alloying atoms.

3.2.1.1 Materials and methods:

The chemical composition of AA2195 is shown in Table 3.2. Samples in the form of ingots were obtained in a T8 temper state (Solution treated for 1h to 783 K, quenched, stretched to 3 % and subsequently aged to 423 K for 30 h).

Vickers micro-hardness measurements were performed using a load of 0.2 kg applied on the sheet sample. The Vickers hardness number (VHN), which was obtained by averaging ten measurements, was found to be (160±7) HV/1.96 and thus confirms the success of the heat treatment.

Small rods (0.3 mm x 0.3 mm x 10 mm) were spark machined from the bulk and then electro-polished to a sharp needle-shaped specimen for atom probe tomography (APT) analyses and scanning transmission electron microscopy (STEM). Electro-polishing was carried out using a solution of 30 vol.% nitric acid in methanol at temperatures between 253 – 298 K in the range of 5 – 7 V.

STEM images were recorded using a Titan CT with a dedicated APT holder (E.A. Fischione 2025 Tomoholder).

APT experiments were performed on both the LAWATAP using the voltage mode at temperatures between 25 – 30 K with a pulse fraction between 20% and 22.5% at a vacuum level of 10^{-8} Pa, and the LEAP- 4000HR using the voltage mode at 22 K and 18% of pulse fraction at 10^{-8} Pa.

The obtained data was visualized using the TAP3D and IVAS software programs provided by Cameca. The compositions of the precipitates were measured quantitatively using the proximity histogram (proxigram) algorithm. All proxigrams, in this study, were computed with a 0.1 nm bin size. To increase the statistical accuracy of the composition, bins containing fewer than 50 atoms were eliminated.

An isoconcentration surface was obtained by sampling the atom probe tomography reconstruction with $0.8 \text{ X } 0.8 \text{ X } 0.8 \text{ nm}^3$ voxels after applying a delocalization procedure developed by Hellman et al. [44] with smoothing parameters of 1.5 nm for the x and y coordinates and 0.75 nm for the z coordinate.

3.2.1.2 STEM evolution of the microstructure:

In this section, the evolution of the microstructure has been accomplished by utilizing a high-angle annular bright field scanning transmission electron microscope HAABF-STEM with an electron tomography mode as described in section 2.2.

The tilt series for STEM tomography was acquired on a 200 kV CT-Titan field emission microscope using Fischione 2050 on an axis tomography holder. The tilt range was +77˚ to –77˚ with a 1˚ increment, resulting in 138 images. The images were aligned manually and reconstructed with a special algorithm. High angle annular bright field scanning transmission electron microscopy (HAABF) STEM - contrast also revealed the existence of both spherical and platelet precipitates in Figure 4.18. As illustrated in this figure, the heterogeneous formation of platelet precipitate can be clearly observed at grain boundaries by imaging the sample from different angles. A low angle grain boundary in Figure 3.18 was identified while rotating the specimen and monitoring the diffraction pattern at various locations within the sample. Moreover, the distribution of platelet precipitates and spherical precipitates within the matrix could be observed. The heterogonous nucleation site of the T_1 phase on the grain boundary agrees well with the previous observation reported by Cassade et al. [80], who proposed that the precipitation of the T_1 phase at sub-grain boundaries results from the easy migration of Cu and Li atoms and the sufficient concentration of mobile vacancies at these locations. Moreover, Lee et al. [11] observed that an increase in aging time caused a rapid precipitation of the T_1 phase both within the

matrix and at sub-grain boundaries, consistent with the (HAABF) STEM image presented in Figure 3.18.

Nucleation of the T_1 phase on the grain boundaries has also been observed in the bright field TEM image in Figure 3.19. This figure indicates the hindrance of the grain boundary and the clear distribution of platelets on it. Thus, it can be concluded that the grain boundaries act as the sinks of solute and vacancies that cause the precipitate to concentrate on its surroundings.

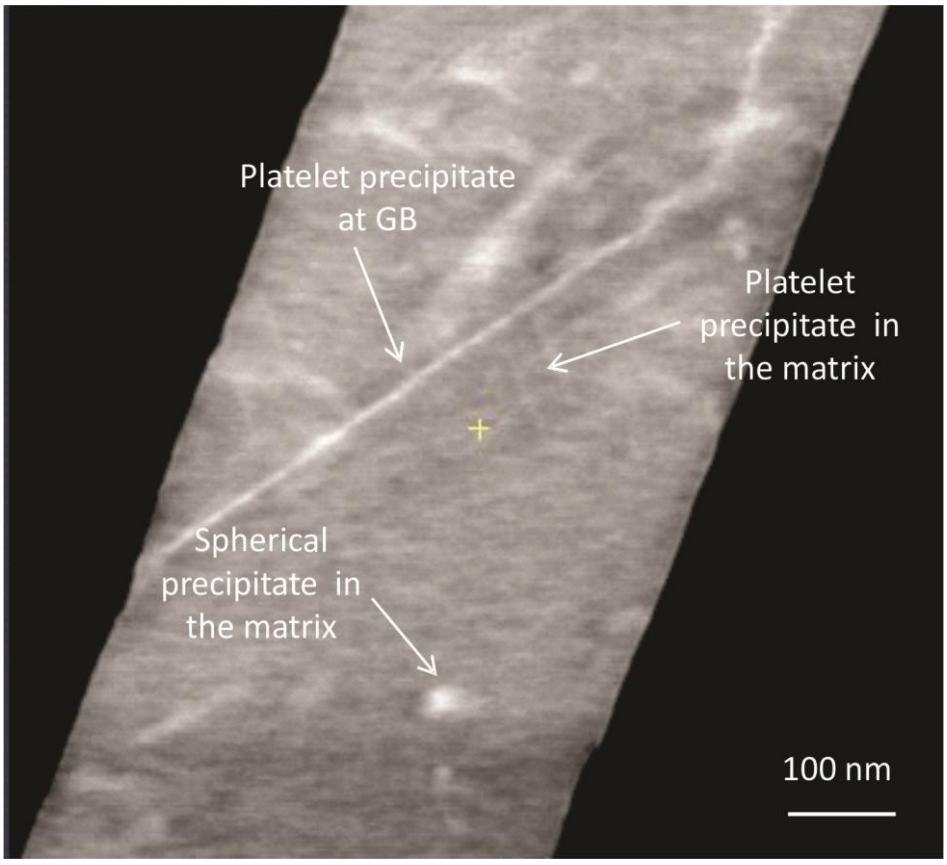

Figure 3.18 High angle annular bright field scanning transmission electron microscopy image showing the heterogeneous formation of a bright imaging platelet precipitate at the grain boundary and the distribution of platelets and spherical precipitates within the matrix.

3.2.1.3 APT analyses:

The presence of several alloying elements such as Li, Cu, Mg, Zr and Ag in AA2195 leads to complex interactions between the different types of precipitates,

which has led to many studies on the evolution of such precipitates in alloys. In this study, the use of atom probe tomography allows for the determination of the chemical composition within small-thickness platelets (less than 2 nm) embedded in an Al matrix as discussed in the following:

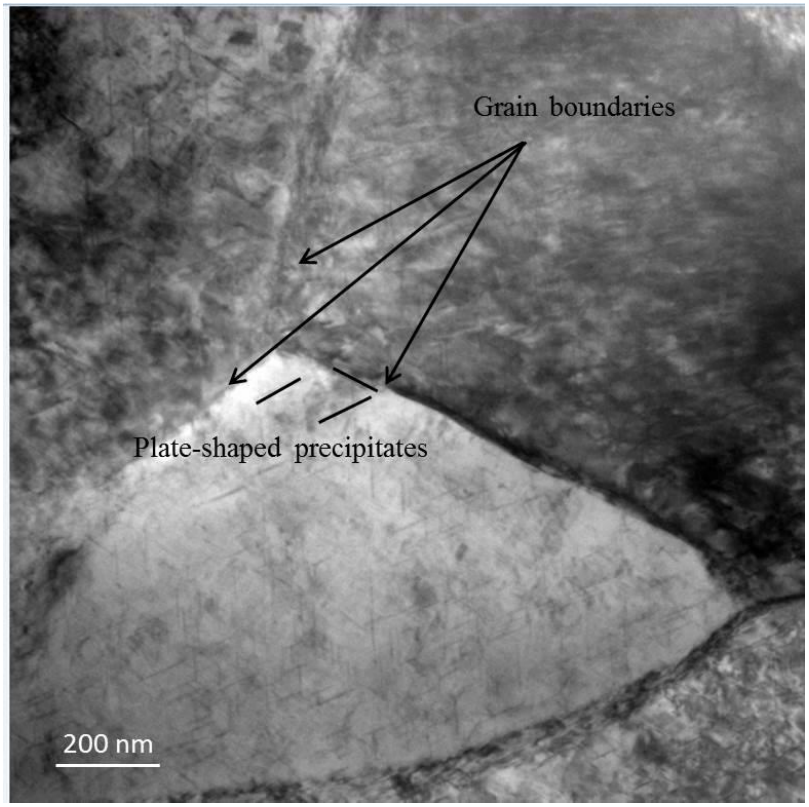

Figure 3.19 TEM bright field image shows the nucleation of the T_1 platelet at the grain boundary and inside the grain.

A) LAWATAP analysis at 30 K and 20% of pulse fraction:

Figure 3.20 shows the reconstructed volume of the sample analyzed by a LAWATAP at 30 K and 20% of pulse fraction (ratio of pulse voltage, V_{pulse} to DC standing voltage, V_{DC}). This Figure demonstrates that platelet precipitates are distributed within the matrix. Based on the knowledge of the angles between different crystallographic directions, it can be confirmed that the two plates in the upper part of the reconstructed volume are T_1 precipitates. The direction of the analysis has been identified as <200>. This identification is based on measuring the distance between the atomic planes in the atom probe tomography data set that are perpendicular to this

zone axis, that is, the <200> direction. As shown in Figure 3.20 (a), the angle between the normal of the T_1 platelet plane, the <111> direction, and the <200> zone axis was found to be (55˚±1), which is within the margin of error for the expected crystallographic angle between these two directions (the calculated value of this angle from the unit cell is 54.76˚). Due to their orientations perpendicular to the <200> zone axis, the remaining platelets in the reconstructed volume can be identified as θ′ precipitates.

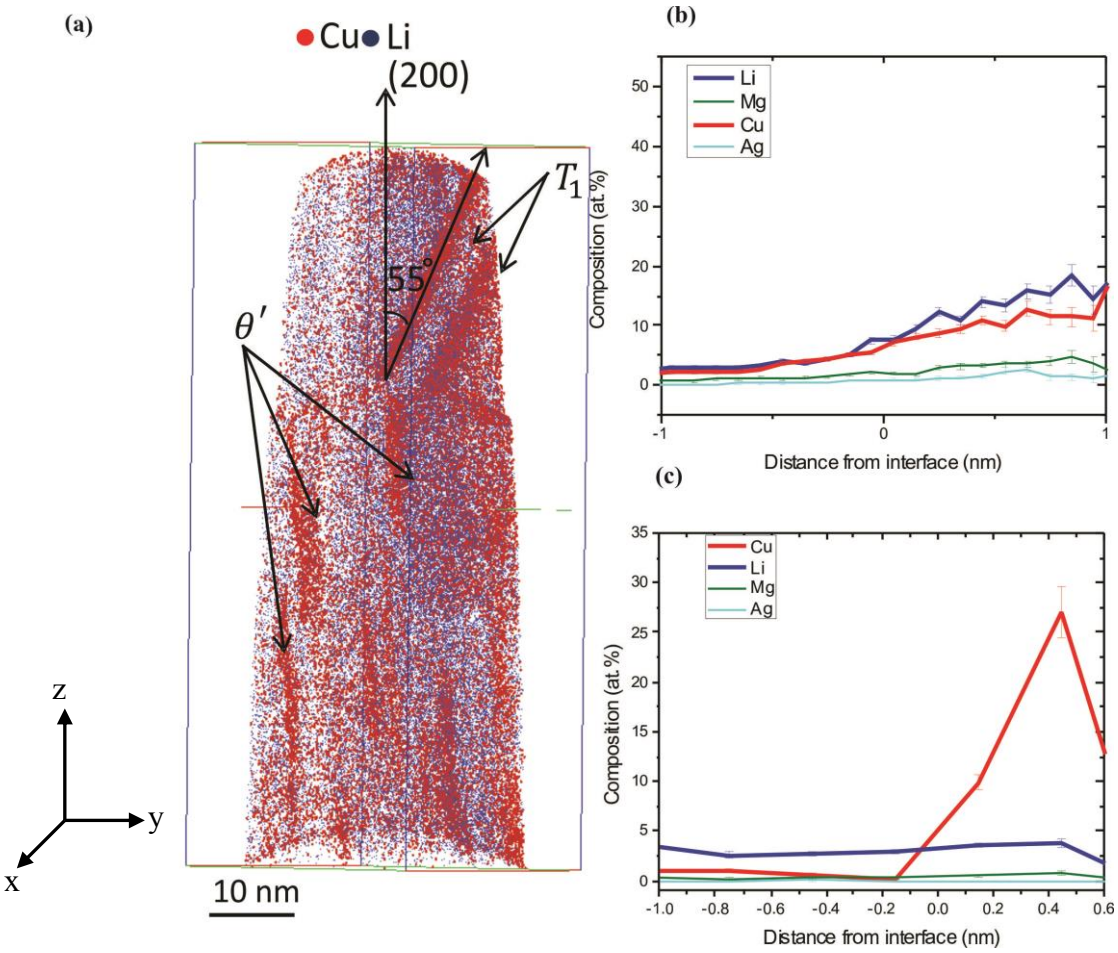

Figure 3.20 LAWATAP analysis of the microstructure at 30 K and 20% of pulse fraction. (a) Reconstructed volume showing the distribution of the T_1 and θ′ phases. (b) Corresponding proxigram composition profile for the T_1 platelet (c) Corresponding combined proxigram composition profile for the θ′ platelet.

A combined corresponding proxigram profile for the T_1 platelets is shown in Figure 3.20 (b). The T_1 precipitates are delineated by 6 at.% Li isoconcentartion surface. The chemical composition for the T_1 platelets was found to be (11±1) at.% Cu, (13±1) at.% Li, (3±1) at.% Mg and (1.5±0.4) at.% Ag, indicating a clear

deviation from the (Al_2CuLi) stoichiometry. A combined proxigram profile from 4 at.% Cu isoconcentration surfaces of θ′ platelets is shown in Figure 3.20 (c). According to this profile, the chemical composition for the θ′ precipitates was found to be (27±3) at.% Cu, (3.8±0.2) at.% Li, and (0.7 ±0.2) at.% Mg. This quantitative analysis reveals a clear evidence for a significant concentration level of Li atoms inside the θ′ platelets, without any indication for the presence of Ag or Zr. The chemical compositions for these platelets are very close to the (Al_2Cu) stoichiometry. The partitioning of Li atoms to the θ′ precipitates might indicate to the possible occurrence of the phase transformation of the θ′ precipitates at the later stages of the ageing.

To obtain a high spatial resolution perpendicular to the platelets, it is desirable to align this direction with the tip axis of the prepared samples. To explain this idea, we need to discuss the texture of our respective material. Because most engineering materials are crystalline in nature, the microstructure can be considered as the combination of morphology and orientation of the constituents. The morphology describes the shape of the constituents, whereas the orientation is connected to its crystallography. On this basis, the texture of a material is a constituent feature of a microstructure. In other words, texture can be defined as the arrangement of building blocks in polycrystalline materials [92]. The texture in rolled sheet material is commonly represented by {hkl}[uvw], which means that the {hkl} planes of the specific grains lie parallel to the sheet plane, whereas their [uvw] direction point is parallel to the rolling direction. The sheet plane is usually perpendicular to the normal direction [ND], whereas its direction is parallel to the rolling direction [RD] (Figure 3.21). The major components of deformation texture in FCC materials (in Al alloy in our case) are {112}<111> . Figure 3.21 illustrates that our respective material possess a strong rolling texture (sheet normal to {110} planes, rolling direction is ⟨112⟩). Thus, it is possible to prepare samples with a defined orientation, e.g. samples were prepared with their axis parallel to the <111> direction. This preparation has been accomplished by cutting the sheet sample as illustrated in Figure 3.22 in a direction parallel to [112] by using a wire-sewing machine and boron-carbohydrates as grinding particles. The sample then was rotated 90˚ to be aligned with [111] direction. The final obtained product from this cutting procedure is a sample with a square shape and well-defined orientation.

Figure 3.23 shows APT results for such preferentially oriented samples. The (111) Al atomic planes can be identified. Thus three out of four orientations of one T_1 precipitate on the {111} matrix planes can be observed (Figure 3.23(a)). The magnified view of one T_1 platelet with resolved {111} planes is shown in Figure 3.23 (b). Figure 3.23 (c) is a proxigram profile from 4 at.% Cu isoconcentartion surface of the T_1 platelet. Even though that the measured chemical composition for this platelet were improved by preforming an APT analysis in this direction, the deviation from the stoichiometric value can clearly be seen in the chemical composition of (14±2) at.% Cu, (14±3) at.% Li, (4±1) at.% Mg and (1.4±0.4) at.% Ag. This quantitative analysis demonstrates the enrichment of Mg atoms inside the platelet without any indication for enrichment at the interface. Furthermore, there is no statistical significant enrichment of Ag or Zr. This corresponds with previous observation reported by Gault et al. [83]. Moreover, rotating the reconstructed volume around the z-axis by approximately 60° shows the presence of other sets of platelets (Figure 3.24). These platelets have also been identified as T_1 and θ' phases in Figure 3.24 (a). The chemical composition of θ' platelets, as shown in the proxigram profile from 5 at.% Cu isoconcentration surfaces in Figure 3.24 (b), is defined as (27±3) at.% Cu, (2.30±0.5) at.% Li, and (0.8±0.5) at.% Mg, with the depletion of the Ag. Figures 3.23 and 3.24 indicate the potential role of the development of texture on the strengthening mechanism [13]. This role can be clearly seen in the interesting microstructure possessed by the rolled specimen.

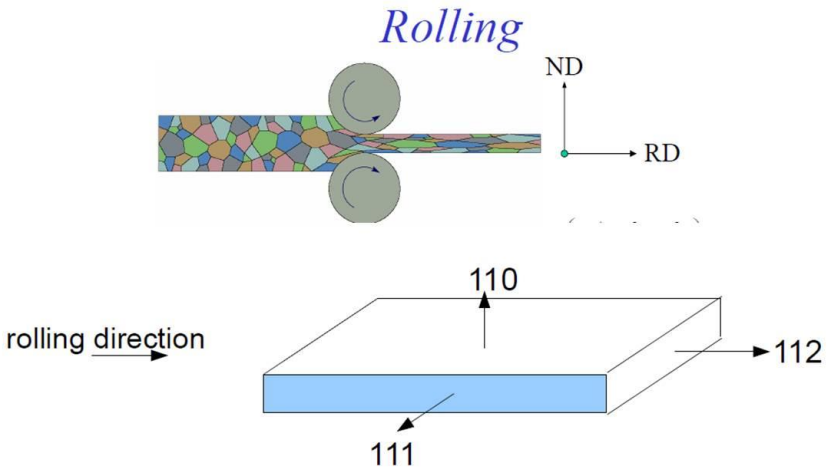

Figure 3.21 Rolling texture of FCC material.

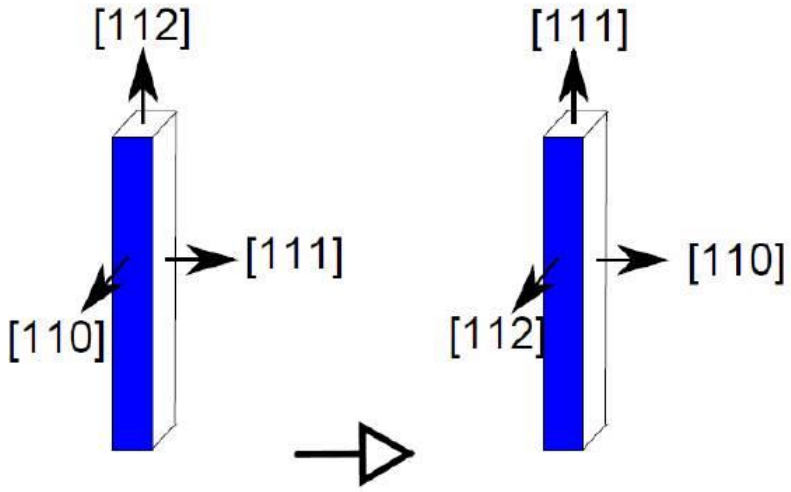

Figure 3.22 Cutting APT sample in [112] direction and then rotating the sample to be in [111] direction.

The deviation of the experimentally measured chemical composition of the T_1 platelet to the (Al_2CuLi) stoichiometry has been observed by Murayama and Hono [36], as well. They interpreted this deviation as a result of the unstable ionization behavior of atoms near or within the T_1 precipitates resulting from the very low evaporation field of Li. Moreover, Gault et al. [83] interpret this deviation as a result of a convolution of the matrix concentration with that of the precipitates due to the presence of trajectory aberrations in the APT analyses. This artifact leads to an overestimation of the Al content inside the platelet. However, significant notes could be observed on the correction method suggested by Gault et al. [83]. Most notably the assumption of having a correct aluminum contents in all precipitates and calculating their chemical composition as a function of apparent aluminum concentration enhances the uncertainties of their measured chemical composition.

As far as the trajectory aberrations are concerned, the thickness of the platelets will be overestimated in the 3D reconstructed volume (Figure 3.20 (a), 3.23 (a) and 3.24 (a)). However, an accurate platelet thickness can be determined by counting the atomic planes of the Al-rich matrix in the <111> direction. By multiplying the number of Al atomic planes by the interplanar spacing of $\boldsymbol{a}/\sqrt{(\boldsymbol{h^2}+\boldsymbol{k^2}+\boldsymbol{l^2})}$ (where $\boldsymbol{a}$ is the lattice parameter for FCC Al, $\boldsymbol{a}$ = 0.405 nm and $\boldsymbol{h=k=l=1}$) the T_1 platelet

thickness was found to be (1±0.2) nm (Figure 3.25). In fact the thickness of the T_1 platelet ranges between 0.8 to 1.4 nm (calculated over 20 precipitates containing in different reconstructed volumes). As the presence of different alloying elements with low chemical concentrations [93] does not affect largely the value of the lattice parameter of the Al-rich matrix (Table 3.2), it can be justified to set the value of the lattice parameter for the Al-rich matrix to be equal to that of pure Al.

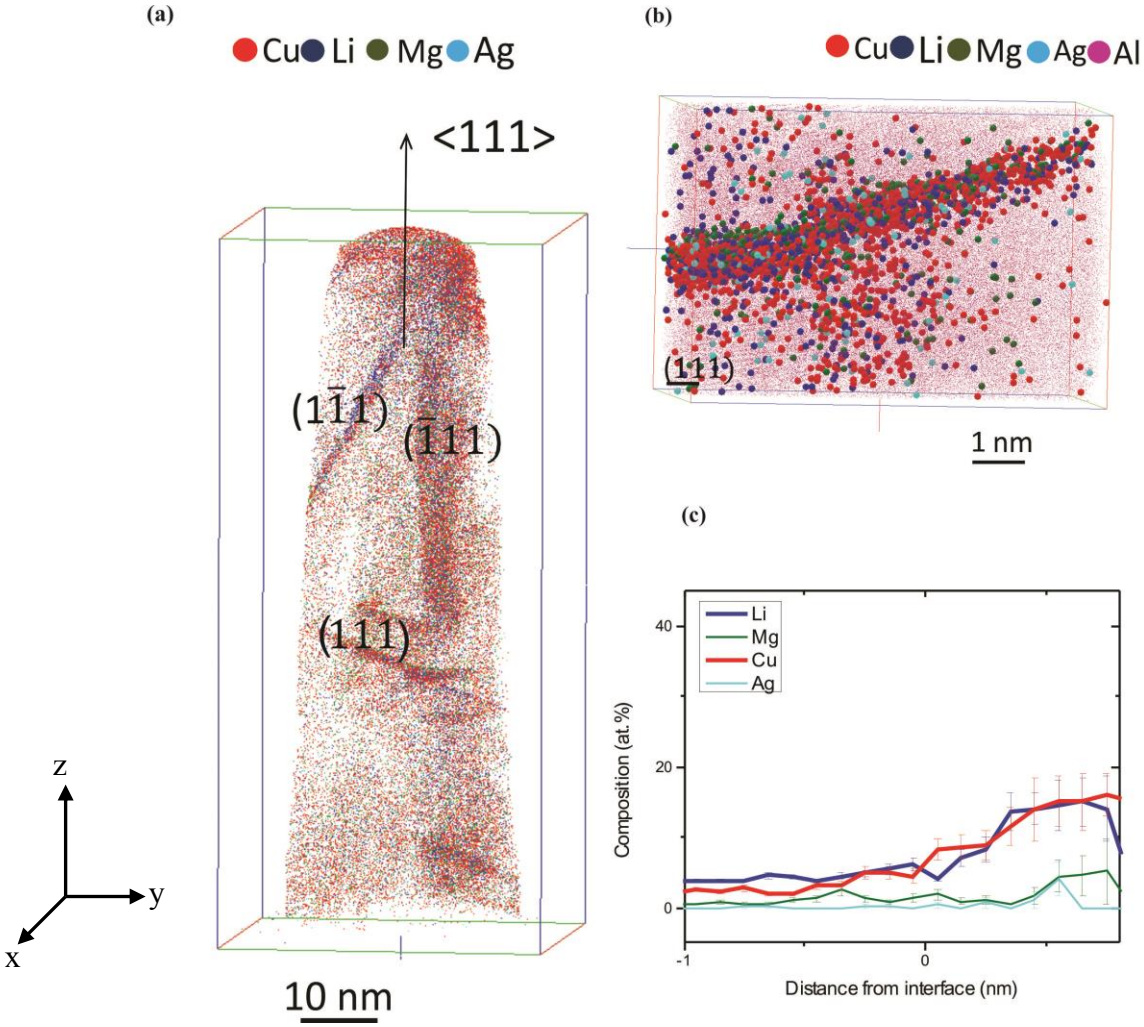

Figure 3.23 LAWATAP analysis for the specimen with rolling texture with the same experimental parameters as in Figure 3.20 (a) Reconstructed volume showing three out of four orientations of the T_1 precipitate on the {111} matrix planes. (b) Magnified view of the T_1 platelet with resolved {111} planes reveals the distribution of Mg within the T_1 platelet. (c) Corresponding proxigram composition profile for the T_1 platelet on the {111} plane.

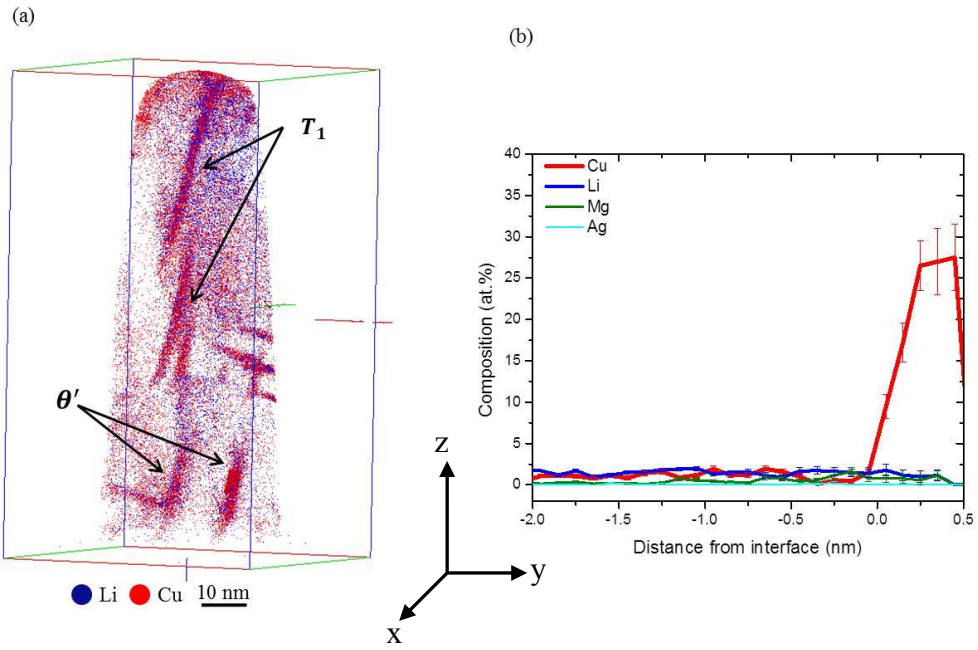

Figure 3.24 Rotation of the reconstructed volume in Figure 3.23 by 60˚ around the z axis. (a) The presences of θ′ platelet in the bottom part of the reconstructed volume (b) Proxigram composition profile for the θ′ platelet.

Furthermore, local magnification effects, that cause variations in atomic density between matrix and precipitates [94], can lead to an underestimation of the Li-and Cu-content of the thin T_1 platelets. These APT artifacts might affect the estimation of the chemical composition for the T_1 platelets precipitates, and hence great care is required for the analyses of this phase. Menand et al. have reported optimized experimental conditions for the analysis of Al-Li alloys which allow minimizing such APT artifacts [89]. These conditions consist of a low tip temperature of 20 to 30 K and a pulse fraction of greater than 15%. The experimental condition might be considered optimal if such field evaporation is directly triggered by the high-voltage pulses applied in the combination with the standing voltage during an APT analysis by using voltage mode. It is known that the most important parameters in an APT experiment are the temperature of the specimen during the analysis and the applied standing voltage and pulse fraction. The field dependence of the field evaporate rate constant for an n-fold charged ion, k_n, at a fixed temperature T is explained as:

$$\frac{dlnk_n}{dlnF} = \frac{Q_o(n)}{2K_BT} \qquad (3.1)$$

Where $Q_o(n)$ is the energy barrier to desorption, and K_B is the Boltzmann constant. From this equation, it is clear that the field dependence of field evaporation rate becomes stronger at lower temperatures [38]. On this basis, APT experiments were slightly changed.

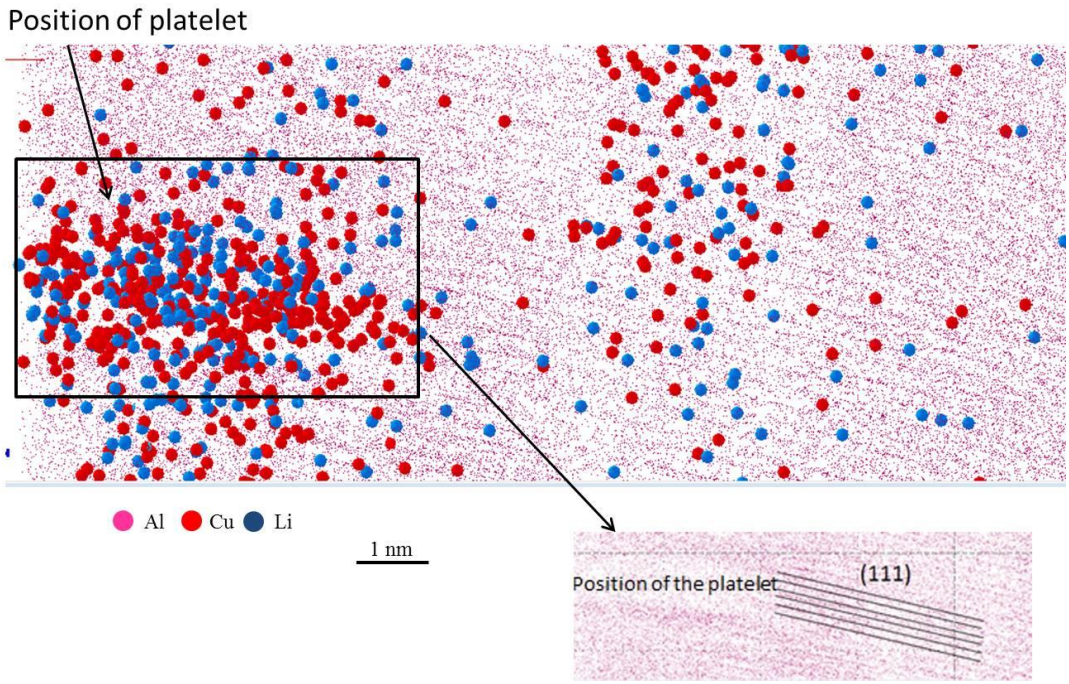

Figure 3.25 Estimation of the accurate thickness for the T_1 platelet.

B) LAWATAP analysis at 25 K and 22.5% of pulse fraction:

The series of images in Figure 3.26 reveals the effect of changing the experimental parameters on the detected chemical composition within the precipitates. Figure 3.26 (a) shows various T_1 and θ′ platelets. The proxigram profiles were computed by following the same procedure as mentioned above. Proxigram profiles corresponding to θ′ and T_1 platelets where θ′ precipitates are delineated by 10 at.% Cu isoconcentartion surfaces and T_1 precipitates are delineated by 10 at.% Li isoconcentartion surfaces are presented in Figure 3.26 (b) and 3.26 (c), respectively. As illustrated in Figure 3.26 (b), the chemical composition for θ′ was found to be (30±2) at.% Cu, (3±1) at.% Li, and (1 ±0.7) at.% Mg. It is worth noting that analyses

of the θ′ precipitates under these experimental conditions resulted in θ′ stoichiometries consistent with the expected (Al_2Cu) equilibrium composition. Given its importance for strengthening Al, a large number of studies of the Al – Cu precipitation sequence have focused on the properties of metastable θ′[95, 96]. Relatively, little is known concerning the compositional evolution of θ′ precipitates, since its nanometer-scale platelet-like morphology makes quantitative analytical electron microscopy analyses extremely difficult. Recent study by Biswas et al. [97] shows that θ′ precipitates are observed upon ageing between 190˚C and 260 ˚C in a binary Al – 1.7 at.% Cu alloy. They observed that after ageing the alloy for 8 h at 190˚C, θ′ precipitates exhibit a range of Cu-deficient core concentration which differs from the equilibrium composition of (Al_2Cu). In contrast, alloy aged at 260 ˚C for 4 h exhibited precipitates with Cu core concentrations close to the equilibrium value. According to the authors, the cause of Cu deficiency in the θ′ precipitates at the lower ageing temperature remains an open issue. In our study, the applied T8 heat treatment implies an artificially ageing the alloy for 30h at 150˚C. It is worth noting that our ageing temperature is located below the metastable solvus boundary for the θ′ precipitates in Al-Cu phase diagram [18]. Our compositional analysis of the θ′ platelet showed the stoichiometric composition consistent with the expected (Al_2Cu) equilibrium composition. This can be explained in term of increasing the ageing time will induce the Cu diffusion to the existing defects in the microstructure resulting in a core concentration close to the equilibrium one. It notable that θ' precipitates also have a small thickness in the microstructure (Figure 3.20, 3.24, 3.26). This might be explained because the presence of Mg may inhibit coarsening by altering the misfit between phases. It can be concluded that this interfacial segregation leads to finer particle dimensions [98].

A combined proxigram profile for several T_1 platelets is shown in Figure 3.26 (c). The chemical compositions for the T_1 platelets was found to be (14±1) at.% Cu, (14±2) at.% Li, (3.8±1) at.% Mg and (0.8 ±0.4) at.% Ag. This confirms both the deviation from (Al_2CuLi) stoichiometry and a potential enrichment of the T_1 phase with Mg. Discussion of the potential role of Mg and Ag in the nucleation mechanism of the T_1 phase and on the hardening processes has been included in section 3.1.6.2.

C) LEAP analysis at 22 K and 18%:

The use of the wider field of view of the detector in the LEAP permits the collection of larger datasets. Furthermore, using a different machine allows to determine any device specific artifacts.

A top view of the reconstructed volume of a sample analyzed by a LEAP in voltage mode at 22 K and 18% pulse fraction is shown in Figure 3.27 (a). The intersections of three T_1 platelets with the (111) pole are visible. According to the proxigram in Figure 3.27 (b) from 8 at.% Li isoconcentration surface of these platelets, this analysis yielded the close values for the chemical compositions of the T_1 platelets, with (14.3±2) at.% Cu, (15.5±3) at.% Li, (2.5±1) at.% Mg and (0.8±0.5) at.% Ag, as LAWATAP analyses.

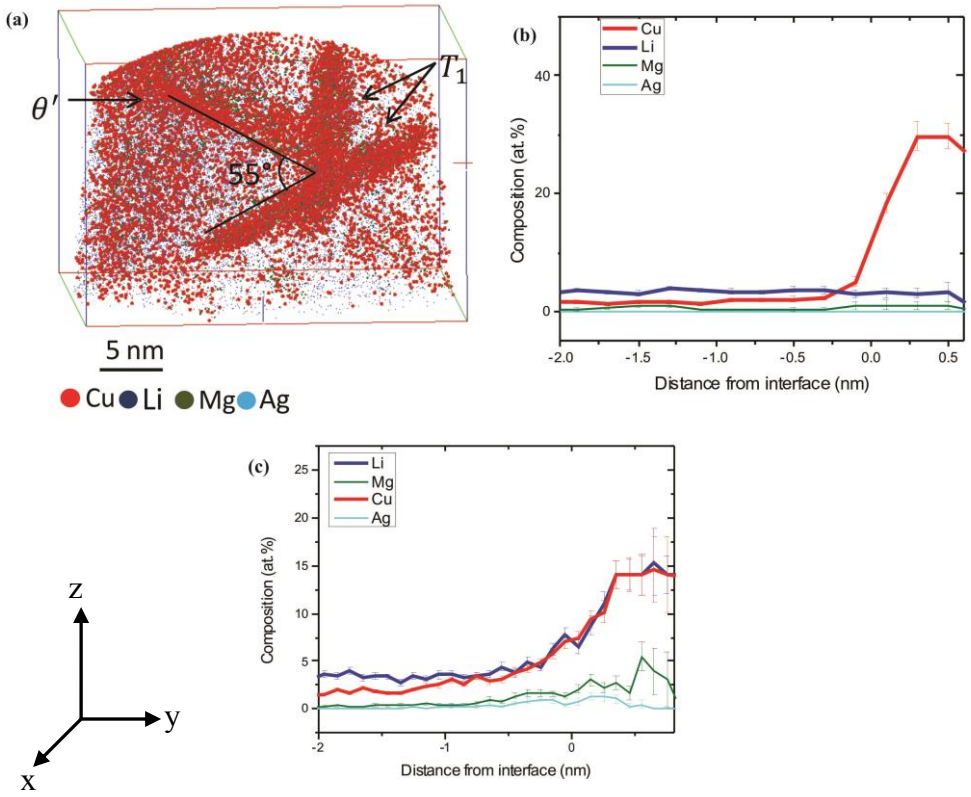

Figure 3.26 LAWATAP analysis with new experimental parameters 25 K and 22.5% of pulse fraction. (a) Reconstructed volume shows T_1 and θ′ platelets. (b) Corresponding proxigram composition profile for θ′ gives an optimistic chemical composition. (c) Corresponding combined proxigram composition profile for T_1 platelet.

One should notes, that the observation of the $\beta'(Al_3Zr)$ precipitates has not been recorded in APT analysis. This is simply, as previously mentioned, due to the fact of the large diameter and small number density of this phase in the microstructure, which make the APT analyses challenging.

The combination of results from different atom probes at different experimental conditions, even including laser based results from Gault [83], suggest that the actual chemical composition for the thin T_1 platelets could differ from the (Al_2CuLi) of the stable bulk phase, since changing the parameters should induce a change in the significance of the artifacts. Furthermore, it seems unlikely that the artifacts would only influence the Cu detection for the T_1 platelets but not the θ' platelets. Even if one assumes that Li changes the evaporation behavior of Cu, it is difficult to understand why it should not also affect Al and thus negate this effect. Such an effect should also result in an extremely decreased atomic density, since about half of all otherwise detected atoms would be missing. But this is not observed at the platelet positions according to the density profiles of the cylinders perpendicular to these thin platelets. In fact, the average difference between the detected atoms in the matrix and the precipitates dose not excess 32 atoms.

In conclusion, it seems reasonable to propose that the concentration in the T_1 phase is indeed non-stoichiometric after treatment of the samples in the T8 condition. This finding is also supported by High angle annular dark field scanning transmission electron microscopy (HAADF) STEM and small angle X-ray scattering (SAXS) results from Donnadieu et al. [99]. In this study the authors investigated a similar alloy, conducting a similar thermo-mechanical treatment. The observed microstructure also consists of a homogenous distribution of thin platelets precipitates with 1 nm thickness and parallel to (111) Al planes. They noted that the composition of the layers of the thin T_1 precipitates may deviate from the (Al_2CuLi) stoichiometry of the stable bulk phase and proposed that this may be due either to the presence of higher Al content than would be expected for the T_1 (Al_2CuLi), or due to the nature of the interface planes. Their results reported on Al content higher than expected for T_1 (Al_2CuLi) phase and the occurrence of matrix/ T_1 interface on Al-Cu mixed layer instead of Al-Li layer. The authors also, suggested that the actual atomic structure of the thin T_1 platelet could present a stoichiometry different from that for

the bulk T_1 phase. As regards the atomic structure of the bulk T_1 phase, several models have been proposed. The first model proposed by Huang and Ardell [100]. According to this model, the T_1 phase structure consists of a stack of hexagonal layers similar to {111} Al planes. The basal plane and the medium one (z = 0 and ½) are formed by a mix of Al-Li layer, while the inner planes (z = ¼ and ¾) are hexagonal layers of Cu and Al atoms. The second proposed model of the structure of the T_1 phase has been made by Howe et al. [82]. In this model, the authors suggested that the basal plane (z = 0) is formed by Al layer, while the medium one (z = ½) is made of Li atoms. The inner planes (z = ¼ and ¾) are somewhat similar to that in Huang and Ardell model. The third structure of the T_1 phase has been proposed by Van Smaalen et al. [101]. Their proposed structure displays mix of Al – Li layers for z = 0 and z = 1/2, which are corrugated, while the inner layers are corrugated Al – Cu layers. The Huang and Ardell study [100] was, until very recently, the generally accepted structure for the T_1 phase. However, the two recent and independent studies, by Donnadieu et al. [99] and Dwyer et al. [102] determined that the structure of the thin T_1 platelets embedded in Al matrix was actually very close to that of the bulk T_1 phase proposed by Van Smaalen et al [101]. But the case might be different for the T_1 precipitates with the thickness less than one unit cell. Thus, it can be concluded that although that Van Smaalen et al [101] structure provides the basis for the structure of the T_1 precipitates, for the earliest stage of precipitation modifications may occur.

On the other hand, more recent APT study proposed by V. Araullo-Peters et al. [85] reported on the presence of the T_1 precursor at the early stage of ageing. However, the observed T_1 platelets in this study are between 5 and 10 nm in thickness with the chemical compositions, also, different from that for the bulk T_1 phase.

In particular, our results demonstrated the presence of lower Li and Cu contents with 1:1 ratio in the thin T_1 platelets. These results confirm the fact of the higher Al content than would be expected for this phase. As far as the matrix/ T_1 interface considered, APT is the more appropriate tool to investigate the local chemistry at the interface. Figure 3.28 displays a higher magnification image for the T_1 platelet. It can be seen that the density of Cu atoms at the matrix/ T_1 interface is higher than that for Li atoms. Moreover, the correlation between Mg and Li atoms is clearly visible. This

observation confirms the assumption of the occurrence of the matrix/ T_1 interface on Al-Cu layer instead of Al-Li layer and the consumption of the first compact Al-Li layer in the nucleation of the T_1 phase. It comes out then that the composition of the T_1 precipitates deviate from that of the stable bulk phase. The deviation of the T_1 phase from thermodynamic equilibrium composition for the stable bulk phase suggests that the T8 condition is corresponding to the thermo-dynamical non equilibrium condition. The obtained microstructure in this condition has an appreciable super-saturation of defects, which means that the nucleation and growth of different phases are still at their intermediate stages.

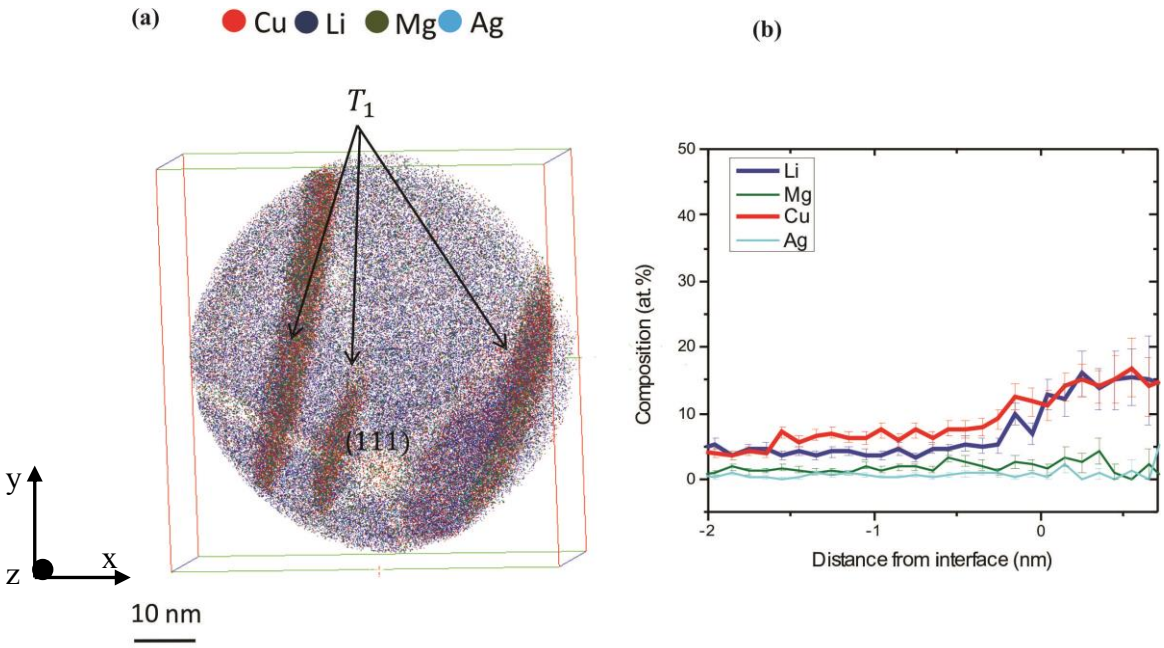

Figure 3.27 LEAP analysis at 22 K and 18% of pulse fraction. (a) Top view of the reconstructed volume of a sample shows the intersections of the T_1 platelets with the (111) pole. (b) Corresponding combined proxigram composition profile for T_1 platelets.

3.2.1.4 Conclusion:

This part of study reports a characterization of the commercial aluminum-lithium-copper alloy AA2195 in the T8 condition using electron microscopy and atom probe tomography. The results confirm that the microstructure of the alloy in this

temper state consists of platelet-shaped $T_1(Al_2CuLi)$, $\theta'(Al_2Cu)$ and spherical $\beta'(Al_3Zr)$ precipitates.

Owing to the ability of atom probe tomography to resolve the chemical position on a sub-nanometer scale, compositional analyses of thin platelet precipitates (less than 2 nm) have been performed. The measured θ'stoichiometry is consistent with the expected (Al_2Cu) equilibrium composition with a significant partitioning of Li atoms within this precipitate. For the T_1 platelets, a deviation from the stoichiometric (Al_2CuLi) of the bulk phase was observed. This phase is enriched with Mg atoms without any indication of the presence of Mg and Ag atoms at the phase/matrix interface. The off- stoichiometry of the thin T_1 platelet cannot be simply attributed to artifacts in the APT measurements and might be considered as a true deviation from the thermodynamic equilibrium composition of the thin T_1 platelets.

The above presented results shows that the T8, the most applied industrial heat treatment procedure, is corresponding to the thermo-dynamical non equilibrium condition in which the nucleation and growth of different phases are still at their intermediate stages.

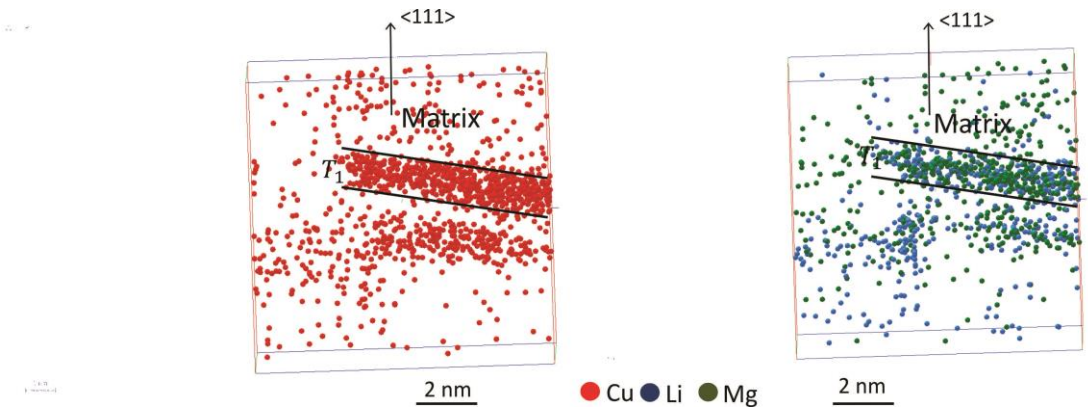

Figure 3.28 The magnified view of the T_1 platelet showing the density of Cu, Li and Mg atoms at the matrix/ precipitates interface.

3.2.2 Engineering of an Al alloy AA2195:

Based on all previous literature, it can be concluded that the Al alloys play a key role in modern engineering. Different reasons lead to huge progress in practical

application of such alloy. However, this practical application needs intensive research on the development and engineering of such important functional material. Although alloying and age-hardening effects were discovered at the beginning of the last century and have been used as the main approaches to improve the strength of Al alloys, it has been recently realized that a better improvement of the microstructure of the alloy and hence its mechanical properties can be achieved by applying several engineering methods [103]. One of these methods is plastic deformation. This operation leads to phase transformation in the material [104]. The scientific basis of this approach, applying plastic deformation, is that the atomic movements driven by an external action—i.e., deformation—are higher than those of conventional thermal diffusion. Thus, the material is forced to undergo a state transformation similar to that which occurs at a certain effective temperature. It has been reported that applied plastic deformation leads to phase transformation in the form of formation or decomposition of an SSSS, dissolution of phases, disordering or ordered phases and amorphous crystalline phases [104].

The use of light structural materials is inevitable in the modern world. The importance of these light structural materials comes from the increasing need for improved fuel economy. Thus, different innovative design strategies have been placed and directed toward weight saving combined with good mechanical behavior. Kamal et al. [105] received a patent on the development of the new 2000 Al alloy bodies by applying a new route on the preparation method. In this case, they applied post-solutionizing cold working following by cold working by at least 25% and thermal heating. They reported on the development with an improvement in the strength of Al alloy products.

The goal of this part of the study is to investigate the effect of different levels of plastic deformation on the hardening behavior of the AA2195. Thermomechanical treatment, which produces an excellent hardness behavior combined with energy savings and cost effectiveness will be produced.

3.2.2.1 Materials and methods:

Commercial aluminum alloy 2195 has been used as the primary material. Samples of as-received material were machined into the shape of tensile samples. This shape is illustrated in Figure 3.29. As shown in this figure, the sample has two

sections: a) gage section and b) grip section. The specimens were first solution heat treated in a molten salt bath (75 wt.% KNO_3, 20 wt.% $NaNO_3$, 5 wt.% $NaNO_2$) for 1 h at 520 °C followed by ice water quenching (Figure 1.2). Then, they were stretched at different stretching levels: 0%, 1%, 2%, 3%, 4% and 5%. The stretching was performed at a cross-head displacement of (1×10^{-4} m/min). The real-time elongation of each specimen was observed through a digital display via a computer interface with an extensometer across an initial gage. The non-stretched specimen (0%) and all stretched specimens (1%, 2%, 3%, 4% and 5%) were placed on quartz ampules that were sealed under vacuum. The specimens were then artificially aged in an electric furnace at 150 °C for different times (0 h (non-aging), 1 h, 10 h, 20 h, 30 h, 40 h) (Figure 3.30).

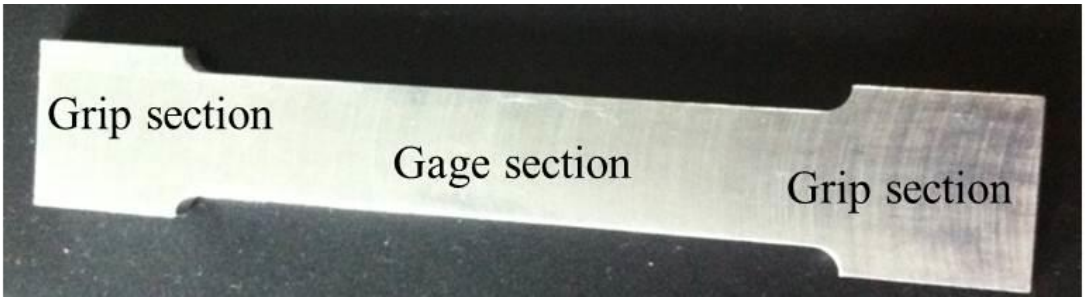

Figure 3.29 Required geometry of tensile sample.

After the treatment, all specimens were tested by the Vickers-micro hardness test. The preparation of the specimens for the hardness test was accomplished by the standard metallurgy method described in section 2.2. The aim of applying this metallographic method is to achieve a clean surface free from oxide particles, which allowed us to achieve the precise values of the hardness. The hardness tests were performed by using a load of 0.2 kg applied to the sample for 10 s. The hardness value was obtained by averaging 10 measurements. The specimen with superior hardness behavior, low energy consumption and a cost-effective preparation method was selected to be analyzed by APT. APT experiments were performed on LAWATAP with the same experimental conditions described in section 3.1.1. Visualization and treatment of the data were conducted as described in sections 2.1.5.1 and 3.1.1.

3.2.2.2 Hardness curves:

The variations of hardness can reveal the precipitation process in the test material to some extent. Figure 3.31 shows the effects of stretching level and aging time on the hardness of AA2195 aluminum alloy. Figure 3.31 (a, b, c, d, e, f) indicates that at the deformation levels of 0% (non-stretched), 1%, 2%, 3%, 4% and 5%, the hardness values are somewhat high at the beginning (at 0 h aging time or non-aging), and then the hardness values decrease following by increasing to the peak hardness value. At the end of the curve, the hardness values decrease to relatively stable values.

The behavior of the hardness curves in Figure 3.31 can be explained as follows. The hardness possessed by all specimens at all deformation levels at 0 h aging time (non-aging) is due to the applied plastic deformation, which leads to phase transformation. The phase transformation needs only a small shift of atoms (not a long mass transfer); hence, different phases from the respective equilibrium phase diagram can be formed and localized [104]. Applying plastic deformation causes movement of the atoms induced by external forces; thus, both accelerated diffusion and phase transformation in the material would be achieved. One should note that the specimen at 0% deformation level (non-stretched) also has a good hardness response even without aging (150 HV at 0 h). In fact, this hardness behavior can be attributed to the presence of β' particles, which are formed during the solidification on the melt. As mentioned in section 3.1.6.1, the $\beta'(Al_3Zr)$ phase is considered to be a hardening phase in the quenched sample [77]. It has been reported that β' particles do not undergo any further change during subsequent processing [106].

The decreasing hardness value at the next step in the curve is unexpected at first glance, considering the rapid aging response following the solution heat treatment. However, this can be explained by the annealing out of the quenched-in excess vacancies formed during the original aging. This action causes the long delay before a significant increase in hardness upon subsequent aging.

The increasing of the hardness values to the peak hardness can be attributed to the formation of the second-phase particles, i.e., precipitates. As discussed before, applying plastic deformation causes the dislocation density and hence the overall number of nucleation sites to increase. Thus, the incubation time required for nucleation will be shortened, and the formation of second-phase particles will occur.

Note that at this stage, the times required to reach the peak hardness are different at different stretching levels: 10 h for the specimens at the 0%, 1% and 2% stretching levels; 20 h for the specimens at the 3% and 4% stretching levels; and 30 h for the specimen at the 5% stretching level. This shift of the time required to reach the peak hardness can be explained in terms of aging kinetics. The number of high-energy sites, dislocations and vacancies increases as the deformation level increases. On this basis, the time required for the diffusion of solute atoms to fill the area of these sites will also increase as the deformation level increases. It seems that increasing the deformation level causes the saturated matrix to require more time to nucleate or incorporate through a dislocation-particle interaction.

The final decrease of the hardness value to a relatively stable value is probably due to approaching equilibrium conditions, i.e., the loss of super-saturation. This is often considered to be the result of over-aging.

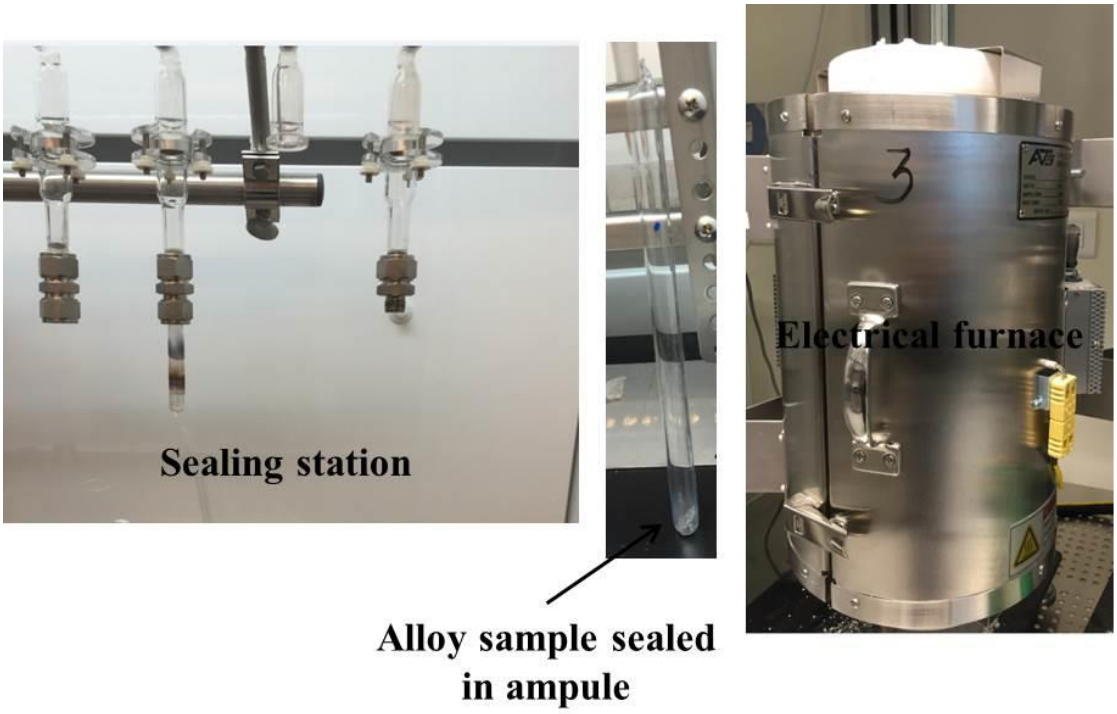

Figure 3.30 Required tool of ageing treatment of stretched Al alloy.

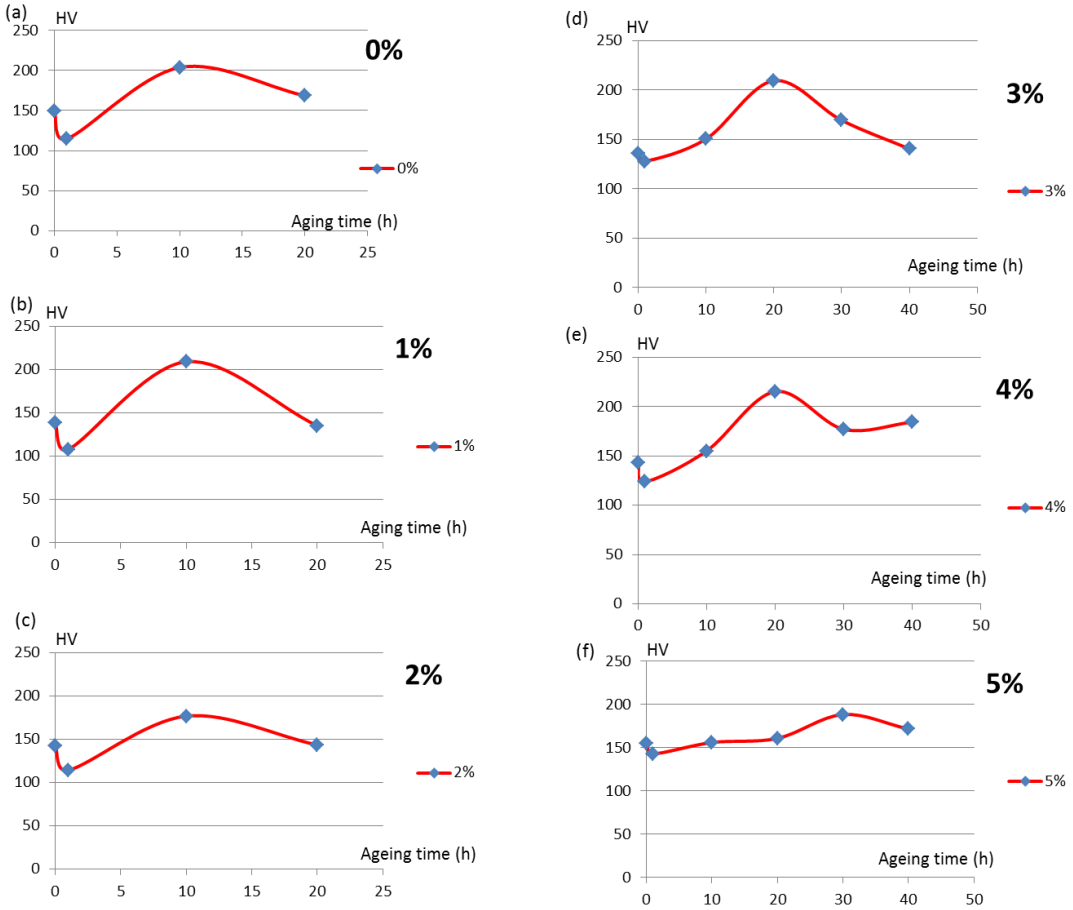

Figure 3.31 Relationship between the ageing time and the hardness values for AA2195 alloys aged at 150 °C for (a) 0 %. (b) 1 %. (c) 2 %. (d) 3 %. (e) 4 %. (f) 5 % stretching levels.

3.2.2.3 APT analysis:

Variation in the hardness values as a function of aging time at several levels of plastic deformation (Figure 3.31) will be used as a guide to judge the optimal condition to engineer the commercial aluminum alloy AA2195. The beneficial effect of stretching prior to aging treatment on the hardness behavior is obvious. The non-stretched sample (0%) and the stretched samples with 1%, 3% and 4% deformation level prior to aging result in high hardness values (higher than 200 HV).

The criteria for selecting the best optimal thermomechanical conditions are low consumption energy and, hence, cost effectiveness, in addition to the yielded superior mechanical properties. Although the non-stretched specimen (0%) has a good level of hardness, the thermomechanical condition that produces this specimen is not recommended as an optimal condition. This is simply due to the absence of applied plastic deformation, which leads to the absence of the uniform dispersion of second-phase particles. For the samples with 3% and 4% deformation, it is clear that the time required to reach the peak hardness is higher by 50% than that required in the case of the sample with 1% deformation. This means that under conditions corresponding to 3% and 4% deformation, the consumption of energy will be high; thus, these conditions cannot be considered optimal. Note that stretching the samples by 3% prior to artificial aging is the procedure applied in industry [87] due to the softening behavior of the specimens under this condition (Figure 3.31 (d)). Examination of the hardness curve at 1% deformation (Figure 3.31 (b)) shows that the high peak hardness value (209.3 HV) is reached after 10 h of artificial aging at 150 °C. It is clear that under this condition, the consumption of energy for preparation is reduced (low deformation level, low aging temperature and shorter time to reach the high hardness value). Thus, this condition is considered to be an optimal condition, which leads to generating a microstructure that achieves maximum hardness at minimum cost and energy consumption.

For intelligent microstructure design in the Al alloy, we need to gain a deep physical understanding of the correlation between the microstructure and macroscopic properties. On this basis, APT analysis was performed for the specimen, showing the high hardness value (i.e., peak age) at the 1% deformation level. Figure 3.32 shows the reconstructed volume of such a specimen. The top view of the reconstructed volume in Figure 3.32 (a) shows the presence of different T_1 platelets. Moreover, interesting cross intersections of these platelets are shown. Some regions enriched with Cu and Ag also appear in the analysis. The chemical compositions of theses precipitates, according to the proxigram profile based on the 1 at.% Li isoconcentration surface, is (10.2±1.6) at.% Li, (9.9±1.8) at.% Cu, (1.1±0.5) at.% Mg and (0.29±0.16) at.% Ag (Figure 3.32(b)). The deviation from (Al_2CuLi) is pronounced.

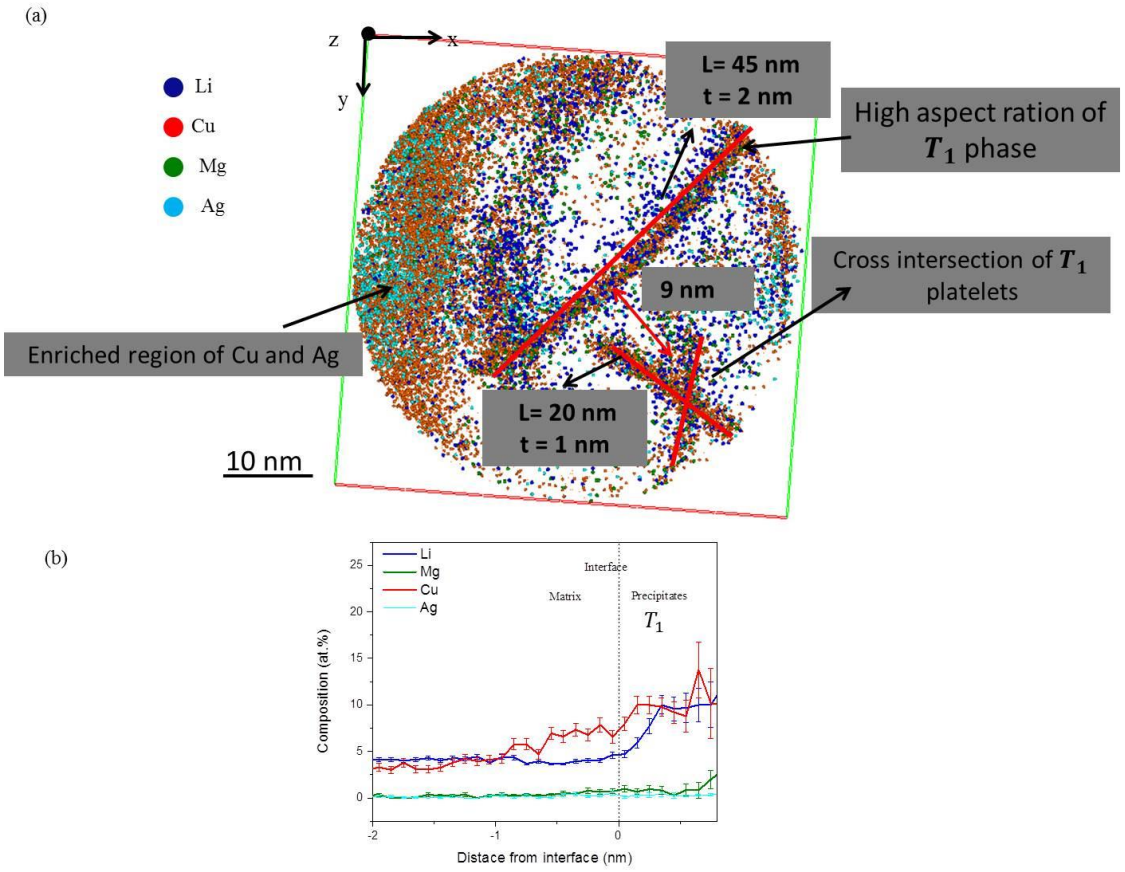

Figure 3.32 LAWATAP analysis of sample at 1 % deformation level (Aged for 10 h at 150 °C) (a) The top view of the reconstructed volume showing the nice distribution and dimension of the nano-features. (b) Composition profile proxigram of the observed T_1 platelets.

From the APT analysis above, it is clear that introducing nano-scale phase particles in the Al matrix and a specific distribution of these particles lead to a huge improvement in the mechanical properties of the alloy. The specific distribution of precipitates with small thickness (between 1 - 2 nm) and closely spaced to each other (~ 9 nm) leads to approach an optimal situation corresponds to the high hardness value and, hence a high level of strengthening especially by knowing that the maximum hardening is usually associated by the spacing between particles equal to 10 nm [13] .This optimal situation arises from the presence of the precipitate particles that are not small enough to be shared by dislocations and yet are too closely spaced

to allow bypassing by dislocations (See Figure 1.11). The increment of the aspect ratio (length to thickness ~ 20-22) causes the formation of a closed network of platelet precipitates which entraps gliding dislocation.

In conclusion, manipulation with second-phase precipitates in the microstructure is an important option to control the mechanical behavior of the complex Al alloy. Applying a plastic deformation prior to artificial aging has been highlighted as an important tool for this manipulation.

3.2.2.4 Conclusion:

The standing goal of this part of the study is to engineer a complex Al alloy AA2195 as an important structural material to have a balance amongst combinations of the high hardness value and low energy consumption preparation method. The proposed strategy is divided into two parts. The first part is the mechanical strategy, in which the mechanical characteristics of the alloy, such as its hardening ability, were employed to test the material. The second part of the prosed strategy is based on the idea of intelligent microstructural design.

In this part of the research, we demonstrate the ability to have a robust microstructure with superior mechanical properties by applying a low-energy-consumption, cost-effective method.

After this detailed investigation of the commercial alloy, it is important to investigate the origins of the different important strengthening phases that exist in our respective alloy. On this basis, investigation of the early stages of the phase decomposition different binary and ternary Al alloys will be presented in the next section.

3.3 Early stage of precipitation on binary Al – Li, Al – Cu alloys and ternary Al – Li – Cu alloys:

Aluminum of high purity in an annealed condition has a low strength near 10 MPa [13]. Generally, pure metals are strengthened by the introduction of obstacles (i.e., any inhomogeneity) in their microstructures to the glide of dislocations. Thus, the introduction of solute atoms into the Al matrix is considered to be an important method of strengthening conventional Al alloys. This introduction of solute atoms

into a solid solution in the solvent atom's lattice typically produces an alloy that is stronger than pure Al due to the differences in the radius, modulus and valance between the Al matrix and the solute atoms [2]. In general, the solute must have an appreciable solid solubility in the matrix at the annealing temperature, must remain in the solid solution after slowly cooling and must not to be removed by reacting with other elements in the alloy [13]. Additions of Li and/or Cu to Al have been identified as an efficient strategy to improve the strength in age-hardenable or heat-treatable Al alloys.

The formation of precipitates in a metal's microstructure during ageing occurs in many different ways. After quenching from a solid solution, the microstructure of Al alloys typically contains regions of solute segregation or solute-atom clusters. These clusters gradually transform into semi-coherent and non-coherent second-phase particles during artificial ageing [2]. The size, shape, volume fraction and coherency of second phase precipitates determine the precipitation hardening of an alloy. These parameters typically depend on the ageing temperature and ageing time. Thus, investigation of the precipitation kinetics in Al alloy is important.

The scale of the microstructures of modern metallic materials is becoming increasingly smaller. A discussion of microstructures at such a small dimension is typically based in crystallographic structures and chemical characteristics relevant to the structure. However, this type of discussion was not possible until the discovery of more advanced tools, such as transmission electron microscopy (TEM) and electron energy loss spectroscopy (EELS). However, all of these advanced techniques have limitations when analyzing nano-scale particles embedded in a matrix phase. The APT technique, particularly in its current form, has a truly quantitative analytical capability to characterize nanometer-scale particles in a metallic system. Thus, it has been used to investigate nano-scale microstructural evolution.

Based on the above discussion, the objective of this part of the study is to investigate the nano-scale chemical composition in the Al – Cu, Al – Li, Al – Li – Cu alloys during precipitation sequence and to describe whether this compositional difference correlates with variations in the observed precipitation kinetics. Knowledge of the decomposition process itself is particularly important for future technical developments.

3.3.1 Materials and methods:

Three different alloys with different chemical compositions were prepared and heat-treated. The first alloy was an Al – 1.7 at.% Cu alloy. The ingot of this alloy was prepared from high purity materials. Al and Cu shots were arc-melted under an Ar atmosphere. Melting was repeated using inert-gas induction melting in a carbon crucible to ensure good mixing of the elements. The second alloy was an Al – 8.2 at.% Li, which was bought as a master alloy due to the difficulty of its lab preparation; this difficulty was caused by the high diffusion coefficient of Li in the melt, which causes Li to typically fluidized on the top of the melt. The third alloy was an Al – 4 at.% Li – 1.7 at.% Cu that was prepared by alloying Cu with an Al – 4 at.% Li master alloy using induction melting. The inductive melting procedure melted the mixed Al, Cu and Li at the casting temperature (750 °C) for 2 min. The composition of the third alloy was selected to be similar to the Li and Cu compositions of the commercial alloy 2195. All three alloys were cast into plates with dimensions of 30 x 30 x 30 mm^3. After casting the samples, they were homogenized for 60 to 70 min at 513 °C in a salt melt (75 wt.% KNO_3, 20 wt.% $NaNO_3$, 5 wt.% $NaNO_2$). The homogenization samples were cut using a low-speed diamond saw into a rod that was 30 um thick and 10 mm long. After cutting the samples, they were re-homogenized at 530 °C for 20 min in high-vacuum quartzite ampules and then quenched in cold water. After water quenching from the homogenization temperature, each alloy was then artificially aged under three different conditions. A summary of the artificial ageing conditions that were used in this study is shown in Table 3.3 along with their indication names. The abbreviations of the names of the artificial ageing conditions are used in the remainder of this chapter. A chart that summarizes the preparation procedure is shown in Figure 3.33.

To prepare APT specimens, the raw material was first ground to a 200 um thickness and was then cutting into blocks of 15 x 0.2 x 0.2 mm^3 using a wire-saw machine. Needle-shaped specimens were then fabricated using the electro-polishing procedure described in section (2.1.1). This electro-polishing procedure was performed in a solution containing 20 vol.% of nitric acid in methanol with a 3-5 V DC electric potential. Specimens were analyzed in a Cameca LEAP HR 4000 device in voltage-pulse mode under a pulse fraction of 18% for the Al – Li and Al – Li – Cu alloys, and 15% for Al – Cu alloy. The specimens were maintained at a cryogenic

temperature near 22 K for the Al – Li and Al – Li – Cu alloys, and near 30 K for the Al – Cu alloy under ultrahigh vacuum conditions near 10^{-9} Pa. A detection rate of 0.001 ions per pulse was maintained throughout the experiments. Visualization and reconstruction of the data have been accomplished using IVAS, a piece of software provided by Cameca.

Table 3.3 Names and description of the three applied aging conditions.

Name of the heat treatment condition	Corresponding aging condition
First stage (1S)	Fully annealed at room temperature (natural aging)
Second stage (2S)	Annealed at 160 °C for 5 min (artificial aging)
Third stage (3S)	Natural ageing at room temperature for 48 h and artificial aging at 160 °C for 5 min

3.3.2 APT analyses:

A) Al – Cu alloy:

The binary Al – Cu alloy is a well-studied precipitation system and forms the basis for a wide range of age-hardenable alloys that are technologically important. The model system for describing the fundamentals of the precipitation sequence in the binary Al – Cu alloy is [107]:

$$\text{GPI} \longrightarrow \text{GPII}(\theta'') \longrightarrow \theta' \longrightarrow \theta$$

Where GPI and GPII are coherent zones, which were named by Guinier and Perston. In the last century, Guinier in France and Perston in England were working independently to produce the first direct experimental evidence of pre-precipitation phenomena in an aged Al – Cu alloy [37] using X-ray diffraction. They deduced the presence of Cu-rich groups of atoms that were coherent with the {100} atomic planes of the Al matrix. These aggregates become known as GP zones. Later, studies showed that the GPI zone could be described as consisting of a single layer of Cu atom on the {001} Al planes, while the structural model of the GPII zone consists of two Cu

{002} layers separated by three Al planes with the stoichiometry of Al_3Cu [108, 109]. The metastable θ' phase, as described is sections 3.1.6.2 and 3.2.1.3, that is considered to be the primary strengthening phase, has a body-centered tetragonal crystal structure with the stoichiometry Al_2Cu [110]. The precipitation sequence ends with the transformation of θ' into the incoherent equilibrium θ phase (Al_2Cu), which exhibits a tetragonal *C16* crystal structure. The presence of these phases in the phase diagram is shown in Figure 1.5.

It is clear that the complete decomposition of an SSSS is a complex process in an Al – Cu system. GP zones and intermediate θ' precipitates are typically formed in addition to the equilibrium θ phase. Models showing the crystal structure of GPI, GPII(θ''), θ' and θ are shown in Figure 3.34. As shown in this figure, GP zones (Figure 3.34 (b, c)) are ordered, solute-rich groups of atoms with two atomic planes in thickness; these zones retain the structure of the matrix and are thus considered to be coherent with it. The intermediate precipitate, θ', may be nucleated from or be present at stable sites in the GP zones. The θ' phase may also nucleate heterogeneously at lattice defects, such as dislocations. The formation of the final equilibrium θ precipitate involves a complete loss of coherency with the parent lattice; thus, it forms only at relatively high ageing temperatures (600 – 700 °C). It is notable that the equilibrium θ phase is coarsely, dispersed and thus marginally hardened from its presence in the material [13].

The increasing use of Al – Cu alloys in commercial applications requires further studies of the properties of the system and in particular the primary strength phase (i.e., the θ' phase). Relatively speaking, little is known about the compositional evolution of θ' compared to its properties. There are few studies in the literature on the presence of small, disordered clusters of atoms prior to the formation of GP zones. Because commercial optimization tools rely upon accurate predictions of alloy microstructures as functions of heat-treatment conditions, it is important to investigate the influence of nano-scale chemical compositions on precipitation kinetics.

Because an APT is capable of resolving nano-scale microstructures including atomic clusters and other fine scale segregation effects, APT has been used to analyze the microstructure of the three Al – 1.7 at.% Cu alloys, which have been subjected to the three heat treatment conditions shown in Table 3.3 (i.e., 1S, 2S and 3S). A typical

example of an atomic probe mass spectrum of Al – 1.7 at.% Cu alloys that have been aged based on 1S or 2S or 3S is shown in Figure 3.35. The number of detected ions is plotted in a log scale. Some of Al ions were detected as hydrides (i.e., AlH_2^+), and Cu ions were also detected the hydrides (i.e., CuH_2^+). The formation of this hydride is most likely caused by hydrogen, which is present as the residual gas inside the analysis chamber. However, whatever the origin of the hydrogen, it can be concluded that this does not affect the analysis because the overall average composition obtained by APT analysis is near the nominal alloy composition (Table 3.4).

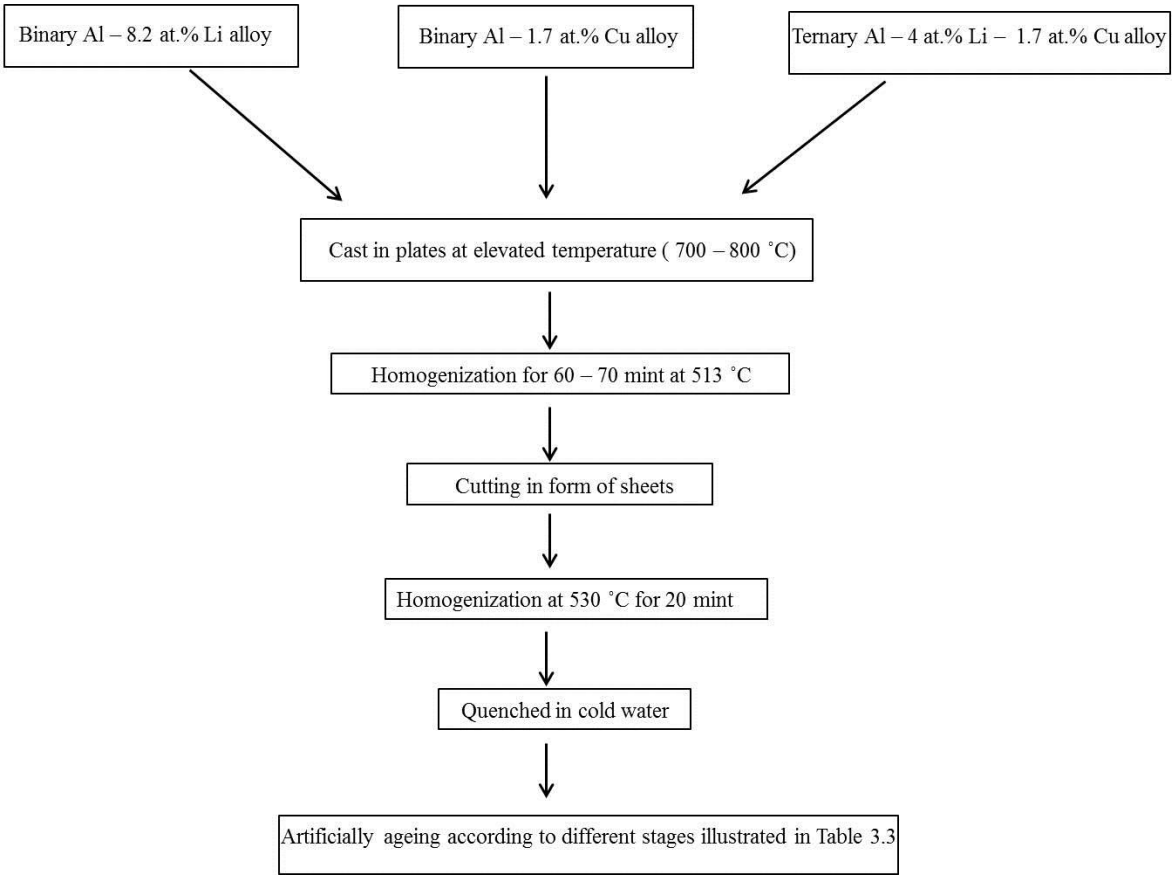

Figure 3.33 Summary of the preparation procedure of binary Al – Cu, Al – Li alloys and ternary Al – Cu – Li alloy.

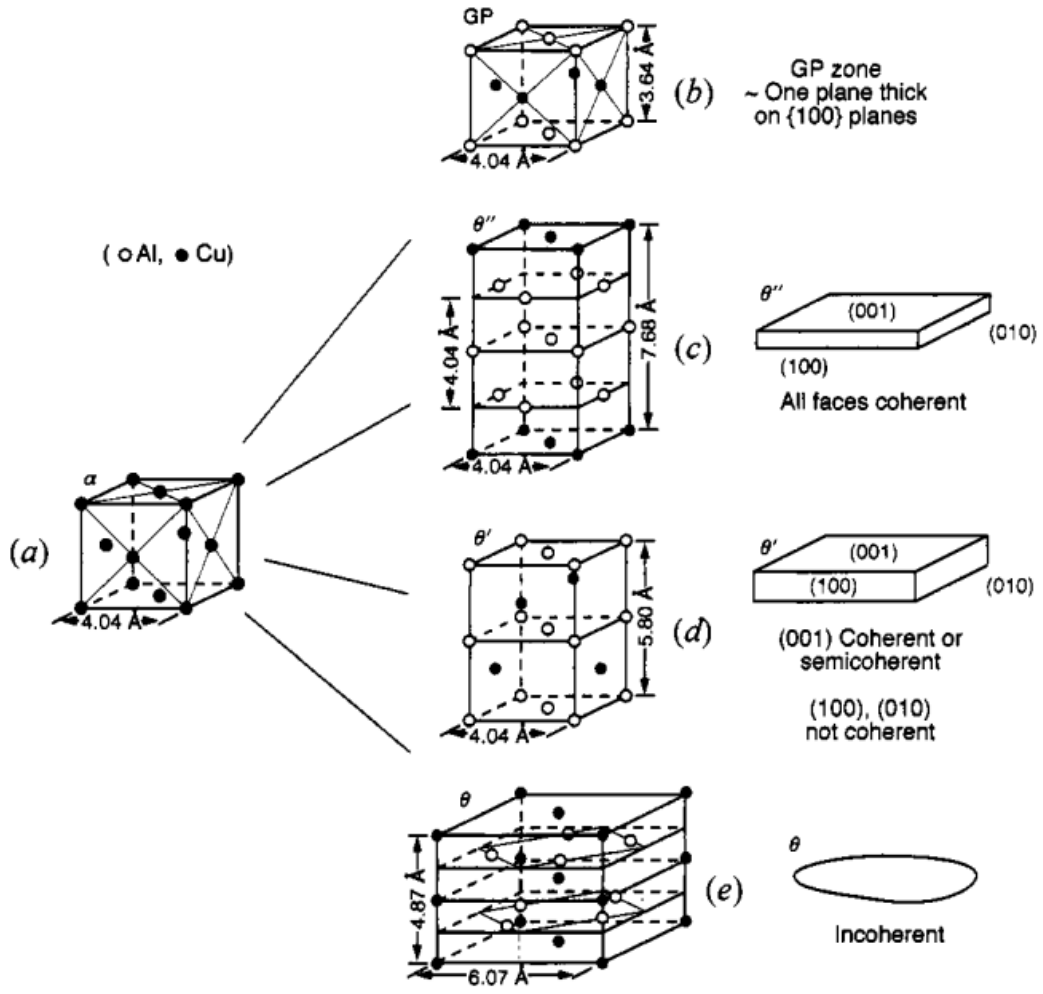

Figure 3.34 Crystal structures of Cu rich phases in Al – Cu alloy. (a) Al matrix. (b) For GPI-zone. (c) For GPII(θ'')-zone. (d) For θ' phase. (e) For θ phase. [35].

Table 3.4 Comparing between nominal and measured chemical composition of analyzed Al – 1.7 at.% Cu alloy.

	Al	**Cu**
Nominal composition (at.%)	98.3	1.7
Measured composition (at.%)	98.64	1.36

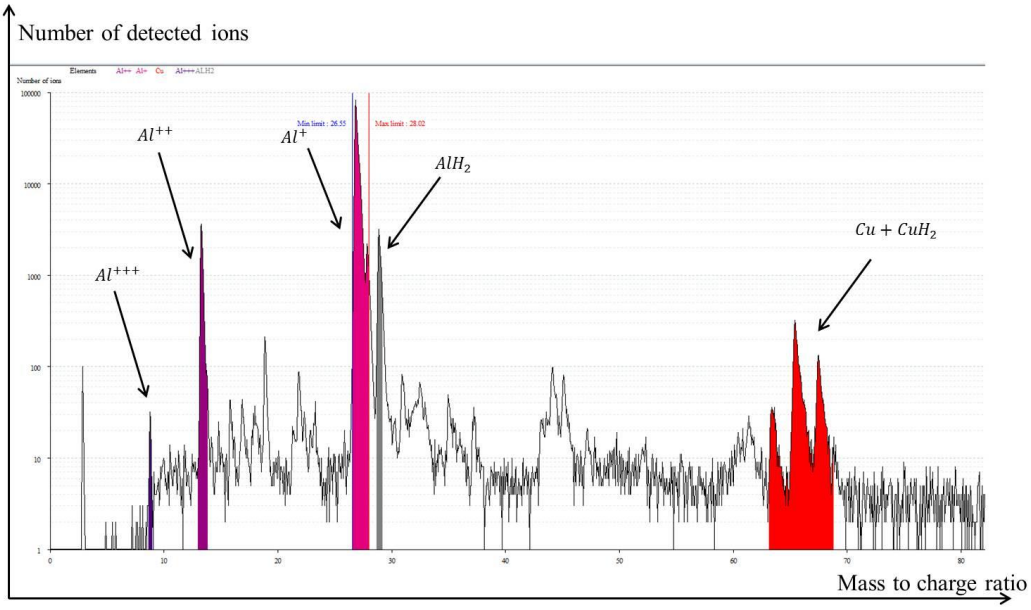

Figure 3.35 Typical obtained mass spectrum of Al – 1.7 at.% Cu alloy showing the presence of hydrides peaks.

Figure 3.36 (a – c) provides a series of Cu-atom maps from APT experiments on Al – 1.7 at.% Cu alloys that have already been subjected to 1S, 2S and 3S heat treatments. The figure shows that there is no spatial correlation in the distributions of the Cu atoms in the majority of the volume. Binomial frequency distribution analysis has been used to identify the presence of nano-scale solute-clustering processes and other segregations, which are typically difficult to visualize in APT datasets. Using this methodology, the identification of fine-scale solute clustering in the early stage of phase decomposition in the alloy investigated in this study is possible. A detailed explanation of the quantitative binomial distribution analysis of nano-scale atom clustering and segregation in the APT data can be found in reference [111]. The binomial distribution of the Cu atoms (*f(n))* in Figure 3.36(a –c) is plotted together with the experimental frequency distribution (*e(n))* (See Eq. 2.7) in Figure 3.36 (d), which clearly shows the agreement between the binomial distribution and the experimental frequency distribution. This agreement confirms the observation of the homogeneity of the microstructures in Figure 3.36 (a – c) especially by knowing that the Pearson coefficient (μ) is equal to 0.19. Thus, this observation indicates that the clusters of Cu atoms have been not recorded under these heat treatment conditions. To determine the precipitation sequence, the ageing time has been increased to 30 min, and the ageing temperature has been increased to 200 °C. Figure 3.37 (a) shows the

APT datasets that were experimentally acquired to evaluate the microstructure for the specimens that were heat-treated by increasing both the ageing time and the ageing temperature. The volume of 3D reconstruction shows the position of Cu atoms. Again, the binomial frequency distribution analysis is used to study the evaluation of the clustering of Cu atoms (Figure 3.37 (b)). The agreement between the binomial distribution and the experimental frequency distribution is clearly shown with the μ value of 0.2, which confirms the homogeneity of the microstructure.

The second step in the context of the evaluation of the precipitation sequence in Al – Cu system is to increase the ageing time to 8 h while maintaining the temperature at 160 °C. Applying this ageing condition produced a thin platelet of θ', as shown in the 3D reconstruction in Figure 3.38(a), where only Cu atoms are shown. A comparison between the binomial distribution and experimental distribution in Figure 3.38(b) shows a clear shift between the two curves, which is a clear indication that the Cu atoms are arranged in the presence of the second-phase particles in the system. The μ value in this case is close to 0.9 which confirms the occurrence the correlation between Cu atoms. The chemical composition of the θ' phase in this case is determined to be as (15.2 ± 4) at.% Cu. This determination is based on the proxigram profile forms from the isoconcentration surface of 8 at.% Cu (Figure 3.38(c)).

The absence of clusters of Cu atoms, GP zones and θ' precipitates from the microstructure of the specimens subjected to the three heat-treatment conditions in Table 3.3 (1S, 2S and 3S) (Figure 3.36) and from the microstructure of the specimens heat treated with increasing ageing time and ageing temperature (Figure 3.37) can be explained as follows. The lack of nano-features in this case is based on the vacancy concentrations. It seems that under these heat-treatment conditions, the Cu atoms are not able to cluster together and thus nucleate and grow; this phenomenon might be due to a diminished excess-vacancy concentration, which arises from vacancy sink sources. Increasing the ageing temperature to 200 °C causes the reduction of the driving force for particle nucleation [98]. Additionally, kinetic limitations during the precipitation sequence in this system are perhaps due to the low diffusivity of Cu into Al (diffusion coefficient $D = 2.89\ X\ 10^{-20} m^2 s^{-1}$ at 190 °C) [112].

The ageing treatment at 160 °C for 8 h produces a thin platelet precipitate that was identified as θ' platelet. The low density of the θ' platelets under this ageing

condition might be related to the short ageing time (8 h). It has been reported that 20 vol.% θ' precipitate has been detected after ageing Al – 4 wt.% Cu alloy for 3.5 days [113]. The transformation of GP zones into θ' precipitates has occurred when the ageing time was > 48 h [114].

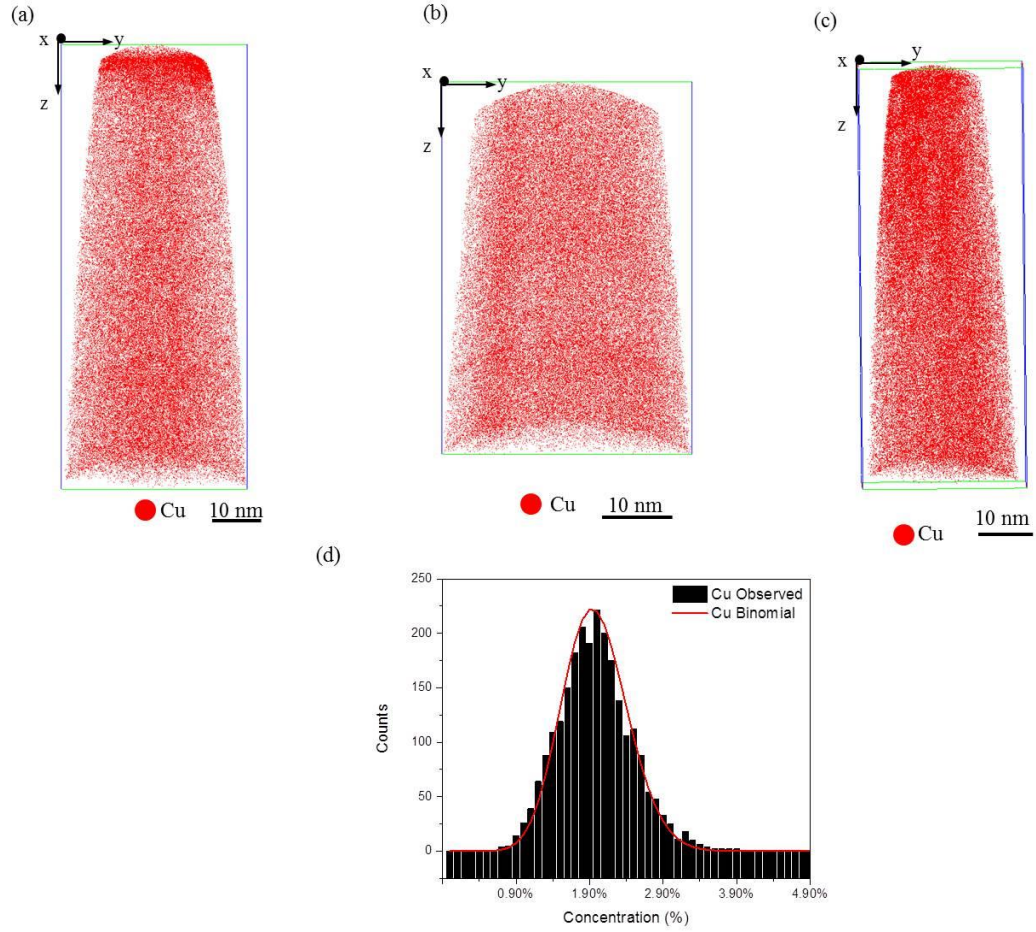

Figure 3.36 Cu distribution within Al – 1.7 at.% Cu datasets corresponding to three stages of heat treatments: (a) 1S. (b) 2S. (c) 3S. (d) Binomial and experimental frequency distribution.

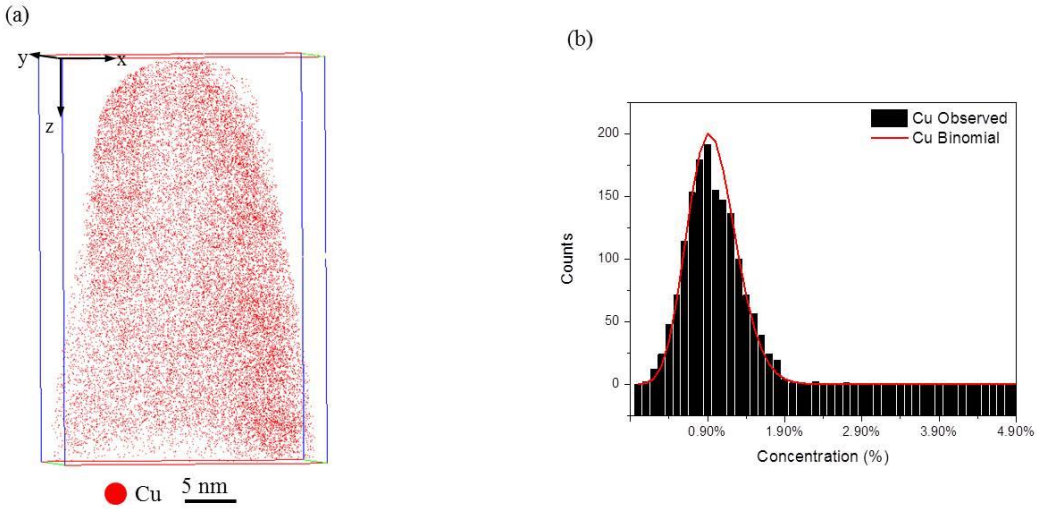

Figure 3.37 Cu distribution within Al – 1.7 at.% Cu datasets corresponding to: (a) Heat treated with increasing aging time to 30 min at 200 °C (b) Binomial and experimental frequency distribution.

The difficulty of detecting GP zones in the microstructure of the proposed alloy system rises from the limited resolution of the APT technique of an individual atomic layer of Cu in a GP zone. The off-stoichiometry of the θ' platelet in Figure 3.38 can be explained in terms of limited Cu diffusion and the limited formation of point defects; these might be the reasons behind the Cu-deficiency at this low ageing temperature.

Based on the Al – Cu phase diagram (Figure 1.5), the full sequence of the transition precipitate will be observed only if annealing or ageing is performed below the GP zone precipitate solvus (i.e., nearly 100 °C) with a long ageing time due to the low diffusivity of Cu into Al. The large diameter and small density of the different precipitates represent other challenges to analyze in the complex precipitation sequence in Al – Cu systems.

B) Al – Li alloy:

The early stages of phase decomposition of Al – Li binary alloys have been reported to be a subject of controversy [115]. Earlier studies by electron microscopy [116, 117] reported that the precipitation process of this system is quite simple:

$$\text{SSS} \longrightarrow \delta' \longrightarrow \delta$$

Where SSS is an abbreviation of "super saturated solid" solution, δ' is the Al_3Li metastable phase with an $L1_2$ structure (Figure 1.8), and δ is a stable $AlLi$ phase with a *B32* structure. These phases in the Al – Li phase diagram are shown in Figure 1.7.

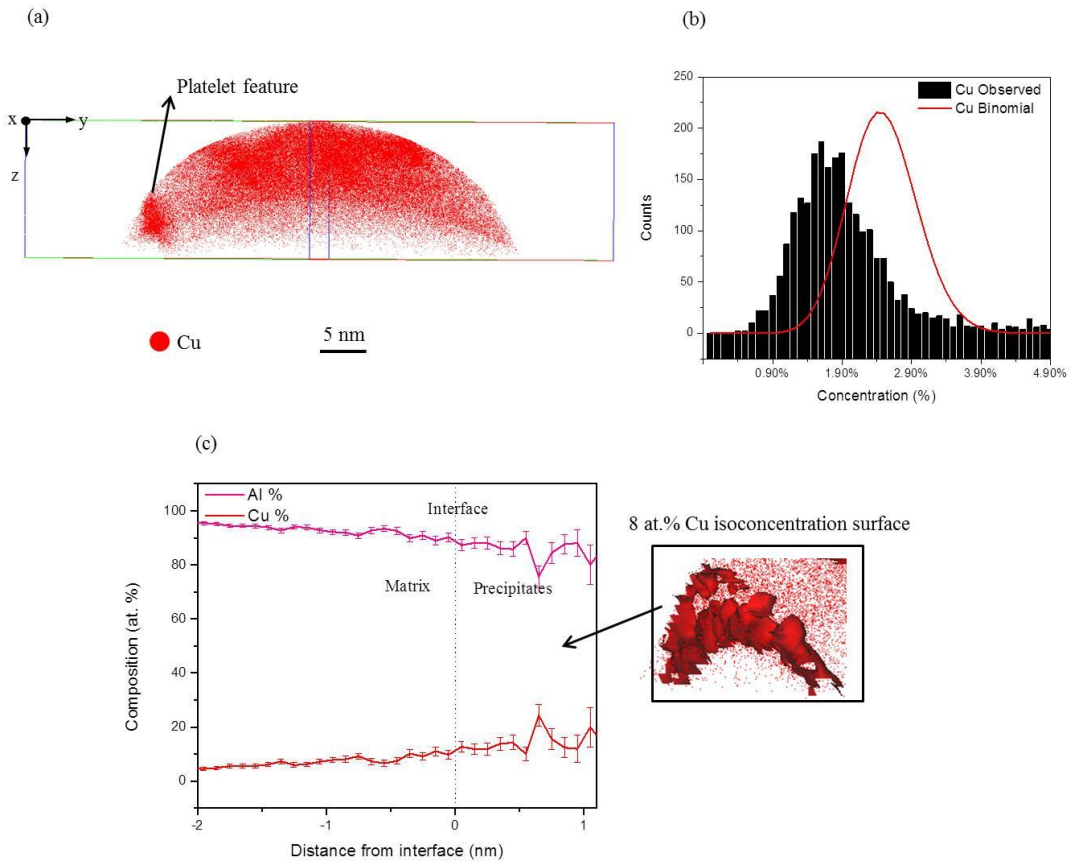

Figure 3.38 Cu distribution within Al – 1.7 at.% Cu dataset corresponding to aging the alloy for 8 h at 160 °C. (a) The reconstructed volume showing the presence of platelet feature. (b) Binomial and experimental frequency distribution. (c) Composition profile of the θ' platelet from isoconcentration surface of 8 at.% Cu.

The TEM images of the as-quenched alloy show a high density of small δ' precipitate particles; thus, it was found that the δ' phase formed during quenching after the solution heat treatment [115]. Controversy on the phase decomposition of this system arose from the presence of disordered GP zones prior to the precipitation of the δ' phase or not. On the other hand, a selected area diffraction pattern (SADP) from the as-quenched alloys showed strong $L1_2$ ordering spots, which suggest the

presence of δ' particles from the beginning of the process [116, 117]. Khachaturyan et al. [118] suggested different transformation paths in this alloy system and investigated transformation bathes from a solid solution to an $L1_2$ phase using the mean field approximation; they suggested that a solid solution decomposes into an ordered structure without any composition change (i.e., congruent ordering) and that this ordered structure is further separated into Li-rich, ordered δ' regions and Li-lean, disordered regions via a spinodal decomposition. There are two models of congruent ordering: nucleation and growth of the ordered domains, and spontaneous or homogeneous ordering. In either case, the quenched SSS should order congruently before the spinodal decomposition proceeds. To prove this transformation path, it is important to show the presence of the congruent order before the compositional fluctuation appears. Different studies have investigated this phenomenon [91, 118, 119]. The primary conclusion that has been drawn from all of these studies is that the kinetics of decomposition are too rapid to be followed by high-resolution techniques such as high-resolution transmission electron microscopy HRTEM and APT.

The objective of this portion of the study is to examine the microstructure at the early stage of decomposition to determine the presence of atom clustering or fine segregation. Because a subtle variation in the heat-treatment condition can exert considerable influence over the volume fraction of already formed δ' particles during subsequent precipitation reactions, an APT has been used to analyze Al – 8.2 Li at.% alloys that have been subjected to the three stages of heat treatment (i.e., 1S, 2s and 3S) shown in Table 3.3.

Example of the APT datasets which were experimentally acquired for the specimens under the 1S or 2S ageing conditions to examine the evolution of the microstructure at the early stage of decomposition is shown in Figure 3.39 (a). Comparing the binomial distribution and the experimental distribution in Figure 3.39 (b) shows a marginal shift between the two curves with μ value of 0.4. It seems that individual applying of the natural annealing condition and individual applying of the artificial ageing condition at 160 °C for 5 min alone do induce the formation of small clusters of Li atoms, which are observed in the microstructure after applying the cluster-search algorithm on the dataset with $d_{max} = 0.6\,nm\,, N_{min} = 20$ and order number of 3 for Li atom. A statistical calculation based on findings from applying

cluster search algorithms show that the microstructure under 1S and 2S heat treatment conditions contains Li clusters with size of (1.3± 0.3) nm, chemical composition of (20 ±1.5) at.% Li and number density ranges between 3 – 4 x 10^{23} m^{-3} (Figure 3.39(c)).

However, the shift between the binomial and experimental distributions becomes more pronounced when the specimen is heat-treated under the 3S ageing condition (i.e., a combination of natural and artificial ageing), as shown in Figure 3.40. The experimental distribution calculated from the reconstructed volume in Figure 3.40 (a) is shown to be shifted to the left compared to its corresponding binomial distribution, μ = 0.7 (Figure 3.40 (b)). Thus, the presence of second-phase particles can expected in this microstructure. Applying the cluster-search algorithm on the dataset in Figure 3.40 (a) (with the same cluster search parameters as in Figure 3.39) shows the presence of Li atoms clusters with size of (2.1 ± 0.2) nm and chemical composition of (22.2 ± 1) at.% Li (Figure 3.39 (c)). The number density of Li clusters under this aging condition is recorded as 6 x 10^{23} m^{-3}. It is worth notable that the number density of Li clusters in the microstructure under 3S heat treated condition is higher than that in the microstructure under 1S or 2S heat treated conditions by around two orders of magnitude.

The presence of second-phase particles or clusters of Li atoms from the microstructure of the samples heat treated with 1S and 2S conditions (Figure 3.39) is expected because a number of studies reported the presence of δ' particles in quenched samples [91, 115]. For our case, observation of these particles has been recorded statistically based on applying the cluster-search algorithm to the datasets (Figure 3.39 (b)) and the difference to the binomial distribution in Figure 3.39(c). A possible explanation for the observation in Figure 3.39 can be a high concentration of vacancies in the microstructure. It has been reported that in Al – Li systems, quenched vacancies and thermal vacancies play important roles in the kinetics [120]. An import factor in controlling the kinetics when ageing after quenching is solute-vacancy binding, where the suggested path is that vacancies become coupled to Li atoms during quenching. However, these vacancy-Li couples can be eliminated during quenching at the recovery stage in case of Al-0.38 at.% Li alloy [120]. But as we deal with alloy contains a high supersaturation of Li (8.2 at.%), the recovery procedure is unexpected after the quenching. The presence of the sufficient density of δ' particles

(or Li clusters) in the microstructure of naturally aging sample can be explained due to the coupling of Li atoms with quenched vacancies, while thermal vacancies play an important role when the specimen aging to 160 °C for 5 min, i.e. under 2S condition. On the other hand, it has been shown that the microstructure of the specimen under the combination of natural and artificial ageing conditions contains a higher number density of Li clusters. This could be explained that both of quenched and thermal vacancies have been contributed to the formation of δ' particles, as shown in Figure 3.40 (c).

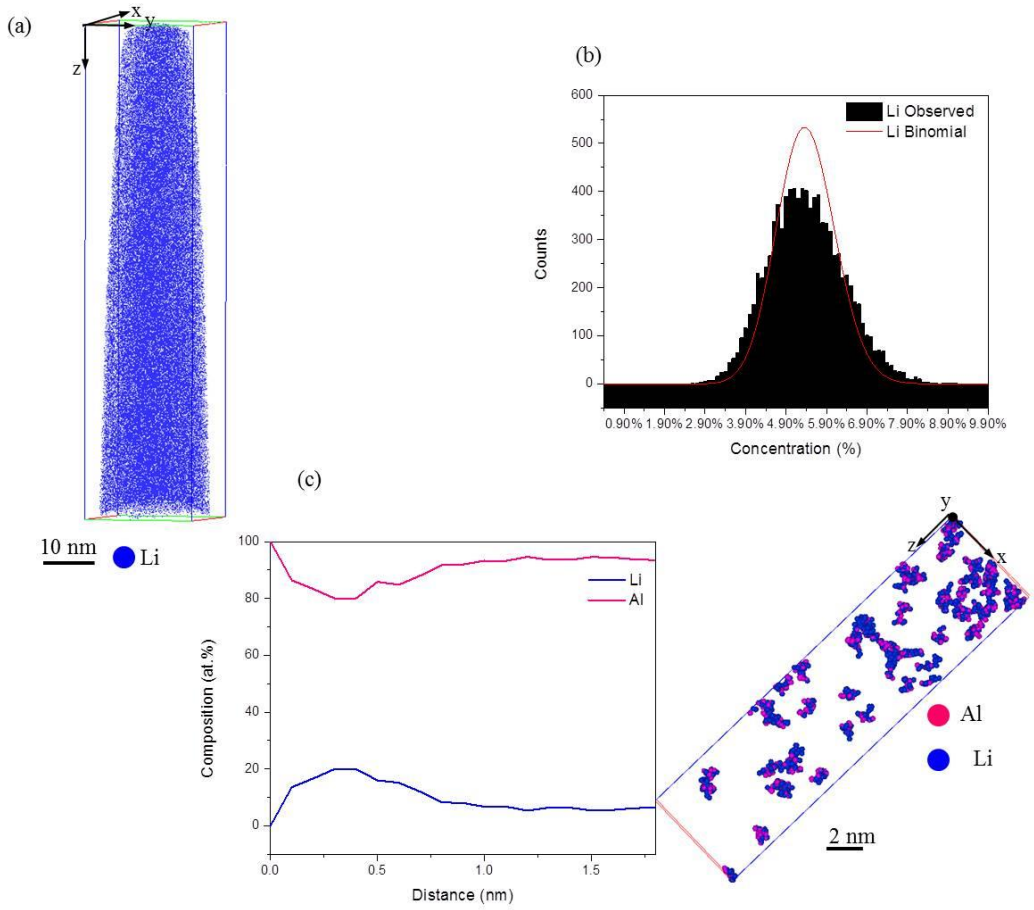

Figure 3.39 Li distribution within Al-8.2 at.% Li datasets corresponds to two stages of the heat treatments (1S, 2S): (a) The reconstructed volume. (b) Binomial and experimental frequency distribution. (c) Distribution of Al-Li clusters with the chemical composition profile.

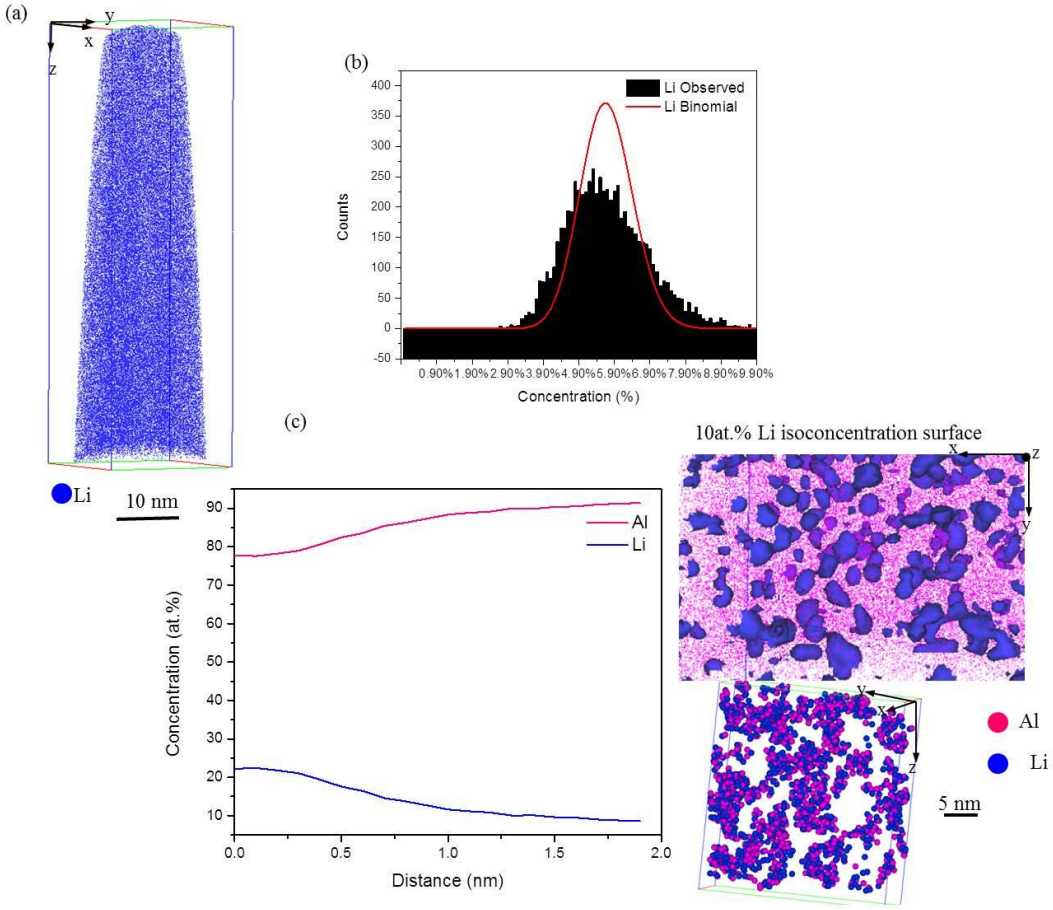

Figure 3.40 Li distribution within Al-8.2 at.% Li dataset for the 3S aging condition. (a) The reconstructed volume. (b) Binomial and experimental frequency distribution. (c) Distribution of Al-Li clusters with the chemical composition profile and the inset corresponds to isoconcentration surface of 10 at.% Li.

C) Al – Li – Cu alloy:

Al – Li – Cu alloys typically exhibit high strengths and good mechanical properties compared to Al – Li alloys. Due to their superior mechanical properties, these alloys are typically used in applications where strength is the limiting factor in the design. The experimental data for Al – Li – Cu systems are primarily concentrated in the Al corner of the phase diagram (Figure 1.3). The first systematic study of the phase equilibria in Al – Li – Cu systems was performed by Hardy and Silcock [16] who reported on a total six ternary solid phases for the first time. The solidus and

solvus temperatures were determined for different ternary Al – Li – Cu alloys with different compositions [121]. The thermodynamic properties of the phases in this system were studied by different researchers [122-124]. As mention earlier in section 3.1.6.2, the $T_1(Al_2LiCu)$ phase is the primary strengthening phase in Al – Li – Cu alloys and is formed congruently near 695 °C [125]. The hexagonal crystal structure of the T_1 phase (Figure 1.4) was first proposed by Hardy and Silcock [16]. The T_1 phase formation was assumed to occur via direct nucleation and growth from a saturated Al solid solution following a stacking fault mechanism [126]. Refinement of the hexagonal structure of Al_2LiCu was performed using single-crystal X-ray diffraction by Van sammleen [101]. Semi-coherent and incoherent precipitation of the T_1 phase was detected and reported in reference [127] without any indication of the presence of quenched vacancies.

The determination of precipitation behavior is typically performed using an advanced technique such as APT for specimens that have experienced different conditions. However, it is difficult to ensure an accurate following of the precipitation sequence due to the complexity caused by the nucleation stage. The competition between different phases in the ternary system increases the challenge in any phase analysis. Co-precipitation is usually dominated by the phase that can minimize the interphase boundary energy and form at defects that can assist in the reduction of the nucleation energy barrier [128]. The simultaneous formation of different phases usually occurs when they are disparate, preferred sites; then, the competition would be for solutes that are necessary for growth; if a phase is metastable, it would dissolve during competitive growth and at the same time, the more stable phase would continue growing. Thus, this portion of the study describes the precipitation behavior in a ternary Al – Li – Cu alloy with Li and Cu compositions similar to that of the commercial alloy AA2195. The goal is thus to understand the origin of precipitation in AA2195 as a complex alloy.

To understand the early stage of decomposition of the microstructure of ternary Al – 4 at.% Li – 1.7 at.% Cu alloy, APT experiments were performed for the specimens that were heat-treated based on the three stages (1S, 2S and 3S) shown in Table 3.3. Figure 3.41 provides a typical Cu and Li atom maps, which are from APT experiments on the ternary alloy that were subjected to 1S and 2S ageing conditions. Similar to the situation in Figure 3.36 for Al – Cu, which have experienced the 1S and

2S ageing conditions, the absence of any inhomogeneity in the microstructure is clearly shown in Figure 3.41 (a); this is also confirmed by comparing the binomial distribution to the experimental frequency distribution in Figure 3.41(b). No shifting between the two curves of the Li and Cu atoms has been recorded and μ = 0.1, which supports the absence of any clustering or solute-atom segregation under these conditions. Again, this could be explained by the low vacancy concentrations found.

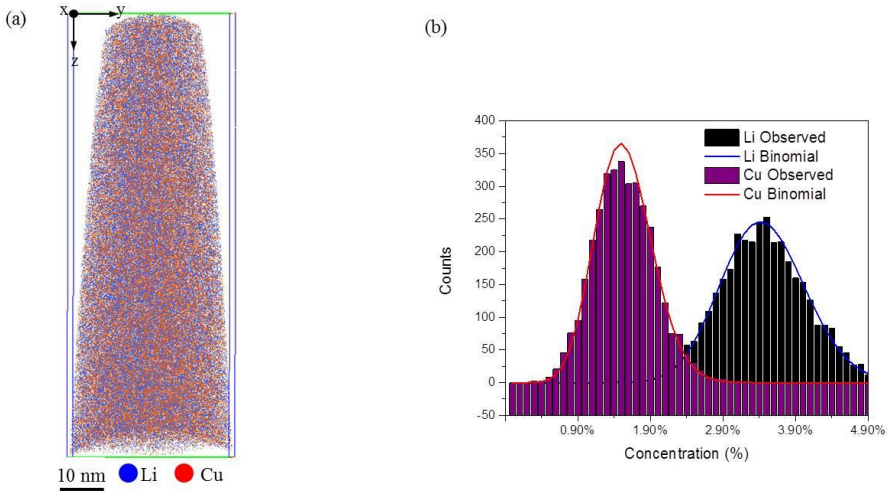

Figure 3.41 Cu and Li distribution within Al-4 at.% Li-1.7 at.% Cu datasets corresponding to the two stages of the heat treatments,1S and 2S. (a) The reconstructed volume. (b) Binomial and experimental frequency distribution for both Cu and Li atoms.

Conversely, the reconstructed volume of the specimen that was heat-treated under the 3S ageing condition in Figure 3.42(a) shows the presence of an inhomogeneity distribution, particularly for Cu atoms. The experimental distribution calculated from this reconstructed volume is shown in Figure 3.42(b). Based on this figure, the experimental distribution for the Cu atoms is shifted to the left compared to its corresponding binomial distribution, while the difference between the binomial and experimental distribution is marginal for the Li atoms, knowing that μ = 0.9 in the case of Cu atoms and μ= 0.4 in the case of Li atoms. Applying both the isoconcentration procedure, which is explained in section 2.1.5.1, and the cluster identification algorithm, which is explained in section 2.1.5.3, in the reconstructed

volume in Figure 3.42 (a) indicates the presence of an enriched region of Cu atoms that is decorated sparsely with Li atoms. The chemical composition of this enriched region is shown in Figure 3.42(c). Based on the quantitative analysis in Figure 3.42(c), the chemical composition of the Cu-enriched region was identified as (33 ± 1) at.% Cu, (5.3 ± 1) at.% Li. Based on this result, the Cu-enriched region can be identified as a θ' precipitate.

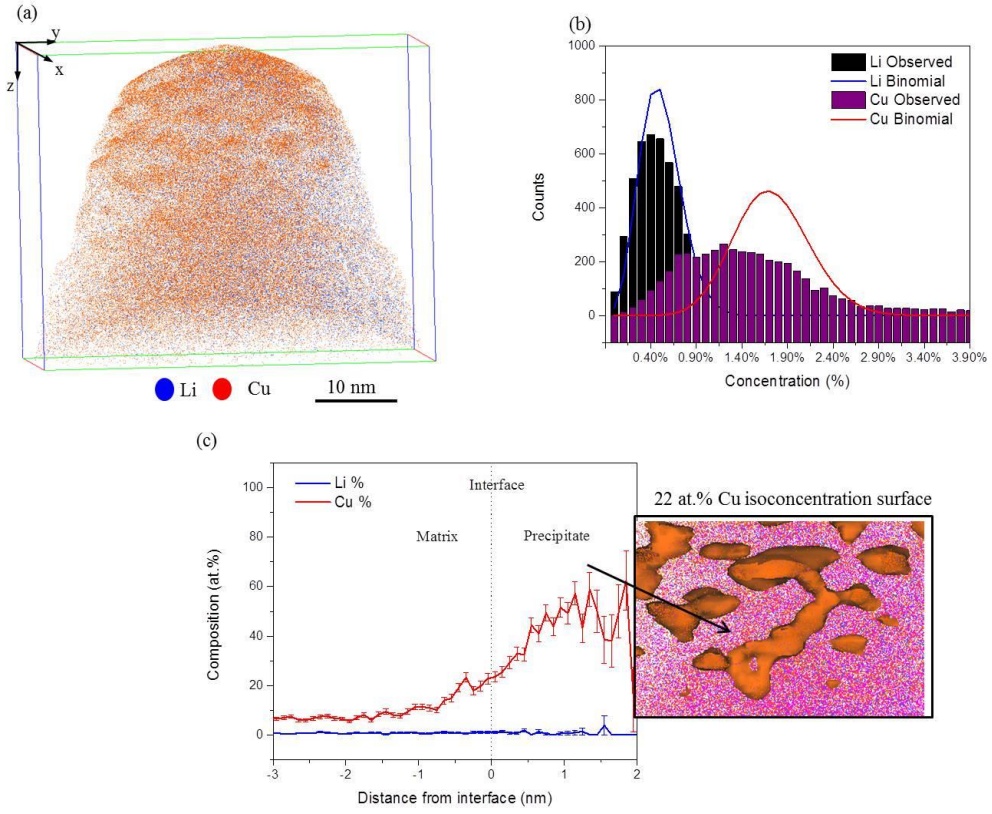

Figure 3.42 Cu and Li distribution within Al-4 at.% Li-1.7 at.% Cu dataset with 3S aging condition. (a) The reconstructed volume showing inhomogeneity in Cu distribution. (b) Binomial and experimental frequency distribution for both Cu and Li atoms. (c) Proxigram through the 22 at.% Cu isosurface of the enriched Cu region visualizes the precipitation of the θ' platelet.

The equilibrium phases shown in Figure 1.3 for the compositions of interest are T_1, T_2 and T_B. However, none of these phases have been detected in the APT analyses performed (Figures 3.41 and 3.42); this result could be explained by the similarity of the precipitation processes in both Cu-rich alloys and binary Al – Cu alloys [129].The presence of Li atoms might modify the orientation relation and structure of the homogenously nucleated zone [116]. The Li atoms are also known to enhance the precipitation of the θ' phase, as shown in Figure 3.42(c). Based on this analysis, it can be concluded that the early stage of the ternary Al – 4 at.% Li – 1.7 at.% Cu alloy starts by the precipitation of the θ' phase which is enriched with Li, and thus would be transfer to the T_1 phase at the later stage of ageing.

To investigate the influence of changing the composition on the precipitation behavior, a new ternary alloy with a nominal composition of Al – 8 at.% Li – 1.7 at.% Cu has been prepared based on the preparation procedure shown in Figure 3.33. In this case, only the 3S ageing condition was applied. Different from the situation in Figure 3.42(a), the microstructure of this specimen is rather homogenous (Figure 3.43(a)). No difference between the binomial and experimental frequency distributions for both Cu and Li atoms was detected, μ = 0.2 for Cu atoms and μ = 0.1 for Li atoms. (Figure 3.43(b)). The homogeneity of this microstructure is likely caused by the fact that Li atoms with a high vacancy binding energy (0.26 eV) trap excess vacancies and postpone or prevent the precipitation reaction of Cu. However, increasing the ageing time to 30 min for this alloy drastically changes the outcome; in this case, the distribution of the δ' particles is clearly shown (Figure 3.44(a)). The deviation from the binomial distribution is shown in Figure 3.44(b), indicating that Li atoms are not fully homogenously distributed in the matrix (μ = 0.7 for Li atoms and for Cu atoms μ = 0.2). Thus, a marginal change in the ageing time induces the precipitation of δ' particles, and the solubility of Li in Al does not seem to be affected by the presence of Cu atoms.

From the detailed analysis above, the APT method used is shown to be able to accurately resolve nano-scale microstructures; thus, the competition between different phases can be explored.

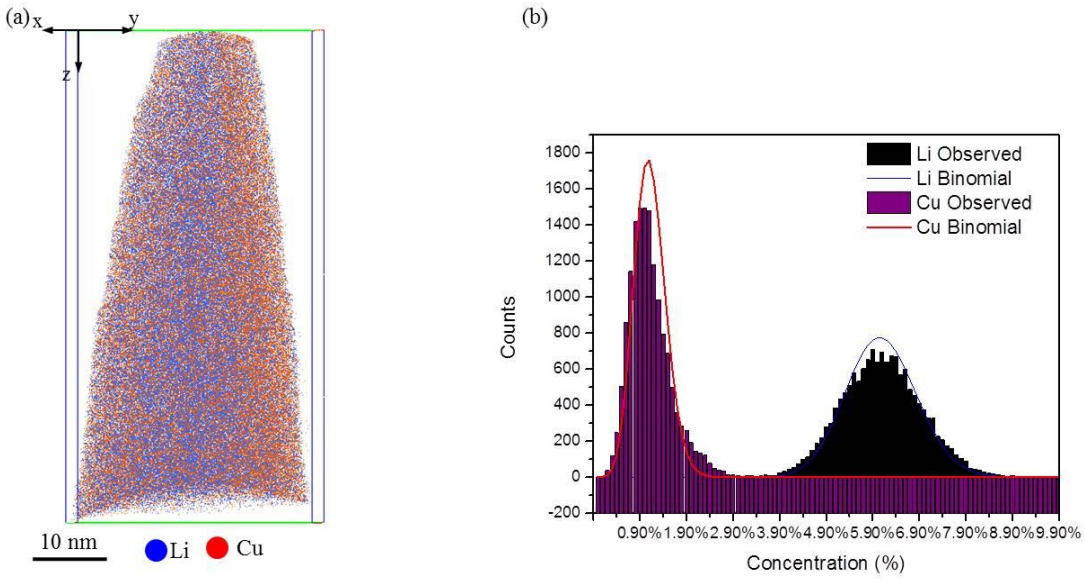

Figure 4.43 Cu and Li distribution within Al – 8.2 at.% Li – 1.7 at.% Cu dataset corresponding to the 3S aging condition. (a) The reconstructed volume. (b) Binomial and experimental frequency distribution for both Cu and Li atoms.

3.3.3 Conclusion:

In summary, within this portion of study, an APT method with a binomial frequency distribution and χ^2 statistics that quantify the deviation from the random has been used to investigate the early stage of decomposition of the microstructure of a binary Al – 1.7 at.% Cu alloy, a binary Al – 8.2 at.% Li alloy and a ternary Al – 4 at.% Li – 1.7 at.% Cu alloy.

Atomic resolution microscopy experiments in conjunction with a statistical test demonstrate that the phase decomposition in Al – 1.7 at.% Cu alloy requires a long ageing time of approximately 8 h at 160 °C to allow the diffusion of Cu atoms into Al matrix. For the Al – 8.2 at.% Li alloy, a combination of both the natural ageing condition (48 h at room temperature) and a short artificial ageing condition (5 min at 160 °C) induces increasing on the number density of the Li clusters and hence increase number of precipitated δ' particles. Applying this combination of natural ageing and short artificial ageing conditions onto a ternary Al – 4 at.% Li – 1.7 at.% Cu alloy induces the formation of a Cu-rich phase (i.e., the θ' phase). Increasing the Li content in the ternary alloy up to 8 at.% and increasing the ageing time to 30 min resulted in the precipitation processes ending with δ' particles.

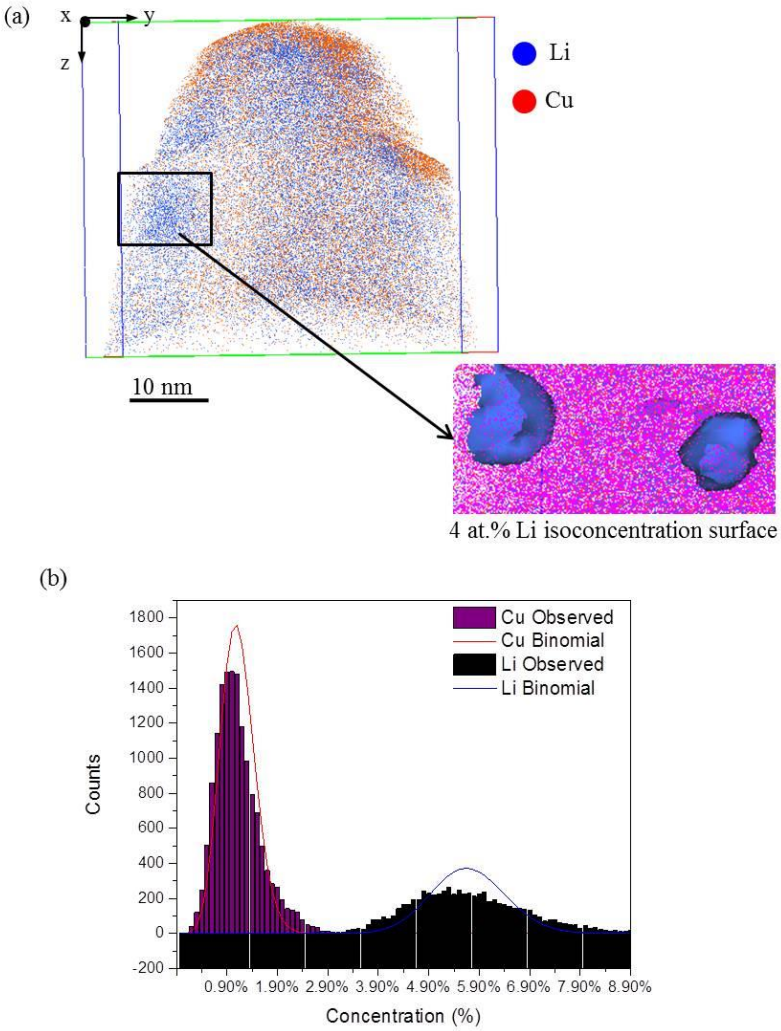

Figure 3.44 Cu and Li distribution within Al – 8.2 at.% Li – 1.7 at.% Cu dataset after aging the alloy for 30 min at 160 °C. (a) The reconstructed volume shows δ' particles (magnified view shows the distribution of δ' in the matrix based on 4 at.% Li isoconcentration surfaces). (b) Binomial and experimental frequency distribution for both Cu and Li atoms.

A key strength of this portion of study is the ability to identify and quantify the fine-scale segregation effects of dilute solutes in Al alloys; this supports the understanding of precipitation behavior in this important technical material.

Based on the above section, it is clear that by using a 3D APT technique, alloying elements can be mapped together with solute clusters and small precipitates. One of the important developments in the history of the APT technique is to introduce a

laser-pulse mode to be used in the same way as the current voltage-pulse mode (section 2.1.4). This method will allow for the optimum application of APT in a wide range of materials. In the next section, the systematic investigation of the microstructural changes in the $\delta'(Al_3Li)$ phase is used to describe the important phenomena associated with the laser-pulse mode.

3.4 Laser-induced reversion of δ' precipitate in Al – Li alloys: study of temperature rise in the pulsed-laser atom probe:

Over the last 15 years, the APT technique has been improved significantly, making it a well-established nano-analysis tool in the field of material science [130]. It has been extensively applied to the investigation of different types of materials due to its ability to map the distribution of single atoms in a material in real space on a nearly atomic scale; thus, using APT allows a better understanding of the physical phenomena involved in a material. The unique properties of this instrument have been used to study variety problems of current scientific and technological interest.

The time of flight (TOF) atom-probe technique was only applied to metallic samples due to the inability to transmit the nanosecond-scale, high-voltage pulses through sample tips with a low electrical conductivity [131]. Many attempts have been made to overcome these drawbacks of the atom probes. The primary concern was to extend the field of application of the technique to include poor conductivity materials. Efforts have also been made to increase the quantity of data resulting from a sample investigation by increasing the field of view [132]. On this basis, the voltage pulses in a conventional atom probe were replaced by an ultra-short laser pulse, which is used to induce field evaporation [131]. However, poor understanding of the laser interaction with the sample remains an issue.

The objective of this portion of the study is to perform a detailed literature review of the current proposed mechanisms for laser-assisted emission and to identify the influence of laser pulse energy in the microstructure of the proposed alloy. Based on the systematic investigation of the microstructural changes influenced by different laser pulse energies, we proposed a simple model to estimate the real specimen temperature via the laser-induced interface reaction in a laser APT analysis.

To date, two models have generally been accepted on the role of the laser pulses. In the first model, a portion of the laser energy is absorbed by the specimen tip, leading to the generation of a thermal spike on the tip; thus, a temperature rise occurs. In this case, evaporation is described by the pure thermal-pulse model (TPM) proposed by Liu and Tsong [133]. In the second model, a strong electromagnetic field is expected at the sample surface due to the high instantaneous power of the laser and due to the enhancement effects related to the sub-wavelength dimensions of the sample [134]. As a result, an ultrafast electric field at the tip apex is generated due to the rectification of the optical field at the specimen surface. This mechanism has been proposed by Vella et al. [135]. The pulsed field induced by optical rectification (OR) acts exactly as a voltage pulse with a sub-picosecond duration applied to the tip. Several results with pure metals, such as aluminum and tungsten, support the OR mechanism [132]. Conversely, recent studies by Cerezo et al. [136] have interpreted their experimental results with a pure TPM; they observed the surface diffusion of atoms caused by femtosecond laser irradiation [137]. Vurpillot et al. measured the temperature of the specimen after a femtosecond laser pulse using a pump-probe method [138] and demonstrated a temperature rise of approximately 600 K for tungsten. It has recently been shown that the interaction of the laser pulse with the tip leads to a complex absorption pattern [139] and ultimately to a confined absorption of the laser energy in a hot spot with the dimensions of the laser wavelength [140]; this suggests that the evaporation of ions during laser-assisted atom-probe tomography is a thermally driven process in which the tip apex is heated to a temperature that allows the thermal promotion of the field-evaporation process [137]. Until recently, there was controversy over the physical mechanism of the field evaporation induced by a laser pulse, but Vurpillot et al.[138] showed that the physical process behind field evaporation assisted by ultra-short laser pulses in metal is described by the TPM model, declaring the influence of OR mechanism to be probably of a second order.

In this part of study, we investigate the details of the laser-induced specimen-heating effect using an interface reaction in an Al – Li alloy as a model system. This alloy is known to have a low-temperature, metastable, miscibility gap [22]. It has been shown that under classical conditions of ageing of this alloy, including solution treatment, fast quench to room temperature and thermal ageing at intermediate temperatures (e.g., 100-200 ˚C), the precipitation behavior was dominated by the

presence of the metastable $\delta'(Al_3Li)$ phase with an $L1_2$ structure [141]. The influence of the laser power on the morphology, the composition and the diffusion of $\delta'(Al_3Li)$ precipitates in the aluminum-lithium-based alloy is identified. A simple model is used to explain the observed experimental behavior and to estimate the corresponding tip-apex temperature for various laser energies.

3.4.1 Materials and methods:

Ingots of Al – 2.0 wt.% (7.8 at.%) Li were drawn into 0.2-mm wires. The composition of the wires was measured via inductively coupled plasma optical emission spectrometry (Varian ICP-OES 720-ES). These wires were solution-treated at 500 ˚C for 30 min, followed by quenching in ice water. Then, the wires were aged at 190 ˚C for 3 h. This heat treatment is known to cause formation of spherical $\delta'(Al_3Li)$ precipitates with $L1_2$ structure [142]. Atom probe tips were prepared via a standard electrochemical polishing procedure using a mixed solution of 30 vol.% nitric acid in methanol at -20 ˚C. APT analyses were performed with both a CAMECA LAWATAP for FIM mode and a CAMECA LEAP 4000X HR using both voltage and laser modes. A diode-pumped (Nd:YAG) solid-state laser operating in the frequency-tripled ultraviolet region with a wavelength of 355 nm, a pulse duration of approximately 12 ps and a repetition rate of 200 kHz was used. The laser pulse energy was systematically varied through the following values: 10, 30, 40, 50, 60, 80 and 100 pJ. The position of the laser spot on the specimen was monitored using a charge-coupled device (CCD) camera. Data were acquired at a base temperature of 22 K and an average detection rate of 0.001 ions per pulse. The base pressure was maintained at less than 10^{-8} Pa during the analysis. The pulse fraction for the analysis in the voltage mode was set to 18%. Field ion images were obtained using Ne gas at 1.2×10^{-3} Pa. Reconstruction of the acquired data was performed using the TAP3D and IVAS 3.6.6, software programs provided by CAMECA.

The reconstruction algorithm used was the standard evolution algorithm [41]. The calibration of the primary reconstruction parameters was performed by observing the correct plane distance between the aluminum atomic planes for the respective crystallographic pole of (111) or (100) and the complete spherical shape of the precipitates. The value of the field strength of the evaporation E_F as tuned to obtain the correct interplanar spacing of pure Al and the complete spherical shape of the

precipitates. The effect of the solute Li on the *d* spacing is considered to be negligible [93]. At 100 pJ, the atomic planes were not clearly resolved; thus, the reconstruction was performed based on the initial tip curvature radius observed via SEM and the corresponding E_F (Vnm^{-1}).

To obtain the chemical composition within both the matrix and the precipitates, the linear composition profile along the cylinder perpendicular to the isoconcentration surface was used. Isoconcentration surfaces delineate the regions containing more than 14 at.% Li; this surface was obtained by sampling the atom probe tomography reconstruction with $1 \times 1 \times 1\ nm^3$ voxels after applying a delocalization procedure that was developed by Hellman et al. [45] with the smoothing parameters of 3 nm for the x- and y-coordinates and 1.5 nm for the z-coordinate. Estimation of the size of the precipitates was performed using a cluster identification algorithm [47] implemented in IVAS 3.6.6 software. Li-containing precipitates were identified using a maximum separation distance of 0.5 nm between Li atoms, and a minimum of 20 Li atoms in each precipitate.

Before and after the APT analyses, scanning electron microscopy (SEM) was used to observe the specimen apex geometry using Quanta 3D microscope (FEI).

3.4.2 Experimental results and theoretical model:

In general, a reference measurement is used to investigate the potential influence of the laser pulse energy in an APT analysis; this can be done by performing an analysis in voltage-pulse mode. In this mode, a standing voltage V_{dc} is applied to the specimen and then a short, additional voltage pulse will initiate the emission of the atoms. Figure 3.45 shows a three-dimensional reconstruction volume of the respective sample analyzed by the voltage pulse mode. At a glance, Li-enriched regions are clearly shown in Figure 3.45(a). This enrichment was found to have a nearly spherical shape. Concentration profiles were drawn across the cylinders perpendicular to these Li-enriched regions, and one typical shape of the profile is presented in Figure 3.45(b) as an example. Within the enriched area, the Li concentration c_{Li} reaches a maximum of 23 at.%, while in the matrix, the c_{Li} is less than 6 at.%, suggesting a precipitation of a Li-rich phase. The average concentration of Li in the precipitate (calculations were performed on 15 precipitates) was determined to be c_{Li} = (22.6 ± 0.9) at.%; this value is similar to that of the $\delta'(Al_3Li)$ phase predicted for the Al-Li system at 190 ˚C

[143]. The average diameter of the precipitates was estimated to be (14.2 ± 3) nm. This result is also in agreement with the results reported by Al-Kassab et al. [119] and Krug et al. [144], hinting at the precipitation of $\delta'(Al_3Li)$. All of the observations described above suggest that the Li-rich phase corresponds to metastable $\delta'(Al_3Li)$. TEM observations showed that this metastable phase is coherent with the Al matrix and has marginal coherency strains and small interfacial energy [145].

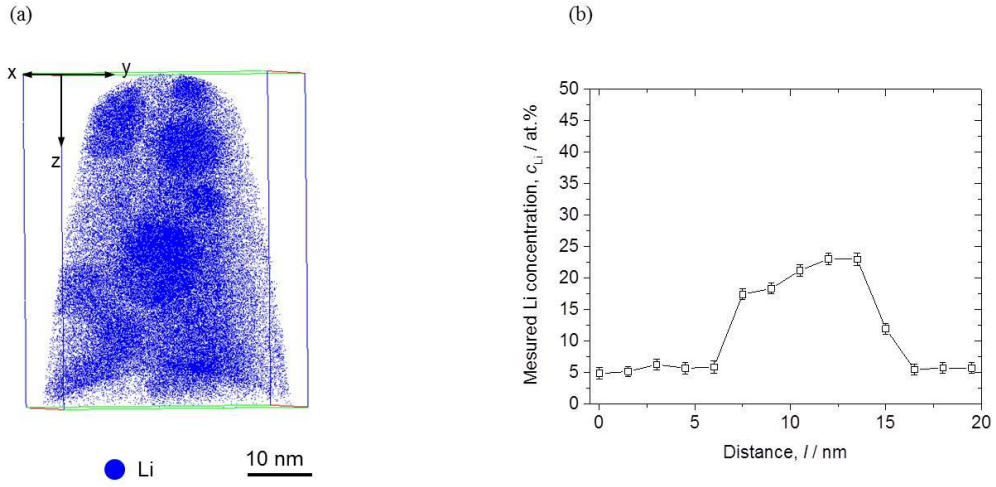

Figure 3.45 Initial microstructure of the tip analyzed by the voltage mode. (a) The reconstructed volume showing the distribution of spherical δ' precipitates (b) Linear composition profile along the cylinder with the size of (x, y = 11 nm and z = 20 nm) perpendicular to the isoconcentration surfaces delineate region containing 14 at. % Li. The average concentration of Li in the precipitate is c_p = (22.6 ± 0.9) at.% and in the matrix is c_t = (5.4 ± 0.8) at.%.

In laser-pulse mode during the APT analysis, a standing voltage V_{dc} is applied to the specimen, and the pulsed field is generated by the laser itself. It is well known that the field strength of evaporation E_F decreases with increasing laser energy, E [131]. This relationship, E vs. E_F, has been confirmed by Figure 3.46, which shows the influence of the laser energy on the field strength of evaporation of the respective microstructure. This result confirms that field evaporation occurs at the effective field evaporation temperature T_{eff} [146] during a pulsed-laser atom-probe procedure; this temperature is higher than the specimen base temperature. Field evaporation will be triggered at a lower electric field F_{eff} than that required in the case of a conventional, high-voltage (HV) pulsed atom probe analysis of an identical specimen.

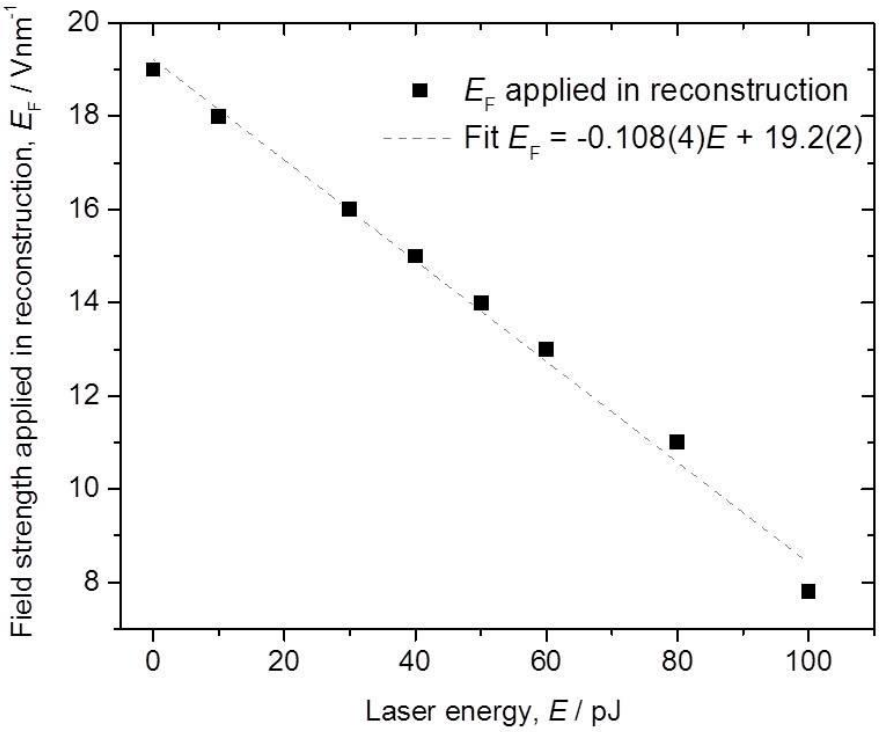

Figure 3.46 Field strength of evaporation E_F applied in reconstruction as a function of the laser energy *E*.

As a result of this thermal process, the morphology and composition of the $\delta'(Al_3Li)$ precipitates might be affected and presumably altered during the laser-mode analysis. Analyses at various laser energies were performed to monitor this effect, as shown in Figure 3.47, which shows a series of reconstructed volumes of the tips analyzed by laser pulses at the following laser energies: 10, 30, 40, 50, 60, 80 and 100 pJ. From Figures 3.47 (a-e), spherical precipitates in the microstructure are clearly visible in the range of laser energies from 10 to 60 pJ. Conversely, Figure 3.47(f) shows that the precipitates begin to lose their distinctive shapes at 80 pJ. At an even higher energy of 100 pJ, precipitates are no longer detected as individual particles (Figure 3.47(g)). Moreover, some enriched Li regions can be seen in the top view of the reconstructed volume in Figure 4.47(h). Reproducibility of this absence of precipitates was confirmed 3 times over 4 experiments. The overall c_{Li} in Figure 3.47 (g, h) ranged from 5 to 19 at.% depending on the region over which the analysis was performed. It should be emphasized in this study that the reconstruction of the data

was performed based on the adjustment of the interplanar spacing of (111) or (100) planes while assuming a hemispherical shape of the tip apex.

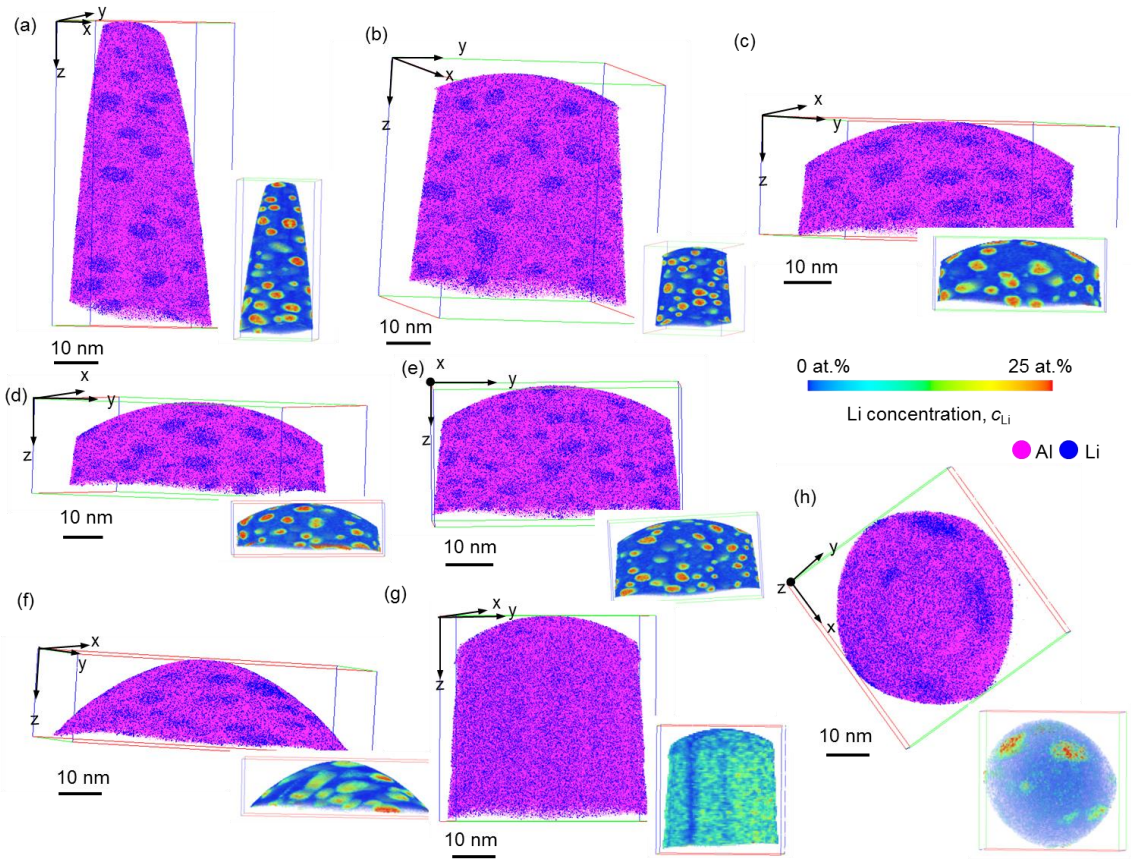

Figure 3.47 Comparison of the morphology of the δ' precipitates under illumination of the laser pulses at various values of energy *E* measured for different samples: (a) 10, (b) 30, (c) 40, (d) 50, (e) 60, (f) 80 and (g, h) 100 pJ.

However, this assumption of a hemispherical tip shape is not always valid [147]. Laser irradiation on a tip is known to often cause tip reshaping, which results in erroneous 3D reconstructions [148]. Thus, SEM observations of the specimen apex geometry before and after the analysis at higher laser energies (i.e., 100 pJ) have been performed to describe the specimen's end form in this study. SEM micrographs of the tip end forms are compared in Figure 3.48. In both cases, the tip end form indeed resembles a nearly hemispherical shape. Consequently, at a laser energy of 100 pJ, the

aforementioned tip-reshaping effect can be ignored. These observations justify using the conventional data reconstruction method in this study based on the assumption of a hemispherical end form of the specimen apex [149].

FIM observations were performed to verify the microstructures shown in the APT results and also to confirm the specimen's apex geometry after the analysis via the voltage-pulse and laser-pulse modes at the higher laser energies. It is known that the calculated field strengths of evaporation E_F of Li and Al are 14 V/nm and 19 V/nm for single charged ions, respectively [38]. Accordingly, it is likely that Li-rich regions undergo preferential evaporation of Li over Al in a FIM image; thus, the surface morphologies are modified as a result of a self-induced process during field evaporation. Consequently, after the field evaporation of the surface, preferentially evaporated regions are less likely to experience the ionization of the imaging gas compared to the rest of the surface and thus should be imaged with a dark contrast with respect to the matrix. This dark contrast was observed also by Hono et al. [115]. This contrast difference is also shown in this study, as identified by the circles in Figure 3.49 (a). In combination with the APT results, it is thus reasonable to consider that these dark spots represent $\delta'(Al_3Li)$ precipitates, and the bright contrast region represents the matrix phase, which is enriched with Al. One bright spot appearing in the image is presumably due to the presence of oxide nuclei on the top most surface of the tip and is of minor importance to this study. Conversely, the image taken after the analysis at a laser energy of 100 pJ allows for completely different impressions. No precipitates are visible; instead, a rather homogenous microstructure with different concentric rings that correspond to different crystallographic poles are observed (Figure3.49 (b)). This is again consistent with the reconstructed volume in Figure 3.47 (g, h). As described earlier, the evolution of field evaporation in the FIM is associated with the self-modification of the surface geometry because the evaporation process is not controlled by other means to accommodate the different values of E_F of the constituent elements. In the APT technique, evaporation is partially controlled by the superposition of the voltage and laser pulses over the DC voltage such that it minimizes the influence of the preferential evaporation; however, this influence is known to be significantly dependent on the pulse voltage (i.e., pulse fraction) and the pulse laser energy.

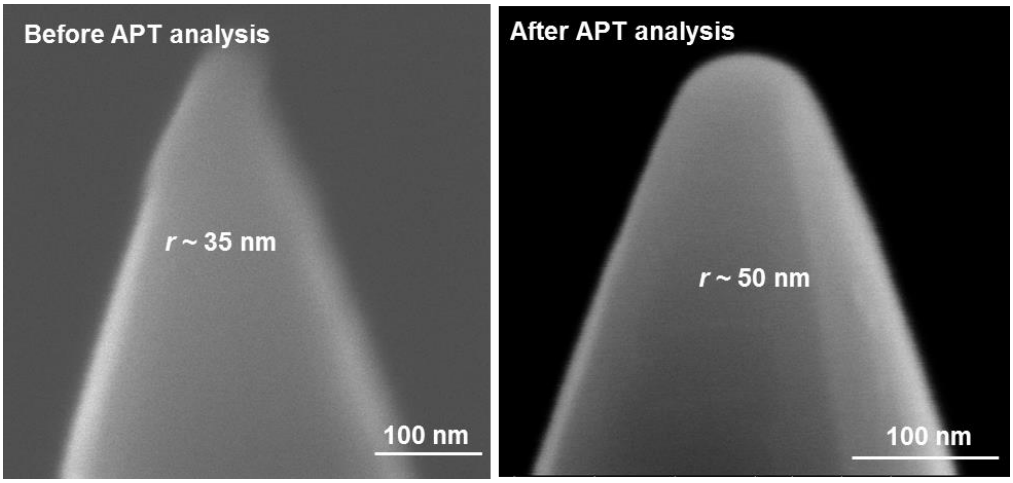

Figure 3.48 Scanning electron micrographs showing the geometry of the tip apex (a) before and (b) after APT analysis by the laser pulse mode at 100 pJ.

Thus, the measured Li concentrations c_{Li} in the proposed samples were carefully examined in both the voltage-pulse and laser-pulse modes at different laser energies. In Figure 3.50, c_{Li} is plotted as a function of the laser energy. In voltage mode (E = 0 pJ), the detected c_{Li} was (5.4 ± 0.8) at.% in the matrix, which is somewhat lower than the expected solubility limit of Li at 190˚C (6 at.%), as reported by Noble and Bray [150]; this implies a marginal influence from the preferential evaporation of Li. However, the error bar verifies that the detected c_{Li} is within the expected range. Similarly, c_{Li} in the precipitates falls within a reasonable range of (22.6 ± 0.9) at.%, closely matching the reported value [143]. It is therefore concluded that the proposed APT measurement is not significantly affected by the mentioned preferential evaporation of Li within the detectable level. However, as the laser energy is increased, a significant departure from those values is observed; c_{Li} in the precipitates' c_p drops to 19.5 at.%, while c_{Li} in the matrix' c_t increases to 7.6 at.%. When considering the expected temperature rise induced by laser irradiation, this trade off relation between c_p and c_t reminds us of the lever rule at the miscibility gap.

To describe the origin of this change in c_{Li}, the precipitates shown in Figures 3.45 and 3.47 were further characterized to obtain quantitative information on the precipitates' diameters, their number densities and their volume fractions. Using the simple law of mass conservation, a relationship for the spherical precipitates between the radius r, the number density N_v and the volume fraction f is given by the following relationship [35]:

$$^{4\pi}/_{3}\, N_v r^3 = f \qquad (3.2)$$

Additionally, the lever rule holds to the following relationship [35]:

$$^{c_0 - c_t}/_{c_p - c_t} = f \qquad (3.3)$$

Where c_0 is the nominal Li concentration in the alloy, c_p is the measured Li concentration within the precipitates and c_t is the measured Li concentration within the matrix.

The methodologies described in (3.4.1) section are used to extract information about the average compositions and the average diameters of the precipitates in all of the reconstructed volumes in Figures 3.45 and 3.47. For using Eq. (3.2), the total analyzed volume has been calculated from the atomic volume for each ion multiplied by the total number of the ions in the analyzed volume. By dividing the number of precipitates by the calculated value of the volume of analysis, an approximate number density of the precipitates was obtained.

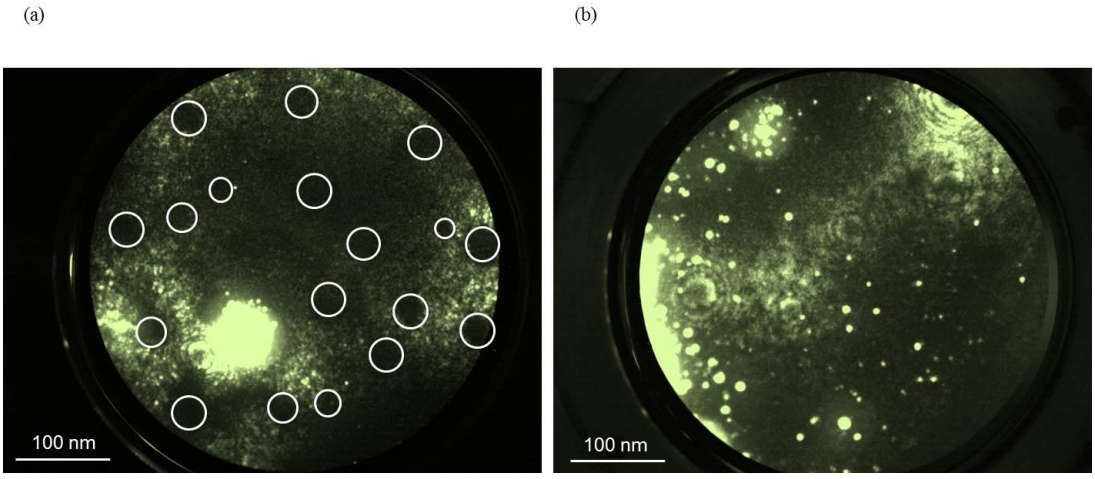

Figure 3.49 Field ion micrographs of the aluminum lithium specimen (a) Taken for the specimen after analysis by the voltage pulse mode, shows the distribution of darkly imaged $\delta'(\mathrm{Al_3Li})$ precipitates as marked by circles. (b) Taken for the specimen after analysis by the laser pulse mode at the laser energy *E* = 100 pJ, shows a homogenous microstructure, with different concentric rings corresponding to different crystallographic poles.

A summary is shown in Table 3.5 as a list of the average diameter d of the precipitates, their number density N_v, their volume fraction f, their average Li compositions within the precipitates c_p and the Li composition of the matrix c_t. Data for 100 pJ is not available due to the lack of precipitates in the volume analyzed, as shown in Figure 3.47 (g, h). Noticeably, the values of d, N_v and f decrease as the laser energy increases from 10 to 80 pJ. Eq. (3.3) was used to confirm the validity of f estimation from Eq. (3.2). The difference between these two estimations by Eqs. (3.2) and (3.3) of f was ±1% at the largest and is thus negligible. Strictly speaking, Eq. (3.3) holds under equilibrium and might not directly account for the metastable miscibility gap, when other stable precipitates such as $\delta(AlLi)$ phase are formed. However, it has been shown that the $\delta'(Al_3Li)$ phase is formed and accounts for most of the precipitates in the Al – 2.0 wt.% Li alloy aged at 200 ˚C within ageing times up to 240 h [142]. This is in a good agreement with the proposed experimental observation; we did not detect phases other than $\delta'(\mathrm{Al_3Li})$; thus, mass conservation is believed to hold between the α (Al matrix) and δ' phases. Therefore, if the change in Li concentrations (i.e., c_p and c_t in Figure 3.50) is associated with the temperature increase due to laser irradiation, the proposed data should follow the suggested metastable miscibility gap of $\alpha + \delta'$ in Al-Li system [22]. Conversely, d, N_v and f were found to decrease with increasing laser energy and thus increasing temperature, which is opposite to the conventional kinetic model of coarsening, which was proposed as the Lifshitz-Slyozov-Wanger (LSW) theory [151].

Our experimental observations above anticipate that the $\delta'(\mathrm{Al_3Li})$ precipitates at various laser energies might involve an evolution of the tip temperature upon irradiation with the laser pulses. However, the extent of the real temperature increase is not yet known, and to date, we cannot compare the results of this study with the Al-Li phase diagram.

We therefore attempt to estimate the tip temperature T as follows. The diffusion lengths L and effective diffusion coefficients D were calculated for the Li atoms from the δ' precipitates at each laser energy by considering changes in the precipitates' diameter Δd as being equal to the diffusion length L. The values Δd have been estimated from the difference between the diameter of the precipitate at each laser energy and their original diameter before applying the laser pulses (i.e., in voltage

mode). If the reaction is assumed to be diffusion-controlled, the effective diffusion coefficients *D* are estimated from the relationship between the diffusion length *L* and the diffusion time *t* [35]:

$$\Delta d \cong L = 2\sqrt{Dt} \qquad (3.4)$$

$$D = {L^2}/{4t} \qquad (3.5)$$

As an approximate of the diffusion time *t*, we assume a diffusion time of 1 second in this study due to the high activation energy of the Li atoms in $\delta'(Al_3Li)$, which is Q = 119 kJmol^{-1} [152], and due to the study of kinetics of reversion by Okuda et al. [153]. In addition, this rough estimate of the diffusion time is based on an estimate of the diffusion penetration distance from a point source. Suppose a δ' particle is a point source of a diffusing substance and *L* in Eqs 3.4 and 3.5 is the diffusion penetration distance. Then, using eq. 3.5, the time required for the Li atoms to diffuse from the δ' particle through a distance of 1 nm in the microstructure is approximately 2.5 s. For simplicity, the diffusion time is set to 1 s due to the variety of precipitate sizes and, therefore, of diffusion lengths for different laser irradiation energies. Assuming that the previously reported value of *Q* is also valid in the sample of the proposed study, and the expected reaction at the precipitate/matrix interface is one elemental process, as proposed in reference [153], the diffusion behavior of Li considered in this study is described by an Arrhenius-type relationship [30]:

$$D = D_0 \exp({-Q}/{RT}) \qquad (3.6)$$

Where *D* is the diffusion coefficient (m^2s^{-1}), D_0 is the pre-exponential factor (m^2s^{-1}), *Q* is the activation energy (kJmol^{-1}), *R* is the gas constant (Jmol K^{-1}) and *T* is the thermodynamic temperature (K).

Using Eqs. (3.5) and (3.6), *T* at each laser energy was estimated. The diffusion lengths *L* and the effective diffusion coefficients *D* for the Li atoms at each laser energy are summarized with their corresponding temperatures *T* in Table 3.6. Based on the table, the diffusion length *L* increases with increasing laser energy and thus temperature. As a result, the estimated diffusion coefficient *D* scales with the temperature *T*. This relationship is more evident in Figure 3.51. These data fall into a reasonable range of

D compared to that of the bulk Al-Li system, where *E* = 10 – 80 pJ. At 100 pJ, only the lower limit of *D* and *T* can be estimated by considering the complete re-dissolution of the precipitates. Based on this crude estimation, the *T* at 100 pJ is at least 540 K (267 ˚C). The real *T* at 100 pJ can be substantially higher than this value. This margin is indicated by the shaded region in Figure 3.51. The estimated *D* in this study could be, however, still somewhat underestimated because the diffusion process of Li might be influenced by the continuous formation of a new surface during the APT analysis itself. This influence is often observed as a surface segregation in the APT analysis of a light element such as hydrogen or deuterium [154]. In this study, such segregation was not experimentally observed. The influence of tensile stresses caused by the DC electric field can also not be ruled out, but its contribution should not be significant based on the voltage APT data.

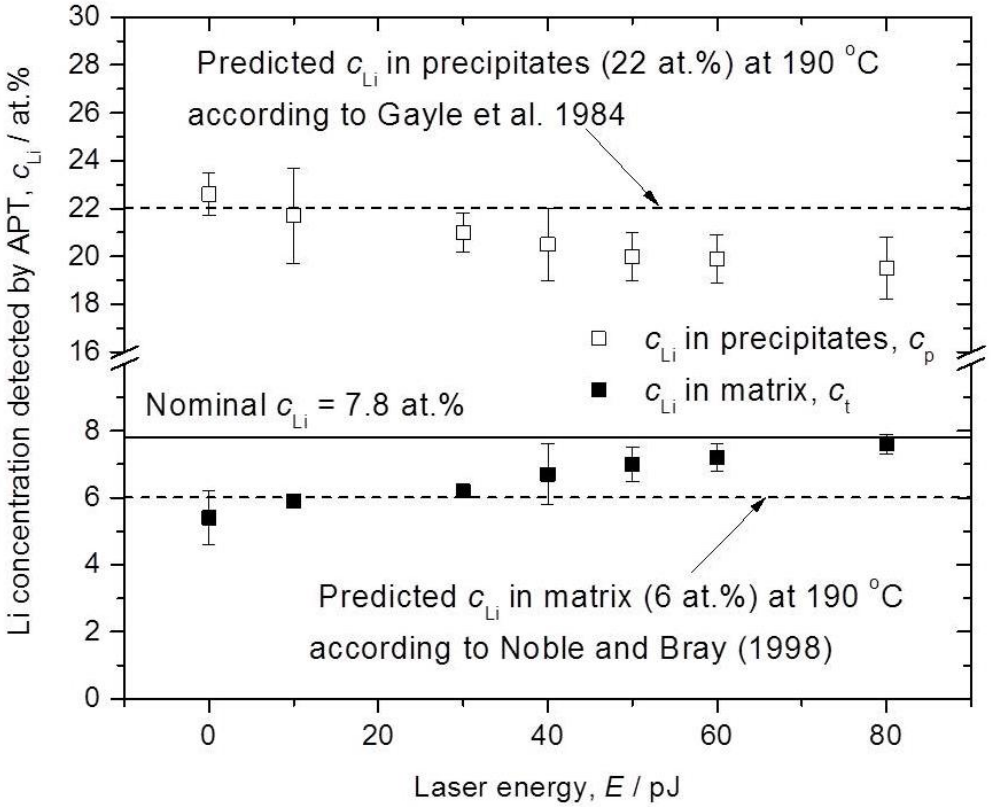

Figure 3.50 Measured matrix Li concentrations c_{Li} in the tip analyzed by the voltage pulse mode and by the laser pulse mode at different values of laser energy as a function of the laser energies *E* (in voltage mode, *E* = 0 pJ).

Table 3.5 Summary of the data obtained for the diameter d, number density N_v, volume fraction f, Li composition c_p in the precipitates and Li composition c_t in the matrix for the sample analyzed both in the voltage mode and laser mode at various values of laser energy. *f* was calculated by Eq. (3.2).

	Diameter d x 10^{-9}(m)	**Number density N_v x 10^{22} (m^{-3})**	**Volume fraction f %**	**Li concentration in precipitates c_p (at.%)**	**Li concentration in matrix c_t (at.%)**
Voltage	14.2 ± 3	10 ± 0.1	14 ± 2	22.6 ± 0.9	5.4 ± 0.8
L 10 pJ	13.4 ± 3.1	9.68 ± 0.5	12 ± 1	21.7 ± 2	5.9 ± 0.1
L 30 pJ	12.8 ± 3.3	9.23 ± 0.1	10 ± 1	21 ± 0.8	6.2 ± 0.2
L 40 pJ	12.4 ± 3.1	9.18 ± 0.01	9 ± 0.1	20.5 ± 1.5	6.5 ± 0.9
L 50 pJ	11.5 ± 3.4	8.39 ± 0.5	6 ± 0.1	20 ± 1	7 ± 0.4
L 60 pJ	10.6 ± 2.6	8.27 ± 0.01	5 ± 0.1	19.9 ± 1	7.2 ± 0.4
L 80 pJ	9.2 ± 1.5	6.25 ± 0.2	2 ± 0.5	19.5 ± 1.3	7.6 ± 0.3

Table 3.6 The calculated diffusion lengths and effective diffusion coefficients for Li atoms from the precipitates and the estimated temperatures corresponding to each point of the laser energy.

	Diffusion length L x 10^{-9} (m)	**Diffusion coefficient D x 10^{-19} (m^2s^{-1})**	**Temperature T (K)**	**Temperature T (°C)**
L 10 pJ	0.8 ± 0.1	1.6 ± 0.4	444.4 ± 3	171.4 ± 3
L 30 pJ	1.4 ± 0.3	4.9 ± 2	460.5 ± 6	187.5 ± 6
L 40 pJ	1.8 ± 0.1	8.1 ± 1	468 ± 2	195 ± 2
L 50 pJ	2.7 ± 0.4	18 ± 5	480.6 ± 5	207.6 ± 5
L 60 pJ	3.6 ± 0.4	32.4 ± 7	490.3 ± 4	217.3 ± 4
L 80 pJ	5 ± 1.5	62.5 ± 30	501.6 ± 10	228.6 ± 10
L 100 pJ	> 14.2	> 521	> 540	> 267

In Figure 3.46, it was shown that the field strength of evaporation E_F monotonically decreases with increasing laser energy *E*. Additionally, the temperature rise *dT* due to laser irradiation was suggested to be nearly proportional to the laser energy *E* [138]. Thus, it is anticipated that the relationship of E_F and *dT* is inversely proportional; this seems to also be valid in the case investigated in this study within the range of 10 to

80 pJ, as shown in Figure 3.52. In this figure, if the linear relationship of dT vs. E_F is extrapolated to the E_F of 100 pJ (7.8 Vnm^{-1}), the corresponding dT produces a temperature of 511 ± 4 K; thus, this dT plus the base temperature 22 K suggests a specimen temperature T of 533 ± 4 K (260 ˚C ± 4). This value is not significantly different from 540 K (267 ˚C), which was separately deduced from the estimated diffusion coefficient via the precipitates' re-dissolution at 100 pJ (see Table 3.6 and Figure 3.51). As described earlier, the estimation of T at 100 pJ via the estimation of D might not be simple; however, both approaches from D and E_F to estimate T at 100 pJ produce comparable values of T (533-540 K, 260-267 ˚C), which implies that a complete re-dissolution of δ' occurs at this temperature range.

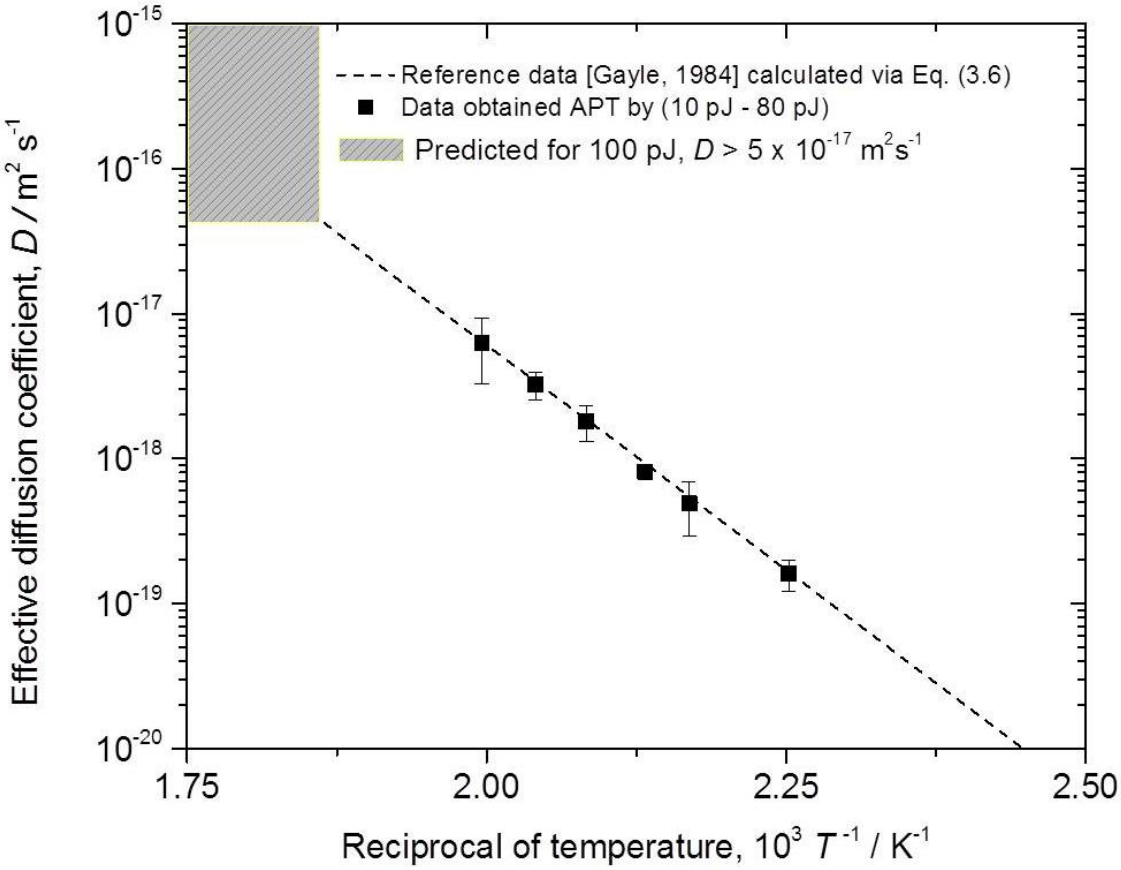

Figure 3.51 Arrhenius plot of effective diffusion coefficients D estimated by using Eqs. (3.5) and (3.6). Estimated values are compared with D values of the bulk Al-Li system [22] (broken line) calculated via Eq. (3.6).

Now, we attempt to compare the proposed values of c_p, c_t and T obtained via the APT technique with the metastable miscibility gap of $\alpha + \delta'$ in the Al-Li system that was previously summarized by Gayle et al. [22] in Figure 3.53. The measured data points are located nearly within the miscibility gap of the diagram. The Li solubility in this study is shown to be in better agreement with the report of Noble and Bray [150] compared to that of Gayle et al. [22] (see data for 10 pJ in Figure 3.53). It is also clear that the average Li concentrations in the α and δ' precipitates follow the gap closure of the miscibility gap with the temperature as the laser energy is increased up to 80 pJ; this behavior is supported by considering the rise in T due to the laser irradiation at the sample tip.

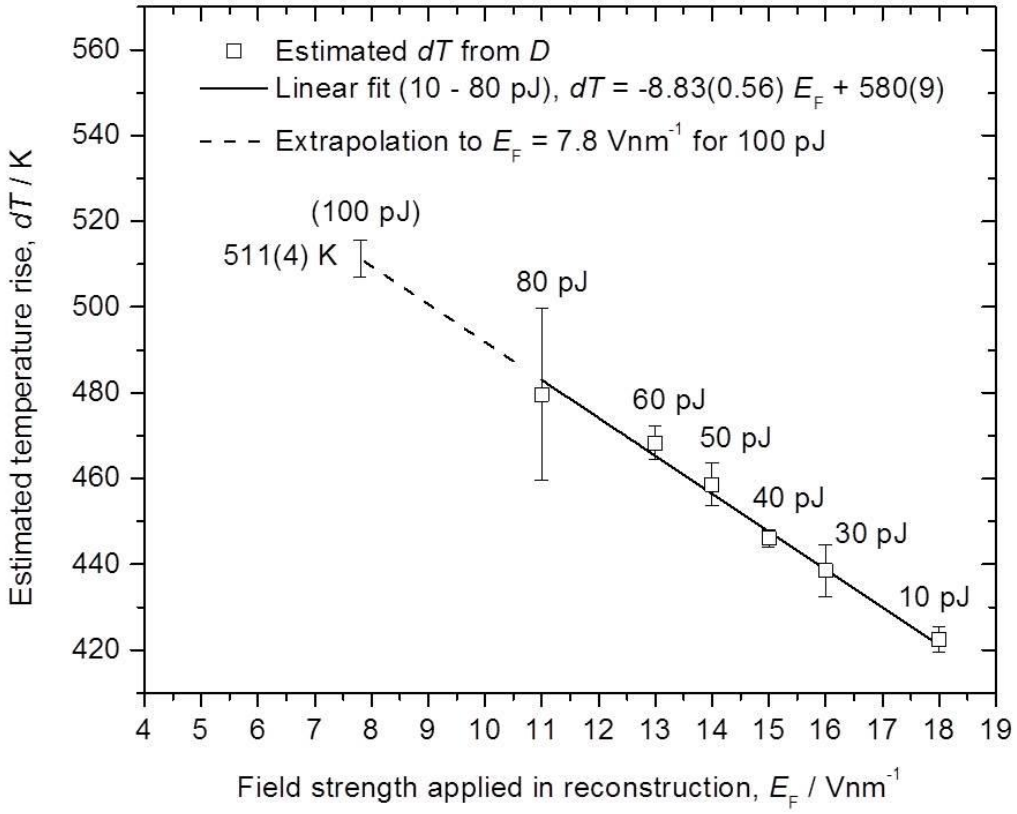

Figure 3.52 Laser-induced specimen temperature rise dT plotted against field strength of evaporation E_F. Inversely proportional relationship between E_F and dT is shown (At 100 pJ, dT is extrapolated from the linear relationship due to the lack of information on diffusion length L).

Judging from the results in Figure 3.47 and Table 3.5, the diameter d of the precipitates decreases with increasing laser energy. This does not correspond to coarsening but rather suggests a partial reversion of the precipitates at 10-80 pJ. The data at 10-80 pJ coincide with the miscibility gap, which is well below the critical temperature T_c; thus, we emphasize here using Figure 3.50 that the Li concentration in the matrix measured in voltage mode and at 10 pJ nearly verifies the solubility of 6 at.% at 190˚C, at which the aging treatment was performed. Departures from this solubility begin at laser energies above 30 pJ, where the corresponding specimen temperature exceeds 190˚C. This experimental behavior indicates that the increase in temperature as the laser energy increases is sufficiently rapid to destabilize all of the precipitates present in the initial microstructure, leading to a supersaturated c_{Li} in the matrix, as shown in Figure 3.50. As noted by Noble and Bray [150], this supersaturation indicates the progressive dissolution of δ' precipitates. The temperature of the α/δ'solvus in the Al – 2.0 wt.% Li alloy has been determined to be near T_c = 513 K (240 ˚C) [150].

Based on this value, the results at a laser energy of 100 pJ corresponds to full reversion, where no clear evidence of precipitation was detected in the FIM observation (Figure 3.49 (b)) or the APT analysis (Figure 3.47 (g, h)). The corresponding temperature at 100 pJ was suggested to be in the range of T = 533-540 K (260-267 ˚C) (Figures 3.51, 3.52). This range of T is in agreement with the reported range of the solvus temperature of δ' in the Al – 2.0 wt.% Li alloy: 513-523 K (240-250 ˚C) [142] [150]. Within this temperature range, the precipitates are nearly fully reverted into the matrix. This influence of the heat on $\delta'(Al_3Li)$ precipitates was further confirmed by conducting a voltage-mode analysis immediately after the laser-pulse mode analysis at 100 pJ. Figure 3.54 shows the reconstructed volumes of an identical tip analyzed using, first, the voltage pulse mode; second, the laser pulse mode at 100 pJ; and finally, the voltage pulse mode. The top view of the reconstructed volume of the tip analyzed using the voltage pulse mode shown in Figure 3.54 (a) confirms the initial stage of the microstructure. Spherical δ' precipitates are present around the (111) crystallographic pole. Irradiating the tip using a laser with a pulse energy of 100 pJ results in solute-enriched regions without spherical δ' precipitates in the Al matrix; these are shown in the top view of the reconstructed volume provided in Figure 3.54 (b). This observation is similar to the

result shown in Figure 3.47 (h). The results of a voltage pulse mode analysis performed immediately after the laser pulse mode analysis whose results are shown in Figure 3.54 (c) are the same as those shown in Figure 3.54 (b). No spherical precipitates are detected; instead, some Li-enriched regions are visible. The depth concentrations measured along the cylinders perpendicular to the Li-enriched regions shown in Figures 3.54 (d, e). Figure 3.54 (d) shows the depth concentration profile of the Li-enriched region shown in Figure 3.54 (b). Once again, the overall c_{Li} ranges from 5 to 19 at.%. The depth concentration profile of the Li-enriched region shown in Figure 3.54 (c) is shown in Figure 3.54 (e). The overall c_{Li} ranges from 6 to 17 at.%. Variations in the shape and composition of the δ' precipitates after irradiation by a laser with a pulse energy of 100 pJ confirm the effect on the local microstructure of the specimen at the apex of the tip. These results suggest that irradiation by a laser pulse energy of 100 pJ has a permanent effect on the microstructure of the specimen at least locally at the tip apex. The disordering of δ' precipitates is also shown to not cause the dispersion of solute Li atoms into the matrix but rather leaves solute-enriched and disordered regions within the matrix [142].

The observations above support the proposed interpretation of the reversion phenomenon observed at 100 pJ. The results in Figure 3.52 indicate that the range of *dT* is between 422 and 518 K; these values are not significantly different from the reported *dT* of 600 ± 50 K, as observed with tungsten using an infrared (IR) laser (λ = 1030 nm) [138] despite the fact that the laser wavelength used in that study was different. Based on the study by Houard et al. [140], UV laser illumination on an Al or steel tip produces a localized energy absorption near the tip apex to a depth of 500 nm in the material, while the IR laser does not. Therefore, it would be reasonable to consider that the proposed case is the former (i.e., the heating zone could be localized near the tip apex). Thus, if the voltage-mode analysis conducted immediately after the laser mode runs through to a sample depth (e.g., 500 nm to 1 μm), the original microstructure of the $\delta'(\mathrm{Al_3Li})$, which is free from the influence of heat, might be progressively detected.

Regarding the thermal properties of the Al-Li system, it is known that the thermal conductivity decreases from (2.50 ± 0.04) $\mathrm{Wcm^{-1}K^{-1}}$ to (0.91 ± 0.02) $\mathrm{Wcm^{-1}K^{-1}}$ with increasing Li concentration in Al from 0 to 2 wt.% in the temperature range of 127 to

185 ˚C [155]. When considering higher Li contents within the precipitates than that of the matrix, the thermal conductivity of the respective microstructure would be even lower, leading to additional heating. Interfaces between these nano-sized precipitates and the matrix would effectively act to scatter phonons [156], which also suggests an increasing temperature. Due to these microstructural phenomena, a direct comparison of the *dT* observed in a microstructure containing hetero- interfaces with that of pure metals is not always valid.

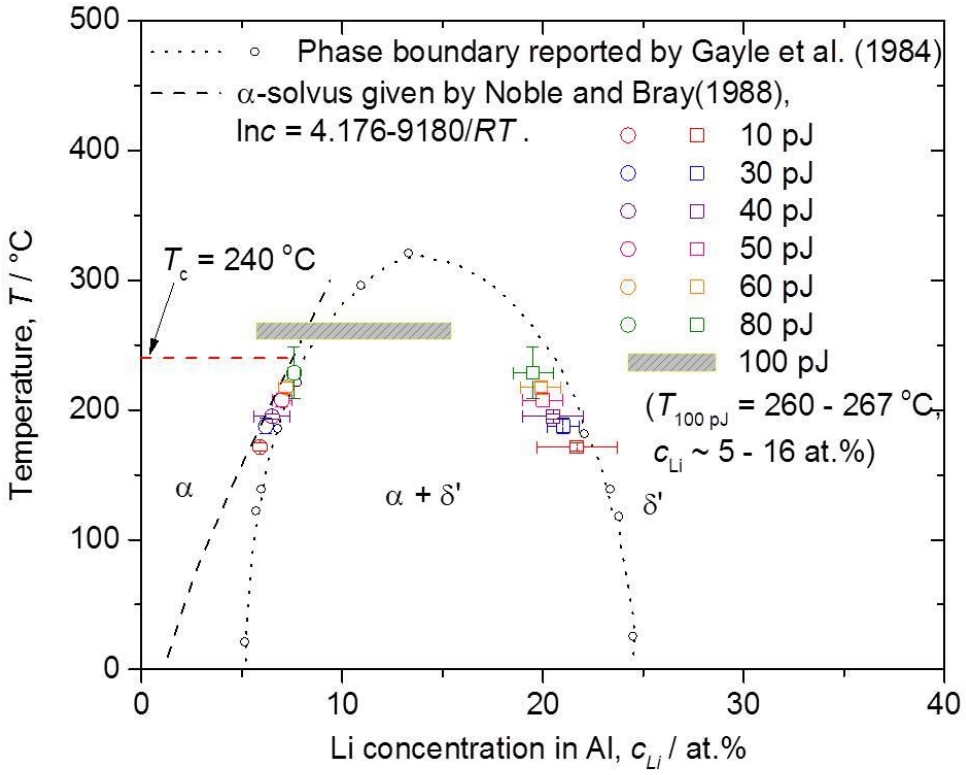

Figure 3.53 Comparison of the experimental Li concentrations and the estimated temperatures with an Al-Li phase diagram adapted from [22, 150]. The data obtained at E = 10 – 80 pJ agree with the miscibility gap, at well below the T_c. At 100 pJ, the tip temperature is estimated to be in the range of solvus temperature of δ' precipitates.

In this study, atom probe tomography presented a series of snapshots during *in-situ* reversion of $\delta'(Al_3Li)$ precipitates, initiated by laser irradiation, using different laser energies for the first time. In addition, the attempt shown in this study might provide a

method to investigate real sample temperatures during laser-APT analyses using an interface reaction itself as a probe.

Examples about the influence of the laser pulse irradiation on the microstructure of Al-based alloy can be found in Appendix A.

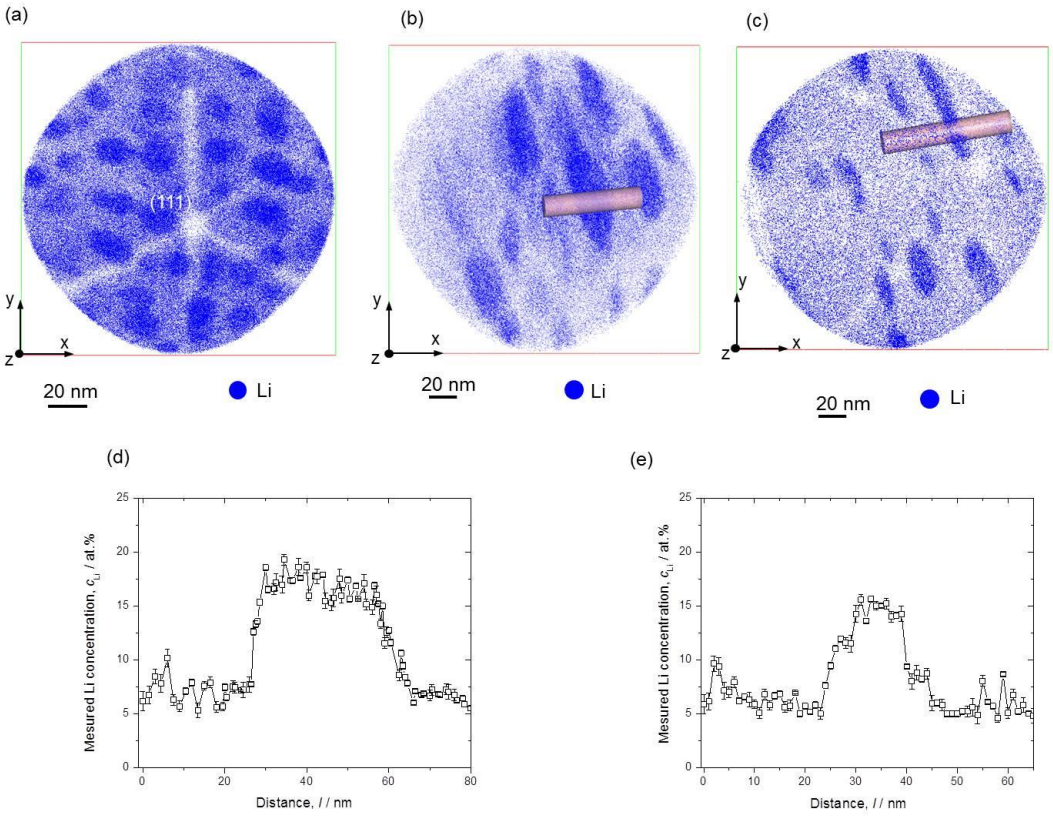

Figure 3.54 Comparison of the morphology and composition of δ' precipitates before and after laser analysis: (a) Top view of the reconstructed volume of the tip analyzed by voltage pulse mode (b) Top view of the reconstructed volume of the tip analyzed by laser pulse mode at 100 pJ (c) Top view of the reconstructed volume of the tip analyzed by voltage mode after conducting laser analysis showing the permeant effect of the heating on the δ' precipitates (d) Composition profile along the cylinder with the size of (x, y = 15 nm and z = 80 nm) perpendicular to Li enriched regions in (b). (e) Composition profile along the cylinder with the size of (x, y = 10 nm and z = 65 nm) perpendicular to Li enriched regions in (c).

3.4.3 Conclusion:

In this study, we report on the influence of the laser-pulse energy on the morphology and composition of the $\delta'(Al_3Li)$ precipitates in a binary Al-Li alloy. The influence of ultrafast laser pulses on the microstructures of the materials was investigated in terms of the variations in the diameter, d; the number density, N_v; the volume fraction, f; and the composition c_p of the precipitates. The temperature increase of the sample via UV laser illumination was investigated by estimating the diffusion length and the diffusion coefficient of Li atoms. A comparison with the Al-Li phase diagram was performed. At a lower laser pulse power, all data were found to be within the miscibility gap of the diagram. However, depending on the laser energy, variations in the Li concentration were clearly detected along the solubility line of the precipitates. At the highest laser energy applied in this study (i.e., 100 pJ), the estimated tip temperature was near the critical temperature of $\delta'(Al_3Li)$ in the Al-2.0 wt.% Li alloy; this is supported by the results, which showed no precipitates in the analysis at this laser energy, which can be attributed to a significant and permanent heating effect causing a reversion of the once-formed $\delta'(Al_3Li)$at the local region of the tip apex. In the course of the systematic investigation of the microstructural changes in the $\delta'(Al_3Li)$ that were caused by different laser pulse energies, this study proposed one simple method to estimate real specimen temperatures via laser-induced interface reactions during a laser-APT analysis. A series of snapshots during *in-situ* reversion of $\delta'(Al_3Li)$ precipitates, initiated by laser irradiation, using different laser energies has been presented for the first time.

The next and last section of this chapter will be devoted to answering two important questions:

1) How can the synthesis of intermetallic compounds, which are critical structural materials in technical applications inside an Al matrix, be achieved? And;

2) How can an advanced, sophisticated analysis technique such as the APT technique be used to describe the mechanism of the proposed method of synthesis?

3.5 APT study of the growth of a single crystal phase synthesized using a molten Al flux:

Al and Mg are two highly important lightweight metals that are commonly used in applications that require reduced vehicle weight to improve fuel economy. Innovations in design strategies are always directed toward weight-saving measures; therefore, it is common to employ lightweight materials [157]. Other light elements such as Si, Ca and Zn are usually added to Al and/or Mg alloys to maximize their functionality. Al – Mg – Si alloys, for example, are versatile heat-treatable alloys with high strength/weight ratios. They are easy to extrude and have good hardening characteristics, and thus find application in a wide range of areas [158]. The potential of these alloys to save weight, improve fuel economy, and decrease exhaust emissions has led to a growing research interest in understanding and discovering new intermetallic compounds that contain light metals, i.e., Al and Mg.

In general, studying the intermetallic phases of known compounds is an important subject in metallurgy. To create advances in the understanding and discovery of new intermetallic compounds, it is also desirable to employ other subjects, such as solid state chemistry. The synthetic tool box for intermetallic compounds contains many powerful techniques. These techniques, such as arc melter and induction heating, involve very high temperatures [159] that pose a serious limitation for these methods. High temperatures usually produce the most thermodynamically stable product and leave little room for kinetic control because of the high energies involved [159]. For this reason, methods that permit reactions to be carried out at lower temperatures are preferable. A molten metal flux is a good example of such a method. Metal flux has been highlighted as an important tool for the exploration of intermetallic compounds. It has also been used as a medium for the synthesis of a new class of intermetallics. This approach allows the discovery of new materials as well as the growth of large crystals of known materials [159]. The method for synthesizing alloys in this approach is simply to mix appropriate metals that will act as flux. The aim is to lower the melting point of the solvent by forming eutectics. Moreover, a mixed flux introduces an additional avenue for controlling the reaction chemistry [29]. It is not necessary to completely dissolve the elemental components of the desired product when using the metal flux methodology, as the flux will act as a transportation

medium that can dissolve a component in one location while the product grows at another location in the sample container [159].

Among the different fluxes used as media for the growth of single crystal phases, Al has been shown to be useful in the synthesis of several interesting intermetallic compounds, due to its good characteristics. It has a low melting point (660 °C) and can dissolve a large number of elements. It dissolves readily in non-oxide acids. A large variety of intermetallic aluminides have been prepared from liquid Al, and many of them feature fascinating new structures. Many of these intermetallic aluminides are also key components in advanced Al alloys [160-162]. In particular, use of an Al / Mg mixture is of practical interest [162]. The Al / Mg phase diagram exhibits a wide, low melting range (40 – 60 at.% Mg, ~ 450 °C) between two binary phases (Mg_2Al_3 and $Mg_{17}Al_2$) [162]. Moreover, Al / Mg mixtures have proven to be good solvents for the synthesis of silicides such as $CaMgSi$ and $R_5Mg_5Fe_4Al_{12}Si_6$ [29, 161].

In light of the information presented above, knowledge of the solidification process and of crystallization within molten Al is required. Here, the synthesis of technologically important phases from an Al metal flux is presented. Then, an APT technique is applied to shed light on the growth mechanism of the different synthesized products.

3.5.1 Materials and methods:

Synthesis: Appropriate quantities of Al sheet (99.9%) obtained from (Sigma Aldrich), Mg metal slugs (99.9%) obtained from (Sigma Aldrich), metallic Ca shots (99.9%) obtained from (Acros Organics) and a Si wafer (99.9 %) obtained from (SVM) were weighed out in a 15 / 15 / 3 / 3 : Mg / Al / Ca / Si mmol ratio in an N_2 glove box and placed in a Ta crucible (Figure 3.55). The Ta crucible was welded shut using an arc-melter (Edmund Buhler Gmbh). After the welding was completed for both sides of Ta crucible, it was placed into a quartzite ampule. The Ta crucible was used to prevent Al vapor from attacking the quartzite, which would lead to loss of the protective atmosphere. After placing the Ta crucible in a sealed, evacuated quartzite ampule and slightly elevating it off of the bottom of the ampule by shaking the quartzite ampule, the ampule was gently placed into an electric furnace. The sample was heated from room temperature to 950 °C and held for 5 h, cooled to 750 °C over a period of 60 h and then held at 750 °C for 20 h, at which point, the reaction tubes were removed

from the furnace. A chart illustrating this temperature program is shown in Figure 3.56. The tube was then quickly inverted and quenched in cold water. It is worth mentioning that stoichiometric reactions cause the formation of a multi-phase product composed of $CaMgSi$, Mg_2Si and Al_2Mg.

Figure 3.55 Used Ta crucible for synthesize.

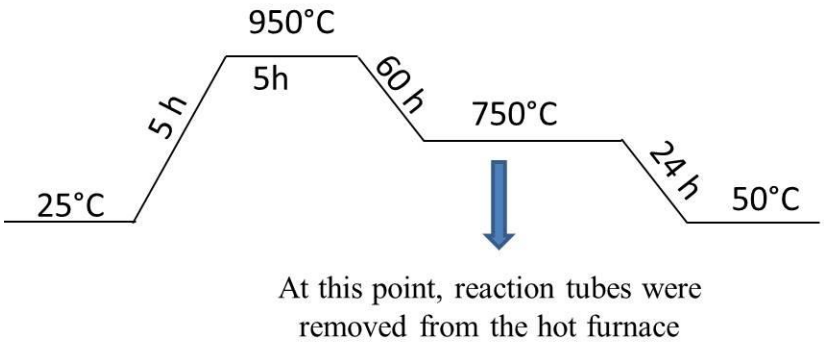

Figure 3.56 Illustration Chart of the applied temperature program.

Elemental analyses: Samples for SEM – EDX analysis were prepared via a standard metallurgy procedure described in section (2.2). An additional step is added where the sample is polished using a cloth and diamond paste with a size of 6, 3, 0.5, 0.2 and 0.1 um, respectively. The samples were then ultrasonically cleaned using acetone. The samples were examined using an SEM (Quanta 200) equipped X – ray spectroscopy (EDX). X – Ray diffraction was carried out after the samples were prepared using the

procedure described in section (2.7). The analysis was carried out using a STOE STADIMP powder diffractometer using $CuK\ \alpha_1$ – radiation operated at 40 kV.

Hardness test: The mechanical properties of the synthesized material have been tested using hardness measurements. Hardness tests were performed using a nano-indentation system (Nano test Vantage) with a load of (200 mN) and dwell time of (10 s). The hardness value has been estimated by averaging the values of 8 measurements taken at different locations in the sample.

APT analysis: Preparation of APT-tips has been done using the FIB method. FIB-based, site-specific specimen preparation was used, as described in section (2.1.2) by using Helios FEI. APT experiments were performed in a Cameca LEAP 4000 HR using a laser pulse mode. (Experimental details for the laser mode can be found in section 3.4.1.) The best analytical parameters were chosen by performing different test analyses. The best parameters for analysis are found to be 50 pJ for the laser pulse energy and 50 K for the base analysis temperature. The detection rate was set to 0.01 ions per pulse. The location of laser spot on the specimen was monitored using a charge – coupled device (CCD) camera. Data reconstruction was carried out using the IVAS software. Optimization of reconstruction parameters was based on the SEM images. The field strength of evaporation was determined using Eq. 2.1 in which the radius of the tip apex (r) was measured using the SEM image, and the value of the voltage (V) at which the field evaporation takes place is known from the APT analysis.

3.5.2 Basic characterization:

The XRD diffraction pattern for the synthesized material is shown in Figure 3.57. The acquired diffraction pattern was found to match the calculated patterns for Al_2Mg, Mg_2Si and $CaMgSi$. An optical micrograph of the microstructure is shown in Figure 3.58. Areas of different contrast are readily seen in the image, and they indicate the presence of different phases within the microstructure.

SEM / EDX analyses were used to quantify the different phases that exist in the material. Selected pieces of synthesized material were arranged on double-sided carbon tape adhered to an Al sample puck. An example of an SEM micrograph is shown in Figure 3.59. Using EDX analysis, the several phases that exist in the

synthesized material were identified as: $AlMg$, Al_2Mg, Mg_2Si and $CaMgSi$. The existence of multiple phases in the microstructure can be explained as follows; as mentioned above, the use of a stoichiometric reaction does not result in the formation of a pure single crystalline phase but instead yields a mixed phase powder composed of $CaMgSi$, Mg_2Si and Ca_2Si [29]. Reactions carried out in pure Mg flux do not usually yield any of the title compounds, such as $CaMgSi$. However, the addition of Al may promote this reaction. Al usually acts either as a transport agent within the flux, or as a solvent for the incorporation of elements that have low solubility in molten Mg. Al metal has been shown in the literature to be a highly reactive solvent that facilitates the growth of aluminide intermetallics [163]. According to the EDX analysis that was applied to different regions of the sample and is presented in Figure 3.59, Al exists in the matrix in the form of $AlMg$ and Al_2Mg, and the incorporation of Al atoms into the observed products, such as $CaMgSi$ and Mg_2Si, was not recorded.

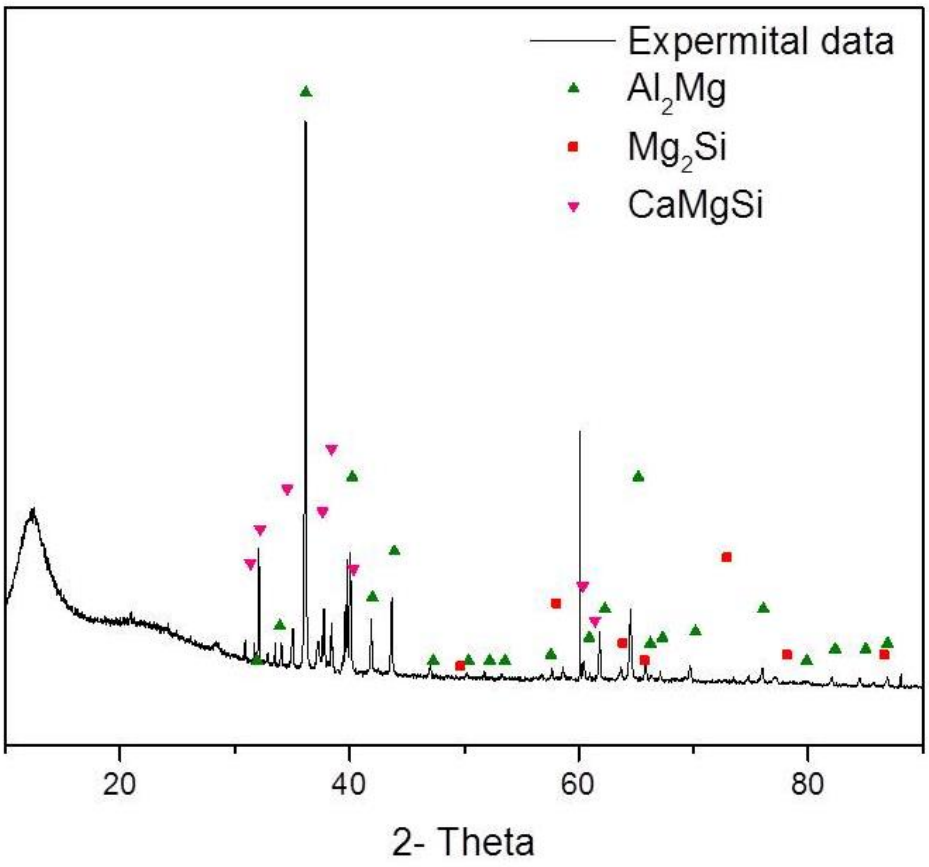

Figure 3.57 XRD diffraction pattern for the synthesized material.

Figure 3.60 shows a magnified SEM image of the synthesized material. Parts of crystals of $CaMgSi$, which are apparent as broken fragments, are shown in this figure along with some amount of the Mg_2Si, Al_2Mg and $AlMg$ phases. EDX analyses of several surfaces on the $CaMgSi$ regions show an average atomic percent composition of 33.8 at.% Ca, 32.35 at.% Mg, 30.95 at.% Si and 2.09 at.% Al, while the average atomic percent composition of Mg_2Si was determined to be 64.39 at.% Mg, 34.27 at.% Si, 0.19 at.% Ca and 1.15 at.% Al. The chemical compositions of the other surrounding regions measured by EDX analysis were found to be 60.03 at.% Al, 36.34 at.% Mg, 3.53 at.% Ca and 0.1 at.% Si, which closely matches the Al_2Mg composition (represented by the light gray region in the SEM micrograph in Figure 3.60), and 52.10 at.% Al, 46.86 at.% Mg, 0.76 at.% Ca and 0.28 at.% Si, which closely matches the $AlMg$ composition (represented by the dark gray region in the SEM micrograph in Figure 3.60). In general, the separation of a single crystal phase from the surrounding flux or matrix has been carried out by centrifugation or by dissolving the excess flux in sodium hydroxide (NaOH) because the Al can be eaten away by NaOH [164]. Dissolving the excess flux or separating out a crystalline product is outside the scope of this study, and so a powder composed of multiple phases was used instead.

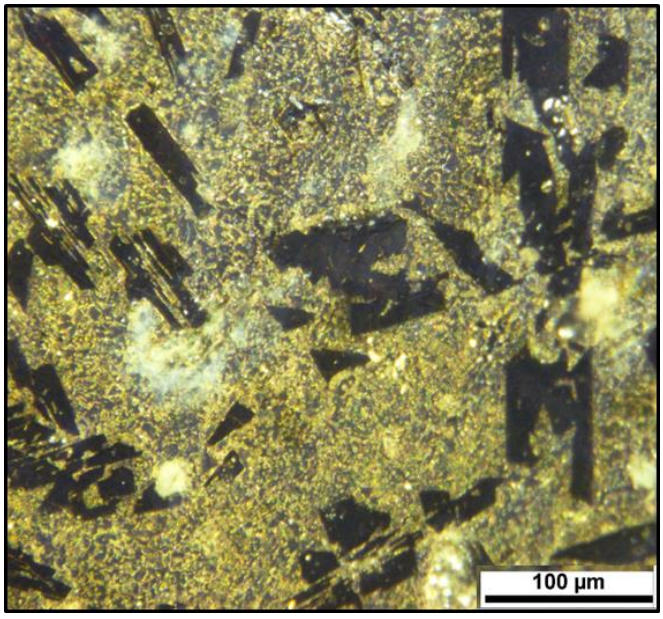

Figure 3.58 Optical micrograph of the microstructure of the synthesized material.

The correlation between the microstructure and the mechanical properties is also of great interest, as the ternary system of Al, Mg and Si is known to have excellent age – hardening characteristics [165]. Moreover, alloying Al/Mg elements with SiC particles has been recorded to yield a good ultimate tensile strength of 250 ± 6 MPa [166]. In our study, the evaluation of the mechanical properties of the synthesized material has been based on its hardness properties. According to the hardness measurement, the material has a relatively high hardness value (2.8 ± 1 GPa), which indicates good mechanical behavior. In this context, investigation of the microstructure of the synthesized material at an atomic scale is promising. Through such an investigation, the correlation between the macroscopic and microscopic properties can be understood. Moreover, an atomic scale investigation will allow the transition between different phases to be followed.

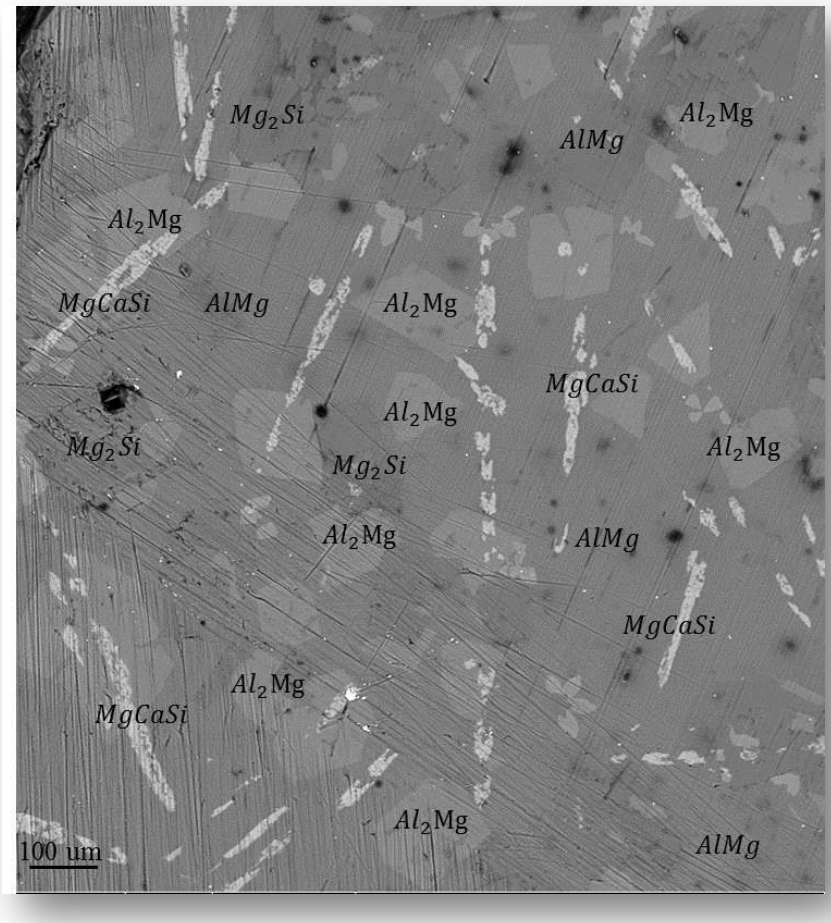

Figure 3.59 SEM micrograph of the microstructure of the synthesized material.

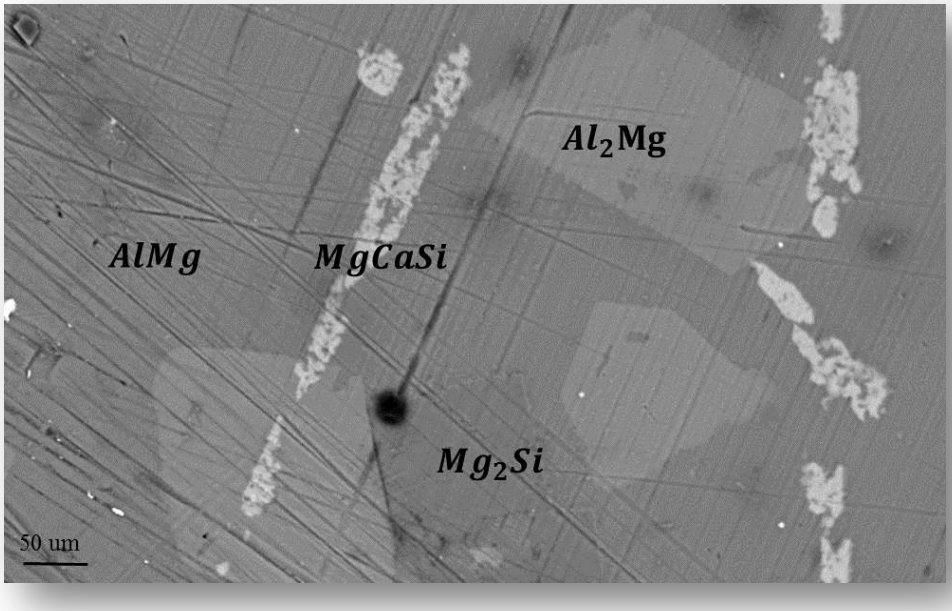

Figure 3.60 A magnified SEM image of the synthesized material showing the appearance of different phases: $CaMgSi$, Mg_2Si, Al_2Mg and $AlMg$.

3.5.3 APT analyses:

Knowledge of the mechanisms that govern the growth of a single crystal product from a molten flux is limited. Therefore, the APT technique is used to investigate this mechanism. As described in section (2.1.2), the first step in preparing an APT needle – shaped specimen using site-specific FIB preparation is to select an area of interest. Figure 3.61 shows the areas on the sample that have been selected for subsequent analysis using APT.

The first APT experiment was devoted to analyzing the matrix or flux region (Figure 3.62). The radius of the tip apex was estimated to be approximately 50 nm (Figure 3.62(a)). Using Eq. 2.1, the field evaporation strength was determined to be 17.3 V/nm. The data set measured is a collection of 5 million atoms (Figure 3.62(b)). The data quality was assessed by observing the desorption map, the mass spectrum and the chemical composition. Figure 3.62(c) shows the desorption map, the hit map that forms during analysis, of the data set in Figure 3.62(b). It is clear from Figure 3.62(c) that the hit density at the detector is almost homogenous, which indicates that the atoms are field-evaporated from the specimen in a highly controlled order. The mass spectrum for this data set is shown in Figure 3.62(d). The quality of the mass

spectrum is good, and the corresponding peaks for the detected ions are clearly resolved and identified. An accurate chemical composition for the whole reconstructed volume shown in Figure 3.62(b) is given in Table 3.7. The distribution of impurity atoms such as Si and Ca in the Al/Mg flux is shown in the 3D atom map in Figure 3.62 (b).

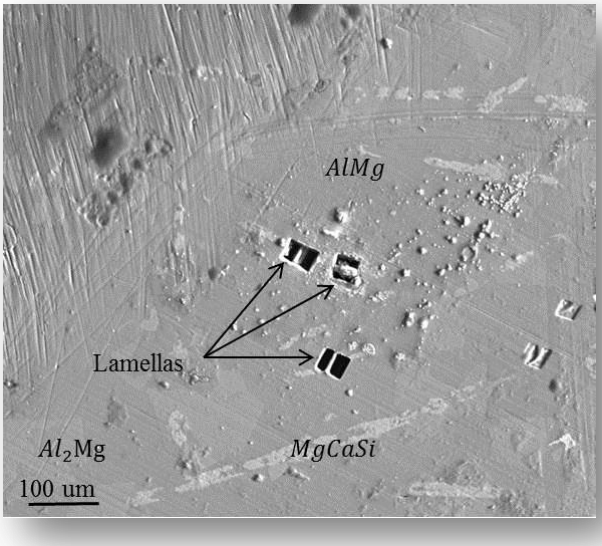

Figure 3.61 SEM micrograph shows the selected areas of interest for the subsequent APT analysis.

Transitioning from the matrix Al/Mg or the flux region toward a single phase region of Mg_2Si comprises the next step of the analysis. In this case, lamella that has been extracted from the sample to prepare an APT tip was selected from the Mg_2Si region (Figure 3.63(a)). Performing APT analysis for this tip yielded a collection of 20 million atoms (Figure 3.63(b)). In this case, the field evaporation strength was estimated, using the tip apex radius, to be 24.2 V/nm. Once again, the desorption map in Figure 3.63(c) and the mass spectrum in Figure 3.63(d) demonstrated that the APT data set is of good quality. The chemical composition of the whole reconstructed volume is shown in Table 3.7. This chemical composition is in fairly good agreement with that obtained via EDX analysis. The distribution of impurity atoms of Al and Ca is also shown in Figure 3.63(b).

Table 3.7 A summary of the phases observed in the synthesized material and their chemical composition.

Name of the phase	Al (at.%)	Mg (at.%)	Si (at.%)	Ca (at.%)
$AlMg$	47.1	47.71	3.7	1.41
Mg_2Si	0.08	66.3	33.4	0.06
$CaMgSi$	0.1	33.5	34	32.4

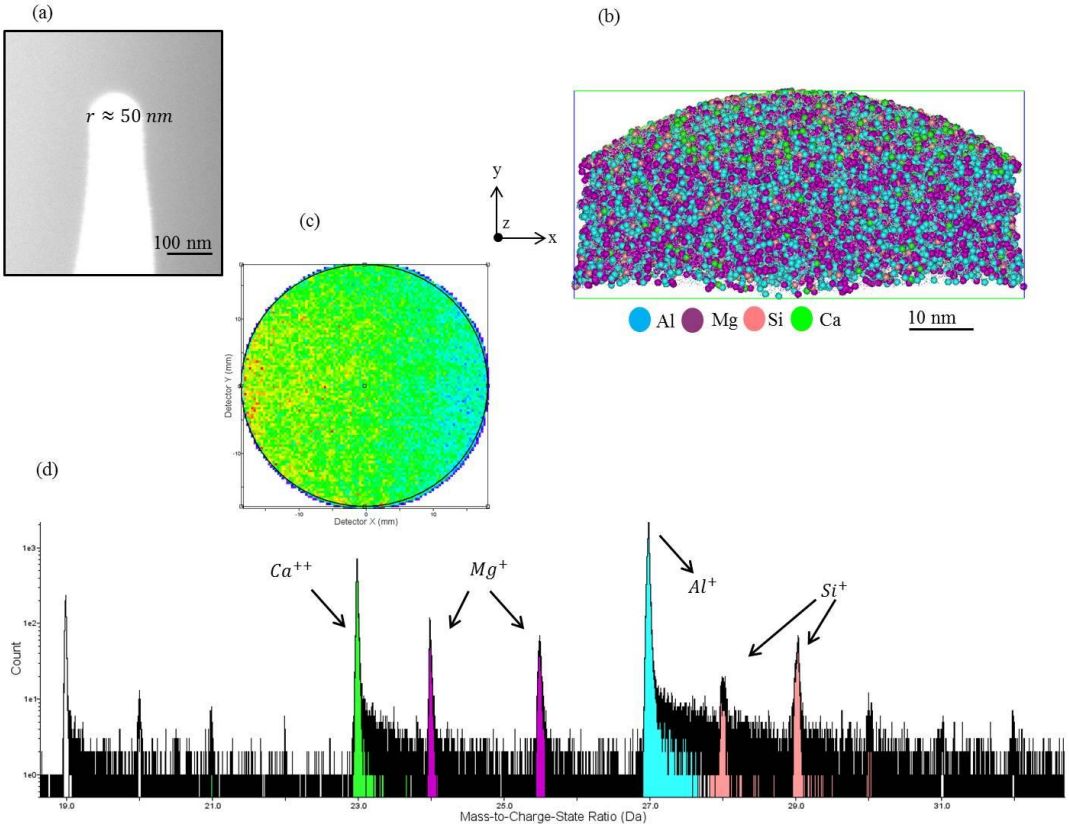

Figure 3.62 APT analysis of the flux region. (a) SEM micrograph showing the measured radius at the apex of the prepared APT tip. (b) The reconstructed volume showing the distribution of different elements. (c) The desorption map. (d) The corresponding mass spectrum.

To understand the growth mechanism, it is important to perform APT analysis in an area of the sample that contains both flux and intermetallic phases. In this case, the position for cutting the lamella was selected to include the area of at the interface between the phases and the flux. The top view of the reconstructed volumes of the analyzed tips that was prepared from selected areas in Figure 3.61 is shown in Figure 3.64. In this case, the presence of different phases is clearly visible.

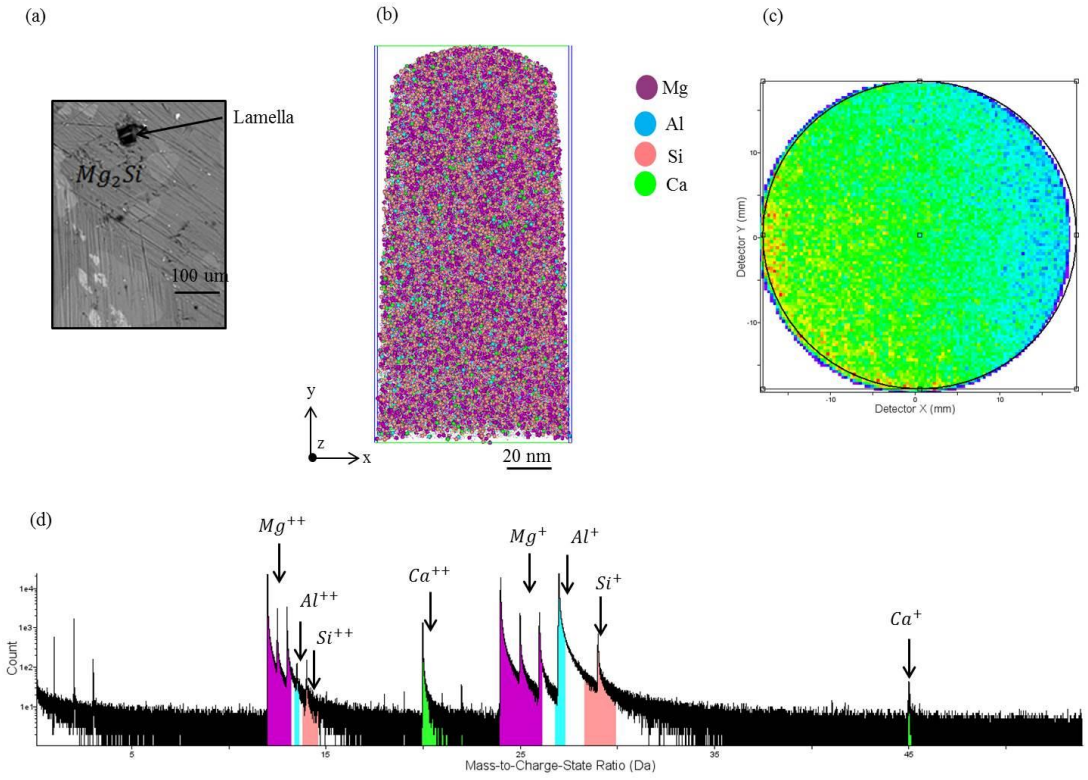

Figure 3.63 APT analysis of the Mg_2Si region. (a) SEM micrograph showing the position of the lamella for the prepared APT tip. (b) The reconstructed volume showing the distribution of different elements. (c) The desorption map. (d) The corresponding mass spectrum.

The APT analysis for the region corresponding to the $CaMgSi$ phase is shown in Figure 3.65. In this case, the distribution of Al was not observed. This observation confirms the idea that Al does not incorporate into the final product. The chemical composition of the reconstructed volume is shown in Table 3.7.

To follow the transition between these phases, different small volumes from the reconstructed volumes in Figure 3.64 were cut and quantified individually. Quantification of the chemical composition was done using the concentration depth profile described in section (2.1.5.2). A series of the small cutting volumes together with their corresponding depth concentration profiles are shown in Figure 3.66. According to the depth concentration profiles drawn from the Figure 3.66(a), the chemical compositions for the observed phases have been identified as Ca_2Si and Al_2Mg. For the observed phases in Figure 3.66(b), the depth concentration profile shows that theses phases are corresponding to $AlMg$ and gSi . Moreover, there is one region in the reconstructed volume represents the presence of Mg_2Si phase according to the depth concentration profile (Figure 3.66(c)).

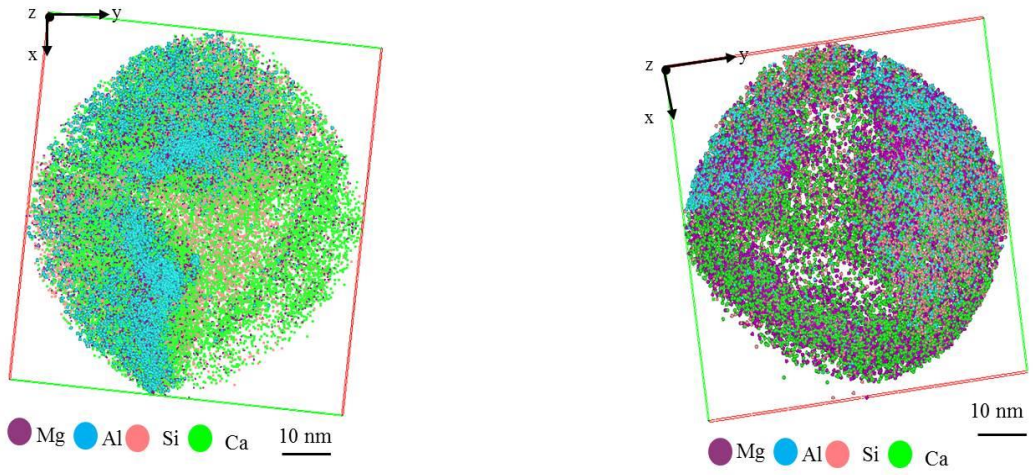

Figure 3.64 APT analysis of the interface region between the flux and single crustal phase. The top view of the reconstructed volumes illustrates the distribution of different phases.

A eutectic flux composed of Mg and Al solidifies at 450 °C, but above this temperature it becomes very viscous and difficult to remove. This could explain the presence of both $AlMg$ and Al_2Mg phases (Figure 3.66(a, b)). Before the crystallization of $CaMgSi$ takes place, the formation of a solid solution between Mg_2Si and Ca_2Si is also observed (Figure 3.66(a, c)). The probability of forming this solid solution was investigated theoretically using density functional theory (DFT) [167]. In this study, the authors reported the substitution of Mg atoms in the Mg_8Si_4 unit cell with Ca atoms and substitution of Ca atoms in the Ca_8Si_4 unit cell with Mg atoms, which clarified the possible formation of an $Mg_2Si - Ca_2Si$ solid solution.

Theoretical investigation of this system also confirmed that $CaMgSi$ of the Ca_2Si-type, where all of the Ca atoms that occupy one type of 4c site are completely substituted by Mg and all other 4c sites remain occupied by Ca, is energetically quite stable. The APT analysis presented in Figure 3.66 proposes that the transition path is happening in which solid solution of Mg_2Si and Ca_2Si reacts with *AlMg* phase. It can be expected that the transition produces the $CaMgSi$ phase through an intermediate $Mg_2Si - Ca_2Si$ solid solution. It has been reported that $CaMgSi$ is the only equilibrium phase in the $Mg_2Si - Ca_2Si$ pseudobinary system [167].

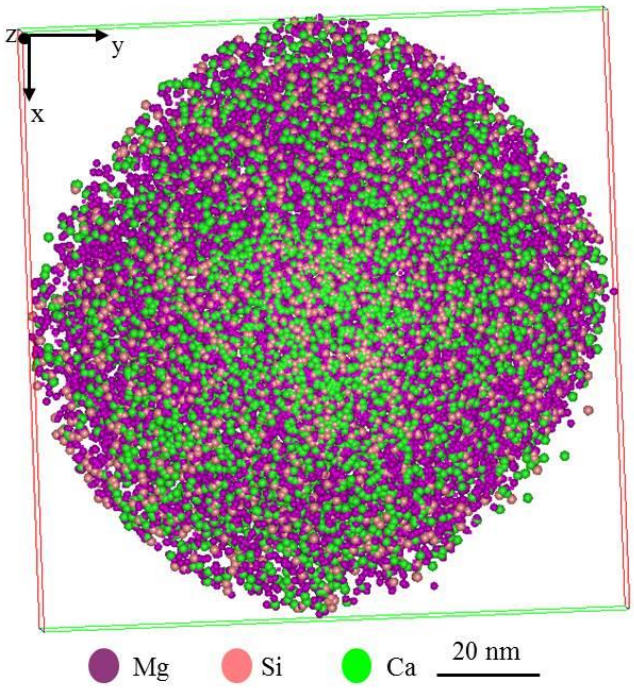

Figure 3.65 APT analysis for the at $CaMgSi$ phase region.

Based on this quantitative APT analysis above together with the DET study [167], the transition from the molten flux to the single crystal phase of $CaMgSi$ can be summarized as follows:

$$AlMg + Al(l) + \quad Mg_2Si + Ca_2Si \longrightarrow Al_2Mg + 2CaMgSi$$

From the SEM micrograph (Figure 3.60) and the above quantitative APT analysis, it seems that the processed reaction to form a single phase of *CaMgSi* is peritectic reaction, in which the two solid phases in equilibrium and the transition has been

performed from solid and liquid phases to different solid phases. However, the shape of *CaMgSi* phase dose not matches the recorded shape of this crystal [29]. This might be explained in the term of short annealed time resulting in uncomplete shape of this crystal.

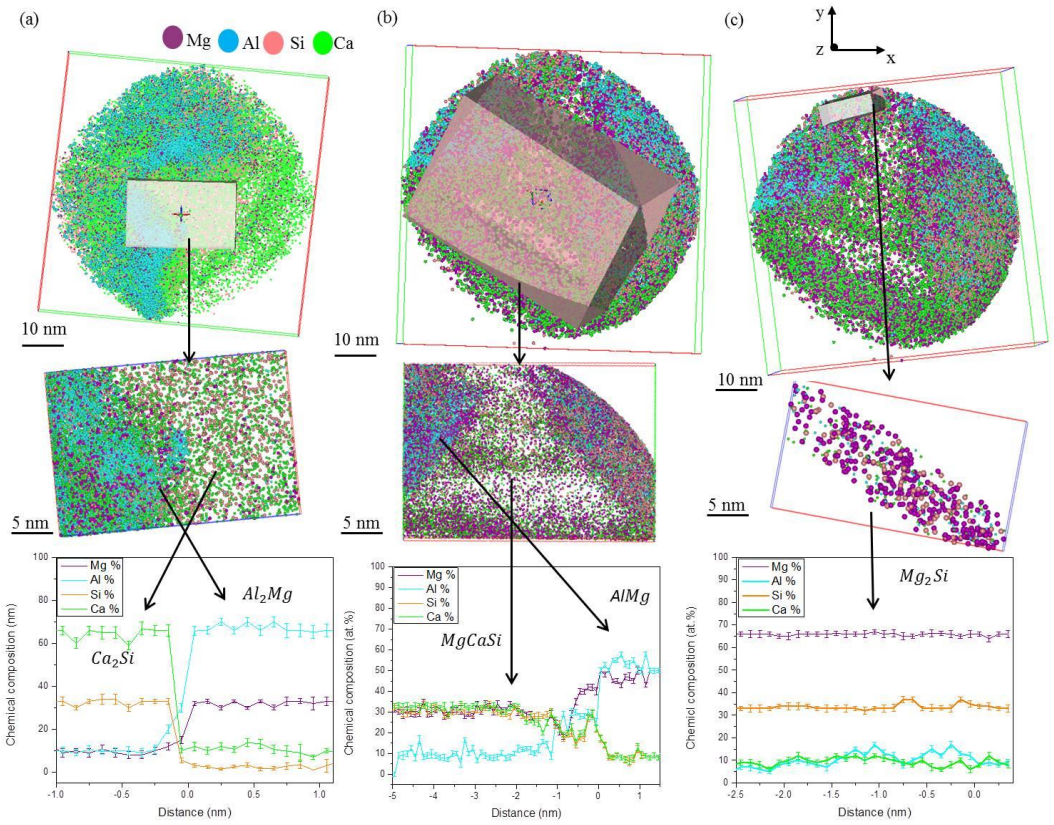

Figure 3.66 A series of the small cutting volumes together with their corresponding depth concentration profiles. (a) At Ca_2Si and Al_2Mg phases. (b) At $AlMg$ and $CaMgSi$ phases. (c) At Mg_2Siphase.

The presence of this mixture of phases in the microstructure, in addition to the distribution of impurity atoms, is responsible for the good hardness characteristics of our synthesized material.

As mentioned above, alloying Al with light elements such as Ca, Mg and Zn usually results in interesting microstructure and produces a material that can be applied in a wide range of applications. On this basis, different Al – Cu – Zn alloys with different nominal compositions and different levels of hardness have been synthesized. A detailed analysis of Al – Cu – Zn alloys is included in Appendix B.

3.5.4 Conclusion:

The great potential of Al liquid as a powerful solvent for the synthesis of important intermetallic phases is demonstrated. Different important phases such as: Mg_2Si, Al_2Mg and *CaMgSi* have been synthesized. The APT technique provides critical knowledge of the nano-scale evolution of microstructure. Intermediate steps in the mechanism of the flux – grown intermetallic phases were investigated. The proposed path of the reaction is:

$$AlMg + Al(l) + \quad Mg_2Si + \ Ca_2Si \longrightarrow \quad Al_2Mg + 2CaMgSi.$$

The processed reaction to form a single phase of *CaMgSi* is peritectic reaction, in which the solid phase of $AlMg$ is reacted with liquid Al and solid solution of Mg_2Si – Ca_2Si to produce other intermetallic phases, i.e. Al_2Mg and *CaMgSi.*

A combination of physical metallurgy and solid state chemistry might use as a direct approach to improve the production of Al alloys.

Chapter 4

Summary and Future Work

In this chapter, a summary of the most relevant findings and achievements of this research will be presented. An overview of future research will also be given. In general, the major results discussed in this dissertation will be outlined, along with several approaches for future work.

4.1 Summary:

This research focuses on an experimental investigation that reveals the link between the physical properties (hardness behavior) and the arrangement of different constituent species in a complex aluminum alloy at an atomic scale. Knowledge of thermodynamics and phase separation in Al alloys can be used to improve the macroscopic properties of these functional materials.

A comprehensive study of the precipitation behavior of an Al alloy has been performed to understand the precipitation – hardening mechanism. A complex Al alloy that has an important role in modern engineering was shown to be improved when an optimistic thermomechanical condition was applied. The following points summarize the most relevant achievements of this research.

- A detailed analysis of the correlation between the microstructural developments caused by the treatment conditions and the hardening process revealed that:

I. Applying a T4 heat treatment condition causes enrichment of the β'/ matrix interface with Li, Cu and Mg atoms. On this basis, the β' phase demonstrates its potential role in the nucleation mechanism for the most important strengthening phase, T_1, under these conditions. The β' phase also contributes to the hardening behavior of the specimen treated with this common industrial heat treatment.

II. Using a T8 heat treatment condition causes a fine distribution of the $\theta'$and T_1 phases within the microstructure. Moreover, suppressing the movement of dislocations due to the intersection of different T_1 platelets causes a good

hardness response in this condition. Growth of the T_1 platelets and absence of the θ' platelets were observed upon increasing the aging time, suggesting the occurrence of phase transformation.

III. Finally, it has been shown that applying a T6 heat treatment condition changes the nucleation mechanism of the T_1 phase. In this case, the T_1 phase nucleates on Mg-enriched regions that contain localized Ag atoms.

- Presented data highlight the role of the industrial heat treatment on the developing of the microstructure, along with an in depth study of distribution of different alloying elements in the strengthening phases. A detailed analysis of the correlation between the microstructure developments owing to the respective treatment condition and the hardening process utilizing different experimental techniques allowed integrity between different techniques. A very good agreement has been found on the obtained results from different methods.

- The APT technique is used to resolve chemical composition of the thin platelet precipitates (less than 2 nm):

I. The measured θ′ stoichiometry is consistent with the expected (Al_2Cu) equilibrium composition, and shows significant partitioning of Li atoms in this phase.

II. The T_1 phase shows deviation from the stoichiometric (Al_2CuLi) ratio of the bulk phase.

III. The T8 condition corresponds to a thermodynamic non-equilibrium condition. The microstructure observed in the T8 condition has an appreciable super-saturation of defects, which suggests that the nucleation and growth of different phases are still at their intermediate stages.

- The ability to create a robust microstructure with superior mechanical properties by applying a low-energy, cost effective method is demonstrated.
- The APT approach, together with the binomial frequency distribution have been proposed to investigate the early stages of decomposition of the microstructure of different alloys with different nominal compositions:

I. The decomposition of an Al – Cu alloy is shown to start after a relatively long aging time (8 h) at low aging temperature (160 °C).

II. Combination of both natural aging conditions and artificial aging conditions induces increasing on the number density of the Li clusters and hence increase number of precipitated δ' particles during the decomposition process in an Al – Li alloy.

III. The decomposition process in a ternary Al – Cu – Li alloy starts with the formation of Cu – rich precipitates.

IV. Increasing Li concentration in a ternary Al – Li – Cu alloy shifts the decomposition path so that it starts with Li – rich precipitates.

- Systematic investigation of the microstructural change of δ' precipitates influenced by different pulsed laser energies has been used to investigate the actual specimen temperature during laser APT analysis:

I. Influence of ultrafast laser pulses on the microstructure was investigated in terms of variations in the diameter d, number density N_v, volume fraction f and composition c_p of the δ' precipitates.

II. Estimation of the diffusion length and the diffusion coefficient of Li atoms from δ' precipitates has been used to estimate the temperature increase in the sample using UV laser illumination.

- By employing different laser energies, APT is presented for the first time in a series of snapshots that show the *in-situ* reversion of a $\delta'(\mathrm{Al_3Li})$ precipitate to be initiated by laser irradiation.
- The APT technique has been applied to investigate the growth mechanism of synthesized intermetallic phases.
- The involved reaction between the flux and the grown intermetallic phases has been identified.

4. 2 Future work:

At the end of this work, some future research paths are suggested to improve future understanding of the precipitation behavior of complex Al alloys. These suggestions are presented in the following sections:

1- The approach presented, which combines mechanical strategy with an intelligent microstructure design, must be extended to achive better engineering of other complex alloys. The main goal is to create an Al alloy that possesses superior

mechanical properties and that can be prepared with cost-effective and low-energy methods.

2- The influence of chemical composition and heat treatment conditions on precipitation kinetics is an area where much research is needed. Even a slight modification of alloy composition or heat treatment conditions alters the whole picture of precipitation phenomena. Synthesis and analysis of a large variety of Al alloys that contain light elements, have different chemical compositions and are subjected to different heat treatment conditions are recommended. The Al phase diagram should be used as a guideline for designing the alloy's composition and selecting the appropriate heat treatment conditions.

3- Understanding the mechanism of the laser pulse mode in APT is an important challenge that also has to be overcome. The proposed method uses systematic investigation of the microstructural changes induced by laser irradiation, and can be extended. Microstructure evolution can be used to understand the laser – material interaction in pulsed – laser APT.

4- New intermetallic compounds with predictable properties can be synthesized using an Al molten flux. The APT technique can then be used to reveal the link between the arrangement of atomic species and the properties of the new synthesized material.

Appendixes

Appendix A

Influence of laser pulse mode on the microstructure of Al alloys

In Section 3.4, the systematic investigation of the microstructure changes of relatively large δ' particles (~14 nm) revealed that the interface reaction that occurs during laser APT analysis can be used as a simple probe for investigating the actual tip temperature. The decision to investigate this particular microstructure was made after first performing different test laser APT analyses on the Al-8.2 at.% Li alloy after heat-treating it according to the 3S conditions specified in Table 3.3 (see Figure A.1). The original microstructure of this sample was found to contain clusters of Li atoms (Figure 3.40), and irradiating this microstructure with a laser confirms the presence of these clusters (Figure A.1). Judging the effects of a laser pulse on such microstructures can be very difficult due to the similarity of the nano-features before and after laser irradiation. For this reason, microstructures containing larger particles are preferable for this investigation.

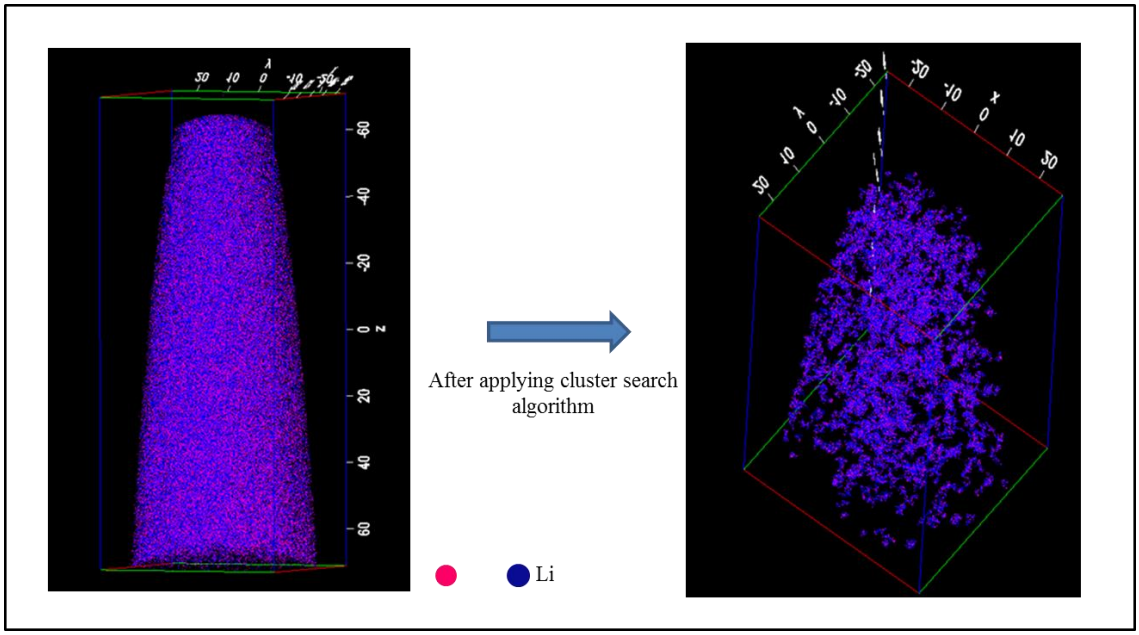

Figure A.1 Laser APT analysis of the Al-8.2 at. % Li alloy showing the presence of small clusters of Li atoms in the microstructure.

The effects of the laser pulse on the microstructure of the complex Al alloy heat-treated under T8 conditions is clearly visible in Figure A.2. In this case, all of the observed platelet precipitates disappeared. A non-uniform distribution of all of the alloying elements was also recorded. This observation was due to an increase in the tip temperature under laser illumination during APT analysis. Obviously, an unexpected heat treatment occurred; to minimize the possibility of this occurring in subsequent experiments, all APT analyses of the Al alloys were performed using voltage pulse mode.

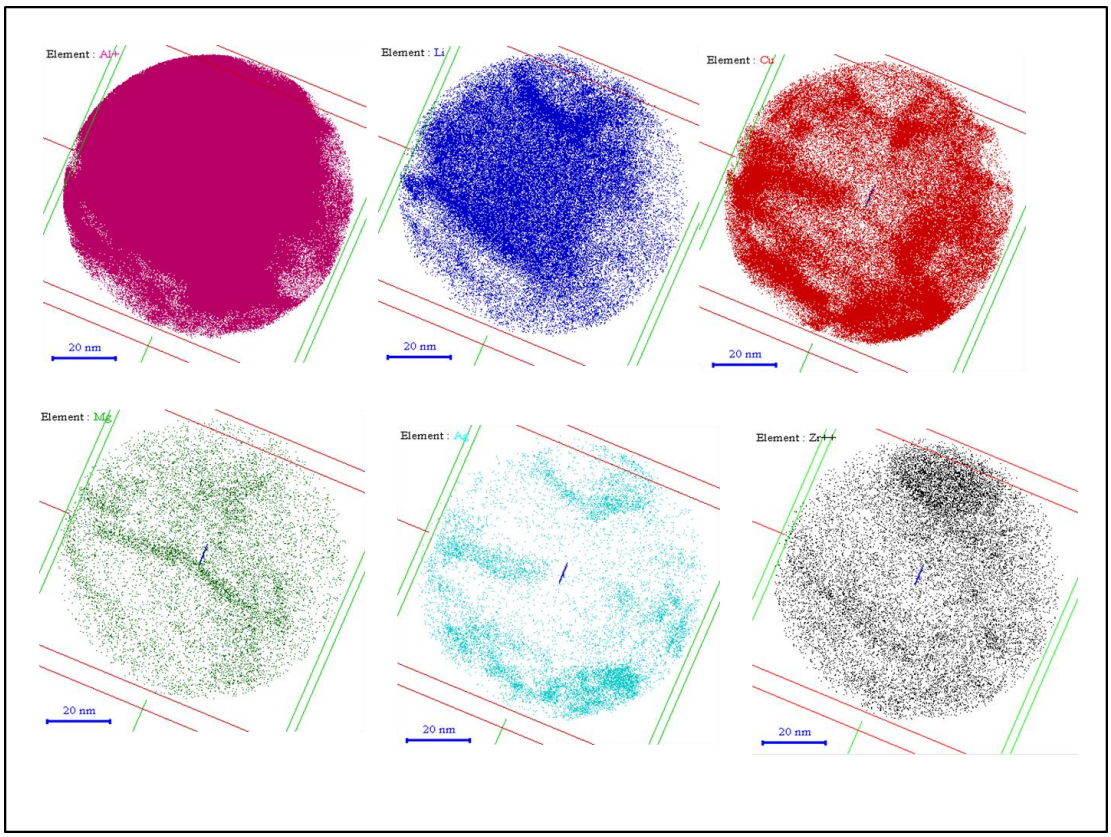

Figure A.2 Top view of the reconstructed volume of laser APT analysis of the AA2195 showing the damaging effects of the laser on the microstructure.

Appendix B

Synthesis of Al – Cu – Zn alloys

As mentioned in Table 1.1, Al alloys may be categorized into different series according to the main alloying elements used for producing each. Pure Al alloys are designated as 1xxx. This series of alloys has very low strength compared to the other series of alloys. Thus, the addition of alloying elements to Al is the principle method employed for producing a selection of different Al-based materials that are used in a wide array of structural applications. There are seven designated Al alloys series used to categorize wrought alloys. These series are 1xxx, which contains Al at 99.9% or higher purity; 2xxx, for which the main alloying element is Cu; 3xxx, where the main alloying element is Mn; 4xxx, in which the main alloying element is Si; 5xxx, or Al mainly alloyed with Mg; 6xxx, in which Mg and Si are both main alloying components; and 7xxx, where the main alloying element is Zn. Investigations of the 2xxx series have shown that Al-Cu alloys typically provide a substantial increase in strength and also facilitate precipitation hardening. Adding Cu to Al, unfortunately, can also reduce its ductility and corrosion resistance. The addition of Zn to Al produces heat-treatable Al alloys with high strength. These alloys can be susceptible to stress corrosion cracking, however, and are not fusion welded. To improve the mechanical properties of Al-Zn alloys, Cu may be introduced into the mix as a highly effective second alloying element. Despite their promise, Al-Cu-Zn alloys are practically absent from industrial applications, and hence, our purpose in this study was to synthesize several Al-Cu-Zn alloys with varying chemical compositions and to investigate their hardness behavior and their microstructure.

Experimental procedure:

One binary Al-Cu alloy containing 33 at.% Cu and three ternary Al-Cu-Zn alloys with compositions of 30 at.% Cu and 20 at.% Zn, 10 at.% Zn, and 4 at.% Zn were prepared from high-purity Al, Cu and Zn. The alloys were melted in a glass carbon crucible, as shown in Figure B.1, and the crucible was then placed in a vacuum sealed quartzite ampule and heated up in an electrical furnace to 800 °C by ramping the temperature over a period of 12 h. The ampule was kept at 800 °C for 183 h and then

quenched in cold water. The conditions employed in this heat treatment step are referred to as as-cast condition and are illustrated in Figure B.2. The second step in the overall heat treatment sequence involves annealing the synthesized alloys at elevated temperature. This was accomplished by heating up the alloys to 500 °C over the course of 6 h, keeping them at 500 °C for 336 h, and finally quenching them in cold water. Samples that have undergone this heat treatment step are considered to be in annealed condition; this is illustrated in Figure B.3.

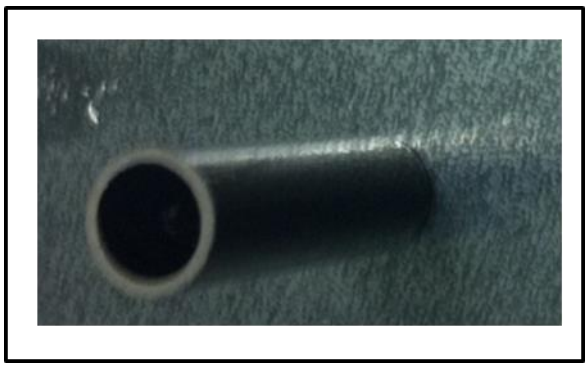

Figure B. 1 Image of glass carbon crucible.

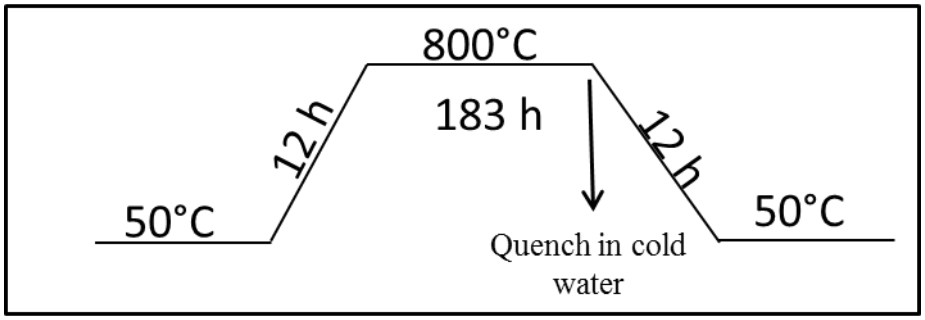

Figure B. 2 Illustration Chart of the as-cast condition.

It is worth noting that several attempts to optimize the synthesis of the Al-Cu-Zn alloys were made with mixed results. For example, the binary Al-33 at. % Cu alloy was successfully synthesized using the arc-melter method (Edmund Buhler Gmbh) (Figure B.4), but making Al-Cu-Zn alloys by the same method proved unsuccessful (Figure B.4). The difficulty in making Al-Cu-Zn alloys by the arc-melter method derives from the low melting point of Zn (419 °C) compared to that of Cu (1083 °C). The significant difference in these two melting points results in the evaporation of the Zn before Cu even starts to melt. Moreover, at high temperatures, the liquid Zn that has boiled away forms an oxidized vapor. Several trial alloy syntheses were also

performed with different types of crucibles to ensure the type of crucible chosen would not interfere with alloy formation. It was found that using a Ta crucible to make Al-Cu or Al-Cu-Zn alloys, for instance, results in a reaction between the alloying elements and the wall of the crucible such that extra peaks corresponding to Ta compounds are detected in the XRD pattern of the resultant material.

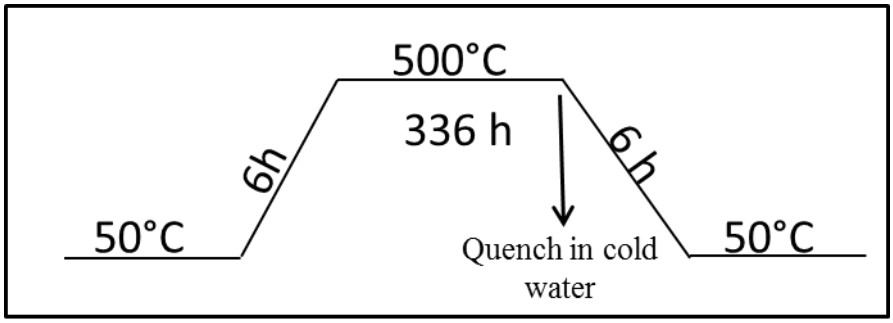

Figure B. 3 Illustration Chart of the annealed condition.

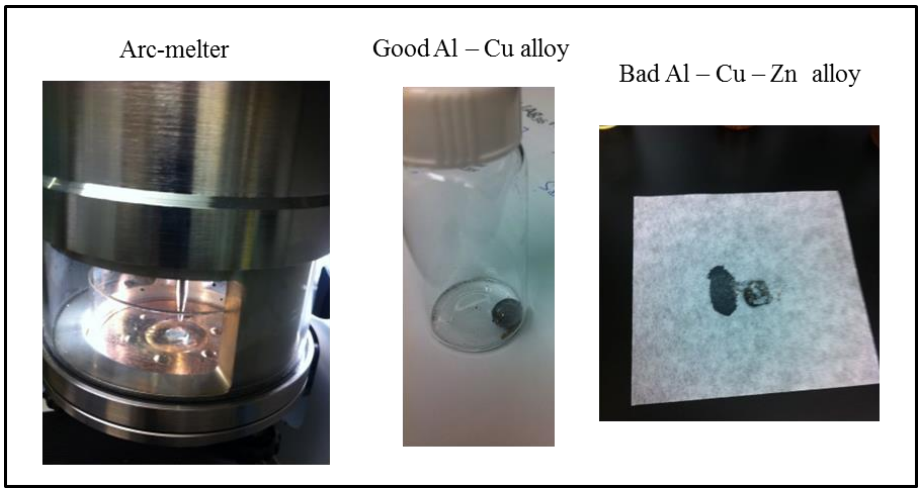

Figure B. 4 synthesis alloys by using arc-melter method yielded good Al – Cu alloy and unsuccessful Al – Cu – Zn alloy.

After the alloys reported in this work were successfully synthesized, characterization of their mechanical properties and microstructures was performed as described in the following section.

Hardness analysis:

The mechanical properties of the synthesized Al-Cu and Al-Cu-Zn alloys were estimated by assessing the hardness behavior of each. The hardness values of the four alloys in both the as-cast and annealed conditions were measured using a nano-indentation system (Nano test Vantage). The samples were prepared using the standard metallurgy procedure described in Section (2.2). Additionally, the samples were polished with a cloth using diamond pastes with decreasing particle sizes of 6, 3, 0.5, 0.25 and 0.1 μm. The hardness value for each alloy was estimated as an average of eight measurements made at different locations on the sample surface. An example of the indention impact on the alloy surface is shown in Figure B.5.

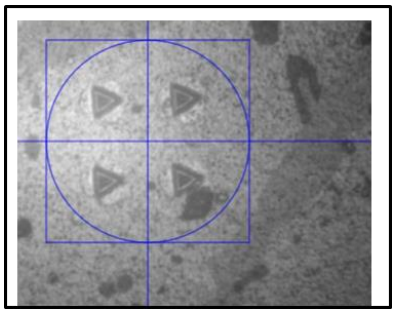

Figure B. 5 Image of the indention impact on the alloy surface.

The average hardness values for the four synthesized alloys in as-cast condition and in annealed condition are shown in Figure B.6. Overall, it is clear that our synthesized alloys possess excellent hardness characteristics. The lowest recorded hardness value was 2.2 GPa for the Al – 50 at.% Cu – 30 at.% Zn sample in the as-cast condition, while the highest hardness value recorded was 6.6 GPa for the same alloy in annealed condition.

To explain this interesting hardness behavior, the microstructure of each specific alloy after exposure to each set of heat treatment conditions was investigated as described in the next section.

Microstructural evaluation:

The microstructures of the synthesized alloys were examined using XRD and SEM/EDX analyses. Table B.1 summarizes the evaluation of the microstructures of

all four alloys in as-cast and annealed condition. The different phases found to exist in each sample are also identified.

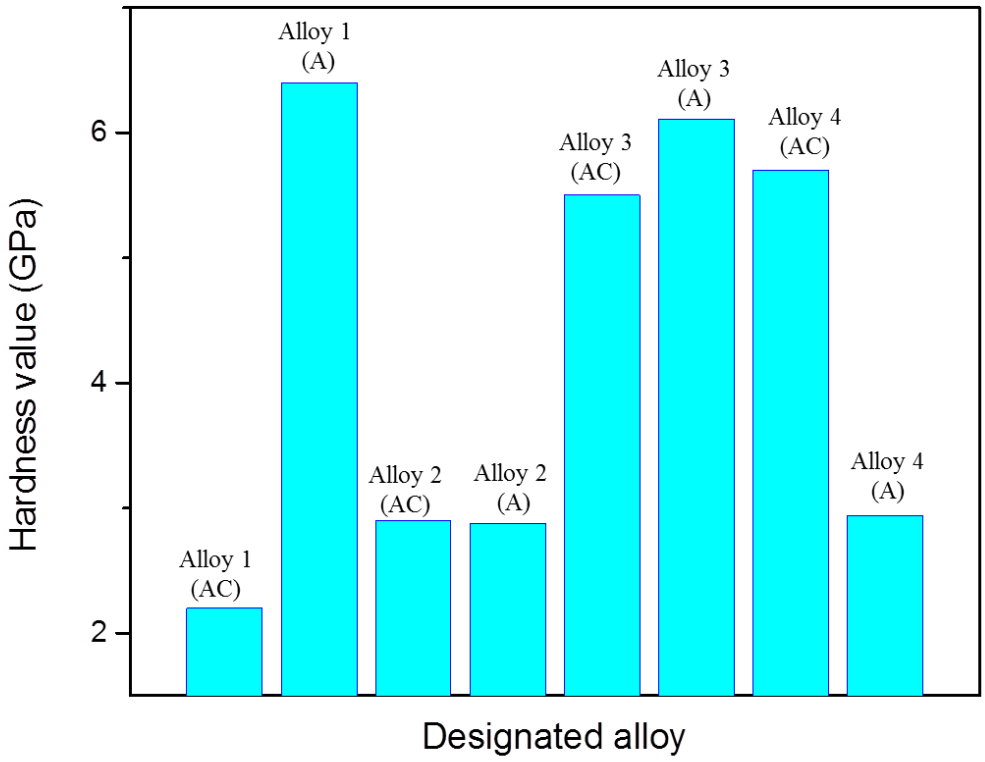

Figure B. 6 Hardness behavior for all synthesis alloys: Alloy 1 (Al – 30 at. % Cu – 20 at.% Zn), Alloy 2 (Al – 30 at. % Cu – 10 at.% Zn), Alloy 3 (Al – 30 at. % Cu – 4 at.% Zn) and Alloy 4 (Al – 33 at.% Cu). (AC) is referred to "as cast condition" and A is referred to "annealed condition".

From Table B.1, it is clear that the Al-50 at.% Cu-30 at.% Zn alloy possesses an exceptionally interesting microstructure that contains strength-providing phases. Annealing the alloy causes these "strength phases" to reach equilibrium and hence drastically improves the hardness of the material (Figure B.6).

Different studies regarding the Al-Cu-Zn phase diagram and the properties of these metallic alloys can be found in references [168-170].

In this Appendix, an approach for synthesizing new alloys with good mechanical properties has been proposed. A high-resolution analytical tool such as APT (performed in a manner similar to that described in Section 3.5) could provide

additional insight into the microstructure of the synthesized alloys. In a broader sense, an investigation into the correlation between the atomic arrangement within materials produced and their physical properties is instrumental to improving existing alloys and discovering new ones.

Table B.1 A summary of the microstructure evaluation of synthesized alloys.

Alloy type	XRD	SEM/EDX
Al – 30 at. % Cu – 20 at.% Zn (As cast).	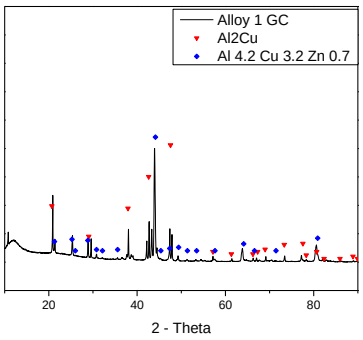	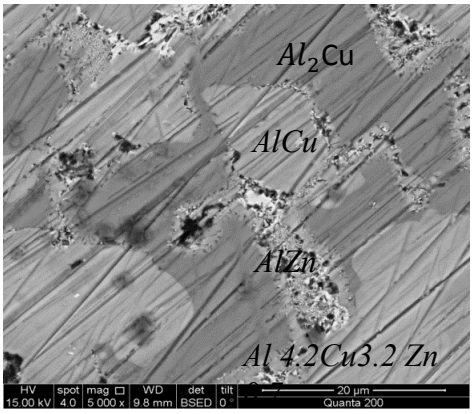 Identified phases: $\theta'(Al_2Cu)$, $\tau(Al_4Cu_3Zn)$ and $\theta(AlCu)$.
Al – 30 at. % Cu – 20 at.% Zn(Annealed).	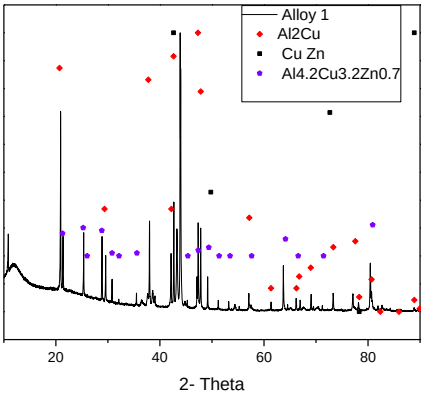	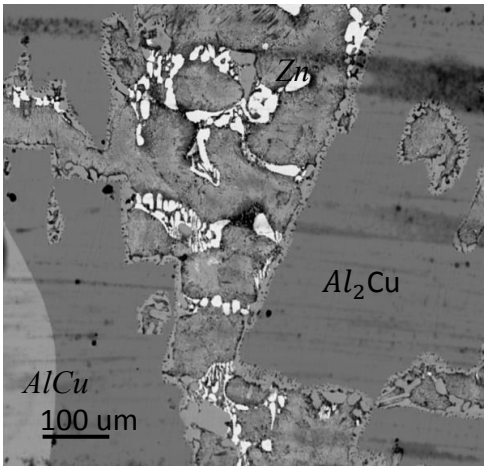 Identified phases: $\theta'(Al_2Cu)$,$\tau(Al_4Cu_3Zn)$, $\beta(CuZn)$ and $\theta(AlCu)$.

Alloy type	XRD	SEM/EDX
Al – 30 at. % Cu – 10 at.% Zn (As cast).	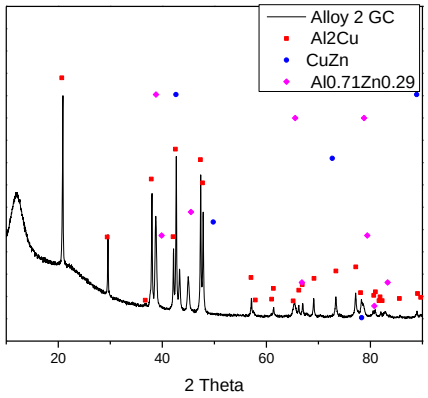	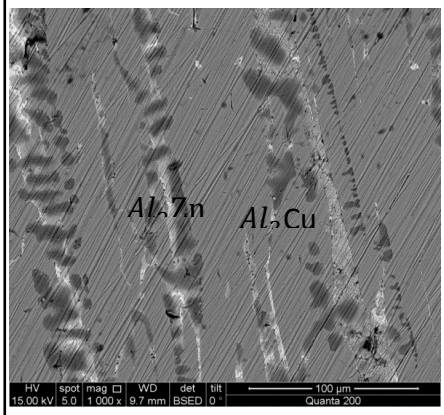 Identified phases: $\theta'(Al_2Cu)$, $\eta(Al_2Zn)$ and $\beta(CuZn)$.
Al – 30 at. % Cu – 10 at.% Zn (Annealed).	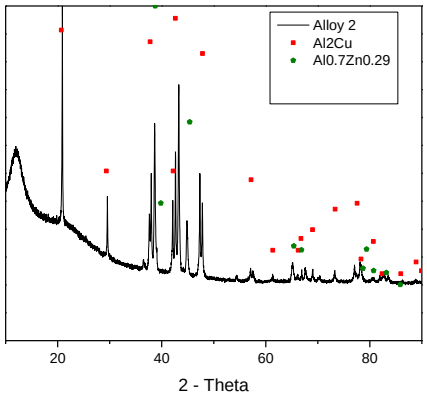	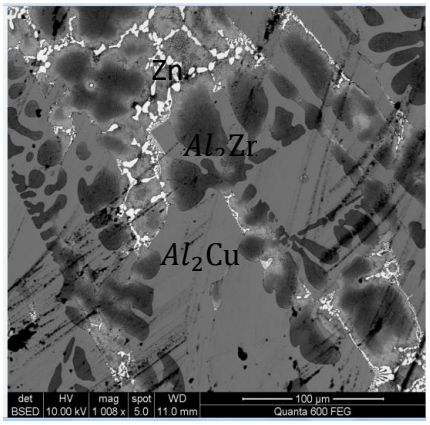 Identified phases: $\theta'(Al_2Cu)$, $\eta(Al_2Zn)$.
Al – 30 at. % Cu – 4 at.% Zn (As cast).	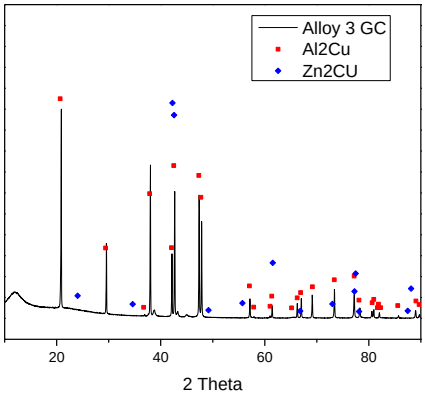	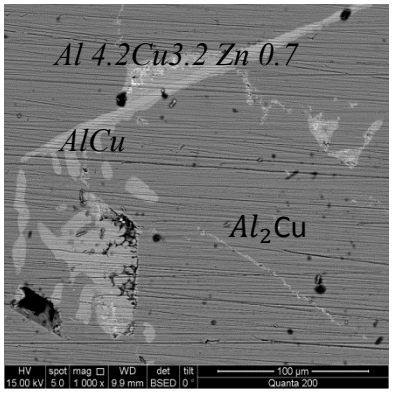 Identified phases: $\theta'(Al_2Cu)$, $\tau(Al_4Cu_3Zn)$, $\gamma\ (Zn_2Cu)$ and $\theta(AlCu)$.

Alloy type	XRD	SEM/EDX
Al – 30 at. % Cu – 4 at.% Zn	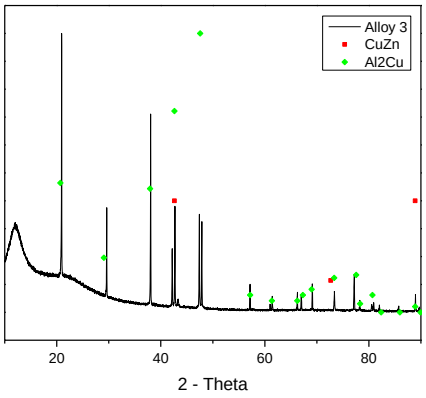	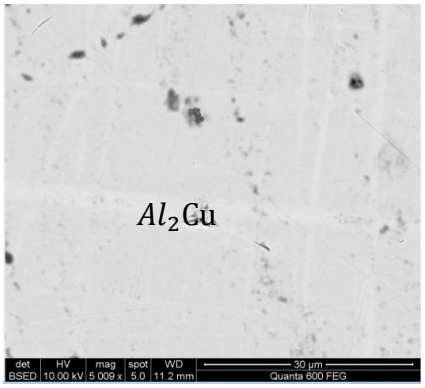 Identified phases: $\theta'(Al_2Cu)$ and $\beta(CuZn)$.
Al – 33 at. % Cu (As cast).	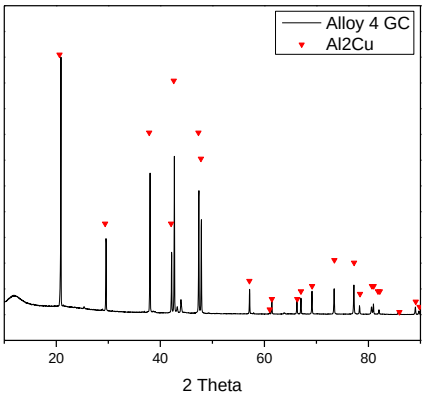	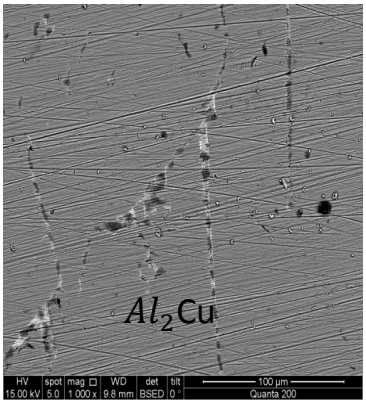 Identified phases: $\theta'(Al_2Cu)$.
Al – 33 at. % Cu (Annealed).	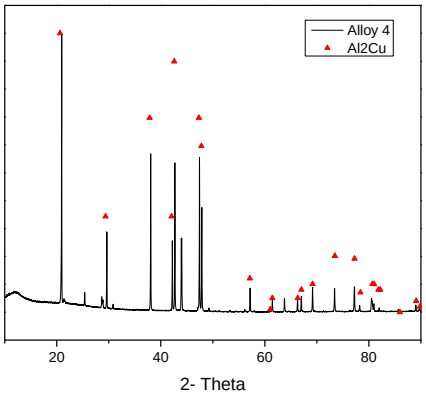	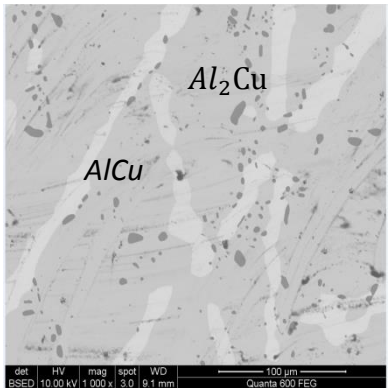 Identified phases: $\theta'(Al_2Cu)$ and $\theta(AlCu)$.

References

1. Firth, N., *Aerospace research at Alcan, Voreppe*, Aluminum International Today, 2010.
2. Totten , G.E. and MacKenzie, D.S., *Physical metallurgy and procssess*, in *Handbook in Aluminum*, Editor. Dekker, M., 2003, Inc: NY, USA.
3. Polmear, I.J., *Light alloys - Metallurgy of the Light Metals*, 1995, Arnold, London.
4. Starke Jr, E.A. and Staley, J.T., *Application of modern aluminum alloys to aircraft*, Progress in Aerospace Sciences, 1996, 32(2–3), p. 131-172.
5. Ekvall, J.S., Rhodes, J.E. and Wald,C.G., *Methodology of Evaluating Weight Savings FromBasic Material Properties*, in *Design of Fatigue and Fracture Resistant Structures*, 1982, ASTMSTP 761(American Society for Testing and Materials), p. 328–341.
6. Quist, W.E., Harinarayanan, G.H. and Wingert, L. *In Aluminum -Lithium Alloys II*, in *TMS-AIME*, Editors.. Starke Jr, E.A. and Sanderd, T.H. 1984, Warrendale, PA, p. 313.
7. Strake Jr, E.A., *The application of the fundamentals of strengthening to the design of new aluminum alloys*, In: Strength of Metals and Alloys Pergamon Press, 1983, ICSMA 6, p. 1025-1044.
8. Starke Jr, E.A., Sanders Jr, T.H. and Palmer, I.G., *New Approaches to Alloy Development in the Al-Li System*, Journal of Metals, 1981, 33(8), p. 24-33.
9. Jata, K.V. and Starke, E.A., *Fatigue crack growth and fracture toughness behavior of an Al-Li-Cu alloy*, Metallurgical Transactions A, 1986, 17(6), p. 1011-1026.
10. Miller, W.S., Cornish, A.J., Tichener, A.P. and Bennet, D., *In Aluminum - Lithium Alloys II*, in *TMS - AIME*, Editors. Strake Jr, E.A. and Sanders, T.H., 1984, Warrendale, PA.
11. Lee, K.H., Lee, Y.J. and Hiraga, K., *Precipitation behavior in the early stage of aging in an Al - Li - Cu - Mg - Zr - Ag (Weldalite 049) alloy*, Journal of Material Research, 1998, 14.
12. The Aluminum Association, *Aluminum Standards and Data*, 1984, Washington D.C.
13. Polmear, I.J., *Light Alloys From Traditional Alloys to Nanocrystals*, 2006, ELSEVIER.
14. Mohamed, A.M.A. and Samuel, F.H., *A Review on the Heat Treatment of Al-Si-Cu/Mg Casting Alloys*, Heat Treatment - Conventional and Novel Applications, 2012.
15. Wang, S.C. and Starink, M.J., *Precipitates and intermetallic phases in precipitation hardening Al – Cu – Mg – (Li) based alloys*, International Materials Reviews, 2005, 50, p. 193 - 215.

16. Hardy, H.K. and Silcock, J.M., *The Phase Sections at 500 and 350°C of Al Rich Al-Cu-Li Alloys,* Journal of Institute of Material, 1955-1956, 84, p. 423-428.
17. Effenberg, G. and Ilyenko, S., *Al-Cu-Li (Aluminium-Copper-Lithium)*, in *Non-Ferrous Metal Systems. Part 2*, 2007, Springer Berlin Heidelberg, p. 1-42.
18. Ringer, S.P. and Hono, K, *Microstructural Evolution and Age Hardening in Aluminium Alloys: Atom Probe Field-Ion Microscopy and Transmission Electron Microscopy Studies,* Materials Characterization, 2000, 44(1–2), p. 101-131.
19. Zahra, A.M., Zahra, C.Y., Alfonso, C. and Charai, A., *Comments on cluster hardening in an aged Al-Cu-Mg alloy,* Scripta Materialia, 1998, 39(11), p. 1553-1558.
20. Muddle, B.C. and Polmear ,I. J., *The precipitate phase in Al-Cu-Mg-Ag alloys.* Acta Metallurgica Material, 1989, 37, p. 777.
21. Laird, C. and Aaronson, H.I., *Structure and Migration Kinetics of Alpha: Theta Prime Boundaries in Al-4 Pct Cu: Part I-Interfacial Structures,* Transaction Metallurgical Society AIME, 1968, 242, p. 1393.
22. Gayle, F., Vander Sande, J. and McAlister, A.J., *The Al-Li (Aluminum-Lithium) system,* Bulletin of Alloy Phase Diagrams, 1984, 5(1), p. 19-20.
23. Starke, E. A., *Aluminum Alloys - Contemporary Research and Applications*, Editors. Vasudevan, A.K. and Doherty, R.D., 31, 1989, Academic Press, Inc.
24. Kumar, K.S., Brown, S.A. and Pickens, J.R. *Microstructural evolution during aging of an AlCuLiAgMgZr alloy,* Acta Materialia, 1996, 44(5), p. 1899-1915.
25. Martin, J.W., in *Micromechanisms in particle-hardened alloys*, Editors. Cahn, R.W., Thompson, M.W. and Ward, I.M., 1980, Cambridge University Press: Cambridge, U.K, p. 56.
26. Deschamps, A. and Bréchet, Y., *Influence of quench and heating rates on the ageing response of an Al–Zn–Mg–(Zr) alloy,* Materials Science and Engineering: A, 1998, 251(1–2), p. 200-207.
27. Murray, J., Peruzzi, A. and Abriata, J.P., *The Al-Zr (aluminum-zirconium) system,* Journal of Phase Equilibria, 1992, 13(3), p. 277-291.
28. Kim, J.M., Seong, K.D, Jun, K.H., Shin, K., Kim, K.T. and Jung, W.J., *Microstructural characteristics and mechanical properties of Al–2.5 wt.% Li–1.2 wt.% Cu–xMg alloys.* Journal of Alloys and Compounds, 2007, 434–435, p. 324-326.
29. Whalen, J.B., Zaikina, J.V., Achey, R., Stillwell, R., Zhou, H., Wiebe, C.R. and Latturner, S.E., *Metal to Semimetal Transition in CaMgSi Crystals Grown from Mg−Al Flux,* Chemistry of Materials, 2010. 22(5): p. 1846-1853.
30. Zhang, J., Fan, Z., Wang, Y.Q. and Zhou, B.L., *Equilibrium pseudobinary Al–Mg2Si phase diagram,* Materials Science and Technology, 2001, 17(5), p. 494-496.

31. Zhang, J., Wang, Y.Q., Yang, B. and Zhou, B.L., *Effects of Si content on the microstruture and tensile strength of an in situ Al/Mg2Si composite,* Journal of Material Research, 1999, 14(1), p. 68-74.
32. Song, C.J., Xu, Z.M. and Li, J.G., *Fabrication of in situ Al/Mg 2Si functionally graded materials by electromagnetic separation method,* Composites Part A-applied Science and Manufacturing, 2007, 38(2), p. 427-433.
33. Madelung, O., *Semiconductors: Data handbook*, 2004, Springer.
34. Haasen, P., *Physical Metallurgy*, 2003, Cambridge University Press.
35. Balluffi, R.W., Allen,S.M. and Carter, W.C., *Kinetics of Materials*, 2005: Wiley Interscience.
36. Murayama, M. and Hono, K., *Role of Ag and Mg on precipitation of T1 Phase in an Al-Cu-Li-Mg-Ag Alloy,* Scripta Materialia, 2000.
37. Polmear, I.J., *Aluminium Alloys - A century of Age Hardening.* Materials Forum, 2004, 28.
38. Miller, M.K., *Atom Probe Tomography: Analysis at the Atomic Level*, 2000, New York: Kluwer Academic/ Plenum.
39. Melmed, A.J., *The art and science and other aspects of making sharp tips,* Journal of Vacuuam Science and Technology, 1991, B9(2), p. 601-609.
40. McKenzie, W.R., Marquis, E.A. and Munroe, P.R., *Focused ion beam sample preparation for atom probe tomography,* Microscopy, Science, Technology, Applications and Education, 2010, p. 1800-1810.
41. Gault, B., Moody, M.P., Cairney, J.M. and Ringer, R., *Atom Probe Microscopy*. Springer Series in Materials Science, 2012, Springer, New York.
42. Larson, D.J., Prosa, T.J., Ulfig, R.M., Geiser, B.P. and Kelly, T.F., *Local Electrode Atom Probe Tomography A User's Guide*, 2013, Springer.
43. Al-Kassab, T., Wollenberger, H., Schmitz, G. and Kirchheiem, R., *Tomography by Atom Probe*, in *High Resolution Imaging and Specrtoscopy of Materials*, Editors. Ruhle, M. and Ernst,F., 2003, Springer series in Materials Science, Berlin Heidellberg, p. 271-320.
44. Hellman, O.C., Vandenbroucke, J.A., Rusing, J., Isheim, D. and Seidmen, D.N., *Analysis of three-dimensional atom-probe data by the proximity histogram,* Microscopy and Microanalysis, 2000, 6(5), p. 437-444.
45. Hellman, O.C., Du Rivage, J.B. and Seidman, D.N., *Efficient sampling for three-dimensional atom probe microscopy data,* Ultramicroscopy, 2003, 95, p. 199-205.
46. Isheim, D., Gagliano, M.S., Fine, M.E. and Seidman, D.N., *Interfacial segregation at Cu-rich precipitates in a high-strength low-carbon steel studied on a sub-nanometer scale,* Acta Materialia, 2006, 54(3), p. 841-849.
47. Vaumousse, D., Cerezo, A. and Warren, P.J., *A procedure for quantification of precipitate microstructures from three-dimensional atom probe data,* Ultramicroscopy, 2003, 95(0), p. 215-221.
48. Williams, D.B. and Carter, C.B., *Transmission Electron Microscopy*, Springer, 2009.

49. Wilhelm, F.J., *The preparation of beryllium specimens for transmission electron microscopy by the Knuth system of electropolishing*, Journal of Scientific Instruments, 1964, 41(5), p. 343.
50. Ünlü, N., *Preparation of high quality Al TEM specimens via a double-jet electropolishing technique*, Materials Characterization, 2008, 59(5), p. 547-553.
51. Leng, Y., *Materials Charectrization, Introduction to Microscopic and Spectroscopic Methods*, 2008, Wiley.
52. Fischer-Cripps, A. C ., *Nanoindentation*, 2011, Springer.
53. Starink, M.J., *Analysis of aluminium based alloys by calorimetry: quantitative analysis of reactions and reaction kinetics*, International Materials Reviews, 2004, 49.
54. Warra, A.A. and Jimoh, W.L.O., *Overview of an Inductively Coupled Plasma (ICP) System*, International Journal of Chemical Research, 2011, 3(2), p. 41-48.
55. Graef, M.D. and Mchenry, M.E., *Structure of Materials, An Introduction to Crystallography, Diffraction and Symmetry*, 2007, Cambridge.
56. Pickens, J.R., Heubaum, F.H., Langan, T.J. and Kramer, L.S., *in Aluminum-Lithium Alloys (proc. of the fifth int. Al-Li Conf.)Editors. Sanders, T. H. and Starke, E. A.*, MCE publications Ltd., 1989, p. 1397.
57. Peel, C., *Aluminum alloys for airframes – limitations and developments*, Material Science and Technology, 1986, 2(12), p. 1169-1175.
58. Lequeu P, Smith, K.P., and Danielou, A., *Aluminum-Copper-Lithium Alloy 2050 Developed for Medium to Thick Plate*, Journal of Material Engineering and Performance, 2010, 19(7), p. 841.
59. Sanders, J.H., *Investigation of Grain Boundary Chemistry in Al-Li 2195 Welds using Auger Electron Spectroscopy*, Thin Solid Films, 1996, 227, p. 121 - 127.
60. Kissel, J.R., Pantelakis, S.G. and Haidemenopoulos, G.N., *Aluminum and Aluminum Alloys*, 2004, New Jersey, Wiiley.
61. McNamara, D.K., Pickens, J.R. and Heubaum. F.H., *In: Aluminium-Lithium Alloys*. in *Proc. 6th Int. Aluminium-Lithium Conf*, 1992, DGM.
62. Chen, P.S., Kuruvilla, A.K., Malone, T.W. and Stanton, W.P., *The effects of artificial aging on the microstructure and fracture toughness of Al-Cu-Li alloy 2195*, Journal of Materials Engineering and Performance, 1998, 7(5), p. 682-690.
63. Doglione, R., Mura, L., Verniani, C. and Firrao, D., *Fracture Behaviour of 2195-T8 Aluminium Alloy Plates*, Materials Science Forum, 2002, 396-402, p. 1341-1346.
64. Gayle F.W., Heubaum, F.H., and Pickens, J.R., *Al-Li alloys*, in *in proceedings of the fifth international Al-Li conference*, Editor . Sander , T.H. and Starke, E.A., 1989, MCE publications, Birmingham, U.K, p. 701.
65. Nayan, N., Govind, N., Suseelan, K., Mittal, M.C. and Sudhakaran, K.N., *Studies on Al–Cu–Li–Mg–Ag–Zr alloy processed through vacuum induction*

melting (VIM) technique, Materials Science and Engineering: A, 2007, 454–455(0), p. 500-507.

66. Gregson, P.J. and Flower, H.M., *Microstructural control of toughness in aluminium-lithium alloys,* Acta Metallurgica, 1985, 33(3), p. 527-537.
67. Ward, N., Abad, A., Lee, E.W., Hahn, M., Fordan, E. and Es-Said, O., *The effects of retrogression and reaging on aluminum alloy 2195,* Journal of Material Engineering and Performance, 2011, 20(6), p. 1003.
68. Park, J.K., *Influence of retrogression and reaging treatments on the strength and stress corrosion resistance of aluminium alloy 7075-T6,* Materials Science and Engineering: A, 1988, 103(2), p. 223-231.
69. Wang, Z.M. and Shenoy, R.N., *Microstructural Characterization of Aluminum-Lithium Alloys 1460 and 2195,* Analytical Services and Materials, 1998, NASA/CR-206914.
70. Gayle, F.W. and Vandersande, B., *Phase transformations in the Al-Li-Zr system,* Acta Metallurgica, 1989, 37(4), p. 1033-1046.
71. Winkelman, G.B., Raviprasad, K. and Muddle, B.C., *Orientation relationships and lattice matching for the S phase in Al – Cu – Mg alloys,* Acta Materialia, 2007, 55, p. 3213.
72. Itoh, G., Cui, Q., and Kanno, M., *Effects of a small addition of magnesium and silver on the precipitation of T1 phase in an Al-4%Cu-1.1%Li-0.2%Zr alloy,* Materials Science and Engineering: A, 1996, 211(1–2), p. 128-137.
73. Shenoy, R.N. and Howe, J.M., *A differential scanning calorimetric study of a Weldalite type alloy,* Scripta Metall, 1995, 33(4), p. 651- 655.
74. Balmuth, E.S., *Particle size determination in an Al-3Li alloy using DSC.* Scripta Metallurgica, 1984, 18(4), p. 301-304.
75. Sha, G. and Cerezo, A., *Field ion microscopy and 3-D atom probe analysis of Al3Zr particles in 7050 Al alloy,* Ultramicroscopy, 2005, 102(2), p. 151-159.
76. Polmear, I.J., *Light Alloys*, in *Metallurgy and Materials Science Series (second ed.),*1989, Edward Arnold, London, p. 97.
77. Chen, Z., Zhag, K. and Fan, L., *Combinitave hardening effects of precipitation in a commerical agerd Al-Cu-Li-X alloy*, Materials Science and Engineering: A, 2013, 588, p. 59-64.
78. Decreus, B., Deschamps, A., De Geuser, F., Donnadieu, P., Sigil, C. and Weyland, M.,*The influence of Cu/Li ratio on precipitation in Al–Cu–Li–x alloys,* Acta Materialia, 2013, 61(6), p. 2207-2218.
79. Khan, A.K. and Robinson, J.S., *Effect of cold compression on precipitation and conductivityof an Al–Li–Cu alloy,* Journal of Microscopy, 2008, 232(3), p. 534-538.
80. Cassada, W.A., Shiflet, G.J. and Starke, E.A., *The effect of plastic deformation on Al2CuLi (T 1) precipitation,* Metallurgical Transactions A, 1991, 22(2), p. 299-306.
81. Schulthess, T., Turchi, P., Gonis, A. and Nieh, T., *Systematic study of stacking fault energies of random Al-based alloys,* Acta Materialia, 1998, 46, p. 2215.

82. Howe, J.M., Lee, J. and Vasudevan, A.K., *Behavior of T1 Precipitate Plates in an Al-2Li-1Cu Alloy,* Metallurgical Transactions A, 1988, 23(279).
83. Gault, B., De Geuser, F., Gabble, B.M., Ringer, S.R. and Muddle, B.C., *Atom probe tomography and transmission electron micrpscopy characterisation of precipitation in an Al - Cu - Li - Mg - Ag alloy,* Ultramicroscopy, 2011.
84. Gayle, F.W., *Structure and properties during ageing of ultra-high strength Al-Cu-Li-Ag-Mg alloy,* Scripta Metallurgical et Material, 1990, 24, p. 79-84.
85. Araullo-Peters, V., Gault, B., De Geuser, F., Deschamps, A. and Cariney, J.M., *Microstructural evolution during ageing of Al–Cu–Li–x alloys,* Acta Materialia, 2014, 66(0), p. 199-208.
86. Strake Jr, E.A., and Bhat, B.N., *Technical Summary In: Aluminum - Lithium Alloys for Aerospace Application Workshop,* NASA Conference Publication, 1994, 3287.
87. Crooks, R., Wang, Z., Levit, V.I. and Shenoy, R.N., *Microtexture, micro structure and plastic anisotropy of AA2195,* Materials Science and Engineering: A, 1998, 257(1), p. 145-152.
88. Chen, P.S. and Bhat, B.N., *Time - Temperature - Precipitation Behavior in Al - Li Alloy 2195,* 2002, NASA/ TM, 211548, Albama.
89. Menand, A., Al-Kassab, T., Chambreland, S. and Sarrau, J.M., *Atom-Probe Study of Aluminium-Lithium Alloys,* Journal of De Physics, 1988, 49-C6, p. 353.
90. Terrones, L.A.H. and Monteiro,S.N., *Composite precipitates in a commercial Al–Li–Cu–Mg–Zr alloy.* Materials Characterization, 2007, 58(2), p. 156-161.
91. Schmitz, G., Hono, K. and Haasen, P., *High resolution electron microscopy of the early decomposition stage of Al-Li alloys,* Acta Metallurgica et Materialia, 1994, 42(1), p. 201-211.
92. Suwas, S. and Gurao, N.P., *Crystallographic texture in Materials,* Journal of the Indian Institute of Science, 2008, 88(2).
93. Kellington,S. H., Loveridge, D. and Titman, J.M., *The lattice parameters of some alloys of lithium,* Journal of Applied Physics: D, 1969, 2.
94. Vurpillot, F., Bostel, A., Menand, M. and Blaveltte, D., *Trajectories of field emitted ions in 3D atom-probe,* The European Physical Journal Applied Physics, 1999, 6, p. 217-221.
95. Vaithyanathan, V., Wolverton, C. and Chen, L.Q., *Multiscale Modeling of Precipitate Microstructure Evolution,* Physical Review Letters, 2002, 88(12), p. 125503.
96. Vaithyanathan, V., Wolverton, C. and Chen, L.Q., *Multiscale modeling of* θ' *precipitation in Al–Cu binary alloys,* Acta Materialia, 2004, 52(10), p. 2973-2987.
97. Biswas, A., Siegel, D.J., Wolverton, C. and Seidman, N.D., *Precipitates in Al–Cu alloys revisited: Atom-probe tomographic experiments and first-principles calculations of compositional evolution and interfacial segregation,* Acta Materialia, 2011, 59(15), p. 6187-6204.

98. Ünlü, N., Gable, B.M., Shiflet, G.J. and Starke Jr, E.A., *The effect of cold work on the precipitation of Ω and θ' in a ternary Al-Cu-Mg alloy,* Metallurgical and Materials Transactions A, 2003, 34(12), p. 2757-2769.
99. Donnadieu, P., Shao, Y., De Geuser, F., Botton, G.A., Lazer, S., Cheynet, M., De Boissiea, M. and Deschamps, A., *Atomic structure of T1 precipitates in Al–Li–Cu alloys revisited with HAADF-STEM imaging and small-angle X-ray scattering,* Acta Materialia, 2011, 59(2), p. 462-472.
100. Huang, J.C. and Ardell, A.J., *Crystal structure and stability of T 1, precipitates in aged Al–Li–Cu alloys,* Materials Science and Technology, 1987, 3(3), p. 176-188.
101. Van Smaalen, S., Meetsma, A., Deboer, J.L. and Bronsveld, P.M., *Refinement of the Crystal Structure of Hexagonal Al2CuLi,* Solid State Chemistry, 1990, 85, p. 293-298.
102. Dwyer, C., Weyland, M., Chang, L.Y. and Muddle, B.C., *Combined electron beam imaging and ab initio modeling of T1 precipitates in Al–Li–Cu alloys,* Applied Physics Letters, 2011, 98(20), p. 201909.
103. Sabirov, I., Murashkin, M.Y. and Valiev, R.Z. *Nanostructured aluminium alloys produced by severe plastic deformation: New horizons in development,* Materials Science and Engineering: A, 2013, 560(0), p. 1-24.
104. Straumal, B., Korneva, A. and Zięba, P., *Phase transitions in metallic alloys driven by the high pressure torsion,* Archives of Civil and Mechanical Engineering, 2014, 14(2), p. 242-249.
105. Kamat, R.G., Newman, J.M., Sawtell, R.R. and Lin, J.C., *2xxx Aluminum Alloys and Methods For producing the Same,* in *Patent Application Publication,* 2014, U.S.A.
106. Rioja, R.J., Bretz, P.E., Sawtell, R.R., Hunt, W.H. and Ludwiczak, E.A., *Aluminum Alloys: Their Physical and Mechanical Properties*, in *Conference Proceedings University of Virginia,* 1986, Charlottesville, VA.
107. Gayle, F.W. and Goodway, M., *Precipitation hardening in the first aerospace aluminum alloy: The Wright flyer crankcase,* Science, 1994., 266(5187), p. 1015-1017.
108. Konno, T.J., Hiraga, K. and Kawasaki, M., *Guinier-Preston (GP) zone revisited: Atomic level observation by HAADF-TEM technique,* Scripta Materialia, 2001, 44(8-9), p. 2303-2307.
109. Gerold, V., *On the structures of Guinier-Preston zones in Al{single bond}Cu alloys introductory paper,* Scripta Metallurgica, 1988, 22(7), p. 927-932.
110. Silcock, J.M., *The [theta]' structure in aluminium-copper alloys,* Acta Cryst, 1956, 9, p. 680.
111. Moody, M.P., Stephenson, L.T., Geguerra, A.V. and Ringer, S.P., *Quantitative binomial distribution analyses of nanoscale like-solute atom clustering and segregation in atom probe tomography data,* Microscopy Research and Technique, 2008. 71(7), p. 542-550.

112. Murch, G.E., Bruff, C.M. and Mehrer, H., *Chemical diffusion tables*, in *Landolt-Börnstein - Group III Condensed Matter*, SpringerMaterials - The Landolt-Börnstein Database.

113. Silcock, J.M., Heal, T.J. and Hardy, H.K., *Structural ageing characteristics of aluminum - copper alloys*, Journal Institute of Meterial, 1953–1954. 82, p. 239.

114. Boyd, J.D. and Nicholson, R.B.m *The coarsening behaviour of* θ'' *and* θ' *precipitates in two Al-Cu alloys*, Acta Metallurgica, 1971, 19(12), p. 1379-1391.

115. Hono, K., Babu, S.S., Hiraga, K., Okano, R. and Sakurai, T., *Atom probe study of early stage phase decomposition in an Al-7.8 at.% Li alloy*, Acta Metallurgica et Materialia, 1992, 40(11), p. 3027-3034.

116. Noble, B. and Thompson, G.E., *Precipitation Characteristics of Aluminium-Lithium Alloys*, Metal Science, 1971, 5(1), p. 114-120.

117. Baumann, S.F. and Williams, D.B., *Effects of capillarity and coherency on δ' (Al3Li) precipitation in dilute Al-Li alloys at low undercoolings*, Acta Metallurgica, 1985, 33(6), p. 1069-1078.

118. Khachaturyan, A.G., Lindsey, T. E. and Morris, J. J. W., *Theoretical Investigation of the Precipitation of* δ' *in AI-Li*, Metallurgical Transactions A, 1988, 19, p. 249.

119. Al-Kassab, T., Menand, A., Chambreland, S. and Hassen, P., *The early stages of decomposition of Al-Li alloys*, Surface Science, 1991, 266, p. 333-336.

120. Ceresaraa, S., Giardaa, A. and Sanchéza, A., *Annealing of vacancies and ageing in Al-Li alloys*, Philosophical Magazine, 1977, 35(1), p. 97 - 110.

121. Dorward, R.C., *Solidus and solvus isotherms for quaternary Al-Li-Cu-Mg alloys*, Metallurgical Transactions A, 1988, 19(6), p. 1631-1634.

122. Moser, Z., Gasior, W., Onderka, B., Sommer, F. and Kim, Z., *Al-Cu-Li system electromotive force and calorimetric studies—Phase diagram calculations of the Al-Rich part*, Journal of Phase Equilibria, 2002, 23(2), p. 127-133.

123. Wang, K., Garoche, P. and Calvayrac. Y., *Electronic Properties of the Quasi-Crystalline Alloy AlLiCu*, in *Proc. ILL/CODEST Workshop on Quasicrystalline Materials*, 1988, Singapore, World Scientific.

124. Wang, K. and Garoche, P., *Phason-strain-field influences on low-temperature specific heat in icosahedral quasicrystals Al-Li-Cu and Al-Fe-Cu*, Physical Review B, 1997, 55(1), p. 250-258.

125. Dubost, B., Colinet, C. and Ansara, I., *An Experimental and Thermodynamic Study of the Al-Cu-Li Equilibrium Phase Diagram*, in *5th Int. Aluminium-Lithium Conf*, Editors. Starke Jr,E.A., Sanders, T.H., 1989, Materials and Component Engineering Publications:,Williamsburg, Va, USA ,p. 28 - 31

126. Noble, B. and Thompson, G.E., $T_1(Al_2CuLi)$ *Precipitation in Aluminium-Copper-Lithium Alloys*, Metarial Science, 1972, 6, p. 167-174.

127. Dlubek,G., Krause, S., Krause, H., Berasina, A.L., Mikhalenkav, V.S. and Chuistov, K.V., *Positron studies of precipitation phenomena in Al-Li and in Al-LI-X (X=Cu, Mg or Sc) alloys,* Journal of physics: Condensed Matter, 1992, 4: p. 6317.
128. Hornbogen, E., *Formation of nm-Size Dispersoids from Supersaturated Solid Solutions of Aluminium,* Material Science Forum, 2000, 331–337, p. 879.
129. Kulkarni, G.J., Banerjee, D. and Ramachandran, T.R., *Physical metallurgy of aluminum-lithium alloys,* Bulletin of Materials Science, 1989, 12(3-4), p. 325-340.
130. Blavette, D., Bostel, B., Deconihant, B., Menand, A., *An atom probe for three-dimensional tomography,* Nature, 1993, 363(6428), p. 432-435.
131. Kellogg, G.L. and Tsong, T.T., *Pulsed-laser atom-probe field-ion microscopy.*, Journal of Applied physics, 1980, 51(2), p. 1184-1193.
132. Gault, B., Vurpillot, F., Vella, A., Gilbert, M., Menand, A., Blavette, D. and Deconinhaut, B., *Design of a femtosecond laser assisted tomographic atom probe,* Review of Science Instrument, 2006, 77(043705).
133. Liu, F. and Tsong, T.T., *Numerical calculation of the temperature evolution and profile of the field ion emitter in the pulsed-laser time-of-flight atom probe,* Review of Science Instrument, 1984, 55(1779).
134. Martin, O.J. and Girard, C., *Controlling and tuning strong optical field gradients at a local probe microscope tip apex,* Applied physics letters, 1997, 70(6), p. 705-707.
135. Vella, A., Vurpillot, F., Gault, B., Menand, A. and Deconihout, B., *Evidence of field evaporation assisted by nonlinear optical rectification induced by ultrafast laser,* Physical Review B, 2006, 73(16), p. 165416.
136. Cerezo, A., Clifton, P.H., Comberg, A. and Smith, G.D.W., *Aspects of the performance of a femtosecond laser-pulsed 3-dimensional atom probe,* Ultramicroscopy, 2007, 107(9), p. 720-725.
137. Cerezo, A., Smith, G.D.W. and Clifton, p.H., *Measurement of temperature rises in the femtosecond laser pulsed three-dimensional atom probe,* Applied physics letters, 2006, 88(15).
138. Vurpillot, F., Houard, J., Vella, A. and Deconihout, B., *Thermal response of a field emitter subjected to ultra-fast laser illumination,* Journal of Applied Physics: D, 2009, 42(125502).
139. Koelling, S., Innocenti, N, Hellings, G., Gillbert, M., Kambham, A.K., De Meyer, K. and Vandervorst, W., *Characteristics of cross-sectional atom probe analysis on semiconductor structures,* Ultramicroscopy, 2011, 111(6), p. 540-545.
140. Houard, J., Vella, A., Vurpillot, F. and Deconihout, B., *Three-dimensional thermal response of a metal subwavelength tip under femtosecond laser illumination.* Physical Review B, 2011, 84(3), p. 033405.
141. Sanders, T.H., Starke Jr, E.A., *Aluminum-lithium alloys*, in *proceding of second imternational aluminum-lithium conference,* 1984, The metalluurgical socoety of AIME, Warrendale, Pennsylvania.

142. Nozato, R. and Nakai, G., *Thermal Analysis of Precipitation in Al - Li Alloys,* Transactions of the Japan Institute of Metals, 1977, 18(10), p. 679-689.
143. Hallstedt, B. and Kim,O., *Thermodynamic Assessment of the Al-Li System,* International journal of Metarial Research, 2007, 98(10), p. 961-969.
144. Krug, M.E., Dunand, D.C. and Seidman, D.N., *Composition profiles within Al3Li and Al3Sc/Al3Li nanoscale precipitates in aluminum,* Applied physics letters, 2008, 92(12), p. 124107.
145. Williams, D.B. and Edington, J.W., *The Precipitation of δ'(Al3Li) in Dilute Aluminum– Lithium Alloys,* Metal Science and Heat Treatment, 1975, 9(1), p. 529-532.
146. Gault, B., Muller, M., Fontaine, A.La., Moody, M.P., Sharig, A., Cerezo, A., Ringer, S.P. and Smoth, G.D.W., *Influence of surface migration on the spatial resolution of pulsed laser atom probe tomography,* Journal of Applied physics, 2010, 108(044904).
147. Marquis, E.A., Geiser, B.P., Prosa, T.J. and Larson, D.J., *Evolution of tip shape during field evaporation of complex multilayer structures,* Journal of Microscopy, 2011, 241(3), p. 225-233.
148. Shariqa, A., Mutasa, M., Wedderhoffa, K., Kleinb, C., Hortenbachc, H., Teichertc, S., Küchera, P.and Gerstld, S.S.A., *Investigations of field-evaporated end forms in voltage- and laser-pulsed atom probe tomography,* Ultramicroscopy, 2009, 109, p. 472–479.
149. Miller, M.K., Cerezo, A., Hetherington, M.G. and Smith, G.D.W., *Atom Probe Field-Ion Microscopy,* 1996, New York, Oxford University Press.
150. Noble, B. and Bray, S.E., *On the α(Al)/δ'(Al3Li) metastable solvus in aluminium–lithium alloys,* Acta Materialia, 1998, 46(17), p. 6163-6171.
151. Jayanth, C.S. and Nash, P., *Factors affecting particle-coarsening kinetics and size distribution,* Journal of Materials Science, 1989, 24(9), p. 3041-3052.
152. Murch, G.E., Bruff, C.M. and Mehrer, H., *Chemical diffusion tables,* Landolt-Börnstein - Group III Condensed Matter,1990, SpringerMaterials.
153. Okuda, H., Tanaka, M., Osamura, K. and Anemiya, Y., *Synchrotron-radiation small-angle scattering measurements of the reversion process of δ' precipitates in Al-8.1%Li binary alloy,* Acta Metallurgica et Materialia, 1993, 41(6), p. 1733-1738.
154. Gemma, R., Al-Kassab, T., Kirchheim, R. and Pundt, A., *APT analyses of deuterium- loaded Fe/V multi-layered films,* Ultramicroscopy, 2009, 109, p. 631-636.
155. Mcdonell, W.R., Albensius, E.L. and Benjamin, R.W., *Aluminum-Lithuim target behaviour*, in *Report WSRC – RC – 89 – 970*,1989, Westinghouse Savannah River Company, Savannah River Site, Aiken SC, USA.
156. Kim, W., Zide, J., Gossard, A., Klenov, D., Stemmer, S., Shakouri, A. and Majumdar, A., *Thermal Conductivity Reduction and Thermoelectric Figure of Merit Increase by Embedding Nanoparticles in Crystalline Semiconductors,* Physical Review Letters, 2006, 96(4), p. 045901.

157. Hirsch, J. and Al-Samman, T., *Superior light metals by texture engineering: Optimized aluminum and magnesium alloys for automotive applications,* Acta Materialia, 2013, 61(3), p. 818-843.
158. Hasting, H.S., Froseth, A.G., Andersen, S.J., Vissers, R., Walmsley, J.C., Marioara, C.D. Danoix, F.,Lefebvre, W. and Holmestad, R., *Composition of β" precipitates in Al–Mg–Si alloys by atom probe tomography and first principles calculations,* Journal of Applied Physics, 2009, 106(12), p. 123527.
159. Kanatzidis, M.G., Pottgen, R. and Jeitschko, W., *The metal flux: a preparative tool for the exploration of intermetallic compounds,* Angew Chem, 2005, 4(43), p. 6996 - 7023.
160. Sieve, B., Gray, D.L., Henning, R., Bakas, T., Schultz, A.J. and Kanatzidis, M.G., *Al Flux Synthesis of the Oxidation-Resistant Quaternary Phase REFe4Al9Si6 (RE = Tb, Er),* Chemistry of Materials, 2008, 20(19), p. 6107-6115.
161. Ma, X., Chen, B. and Latturner, S.E., *Synthesis and Properties of New Multinary Silicides R5Mg5Fe4AlxSi18–x (R = Gd, Dy, Y, x ≈ 12) Grown in Mg/Al Flux,* Inorganic Chemistry, 2012, 51(11), p. 6089-6095.
162. Ma, X., Lu, J., Whalen, J.B. and Latturner, S.E., *Flux Growth and Magnetoresistance Behavior of Rare Earth Zintl Phase EuMgSn,* Inorganic Chemistry, 2013, 52(6), p. 3342-3348.
163. Latturner, S.E. and Kanatzidis, M.G., *RE(AuAl2)nAl2(AuxSi1−x)2: A New Homologous Series of Quaternary Intermetallics Grown from Aluminum Flux,* Inorganic Chemistry, 2008, 47(6), p. 2089-2097.
164. Canfielda, P.C. and Fiska, Z., *Growth of single crystals from metallic fluxes,* Philosophical Magazine Part B, 1992, 65(6), p. 1117-1123.
165. Chakraborti, N. and Lukas, H.L., *Thermodynamic optimization of the Mg-Al-Si phase diagram,* Calphad, 1992, 16(1), p. 79-86.
166. Valdez, S., Campillo, B., Perzo, R., Martinez, L. and Garcia, H.A., *Synthesis and microstructural characterization of Al–Mg alloy–SiC particle composite,* Materials Letters, 2008, 62(17–18), p. 2623-2625.
167. Imai, Y., Mori, Y., Nakamuras, S. and Takarabe, K., *Energetic prediction of Mg2Si–Ca2Si pseudobinary system using first-principles calculations,* Journal of Alloys and Compounds, 2013, 558, p. 179-187.
168. Raghavan, V., *Al-Cu-Zn (Aluminum-Copper-Zinc),* Journal of Phase Equilibria and Diffusion, 2010, 31(1), p. 41-42.
169. Abou El-khair, M.T., Daoud, A. and Ismail, A., *Effect of different Al contents on the microstructure, tensile and wear properties of Zn-based alloy,* Materials Letters, 2004, 58(11), p. 1754-1760.
170. Savaşkan, T., Hekimoğlu, A.P. and Pürçek, G., *Effect of copper content on the mechanical and sliding wear properties of monotectoid-based zinc-aluminium-copper alloys,* Tribology International, 2004, 37(1), p. 45-50.

Publication

Conferences

1. M. Khushaim, T. Al-Kassab, T. Boll, F. Haider, J. Leese and M. Kreissle, A study of the 3D microstructure of an aluminum – Lithium Copper based alloy, IFES 2012, proceeding of the 53 th International Field Emission Symposium, University of Alabama, USA, 2102.
2. M. Khushaim, J. Leese, T. Boll, F. Haider and T. Al-Kassab, Tomographic Atom Probe Characterization of Aluminum Lithium Based Alloy, German physical Society meeting, University of Regensburg, Germany, 2013.
3. M. Khushaim, T. Boll, F. Haider and T. Al-Kassab, Atom probe tomography analyses of precipitation in the AA2195 aluminum lithium alloy, German physical Society meeting, Technical University, Dresden, 2014.
4. M. Khushaim, R. Gemma and T. Al-Kassab, Influence of the Laser-Pulse Energy on the Field-Evaporation Behavior of δ' Precipitates in an Aluminum Lithium Alloy, International Conference on Atom Probe Tomography and Microscopy, Stuttgart, Germany, 2014.
5. M. Khushaim, Touching atoms – modern materials design by atom probe tomography, EFFAT-KAUST Lectures Series of Promising Fields, Jeddah, 2014.
6. M. Khushaim, J. Seibert, F. Haider and T. Al-Kassab, Influence of the heat treatment on the precipitation behavior on agehardenable commercial Al based alloys AA2195, German physical Society meeting, Technical University, Berlin, Germany, 2015.
7. M. Khushaim, J. Seibert, F. Haider and T. Al-Kassab, Atom probe tomography studies of the effects of industrial heat treatment on the precipitation kinetics on aluminum alloy 2195, German physical Society meeting, Technical University, Berlin, Germany, 2015.

Articles

1. M. Khushaim, T. Boll, J. Seibert, F. Haider and T. Al-Kassab, Characterization of precipitation in Al-Li alloy AA2195 by means of atom probe tomography and transmission electron microscopy, Advanced in Condensed Matter Physics, Volume 2015, 647684, 2015.
2. M. Khushaim and A. Rothenberger, Influence of Industrial heat treatment on the precipitation kinetics of an Al-Cu-Mg-Ag-Zr alloy, International Journal of Metallurgical and Materials Engineering, 1: 113, 2015
3. M. Khushaim, R. Gemma and T. Al-Kassab, Laser-induced reversion of $\boldsymbol{\delta'}$ precipitates in an Al-Li alloy: Study on temperature rise in pulsed laser atom probe, physics: Instrumentation and Detectors, arxiv 1509.08785, 2015.

4. M. Khushaim, T. Boll and A. Rothenberger, Atom probe study of early stage of precipitation on binary Al – Li, Al – Cu alloys and ternary Al – Li – Cu alloy, submitted.
5. M. Khushaim, R. Gemma, B. Davaasuren and A. Rothenberger, APT study of the growth of a single crystal phase synthesized by an Al molten flux, to be submitted.